BOREXINO

at Gran Sasso

Proposal for a real time detector
for low energy solar neutrinos

VOLUME 1
August 1991

Edited by: G. Bellini, M. Campanella, D. Giugni
Dept. of Physics of the University of Milano
I.N.F.N-Milano
Via Celoria, 16 – 20133 Milano – Italy

R. Raghavan
AT&T Bell Laboratories Murray Hill NJ - U.S.A.

BOREXINO COLLABORATION

C. Arpesella, A. Donati, A. Falgiani, D. Franciotti, R. Tartaglia
Laboratori Nazionali del Gran Sasso
Assergi (AQ) - Italy

S. J. Freedman
University of California
Berkeley CA -USA

M. Deutsch, V. Lia
Massachusetts Inst. of Technology
Cambridge MA - U.S.A.

Yu. Filippov, A. Golubchikov, A. Kulkov,
S. Prakhov, O. Smirnov, O. Zaimidoroga
Joint Inst. for Nuclear Research
Dubna - U.S.S.R.

F. von Feilitzsch, C. Hagner, L. Oberauer, S. Schoenert
Technical University Munich
Garching - Germany

F. Gatti, V. Gracco, G. Manuzio,
G. Testera, S. Vitale
Physics Dept. of the University and INFN
Genova - Italy

G. Heusser
Max-Planck Inst. f. Kernphysik
Heidelberg - Germany

S. Pakvasa
University of Hawaii
Honolulu HI - U.S.A.

P. Trincherini
C.C.R. Euratom, ISPRA, (VA) - Italy.

G. Alimonti, R. Bassini, G. Bellini, S. Bonetti,
S. Brambilla, M. Campanella, W. Cavaletti., P. D'Angelo,
M. di Corato, M. Giammarchi, D. Giove, D. Giugni, P. Inzani,
I. Iori, S. Malvezzi, L. Manduci, I. Manno, E. Meroni,
A. Moroni, L. Perasso, F. Ragusa, G. Ranucci, G. Salmini,
R. Scardaoni, D. Torretta, V. Torri, P. Ullucci
Physics Dept. of the University and INFN
Milano - Italy

T. Kovacs, J. Mitchell, P. Raghavan, R.S. Raghavan
AT&T Bell Laboratories
Murray Hill NJ - U.S.A.

P. Benetti, B. Bertotti, G. Cecchet, A. De Bari,
A. Minoia, L. Pezzotti, A. Perotti
Physics Dept. of the University and INFN
Occupational Medicine Laboratory of the Univesity
Pavia - Italy

B. Alpat, F. Elisei, G. Levi, G. Mantovani
F. Masetti, V. Mazzucato
Physics Dept. of the University and INFN
Perugia - Italy

R. Steinberg
Drexel University
Philadelphia PA - U.S.A.

J. Cilc, J. Dostal, Michael Finger, Miroslav Finger,
Z. Janout, F. Kubalek, M. Tomasek
Charles University, Prague
The Czech Technical University, Prague - Czechoslovakia

F.P. Calaprice
Physics Dept., Princeton University
Princeton NJ - U.S.A.

TABLE OF CONTENTS

VOLUME I

Chapter III – NEUTRINO SIGNALS & SIGNATURES

Chapter IV – NEW NEUTRINO PHYSICS - PROPOSALS AND TESTS

Chapter V – PHYSICS PROGRAM OF BOREXINO

PART II – TECHNIQUE

Chapter VI – THE DETECTOR

Chapter VII – THE LIQUID SCINTILLATOR

Chapter VIII – SIGNAL DETECTION

Chapter IX – FRONT-END AND READ-OUT ELECTRONICS

Chapter X – SIGNAL RESPONSE

Chapter XI – RADIOPURITY OF LIQUID SCINTILLATOR

Chapter XII – BACKGROUND

TABLE OF CONTENTS

VOLUME II

BOREXINO

A REAL TIME DETECTOR FOR LOW ENERGY SOLAR NEUTRINOS

INTRODUCTION

The Sun produces energy by the fusion of four protons into a helium nucleus. The process is accomplished by a chain of nuclear reactions (the "pp" chain) starting with the weak interaction reaction $p+p \rightarrow d+e^{+}+\nu_e$, and making progressively heavier elements upto ^{8}B. The only way to test this fundamental theory of stellar processes is to detect at the earth, the only reaction product that can escape the sun, the weakly interacting neutrino. A rich spectrum of neutrinos is predicted for the pp-chain. The dominant part of the flux (98%) is emitted at energies ≤1 MeV comprising the above "pp" neutrinos and those from the decay of ^{7}Be in the sun. Only a tiny fraction (10^{-4}) of the flux is emitted at higher energies upto 14 MeV, due to the decay of ^{8}B.

Solar neutrino experiments operating so far, are based on two strategies. First, elegant radiochemical techniques have been used to detect the flux at low energies via ^{71}Ga (SAGE, GALLEX) and at high energies, via ^{37}Cl (HOMESTAKE). However, the detection is not real-time, nor is the neutrino energy measurable. Secondly, adapting a high energy method —Cerenkov detection and its directionality—real-time ν detection has been accomplished (KAMIOKANDE-II; K-II). However, because of the low luminosity of the Cerenkov effect and high backgrounds, only the weak ^{8}B ν flux >7.5 MeV can be measured. This technique has been adopted also for both the new detectors in construction —SNO and SUPERKAMIOKA (1 and 22 kTon target masses). Thus, so far, none of the present or future detectors can directly observe the sub-MeV neutrinos from the main energy production reactions in the sun.

We propose to accomplish this task with a new type of detector, BOREXINO to be built at the Gran Sasso Underground Laboratories in Italy. The key technical ingredient is

the detection medium - a scintillation liquid of ultrahigh radioactive purity [10^{-15} to 10^{-16} g (U,Th)/g]. It leads not only to the very low backgrounds needed but a high signal sensitivity stemming from the high luminosity of the scintillator. Borexino will be able to observe neutrinos signals of energy >0.25 MeV. With such a threshold, far below present or proposed real-time detectors, Borexino will focus on the specific real-time observation of **^{7}Be solar neutrinos** using ν-e scattering as the detection reaction.

Over the last 20 years, the results from the Homestake solar neutrino detector of Davis and coworkers and a concurrent development of astrophysical theory have revealed that experiment is in serious disagreement with theory. The solar neutrino flux is much *lower* than that expected from predictions based on the"standard solar model" (SSM) as developed by Bahcall and Ulrich. Indeed, basic revisions of present astrophysical ideas underlying the SSM may be necessary to resolve the discrepancy —often called the "solar neutrino problem" (SNP). The Homestake results have been largely confirmed by K-II (albeit with some difference in detail) by directly counting ^{8}B neutrinos and establishing their solar origin. Recent, very preliminary results from the radiochemical Soviet-American Gallium experiment (SAGE) leave open the possibility of a depletion of the flux of even the relatively model-independent p-p solar neutrinos.

Could non-astrophysical phenomena be the cause of the SNP ? The missing neutrinos may be undetectable in present experiments because they are no longer of electron-type flavour, having been flavour-converted in the solar matter or in the vacuum *en route* to the earth. Such effects arise from non-zero masses and a flavour-mixed structure of the neutrino. The Mikheyev-Smirnov-Wolfenstein (MSW) effect in solar matter is a strong motivator for a search for neutrino flavour conversion using solar neutrinos. Recent indications of a time-variability of the Homestake results could suggest also the possibility of a large neutrino magnetic moment. Stimulated by these developments and facing an apparent astrophysical impasse, the focus of future solar neutrino experiments is on new neutrino physics. The upcoming high energy detectors, SNO and SUPERKAMIOKA, aim to measure the spectral shape of ^{8}B neutrinos and their total flux regardless of flavour using neutral currents, seeking general evidence for flavour conversion.

Crucial information resides, however, in the sub-MeV region of the neutrino spectrum. Specific data on ^{7}Be solar neutrinos is important for solar astrophysics because these neutrinos probe a significant link in the main reaction sequence in the sun, a distinct physical region of solar energy production and a different dependence on the solar temperature as compared to ^{8}B neutrinos. At the same time, these neutrinos offer new

tools for probing neutrino physics independent of solar astrophysics. A key aspect is the **monoenergetic** nature of the ^{7}Be neutrinos. Another is the high flux; though our detector (with a 0.1 kTon target mass) is the smallest of the new devices, the signal rates will be the highest, **~50 events/day** (SSM), two orders of magnitude higher than those typically observed so far. The energy of ^{7}Be neutrinos is in the right range for searching for direct consequences of flavour conversion in the parameter regions indicated by present experiments. Finally, ν-e scattering at low energies (not observed so far), is a sensitive probe of other non-standard neutrino properties. With these tools, Borexino can address key physics and astrophysics questions answerable only at low energies and with such high signal rates. The types of measurements possible in Borexino are summarised below. They will be sharply relevant to the SNP whether present indications of a low Ga signal are confirmed or not.

• Time variation (of various types) of the neutrino signal will be a principal experimental tool in Borexino. The variability provides a signature of the prevailing physics via the type of time-variation and a powerful means for filtering out the ν signal from background. Diurnal variations of the ^{7}Be flux can directly demonstrate **MSW flavour conversion** in a broad parameter region with mass differences $\Delta m^2 < 10^{-6}$ eV^2 (consistent with a low Ga signal). Seasonal flux variations (consistent with larger Ga signals) can reveal the unambiguous presence of **vacuum oscillations**. A scintillator radiopurity of 10^{-15} g/g is sufficient for a sensitive detection of these time-variabilities. The specificity of the temporal effects is adequate to determine the **neutrino parameters**, which lead also to the **astrophysical fluxes** of the ^{7}Be and ^{8}B neutrinos. In this broad parameter range, only Borexino can provide such specific results of major significance to physics and astrophysics.

• A determination of the ^{7}Be ν flux is important if ν physics is not the major cause of the SNP (as indicated by the absence of the above effects and a large Ga signal approaching SSM values). In astrophysical scenarios, the ^{7}Be ν signal in Borexino will also be typically large (~50 events/d). In such cases, a flux determination can be made directly as well as by a temporal effect —the yearly variation via the $1/R^2$ effect due to the earth's orbit. The latter is a direct solar signature for the Borexino signal regardless of new physics or astrophysics. A direct flux measurement is possible with a scintillator purity of ~10^{-16} g/g; even with 10^{-15} g/g purity (corresponding to a background of ~100/day), the yearly variation of the solar signal in Borexino can be filtered out and the ^{7}Be flux can be measured to a precision of ~30% or better in three years of live-time.

• Electron scattering at low energies, the main detection reaction in Borexino, brings a unique bonus — a high sensitivity to a **neutrino magnetic moment**, which can be detected in the low energy recoil electron spectra of ^{7}Be solar neutrinos. If differences in the Homestake vs. K-II results are caused by magnetic ν scattering, the effect will be magnified at low energies. The Borexino signal will be severely incompatible with the Ga signal. In this case, an independent, absolute measurement of the moment (to a limit of $\mu_\nu \sim 2\times10^{-11}\mu_B$) can be made by exposing Borexino "on" and "off" to antineutrinos from a relatively accessible, terrestrially produced (fission-product) radioactive source such as ^{90}Sr.

• While the accent in Borexino is on low energies, a spectral measurement of the high energy ^{8}B neutrinos is also possible, at a rate about three times that at K-II. Though the rate is low compared to that expected in SNO or Superkamioka, Borexino can observe the shape at the important lower energy region. These data offer a high energy back-up evidence for new neutrino physics in parameter regions with $\Delta m^2 < 10^{-5} eV^2$ (with large or small Ga signals).

• In the case of **Majorana neutrinos** with (transition) magnetic moments, the "appearance" of a small flux of solar antineutrinos (>5 MeV) is predicted for parameter regions consistent with a low Ga signal. Sensitive $\bar{\nu}_e$ signatures applicable in Borexino can limit the coupling of Majorana neutrinos in solar magnetic fields to values of the order of $10^{-10}\mu_B$ kGauss.

Almost all the physics results from Borexino will be based on specific signatures of the physics and of solar origin of the signal,without need for specific background determinations. Supplementing these facilities, Borexino will also be equipped with tools for characterising the operating background and calibrating the neutrino flux. The spectroscopic power of the scintillation technique provides the means for on-line monitoring of the detector calibrations and background. The ^{90}Sr source experiment offers not only potential new physics but also a source calibration of the solar signal on a quantitative and absolute basis.

If Borexino is well matched to the new questions of the science, the technology is also ripe, based on more than a decade of experience with a series of water Cerenkov detectors much larger than Borexino. The use of a liquid scintillator instead of water in this general design (as proposed in Borexino) is the *logical next step towards lowering the threshold of real-time neutrino observations to unprecedented levels.* A mixture of trimethylborate (TMB, >80%) and pseudocumene (PC, <20%), both available in large quantities, yields a

high event-luminosity vital for low-energy sensitivity. The basically new technical feature is the ultrahigh radiopurity of the scintillator. The development work in Borexino has focussed on this problem for more than three years with dramatic progress. The range of intrinsic radiopurities of 10^{-15} to 10^{-16} g/g observed so far in the above liquids will be sufficient to carry out the physics program outlined above. We expect to reach the goal of a purity of 10^{-16} g/g in further development. Research on radiopurity will now focus on aspects governing "operational" purity using counting tests with a major new facility—a water-shielded 4-ton liquid scintillation device to be constructed with priority at Gran Sasso. Liquid scintillator batches and ancillary engineering materials to be used in Borexino will be tested and controlled for radiopurity using this facility.

To summarise: we propose to construct a new type of solar neutrino detector based on an ultrapure liquid scintillator to observe low energy solar neutrinos, especially from ^{7}Be in the sun. Such observations are beyond the reach of present or pending solar neutrino detectors. The experiment accents the search for relatively background-independent "appearance" effects with decisive physics implications. The possible scientific results are of immediate relevance to current theoretical questions and could have a dramatic impact on neutrino physics and astrophysics.

In this volume, we first review the current experimental status in chapter I; in chapter II, we present an overview of Borexino, summarising the new aspects of importance to low energy work, viz, the radiopurity and live monitors for detector calibrations and operating background. Signal reactions and signatures are treated in chapter III. Current neutrino physics proposals and the possible tests are reviewed in chapter IV. The physics program of Borexino is outlined in chapter V. The following chapters elaborate the major technical characteristics further, with details on the conceptual design, scintillator properties and its radioactive purity, signal detection hardware, electronics, simulations of the detector performance and the background from external sources. A second volume contains a series of technical appendices. A separate issue contains the design of the Counting Test Facility.

PART I

PHYSICS

Chapter I

SOLAR NEUTRINOS - STATUS & FUTURE

1.1 *The Neutrino Spectrum from the Sun*

Modern astrophysics is built on the keystone of nuclear fusion as the fundamental process of the stellar interior. Since the establishment of the basic framework of the subject by Bethe [1.1] more than fifty years ago, experimental and theoretical studies in both nuclear physics and astrophysics have developed and refined the global and specific aspects of this concept. The results of the Homestake experiment [1.2] have had a strong influence on theory, resulting in the development of the "standard" solar model (SSM) by Bahcall and Ulrich [1.3] [1.4]. The basic constructs of this model are: i) The sun is a main sequence star in a state of hydrostatic equilibrium between nuclear and gravitational sources of energy; ii) The energy production is primarily via the proton-proton (p-p) reaction cycle, involving the fusion of 4 protons to create a He nucleus, with marginal contributions from the carbon-nitrogen-oxygen (CNO) cycle; iii) Energy is transported from the core to the surface by radiation and convection. Parameters such as initial elemental abundance and opacities of solar matter as well as nuclear physics quantities such as the weak coupling constant and reaction cross-sections at energies typical of the central solar temperature are also basic input ingredients in the solar model calculations. The output is a model of the present-day sun after an evolution of ~4.5 billion years, matching all its known observable such as mass, diameter, surface properties such as luminosity, temperature and chemical distribution as well as dynamical data such as the surface rotational velocity.

The principal predictions of the SSM relate to the solar interior and set forth a detailed construction of the nuclear reaction sequences (Fig.1.1) and thus the neutrino production rates (and their radial variations), besides estimates of the central temperature, the central

Nuclear reactions in the pp-chain

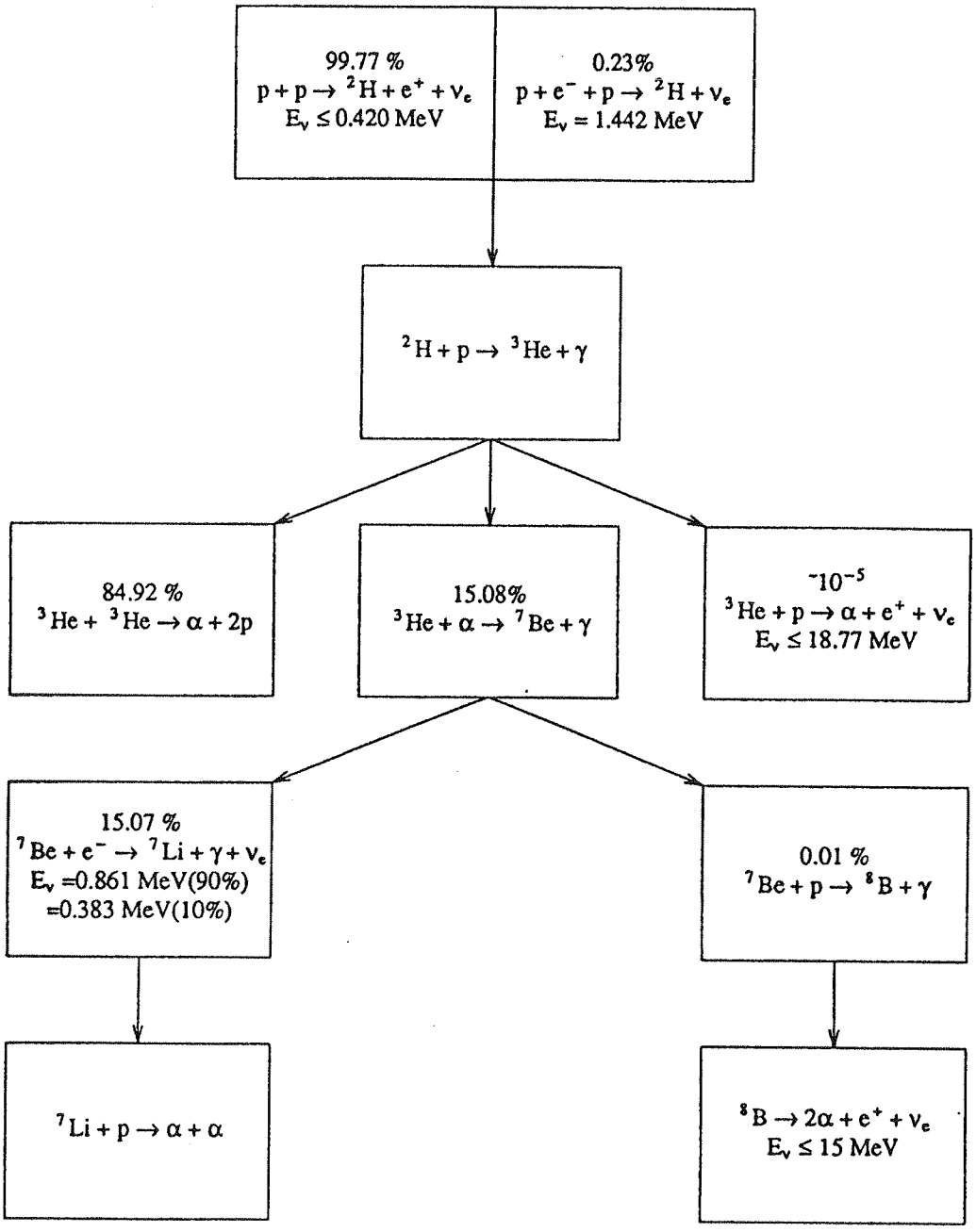

Figure 1.1. Nuclear fusion reaction sequences in the Sun [ref. 1.4]

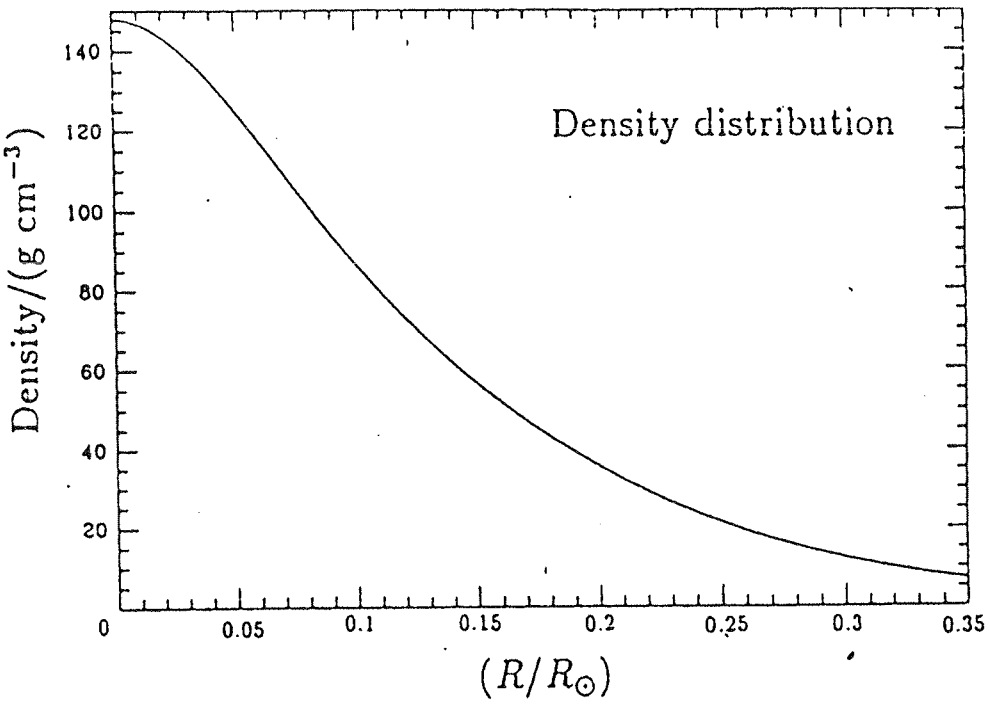

Figure 1.2 Radial variation of the central density of the Sun [ref. 1.4]

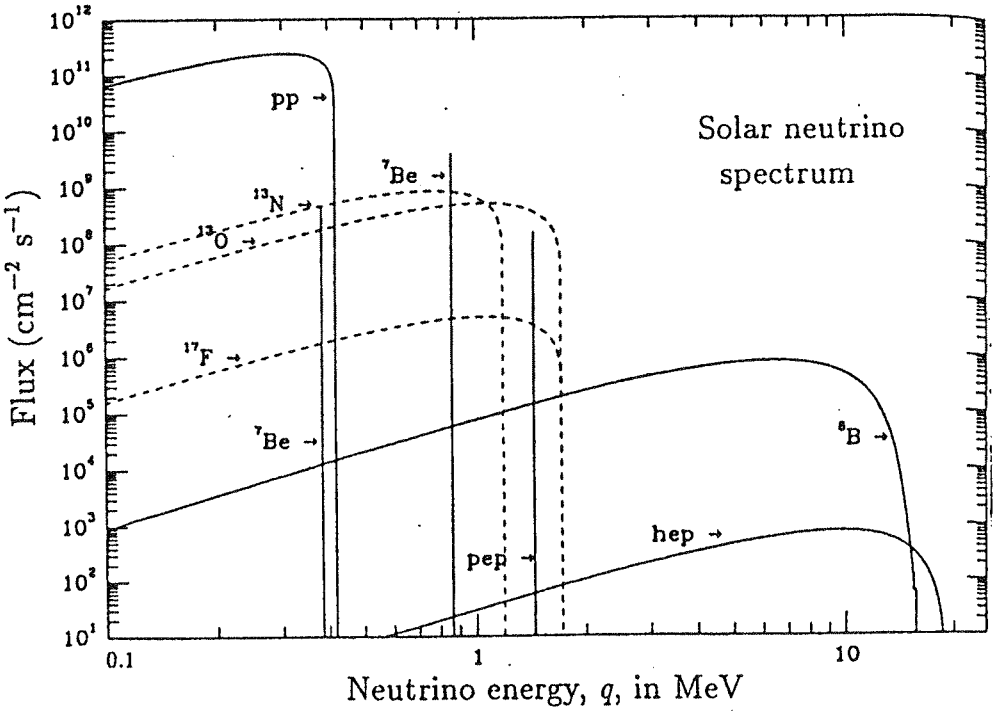

Figure 1.3 Neutrino Spectrum from the Sun [ref. 1.4]

Table 1.I Solar Neutrino Fluxes in the Standard Solar Model

Source	pp	pep	^{7}Be	^{13}N	^{15}O	^{17}F	^{8}B
Flux (10^{10} cm^{-2} s^{-1})	6.0	0.014	0.47	0.06	0.05	0.00014	0.00058
Uncertainty	2%	5%	15%	50%	58%	46%	37%

solar density (and its radial variation (Fig. 1.2)) etc. The predictions of interest to measurement are the fluxes of solar neutrinos on earth as embodied in the solar neutrino spectrum shown in Fig. 1.3.

The principal feature of the solar neutrino spectrum is the strong flux of low energy neutrinos from the pp reaction, emitted as a continuous spectrum with an endpoint of 0.42 MeV. The pp flux (see Table 1.I for a list of solar neutrino fluxes predicted by the SSM) and the much weaker line at 1.44 MeV from the "pep" reaction (a variant of the pp reaction), are the only components of the spectrum that are relatively model-independent. All other features are solar model-dependent and basically fall into two groups, a strong monoenergetic line feature at 0.86 MeV due to the decay of ^{7}Be in the sun and a weak continuous spectrum of neutrinos extending up to 14 MeV due to the decay of ^{8}B. The Be and B neutrinos are thus neatly separated into the low and high energy regions but the ^{7}Be ν flux is ~800 times that from ^{8}B. These two features are respectively, strongly (T^{8}) and acutely (T^{18}) sensitive to the central temperature of the solar core and thus solar model details. The remaining components with continue up to ~2 MeV arise from the small amount of CNO burning resulting in the decay of O, N and F isotopes in the sun.

1.2 *Experimental Status of Solar Neutrino Research*

Until 1987, the only solar neutrino data at our disposal came from the Homestake ^{37}Cl detector of Davis et al [1.2]. For the last 3-4 years the K-II detector has been in operation.[1.5] In 1990 the SAGE detector began solar neutrino observations [1.6].

We expect that GALLEX, a detector similar to SAGE and based on the same neutrino detection reaction, will begin operations this year [1.7]. Table 1.II lists the vital statistics of the three operating detectors and the currently claimed data.

The different detection mechanisms and signal sensitivities of the three experiments must be carefully taken into account in drawing inferences from the data.

The Homestake ^{37}Cl Experiment [1.8] : The basic reaction is inverse β-decay of ^{37}Cl:

$$\nu_e + {}^{37}Cl \rightarrow e^- + {}^{37}Ar \ (t_{1/2} = 35d), \qquad (1.1)$$

which is sensitive to neutrinos of energy above a threshold of $E_{th} = 0.814$ MeV. The detector consists of a tank of 615 t of $C_2\ Cl_4$ which is exposed to solar neutrinos for a period comparable to 35d, accumulating the ^{37}Ar released in reaction (1.1). At the end of

Table 1.II. Solar Neutrino Experiments: Properties and Results

	HOMESTAKE	SAGE	K-II
Reaction	Inv. β	Inv. β	(ν_e) Scatt.
	ν_e only	ν_e only	$\nu_e, \nu_\mu, (\mu_\nu)$
Target	^{37}Cl	^{71}Ga	Electrons
Threshold	860 keV	235 keV	7.5MeV (cut)
Type	Chemical	Chemical	Counting
	Time Integral	Time Integral	Real Time
	Energy Integral	Energy Integral	Spectroscopic
	No ν- Signature	No ν- Signature	Directionality
pp (<0.42)+pep (1.44 MeV)	0.2 SNU	74 SNU	-
^{7}Be, O,N,F(<1.7 MeV)	1.6 SNU	44 SNU	-
^{8}B (<14 MeV)	6.1 SNU	14 SNU	Calculable
Total SSM Signal	7.9 SNU	132 SNU	Std. rate
Result (1σ)	2.1(0.3) SNU	20(50) SNU	0.46(0.05)(0.06 sys)xStd.

the exposure period the Ar atoms are flushed out by purging the tank with He gas and collected into a well-shielded proportional counter observing the 2-3 keV Auger electrons emitted in the electron-capture decay of ^{37}Ar. The basic method is thus radiochemical. The Homestake detector is specific for electron type neutrinos (ν_e) but time-integrating, neutrino energy-integrating and non-specific as regards a signature for the neutrino event. The SSM predicts a total capture rate (with a 3σ uncertainty) of 7.9(1±0.37) SNU (1 SNU $=10^{-36}$ captures/target atom/sec). Of this signal, 6.1 SNU is due to high energy ^{8}B neutrinos. The minimum model-independent rate is 0.2 SNU from the pep reaction, while

the Be, O and N neutrinos contribute 1.5 SNU, totalling 1.7 SNU for all low energy neutrinos. A contribution of ~0.1 SNU may be present from other sources. The ~20-year time-averaged signal currently observed at Homestake is 2.1(3) SNU [1.9].

SAGE and GALLEX: These detectors are based on the target nucleus ^{71}Ga [1.10] and are of radiochemical type similar to Homestake, sharing its general merits and limitations. The importance of these experiments lies in the fact that the detection reaction

$$\nu_e + {}^{71}\mathrm{Ga} \rightarrow e^- + {}^{71}\mathrm{Ge}\ (t_{1/2} = 11.34\ \mathrm{d}) \qquad (1.2)$$

has a much lower threshold at 0.233 MeV, thus enabling sensitivity to the p-p neutrinos. Because of their high flux, the Ga detectors have a smaller target size (30 to 60 tons). However, ^{71}Ga also has a sizable sensitivity to higher energy solar neutrinos. The SSM predicts a total signal of 132 (+20 -17) SNU for SAGE and GALLEX [1.4], of which ~57% is due to a model-independent signal from pp (+pep) neutrinos. A signal distinctly less than ~50% of the SSM rate above would be an important result indicating the possibility of a non- astrophysical explanation for the SNP.

Kamioka-II: Unlike the above two experiments, K-II is a real-time detector capable of energy spectroscopy of solar neutrinos. It operates by the elastic scattering process:

$$\nu + e^- \rightarrow \nu + e^- \qquad (1.3)$$

which in principle has no threshold but is limited by a practical cutoff, at present, ~7.5 MeV. It is thus sensitive solely to the high energy B neutrinos. The reaction, while dominantly sensitive to ν_e, responds to neutrinos of all other types (via the neutral current) with ~15% of the ν_e cross section. The signal detection in K-II is via the Cerenkov effect of the scattered electrons. Thus the electron track direction and thus the incoming neutrino direction can be determined since the elastic scattering process (1.3) is highly forward-peaked. A direct correlation to the sun can thus be established. The background in K-II is high; still, the directional signature allows not only a measurement of the ^{8}B solar neutrino flux but also their qualitative spectral shape as well as the real-time variability of the signal.

The K-II detector is a large tank of water in which ~1000 large phototubes are immersed to observe the weak Cerenkov light from a central fiducial mass of 680 tons. The current results are [1.11] :

i) ^{8}B neutrinos correlated to the sun are observed at a flux of 0.46(6)x SSM.

Figure 1.4 Possible correlation of the Homestake signal to the solar cycle [from ref. 1.13]

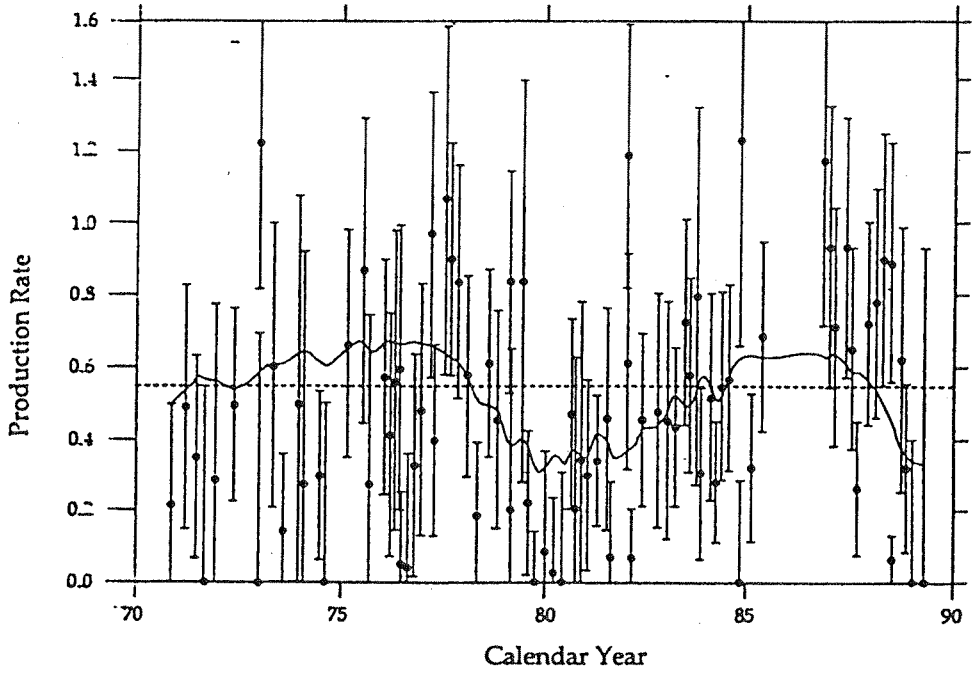

Table 1.III. Time dependence of Solar Neutrino Flux: Homestake vs. K-II

Data Set	Experiment	Data Period	Observed Flux
I	Homestake K-II	1986.8 - 1988.3 1987.1 - 1988.5	4.2(0.7) SNU 0.48(0.09)(0.08) x STD Model
II	Homestake K-II	1988.3 - 1989.5 1988.6 - 1990.4	1.2(0.6) SNU 0.45(0.06)(0.06) x STD Model

ii) the spectral shape is broadly consistent with standard shape of the β-decay of ^{8}B in the sun. These results are epochal, directly demonstrating for the first time, neutrino emission from the sun.

Time-dependence of the Solar Neutrino Flux: Perhaps the most interesting (and controversial) result to emerge from Homestake in recent years is an indication that its signal may not be constant in time. An increasingly significant time-variability may be observed, crudely correlated to the last two solar cycles (~20 years) during which the device was on [1.9]. Statistical analyses of the Homestake data as a function of time [1.12] [1.13] while far from definitive, do find that a time variation cannot be excluded (see e.g. Fig. 1.4). In contrast, the K-II flux is found to be approximately constant (30%) in the same time interval when the Homestake flux was varying strongly (see Table 1.III) [1.14]. Since both detectors are dominantly sensitive to the same ^{8}B neutrinos, new ideas are necessary to reconcile both these observations.

Significance of Present Results: Some basic inferences can be drawn from the present data:

- From the directionality of the K-II signals and the qualitative spectral shape, we know now that the sun is generating ^{8}B neutrinos albeit at about 45% of the expected rate.
- There can no longer be any question of the nuclear origin of the sun's energy and of the basic correctness of our view of the evolutionary stage of the sun.
- The K-II result confirms the signal deficit observed by Homestake, showing that the SNP is a real problem.
- The SAGE result tends to indicate the likelihood of a Ga flux <50% of the SSM value, thus solar model-independent pp neutrinos may also be depleted.
- If the above is confirmed, the observed fluxes deviate from the predictions of the SSM across the board in energy.
- The *time-averaged* fluxes at Homestake and K-II are inconsistent with a purely astrophysics explanation [1.15]. Given that the sun produces at least 46% of the SSM ^{8}B flux (K-II), Homestake should observe at least [2.8(^{8}B)+0.2(pep)+ 1.1 (^{7}Be etc)] ≈ 4.1 SNU compared to the observed 2.1(3) SNU. The estimate is obtained by a slight change in the central temperature such that the ^{8}B flux is reduced to agree with K-II. Then, using the relative temperature dependence of the Be (T^8) and B (T^{18})] fluxes in the SSM framework, the ^{7}Be (and other low energy) flux can be calculated to be ~71%

of the SSM flux. The pep flux is unchanged.

- Notice that in the quiet sun periods, Homestake indeed observes (see Table 1.III) a flux of ~4.2 SNU as estimated above.

- Time-varying fluxes (if confirmed), are not likely to be explained purely on the basis of the standard astrophysics of the interior energy mechanism of a quasi-static sun.

In principle, the final results of the Ga experiments may provide vital clarifications in the above picture. However, on the basis of the results available so far, we cannot yet make the fundamental decision if astrophysical models or neutrino physics is the major factor underlying the SNP. Both scenarios must therefore be considered in the possible results in the next round of experiments.

Astrophysical Solution?: If the low (time-averaged) flux of the Homestake experiment is the valid result, astrophysical solutions are relatively difficult without basic revisions of present ideas. The value of another model dependent neutrino flux is thus of great astrophysical interest. The only other major component is the ^{7}Be neutrino flux. These neutrinos, part of the main energy production reactions, arise in a region intermediate between that of the pp neutrinos (where most of the energy is produced) and the innermost regions of the ^{8}B neutrinos. ^{7}Be neutrinos have a temperature dependence different than either of the above. The value of this flux (together with that of ^{8}B neutrinos) will provide an important test of variant models. If the observed ^{7}Be flux is large, nearly SSM, then it could pinpoint parameters specific to a reduction of the ^{8}B neutrino flux as the target for possible solar model changes. Note that in these cases the signal in the Ga experiments will also be large.

Neutrino Physics Solutions?: A strongly reduced flux of Be neutrinos would probably require radical changes in the solar model; several ad hoc models have been considered in the literature (see [1.4]). In this case, new neutrino physics may then be a more likely possibility, especially if a sufficiently small signal is also observed in the Ga experiments. In these scenarios, even a flux limit clearly excluding an SSM-type value is useful. Most neutrino scenarios predict other types of effects with a more decisive impact. They will be sought in the next round of experiments. For example, at high energies, the ^{8}B spectral shapes and neutral current observations will be useful. Observations on low energy Be neutrinos are very pertinent for specific information on the major neutrino scenario because of the high flux and, in particular, their monoenergetic nature. The Be flux will be low because of flavour conversion; however the signal will also show striking periodic increases based on day-night or seasonal time-bases and provide a direct demonstration of

flavour conversion. Other effects on neutrino scattering, observable only at low energies, can contribute to a model-independent search for neutrino magnetic moments.

1.3 *Solar Neutrino Experiments — The Next Round*

Of the diverse solar neutrino detectors proposed over the years, three major programs, SNO (Sudbury Neutrino Observatory), SUPERKAMIOKA and BOREXINO are real time experiments in advanced stages of development (SNO and SUPERKAMIOKA are approved projects). The first two are kiloton class detectors operating on the high energy ^{8}B neutrinos, with the special features of neutral current signals (SNO) and the largest detector mass so far (Superkamioka). Borexino is the smallest (0.1kton) device and will introduce the unique feature of real-time spectroscopy of low energy ^{7}Be neutrinos. The main specifications are compared in Table 1.IV.

SUPERKAMIOKA: [1.16] With a total mass of 50 kton, this detector is a massively upgraded version of K-II; solar neutrino studies are one of its major objectives, based on light water Cerenkov techniques observing of ν-e scattering. The fiducial mass (FM) for these studies is 22 kton of water, observed by 11,200 (50 cm dia.) phototubes providing an effective coverage of 40%. The spectroscopic resolutions are generally improved from those at K-II. An analysis threshold of 6.5 MeV is expected (goal ~5 MeV). Directionality will remain the basic signature to overcome the inherently high backgrounds.

The main result is expected to be a measurement of the spectral shape of ^{8}B neutrinos, much improved from the present K-II result because of the larger signal rate of ~20 events/d (31/d) with E_e >5 MeV (=0.46 ϕSSM), compared to the present 0.39/d above 7.5 MeV. A deviation from a standard β-spectral shape can thus be established for ^{8}B solar neutrinos.

SNO: [1.17] This detector is based on 1 kton (FM) of heavy-water contained in a transparent acrylic vessel and observed by ~9,700 phototubes (20cm dia.) situated in a 3m thick light water envelope. Signal detection is by Cerenkov techniques with an event threshold at 6 MeV, thus SNO is sensitive only to ^{8}B neutrinos. Besides ν-e scattering which contributes a relatively weak signal, the main modes of the detection employ the deuteron as the target via: (1) $\nu_e d \rightarrow e^- pp$, which proceeds via the charged weak current; and (2) $\nu\ d \rightarrow \nu pn$, ($n + Cl \rightarrow 8$ MeV $\Sigma\gamma$s) which proceeds via the weak neutral current, irrespective of the neutrino flavour. The latter measures the integrated flux for all types of

Table 1.IV Solar Neutrino Experiments —The Second Round

	SUPERKAMIOKA	SNO	BOREXINO
Detection Medium	H_2O	D_2O	Liq. Scint. (B)
Reaction Targets	e^-	d, e^-	e^-, ^{11}B, p
Fiducial Mass (kton)	22	1	0.1 (0.2)
Rock-to-FV shield (mwe)	6	5	5.5
Phototubes (cm dia)	11,200 (50)	~9700 (20)	1660 (20)
Effective Coverage (%)	40	40	50
Trig. Thresh. (MeV)	4 - 5	5	0.1
Analysis Thres. (MeV)	5 - 6	6	0.25
Energy Res. (1σ %)			
(10 MeV)	14	14	4
(1 MeV)	-	-	7.5
Spatial Res. (1σ cm)			
(10 MeV)	50	70	10
(1 MeV)	-	-	13
BORON-8 ν ev/d			
1. Neutral Current (SSM)	-	8	~0.02
Signature?	-	No	-
2. Charged Current (SSM)	-	18 (>6 MeV)	0.65 (>4 MeV)*
(MSW)	-	8	0.3
Signature?	-	No	Delayed Coinc.
3. Electron Scattering (SSM)	43 (>6 MeV)	2 (>6 MeV)	1.0 (>4 MeV)*
(MSW)	20	0.9	0.45
Signature?	Directional	Directional	No
BERYLLIUM-7 ν ev/d			
Electron Scattering (SSM)	-	-	50 (0.25-0.8 MeV)
(MSW)	-	-	10
Signature?	-	-	$1/R^2$ Time Var.
ANTINEUTRINOS?	(Yes)	Yes	Yes
Signature?	No	Delayed Coinc.	Delayed Coinc.
Min E $\bar{\nu}_e$ (MeV)	?	~7.5	~2

* With active volume of 0.24 kton defined by software.

neutrinos of energies above E_{th}=2.224 MeV. In addition, SNO is sensitive to antineutrinos: (3) ∇_e d→e⁺ nn, the neutrons being detected as with reaction (2) above. Reactions (1) and (2) do not have a signature, however, the detector is being designed with great care to have sufficiently low background. SNO will be placed at a depth of 6000 mwe, much deeper than the location of K-II.

The signal rates in SNO are, for reaction (1): 7/d (0.46 SSM); and for (2): 8/d (MSW), 4/d ("astrophysics" solution). The principal result expected from SNO is a measurement of the solar neutrino flux via the neutral current, reaction (2) above. A flux determined by (2), if different from that measured by (1) the charged current mode, could be a direct demonstration of flavour non-conservation, provided flavour conversion takes place to non-sterile states.

BOREXINO / BOREX: The Borex program, in contrast, is based on liquid scintillation spectroscopy; the design however, is similar, the scintillator replacing the heavy water in SNO. The liquid scintillator is a mixture of trimethylborate (TMB 85%) and an aromatic liquid such as pseudocumene (PC 15%). It contains ~9% boron (^{11}B 80%); electrons and protons will act as the ν/∇ reaction targets. A key point of the scintillation technique is that the signal event threshold can be set at ~0.25 MeV compared to >6 MeV with Cerenkov techniques. In a sequence similar to K-II→Superkamioka, the Borex program is planned in two phases, the first being BOREXINO with a scintillator FM of 0.1 kton and the second phase, BOREX, with 2 kton.

The signal reactions are: (1) ν ^{11}B→^{11}Bν'γ, mediated by the weak neutral current; (2) the inverse β-decay of ^{11}B (charged current); (3) ν-e scattering and (4) $\bar{\nu}_e$p→e⁺n. All the above, except (1) can be employed in both phases of the program. The main objective of Borex will be the observation of ^{8}B neutrinos via reactions (1) to (3), but focusing on the neutral current detection via (1).[1.18] The signal rates (0.46 SSM flux) of (2) and (3) are 2.4/d and 3.6/d while that of the neutral current reaction (1) is low, 0.4/d. However, it can be observed with a signature in the form of a γ-ray doublet at 4.5 and 5 MeV; this operation requires a scintillator of ultrahigh radiopurity. TMB has been found to be extraordinarily suitable in this respect.

BOREXINO, the first phase of the Borex program, aims to exploit the ultrapurity of the TMB scintillator because the purity is sufficient also to observe *low energy, high flux* ^{7}Be neutrinos (via reaction (3)), taking advantage of the very low signal threshold of the

technique. This leads to the central feature of Borexino: *real-time observations of* ^{7}Be *solar neutrinos at signal rates of up to 50 events/day* despite a target size 10 to 200 times smaller than SNO or Superkamioka. These rates enable a unique sensitivity to flux variations with time, facilitating

(i) a solar signature based on the $1/R^2$ effect of the earth orbit

(ii) a search for a day-night or seasonal effect. For ^{7}Be neutrinos, these effects are sensitive "appearance" effects of flavour conversion.

Spectroscopic sensitivity in Borexino will extend also to the ^{8}B neutrinos, via reaction (2) (with ^{11}B as the target) and (3), the former because of the use of the TMB scintillator. Finally, reaction (4) comes "free" in Borexino by which $\bar{\nu}_e$'s can be observed at energies as low as ~4 MeV compared to typical cutoffs at 7-8 MeV elsewhere. The key is a delayed coincidence neutron signature exploiting the presence of ^{10}B in the TMB scintillator. Reactions (3) and (4) are sensitive to effects of a neutrino magnetic moment; in fact, Borexino will be one of the most advanced experiments in the search for several aspects of the magnetic moment possibility.

The pioneering experience of Borexino will clearly benefit the next phase of the larger Borex detector. Though aimed at neutral current detection at high energies, Borex can also continue all the low energy investigations of Borexino with 20 times higher signal rates. For example ^{7}Be neutrinos can be observed with rates of up to 1000/day, enabling a *"daily neutrino watch"* on the sun.

References

[1.1] H. Bethe, Phys. Rev. 55. 434 (1939).

[1.2] R. Davis, Phys. Rev. Lett. 12, 300 (1964).

[1.3] J. N. Bahcall and R. Ulrich, Rev. Mod. Phys. 60, 297 (1988).

[1.4] J. Bahcall, *Neutrino Astrophysics*, (Cambridge U. Press) 1989.

[1.5] K. S. Hirata et al, Phys. Rev. Lett. 58, 1490 (1987).

[1.6] T. Kirsten, Nucl. Phys. (Proc. Suppl) B19, 77 (1991).

[1.7] A. Abazov et al, Nucl. Phys. (Proc. Suppl) B19 84 (1991).

[1.8] The first ideas for the ^{37}Cl experiment were suggested independently by B. Pontecorvo, Chalk River Report PD-205 (1946), and by L. W. Alvarez, University of California Radiation Laboratory Report UCRL-328 (1949).

[1.9] B. Cleveland et. al., Proc. 25 ICHEP, Singapore 1990 (World Scientific). p 667.

[1.10] V. Kuzmin, Sov. Phys. (JETP) 22 1051 (1966).

[1.11] K. Hirata et al, Phys. Rev. D44, 2241 (1991).

[1.12] J. N. Bahcall and W. Press, Ap. J. 370, 730, 1991; J. W. Bieber et al, Nature, 348, 407 (1990); L. Krauss, Nature 348 403 (1990); H. Ninakawa and H. Minakata, Int. J. Mod. Phys. A6, 2347 (1991)

[1.13] B. W. Fillipone and P. Vogel, Phys. Lett. B246, 546 (1990).

[1.14] A. Suzuki et al, Phys. Rev. D43, 3557 (1991)

[1.15] J. Bahcall and H. Bethe, Phys. Rev. Lett. 65, 2233 (1990); M. Spiro and D. Vignaud, Phys. Lett. B242, 279 (1990); S. Pakvasa, Proc. 25 ICHEP Singapore 1990 (World Scientific) p. 698.

[1.16] Y. Totsuka ICRR (U. Tokyo) Preprint (Dec 1990).

[1.17] G. Ewan et al, Sudbury Neutrino Observatory Proposal (1987)

[1.18] R. S. Raghavan, S. Pakvasa and B. A. Brown, Phys. Rev. Lett. 57 (1801) 1986; R. S. Raghavan and S. Pakvasa, Phys. Rev. D37, 849 (1988); R.S. Raghavan et al., Design Concepts for Borex, AT&T Bell Labs Memorandum (1988); T. Kovacs et al, Solar Phys. 128, 61 (1990).

Chapter II

BOREXINO

This synopsis of Borexino contains an overview of the design, operation and physics potential (§2.1). Sections §2.2-4 contain elaborations on key aspects of low energy operation: viz., scintillator purity and live determination of the detector response and the radioactivity background.

2.1 *Overview*

Conceptual Design of Detector: The aim of low energy neutrino observations in Borexino requires a design for a *low signal* threshold as well as a *low event* threshold suitable for solar neutrino signal rates. The first need is satisfied by the choice of the high luminosity liquid scintillation technique and high-quality phototubes. The second criterion sets limits on the background at low energies. The internal background is determined by the radioactivity of the scintillator itself. The external background is determined by the design of the scintillator containment, phototube arrangement and the shielding against environmental radiations. The physical design of Borexino utilizes state -of-the-art technology and materials with purities available in the large scale at reasonable cost. The overall aim of the design is to make the external background small enough that only a single material -the liquid scintillator - determines most of the background in Borexino operation.

Figure 2.1 Conceptual design of Borexino (watershield option).

In Borexino, a central spherical volume of liquid scintillator, ideally in a "wall-less" container, is submerged in a shield volume of water. The scintillation light is detected by phototubes (PMT) distributed concentrically around the active volume. The measured quantities are:

(i) energy of the event derived from the number of PMT's triggered (thus the collected photoelectron (pe) charge).

(ii) the spatial location of the event from the time-differences in the PMT triggering and event reconstruction using the optical times-of-flight.

The overall design of Borexino arrives at a signal threshold at ~0.075 MeV (set mainly by the basic trigger defined as a ~15-PMT coincidence) and a solar neutrino event threshold of ~0.25 MeV (set mainly by a possible ^{14}C background).

The basic dimension of the detector is the fiducial target mass (FM), 100 tons of scintillator, in a sphere of diameter 6m. The minimum size of the detector (16m dia.) is set by the shielding thickness of ~5mwe required to suppress background from the rock environment of Gran Sasso. Within these two constraints, the architecture can be divided into two parts: the containment of the liquid scintillator and the structure of the external shielding with a suitable PMT arrangement. The liquid scintillator will be contained in a transparent acrylic vessel laminated with a teflon (tedlar) film. The diameter of the vessel is 8.5m. The ideal of "wall-less" container is satisfied by choosing (by analysis software) a fiducial volume suitable for the particular type of physics; for low energy work a fiducial diameter of 6m is foreseen. The outer thickness of 1.25m of scintillator is the final shield against external background, in particular from the radioactivity of the acrylic shell itself.

For the architecture beyond the acrylic vessel, two alternative designs are under study. In the simpler design (Fig. 2.1), the vessel is immersed in a large tank of water of moderately high purity (~10^{-13}g/g). The thickness of water shield is ~4m. Low-radioactivity PMT's coupled to light-guides are placed on a support frame in the water at ~2m from the acrylic vessel.

The alternate scheme envisages PMT's operated in air. The water shield, now only 2m thick, is contained in a smaller tank. The PMT's are held by stand-offs on the outer surface of this tank, observing the fluid volume via sealed optical windows on the tank wall. The shielding is completed by an external structure of low radioactivity concrete. More details on both designs are given in chapter VI. Preliminary engineering concepts, construction sequences oriented towards strict environmental control especially during the acrylic assembly and a laboratory layout in Hall C (LNGS) – the intended location of

Borexino – are discussed in Appendix I and II.

Signal Detection, Response, Spectroscopy: The liquid scintillator in Borexino will be mostly trimethylborate (TMB), a highly transparent liquid of ultrahigh radiopurity, mixed (≤20%) with an aromatic additive such as pseudocumene (PC). The major reasons for choosing TMB as the main constituent of the scintillator are:

I) very high radiopurity, so far the highest observed so far among suitable liquids.
II) very low absorption (λ=25m) and scattering (λ_S=60m) of the scintillation light.
III) high optical scintillation efficiency with only a small addition of aromatic component.
IV) boron in the scintillator which extends observations to high energy neutrinos via ^{11}B and to antineutrino signatures via ^{10}B.
V) large scale availability at reasonable cost.

A wide range of scintillation mixtures have been studied; the light output e.g., varies from 25 to 45% of that of anthracene, and for the typical mixture, the scintillation lifetime is ~3.5 nsec, the effective light attenuation length λ is 12-14m and the Rayleigh scattering length ~30m. The scintillation light will be detected with an effective geometrical optical coverage of the order of 40-50% by some 1660 8" PMT's (EMI 9351; low radioactivity Schott 8246 glass) coupled optically to parabolic reflectors.

The dimensions of the fiducial volume are such that most low energy events will be observed *calorimetrically*, i.e. compton showers or β - or γ - γ cascades will appear mostly as energy-summed line features. The dimension of the F.V. is defined by software, ranging from 6m (100 tons) to 8.5m dia (240 tons). Simulations of the responses in energy and spatial resolution for the 6m F.V. are shown in Table 2.I (see also Chapter X). The simulations account for factors such as the scintillation lifetime, liquid scattering and absorption, collection efficiency of the light guide, the quantum efficiency and time jitter of the PMT's as well as refraction and reflections at boundary layers and at the PMT's. The scintillation lifetime for heavy particle events are longer than for electrons; this can be used to identify them by pulse-shape. For example, ~5 MeV α's can be discriminated from equivalent energy electrons ~85% of the time. Details on the scintillator and the PMT's are given in chapter VII and chapter VIII. Montecarlo simulations of reconstructions of the signal response are discussed in chapter X.

Solar Signals, Event Rates: The main signal in Borexino will be due to low energy solar neutrinos <1 MeV. Neutrinos from the decay of ^{7}Be (0.86 MeV) will produce the

*Table 2.I Energy and Spatial Resolution in Borexino**

Event Energy (MeV)	pe(σ)	Δ E (σ; keV)	Δ R (σ; cm)
0.1	19(4)	24	52
0.2	37(6)	32	35
0.5	94(9)	50	18
1.0	188(14)	76	13

*Scintillation Output= 33% of Anthracene. Electron events randomly located in the FV.

Table 2.II Neutrino Signal Rates in Borexino (100 t Fiducial Mass)

Case	Event Rate/Day (0.25-0.8MeV Signal Window)
I. Standard Solar Model	50
II. "Neutrino Physics" (MSW)	10

dominant part (90%) of this signal. The detection reaction is ν-e scattering, thus the measurable recoil electron spectrum from the ^{7}Be ν line feature is nearly flat, extending from a low energy cutoff of 0.25 MeV to a scattering edge at ~0.7 MeV (See chapter III). (The lower cut-off is decided mainly by the ^{14}C content of the scintillator). The ν spectral range in Borexino is not limited to low energies. High energy ^{8}B neutrinos (>4MeV) at K-II fluxes can be measured with event rates ~250/yr, more than twice that at K-II. The ^{8}B ν spectral shapes, especially, at energies lower than at K-II are also accessible. Finally, antineutrinos >4 MeV can be spectroscopically observed above internal background. Above 5 MeV, where power reactor ν̄ background is low, they can be specified as "extra-terrestrial" in origin.

Table 2.III Total Background Rates in Borexino (100 t Fiducial Mass)

Purity	(Int.+Ext.)= Total Bgd./day
A. High Purity [U/Th (10^{-16}g/g; K(10^{-14}g/g)]	11+2= 13
B. Low Purity [U/Th (10^{-15}g/g; K(10^{-13}g/g)]	110+2= 112

The signal rates in the low energy window can be typified for two yardstick scenarios. Case I is the SSM which predicts a total signal of ~50 ν-e events/d from ^{7}Be solar neutrinos. Case II is a "neutrino physics" solution which assumes that the reduction of the K-II flux is entirely due to the MSW effect. This scenario in which most of the ^{7}Be neutrinos are converted to ν_μ type predicts a signal of ~10/day. Table 2.II summarises these signal possibilities for a F.V. of ~100 tons.

Background Ranges: Borexino is designed so that radioactivity external to the F.V. (detector materials and rock) and that from cosmic-ray muons produce only a small part of the background at low energies in Borexino; most of it is expected from the residual radioactivity in the liquid scintillator itself. A yardstick for background estimates is thus provided by the content of U and Th in the scintillator. The current results indicate that a U/Th purity in the range of 10^{-15} to 10^{-16} g/g can be expected (see §2.2 and chapter XI). Table 2.III summarises the total background rates in the low energy window for this purity range. The external component is <3/d, two of them due to the external materials and one due to the rock. The cosmic ray induced component is negligible in this energy range. The internal component is the final residue after a series of on- and off-line cuts in the analysis (see §2.4).

The signal/noise in the "astrophysical" scenarios (I) thus ranges from ~0.5 to ~4. In these scenarios the Be ν flux can be measured by spectroscopic techniques alone for S/N >1 (see spectral profiles in chapter III). For S/N<1 the flux can be derived by the application of a solar signature. Thus, for larger ^{7}Be signals typical of the SSM, the flux can be measured for the full purity range from 10^{-15} g/g to 10^{-16} g/g. For small signals typical of neutrino scenarios, only a limit on the flux can be set. Other effects will be used to observe physics involved in these cases.

Solar Signature: A solar origin of the signal can be established on a basic level by the seasonal time variation due to the $1/R^2$ effect (±3.5% /6 mo.) of the eccentricity of the earth's orbit. The solar signal part of the observed events, varying with a known period/phase and the relatively constant background part can be extracted independently even in the high background case B of Table 2.III. The signal in the "astrophysical" Case I can be measured and clearly distinguished from the "neutrino physics" Case II in a live time of a few years (see §3.1). The $1/R^2$ solar signature for the Be signal in Borexino can thus lead to flux measurements despite S/N <1 just as Cerenkov directionality helps K-II solves more severe background problem.

Background Monitors: Spectroscopy of the *background* is an important aspect in

Borexino. (§2.4). Parts of the U/Th output consist of α's and radiations emitted in delayed coincidence cascades (e.g. β-α decay of ^{214}Bi via 164μsec ^{214}Po). They can be directly tagged, the former, by pulse-shape discrimination and the latter by the spatial coincidence and delay time-correlation. Since the cascades are in equilibrium with adjoining nuclides in their local segment in the decay chain, the background due to their precursors/daughters can also be determined (statistically).These cuts can result in a sizable reduction in the low energy background in Borexino (§2.4).

Live Monitors for Absolute Calibrations: The presence of correlated cascades provides Borexino the convenience of a live internal calibration mechanism (§2.3). Ensembles of tagged events from β - α cascades in ^{212,214}Bi and ^{208}Tl provide a total of 15 different spectra of time, space and energy distributions of the β and the α components of these correlated events. Since precise nuclear lifetime and energy distributions and a spatial coincidence of the two events are specified, these tagged events directly test the energy/spatial reconstruction sensitivity in Borexino. Thus the overall spectroscopic response of the detector can be monitored live on an absolute basis.

Source Calibration of Neutrino Signal: The low energy scattering signal in Borexino can be calibrated by a radioactive source of antineutrinos such as ^{90}Sr-^{90}Y, a pure β emitter (§3.4). Such sources are commercially accessible as a fission product in excess of 5 MCi strengths and are much less expensive than e.g., ^{51}Cr proposed for calibrating the Ga experiment. The safety and handling of the ^{90}Sr sources are well established by longstanding applications. A 1 MCi Sr source placed just outside the detector tank will induce a ($\bar{\nu}_e$-e) scattering signal of the same order as a standard sun. A direct calibration of the solar neutrino scattering signal in Borexino is thus possible.

Physics Potential: Borexino will be the first detector to specifically observe the ^{7}Be neutrinos, the first one optimized to count both Be and B neutrinos (0.25 to 14 MeV) and the first one able to observe solar neutrino signal rates as high as ~50 events/d. Borexino will thus address both astrophysical and neutrino physics aspect of the SNP from unique new perspectives (see Chapter V).

- A day-night or seasonal variation of the Be signal will provide a direct and compelling demonstration of flavour conversion, unraveling quantitative results on the neutrino parameters and the astrophysical fluxes of Be and B neutrinos with dramatic impact on neutrino physics. These experimental effects and the consequent specific conclusions are possible only in Borexino. This scenario covers the broad parameter region of $\Delta m^2 < 10^{-6}$ eV^{2}consistent with a low Ga signal.

- The ^{7}Be neutrino signal, regardless of magnitude, is new ground. If the "astrophysics" solution is prevalent, a reasonable measurement of the flux is possible. For most neutrino physics solutions, the flux is low enough to be distinguished from the astrophysical solutions even though only a limit can be set. If no diurnal or seasonal variations of the signal are observed, a broad parametric region of neutrino mass differences with $\Delta m^2 < 10^{-6}$ eV^2 can be ruled out. A new measurement of the flux of B neutrinos can be made, especially at lower energies, and the spectral shape can indicate new neutrino physics.
- A stringent limit on the neutrino magnetic moment can be set by $\bar{\nu}$-e scattering at low energy in the ^{90}Sr source experiment; this is new territory unique to Borexino.

2.2 *Radiopurity of Materials*

2.2.1 *The Liquid Scintillator*

Sources of Internal Background: The event thresholds in Borexino set low limits on the internal background and thus high demands on the radiopurity of the scintillator, with "design" levels in the range 10^{-15}g/g to 10^{-16}g/g U/Th (see Table 2.III). The major sources of background in the low energy window are the natural radioactivities of U, Th and K. For purity at or better than the design level, i.e. $\leq 10^{15}$g/g, "active" reductions are possible by spectroscopy in Borexino. They set an order of importance of the individual nuclides in the U, Th chains (see §2.4 for details).The ^{232}Th chain and the ^{226}Ra part of the ^{238}U chain are relatively less critical. Thus the contributions of ^{238}U itself and ^{40}K though important, can be determined by different means and removed. Untaggable ^{210}Pb (intrinsic and derived from external sources, see below) may be the limit-setter of the lowest possible backgrounds from natural radioactivity. In addition, untaggable low energy activities such as cosmogenic ^{14}C, ^{7,10}Be, are important for low energy work in Borexino and must be removed sufficiently from the scintillator.

Surface Contamination: In addition to the above intrinsic radiocontaminants, impurities can be derived by surface contact with walls of containers, plumbing and in final measure, from the acrylic vessel in the detector. Two special problems, both connected to radon, are important. The first is the direct diffusion of Rn from the bulk of the acrylic into the scintillator volume. The large difference in the bulk purities of the

acrylic and the scintillator (10^{-12} vs 10^{-15} or 10^{-16}) makes it important to investigate the rate at which Rn diffuses out of the acrylic/tedlar interface with the scintillator. Secondly, the decay of radon in ambient air leads to radiolead (^{210}Pb) which tends be plated and thus accumulated on plastic surfaces. This problem has to be controlled during and after the processing of the acrylic. The critical question is that of leaching of the radiolead from the inner tedlar surface into the scintillator. Study of surface contamination in general, the radiolead problem in particular, are in the initial stages. A start has been made regarding U/Th chemical leaching in small plastic (teflon) containers and, in ongoing studies, for industrial type volumes.

Main Results on Radiopurity: The intrinsic purity of the main scintillator component TMB can reach and perhaps surpass design levels for most of the above impurities. That of the minor component PC, somewhat less demanding than for TMB, is also expected to be in the range assumed in Table 2.III. The main results are: (see Chapter XI for details)

- Direct determination in small (1 L) samples of TMB reveal: ^{238}U @ 3×10^{-15} g/g and ^{232}Th @ $<1\times10^{-15}$ g/g [2.1]. A ~50 L sample of TMB has also be analysed. Preliminary results show a ^{238}U content of 5×10^{-16} g/g. The rough scaling of the two results with surface/volume indicate that with the larger volume/surface typical of Borexino operation, the observable purities could be even higher.
- Estimates from measured decontamination factors in the preparative steps of TMB show that extreme intrinsic purities may be typical, with: Th $<5\times10^{-17}$ g/g, Ra $<5\times10^{-18}$g/g of U equivalent, K $<10^{-14}$g/g. Most other impurities (including Pb) are also purged by large factors similar to that for Th. These results thus support the above prognostic.
- The results for PC (1 L commercial samples) are: ^{238}U ~1.5×10^{-15} g/g and ^{232}Th ~ 8×10^{-15} g/g [2.2]. Purity lower than in TMB can be tolerated in PC.
- Upper limits have been set on the content of ^{14}C in a petrochemical. In CO gas derived from natural gas (chosen as a typical petrochemical), the result was $^{14}C/^{12}C < 0.75\times10^{-18}(1\sigma)$, a new limit for ^{14}C in "old" material [2.3]. Since the methanol for TMB and the aromatic components are of petrochemical origin, this result is of significance. Such a limit, if valid in the scintillator, would allow a low-energy cutoff at ~0.25 MeV in the signal window.

Analysis Methods—Mass Spectroscopy, Radiotracers: The impurity levels of interest to Borexino and the variety of contaminant species in question necessitate a wide ranging program using several ultrasensitive analytical techniques. New methods were developed to extend their ranges to cover our problems. A full account is given in chapter XI; the

following is a summary.

The ultrahigh purities of Borexino materials are usually at or below sensitivity limits of even the best analytic method, ultrasensitive mass spectroscopy. The problem was solved by developing suitable preconcentration methods [2.1]. In the case of TMB, sub-boiling distillation and analysis of the residue was the standard procedure, the validity of which was verified by radiotracer methods (see below) even at impurity concentrations of 10^{-14}g/g prevailing normally in initial commercial samples. These analyses were carried out in laboratory volumes ~1L in clean room ambience. The results on U/Th in TMB mentioned above are derived from these measurements. More recently, TMB samples in semi-industrial volumes ~100L have been studied (see Appendix VI). Preconcentration by sub-boiling distillation was carried out in a specially designed all-teflon apparatus in the normal ambience of a TMB plant. The larger volume and the volume/surface ratio minimise effects of blank fluctuations as well as surface contamination.

Preconcentration procedures were also employed to improve existing abundance limits on ^{14}C in "old" material by accelerator mass spectroscopy. To overcome the blank and background limits in the measurement, CO gas from natural gas was isotopically enriched by liquid CO distillation to levels upto 99% of ^{13}C (thus enriching ^{14}C by x200)[2.3].

Tracer methods were developed for contaminant, such as ^{226}Ra, ^{210}Pb etc., with undetectable small concentrations. Radiotracer spikes of the impurity elements were used to trace their separation in the processes by which the material is made. The impurity content at the initial stage can usually be measured directly, thus the tracer decontamination factor yields the typical purity in the final stage. This was particularly applied to the preparative steps of TMB. The radiotracers were: a) ^{227}Ac, with short-lived, γ-emitting Ra and Th daughters; b) ^{22}Na (as proxy for the natural activity ^{40}K); c) fission products such as ^{137}Cs and ^{60}Co and d) ^{210}Pb, observed by internal scintillation counting. The main conclusions from the radiotracer work are:

- The chemical preparation steps of TMB are extremely effective in removing a wide range of impurities. The intrinsic purity of TMB is determined only by the last 2 steps in which a TMB-MeOH azeotrope is phase separated by the addition of LiCl, and a final distillation made to remove traces left by the LiCl. The measured decontamination factors for U, Th, Ra, Cs, Na (proxies for K) and Co in these two steps are typically at least 10^8. Thus, even with the technical grade LiCl used in the production (U, Th ~5 ppb; K <1ppm), the final TMB can retain only $<5\times10^{-17}$g/g Th and $<10^{-14}$g/g K (Na, Cs proxy). *These results demonstrate the mechanism of the remarkable purification of TMB by some ten orders of magnitude, starting from the*

10^{-7}g/g U/Th contamination typical of the initial mineral from which TMB is made. The ultimate limits to purity are thus likely to be surface-related rather than intrinsic.

- Ra is removed ~10 times more efficiently than Th.
- Pb is removed by $>5x10^{7}$ in the azeotrope itself, even before the LiCl step. Further removal in that step is highly likely.
- The decontamination factor of TMB distillation was shown to be ~1000 even in the ~10^{-14}g/g regime; the validity of using the residue as the impurity concentrate was also verified.
- Decontamination factors for Be from (colemanite boron ore→TMB) has been measured (by direct methods) to be >1000. More sensitive radiotracer methods using proton activation of TMB via ^{10}B (p, α) will be applied to study Be isotopes activated in situ in TMB. Decontamination of cosmogenic ^{7}Be by a factor ~10^{5} is required.
- Leaching from teflon container walls was studied. Teflon vials were found to be contaminated by technical grade cleaning acids normally used for the purpose. Subsequently, Th (but not Na(K)) was seen to leach back into TMB. The results suggest that the impurity levels ~10^{-15}g/g observed the 1L TMB analyses (see above) can be accounted for by leach-in.
- Radon permeability of plastic layers, especially tedlar (the laminate layer of the acrylic vessel in Borexino) was measured by α counting to be ~10^{-4}, sufficient to reduce radon diffusion into the active volume from the acrylic to negligible levels.

In summary, the measured decontamination in the TMB manufacturing process show that the method is naturally conducive to ultrahigh intrinsic radiopurity of the final TMB product not only regarding U/Th but most other nuclides of concern to Borexino. The overall results so far, provide a quantitative basis to adopt a "design range" for the bulk radiopurity of the Borexino scintillator as:

10^{-16} to 10^{-15}g/g for U/Th and 10^{-14}g/g for K.

2.2.2 *Other Materials*

Materials in the containment/shielding architecture of Borexino themselves create background due to their finite radiopurity. Closer to the centre, the higher the purity requirement. Conservative material purities known to be available in the large scale are

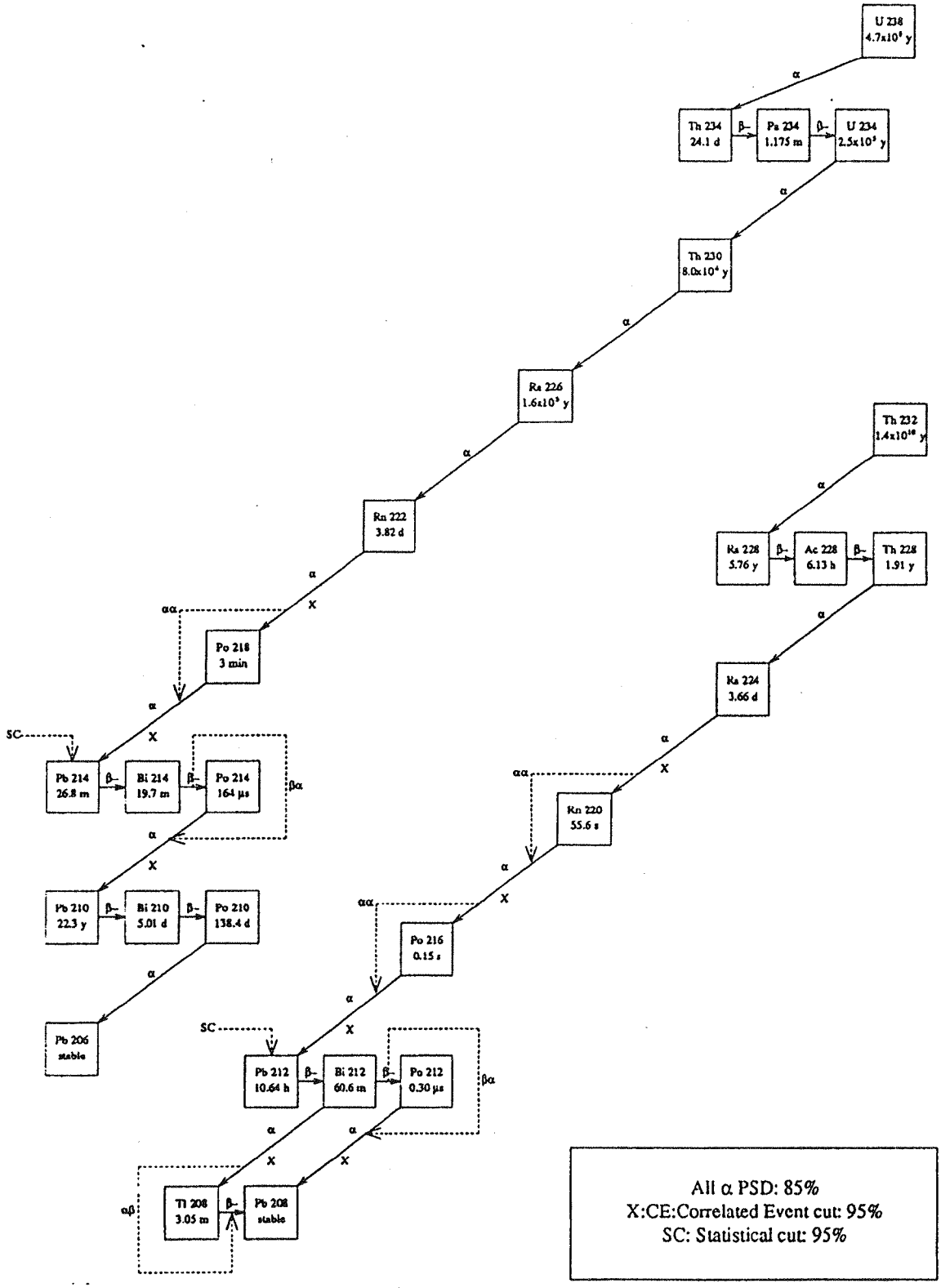

Figure 2.2 The U and Th decay series. Correlated cascades are indicated by dashed line links. Inset indicates possible tags and their efficiencies.

adopted. The overall design is such that the background due to the external materials is very small compared to the scintillator background. We mention here only selected aspects (see chapter VI for details).

Acrylic: The purity of the laminated acrylic container is important since it is situated closest to the active volume. Most known data suggest that a bulk purity of 10^{-12}g/g can be reasonably expected from acrylic samples although purity of 10^{-13}g/g has been observed in the laboratory [2.4]. We have adopted the lower purity.Worse purities can be tolerated in the design. The purity of the thin (<100μ) tedlar laminate can be nominal, $<10^{-9}$g/g, set mainly by the radon permeability measured above as long as it *applies also to internal radon in the tedlar.*

Water: Large amounts of water (1 to 4 ktons) will be the mainstay of the shielding. The design purity is 10^{-13}g/g. Mass spectroscopic studies of samples of water from the LNGS area purified by routine methods show that this standard can be readily met on the large scale in practice. A continuous purification system will be used in the detector.

Phototubes: Though remote from the active volume, the PMT's needed new technology since the content of U, Th and especially K of available PMT glass was too high. Fortunately, significant progress has recently been made in reducing the impurity contents in a new type of glass (Schott #8246)[2.5] which has been chosen for the Borexino PMT's (see chapter VI and VIII).

2.2.3 *Counting Test Facility, Quality Control*

The laboratory research phase above deals with material analysis and development of purification methods and material handling techniques. The next phase will be on-site research using two test facilities to be installed in Gran Sasso. The first is a "Volterra" type sub-boiling distillation unit at the 100 L scale for preconcentration/mass spectroscopic analysis (Appendix VI). The second will be a major counting test facility using Borexino scintillators at the ~4ton level (see the Borexino Memorandum on the Counting Test Facility). With this device, purity research conducted so far by analytical methods, will be extended to live counting tests. Criteria for batch quality control not only for scintillator radiopurity (of ^{14}C at $\geq 10^{-18}$ and U/Th $\geq 10^{-15}$) but also radiopurity of other materials, particularly construction size acrylic panels etc. ($\geq 10^{-12}$g/g) will be developed.

Correlated Cascade Events: Radioactivity in the scintillator, while imposing a high background, provides at the same time the means to tag a large part of it. The taggable nuclides assist in two key ways in Borexino operations: as calibration beacons and as removable background. For the latter, several means are available (see §2.4). For calibrations, correlated events are important. In the U and Th chains, such events are generated by α-α and β-α cascades linking intermediate nuclei with convenient lifetime (see Fig. 2.2 for their locations). They can be tagged using the signatures of their time-correlation and the specification that they occur in the same spatial location. The trigger rates in the detector (§2.4) allow operation of these tags even for the "low purity" scintillator such as case B of Table 2.III.

Live Calibrations: In the ensemble of events tagged by time and spatial coincidence,

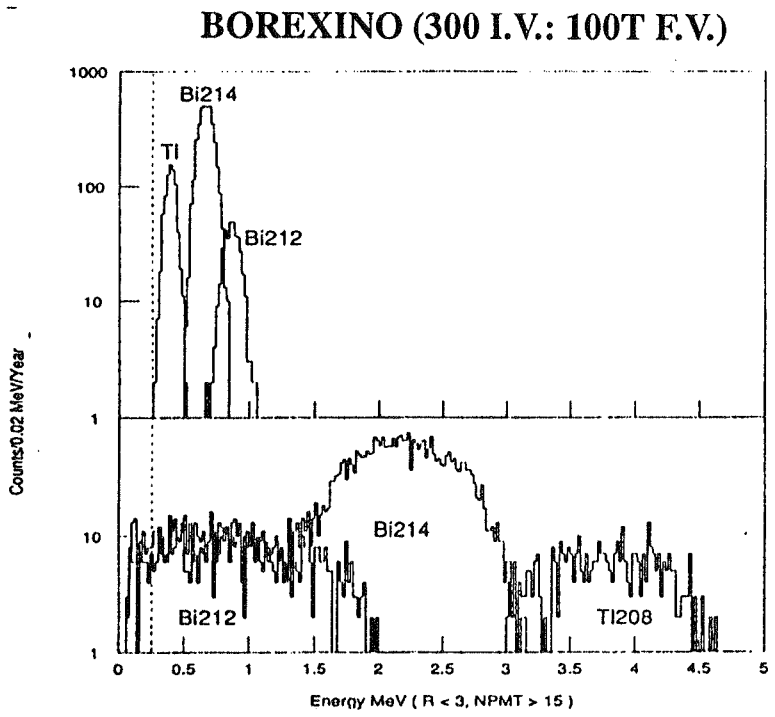

Figure 2.3 Simulated tagged spectra of (a) α's and (b) (β+γ)'s of the correlated cascades of $^{212,214}Bi$ in Borexino.

the different cascades can be sorted out by the nuclear lifetime (0.3μsec to 3 min) and the energy regime of the event. The sorted event-groups can be re-sorted into sets of spectra in the energy and spatial dimensions. Thus, the three important taggable β - α cascades in the decays of ^{212,214}Bi yield 15 different spectra comprising 3 temporal, 6 spatial and 6 energy distributions from the two radiations of each cascade, providing the means for calibrating the detector in all these three dimensions. For example, Fig. 2.3 shows an operational reconstruction of the 6 energy spectra observable in Borexino due to the calorimetric β+γ events and their α counterparts from the three Bi cascades. The β+ γ spectra in (b) cover the low energy regime with calorimetric endpoint markers at 2.25 MeV (^{212}Bi), 3.27 MeV (^{214}Bi) and at 3.2 and 5.0 MeV (^{208}Tl). These markers as well as the precisely calculable individual spectral shapes can calibrate energies of Borexino events on an absolute basis. The coincident α spectra show sharp lines at the visible (quenched) energies in the region <1 MeV (see §7.1.5). They are thus excellent monitors of the spectral stability (if not the absolute energies) in the region of interest of the Be signal.

An iterative procedure can be foreseen for determining the prevailing quality of event reconstructions. The initial step in the analysis starts with the timing data, with a simple collection of only events coincident in broadly specified time-ranges regardless of their location in the full active volume of the scintillator. In the second step, each of the candidate event can be tested by the criterion that the two components of a valid correlated event must be spatially coincident. The procedure thus iteratively tests the spatial reconstructability of the events by demonstrating a clear decay curve with the correct lifetime; the admixture of the random events at long delays can show the limits of the process. The variances in spatial reconstruction can thus be determined for locations sampled throughout the active volume. The software definition of the fiducial volume can then be tested. The event-groups with distinct decay curves obtained at this stage can be identified as specific nuclear cascades by the lifetime. The known nuclear data of these cascades specify the nature and the energy distributions of the two correlated radiations. Against this absolute calibration scale, the quality of reconstruction of energies and spectral distributions of events at random but known locations in the active volume can be tested.

The U/Th radiation cascades are thus live monitors, randomly sampling the full active volume and calibrating the time, energy and spatial response of Borexino. The overall temporal stability of the detector operations can thus be monitored continually on an absolute physical basis.

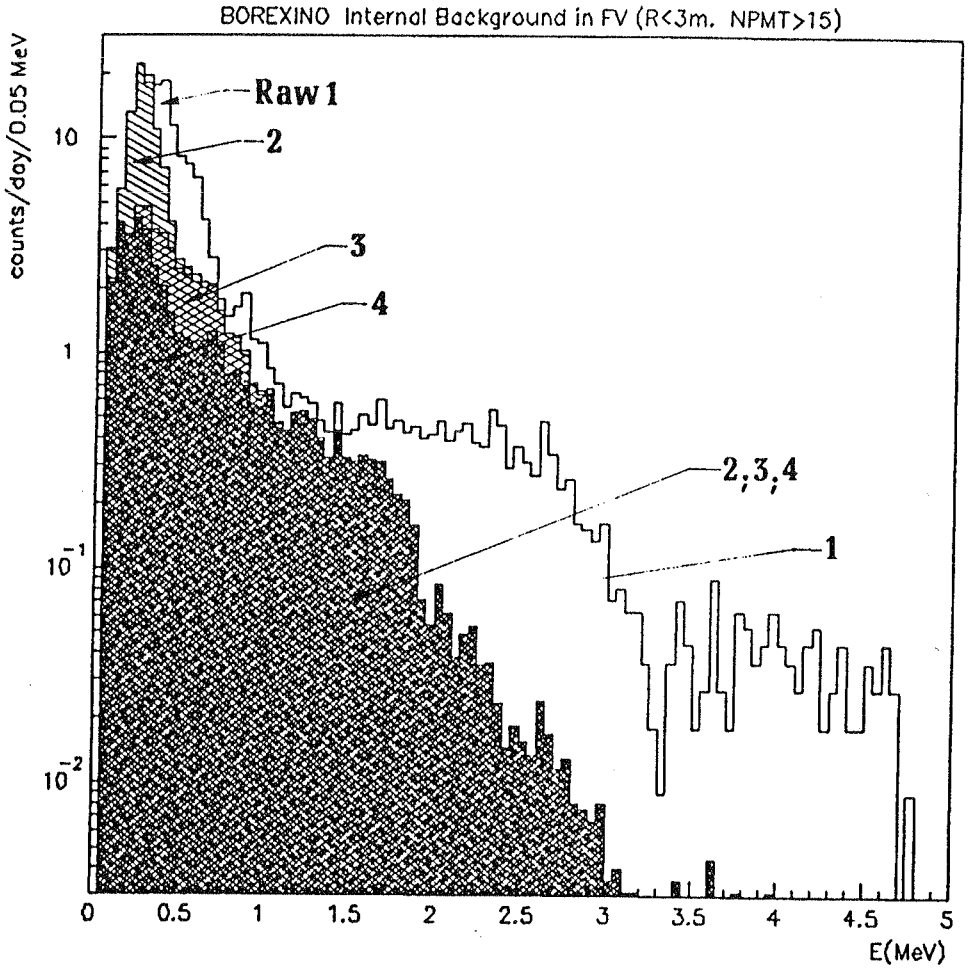

Figure 2.4a Background spectroscopy in Borexino showing the effect of successive cuts: (1) raw; (2) after CE cut; (3) after PSD cut; (4) after SC cut. These cuts are made on-line or off-line with internally measured data.

2.4 *Determination of Operating Background*

Internal Background Tags: The dominant background in the F.V. is that from the radioactivity of the scintillator. Assuming U, Th and K as the only contributors, the structure of the internal background can be determined by on and off-line analysis using several types of tags and other indicators. The extent to which this can be carried out in Borexino was analysed using Montecarlo simulations (Appendix V). Fig. 2.4a shows the

Figure 2.4b Composition of untagged residue spectrum (4). The simulated components of ^{210}Bi (Pb), ^{234}Pa (U) and ^{40}K which survive the cuts I-III are shown.

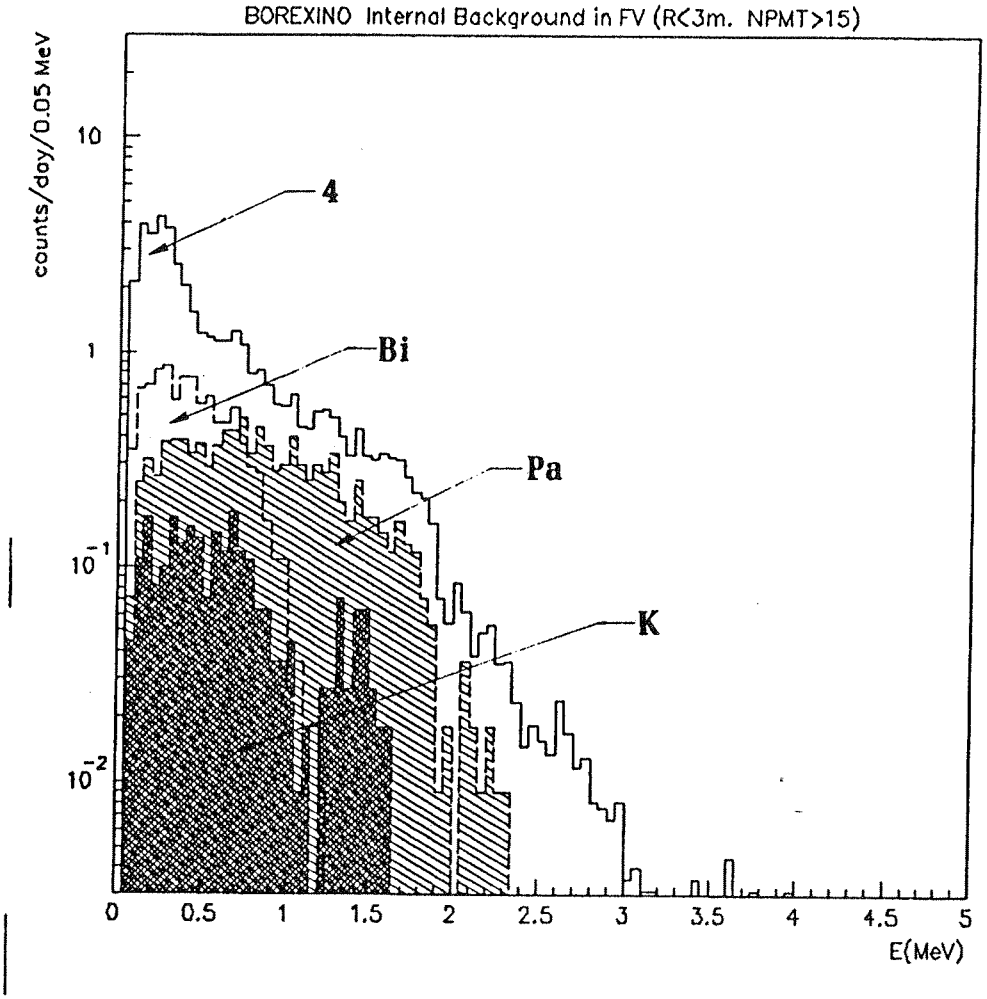

simulated raw internal background (curve 1) visible in Borexino for a (case A) "high" purity scintillator. The "peak" at low energies is due to α's; its position relative to the ^{14}C cutoff at ~0.25 MeV is decided by the "adjustable" quenching properties of the scintillator (see §7.1.5). By optimizing the quenching, the low energy α's could possibly be degraded below the cutoff, thus making them less important. The bump at ~0.7 MeV is from the ^{214}Bi cascade. The structure of curve (1) in Fig. 2.4a can be largely characterised by the following successive on- and off-line experimental cuts.

Cut I: Correlated Events (CE): The correlated events discussed above are taggable

components of background. The efficiency of tagging depends on the intermediate lifetime and the uncorrelated trigger rate. From the simulated background of Fig. 2.4a, in the signal window of (0.25 to 0.8) MeV, the raw trigger rate is ~0.8/day/1m^3. The uncorrelated rate is ~0.4/day/m^3, divided about equally between α's and the $\beta+\gamma$'s. Consider the worst case of the 3 min. α-α CE, between ^{222}Rn and ^{218}Po, (see Fig. 2.2) which occurs at a rate of 0.08/m^3/day. With a reasonable discrimination of α events, 95% of them can be tagged in a volume of 2m^3 incurring a random coincident admixture of <1%. Even for a x10 worse purity, the random admixture is <10%, explicitly visible in the time-distribution. For all other CE's, random admixtures are low to negligible. We shall adopt a standard tag efficiency of 95%.

Cut II: Pulse Shape Discrimination (PSD): As mentioned in §2.1, the scintillation pulse shape can be used to tag heavy particles, in particular α events. Scintillation lifetime (chapter VII) in the various mixtures were measured and the data applied in realistic simulations (including optical scattering and reflections in the detector). The results indicate that a PSD can be performed in Borexino upto a high level of 90% recognition of α events at the expense of 6% electron events mistaken as α's (chapter VIII). The PSD efficiency varies with the mixture; the final choice will be made at more advanced stage. A typical figure of 85% PSD will be assumed for this discussion.

Cut III: Statistical Background Cut (SC): The identification of a taggable impurity species automatically reveals the concentration of other impurities in the local segment of the decay chain since these adjoining activities are in equilibrium. For example, the number of ^{218}Po atoms tagged by delayed coincidences determine that there are equal numbers of ^{214}Pb,^{214}Bi and ^{214}Po atoms. Since the detector response is experimentally well defined by on-line calibrations discussed above (§2.3), the radiation spectra of the activities in the segment can be correctly constructed and statistically removed (off-line) from the residual spectrum after the live cuts. This is particularly useful for two cases, ^{212,214}Pb (SC in Fig. 2.2). These two nuclides are preceded and followed by CE tags which can even indicate the approximate locations of the Pb species as aids for constructing their spectra. We assume that their content can be assessed to ~5%, thus a "tag" efficiency of 95%.

Cut IV: The Uranium Cut: The three cuts above are based on *on-line* information. A further cut is possible by data derived externally. The ^{238}U content can be measured directly by laboratory analytical methods to ~95%. The activity of ^{234m}Pa, which directly follows ^{238}U can thus be estimated statistically in a manner similar to *Cut III.*

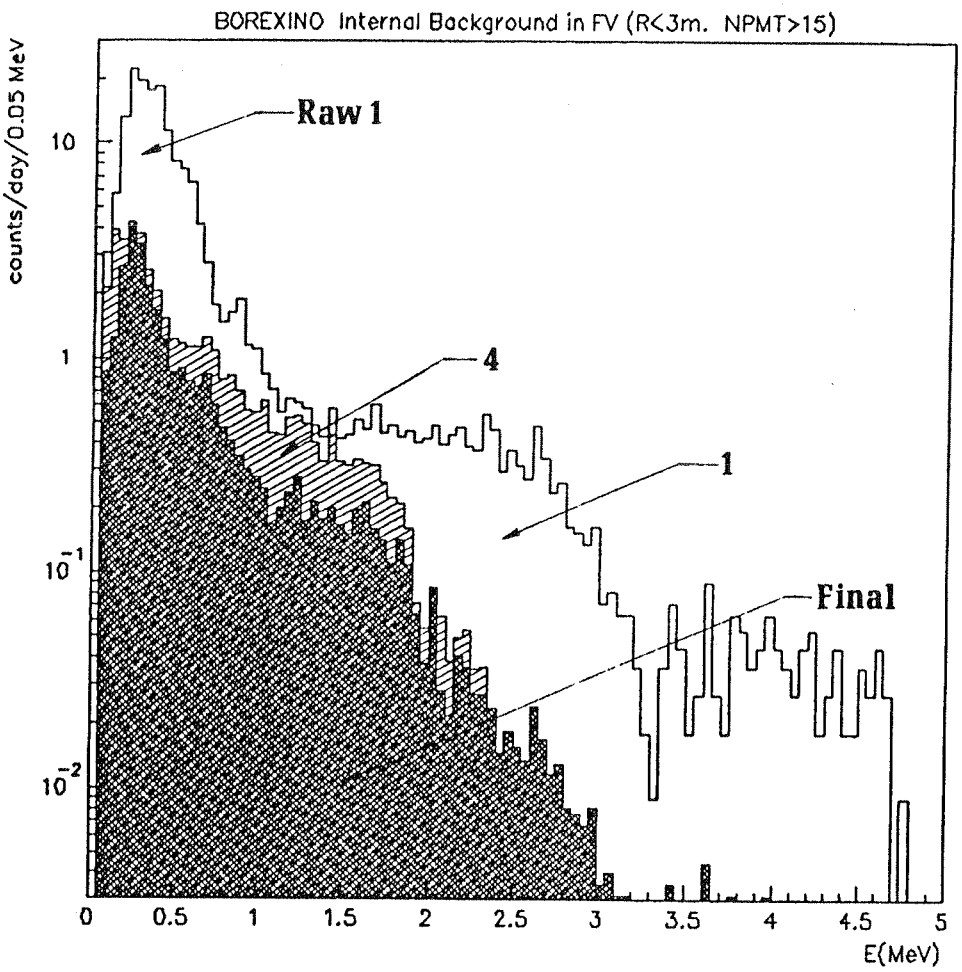

Figure 2.4c Action of the final ^{238}U cut-IV (lowermost) in comparison with raw spectrum (uppermost) and up to Cut III spectrum (4) in the middle.

The spectral effects of the successive operations of the above cuts on the radioactivity background in Borexino for the "high purity" scintillator can be seen in the Montecarlo simulations of Fig. 2.4a. Curve (1) is the raw spectrum, with events > 2 MeV being due mostly to ^{214}Bi ($\beta+\gamma$)'s; above 3 MeV they are due to those of ^{208}Tl. Application of the CE cut-I results in curve (2). The background >2 MeV is tagged away, so is most of that at low energies. The PSD cut-II results (curve 3) in a key reduction at low energies, higher energy α's being already tagged off. The off-line SC cut-III results in curve (4); the reduction is specifically in the signal window. Fig. 2.4b shows the composition of the spectrum after *Cut III* (curve 4). Besides a non-negligible fraction of surviving α's, it consists mainly of β's from three nuclides: the 1.1 MeV, 100% β decay of ^{210}Bi in equilibrium with ^{210}Pb, the 2.29 MeV,~100% β decay of ^{234m}Pa in equilibrium with the

primary ^{238}U and ^{40}K. Among the survivors, Fig. 2.4b shows that ^{40}K is the least important; if its content relative to U is much higher than assumed here, its γ-ray line at ~1.46 MeV will outgrow the spectral profile of curve (4) and become explicitly observable. With the known intensity of this line feature, the rest of the ^{40}K β spectrum can be constructed, thus the contribution from K can be removed if necessary. Finally, the contribution from U-Pa can be removed (U cut-IV, 95%). Fig. 2.4c shows the overall action of cuts upto III (middle) and upto the final cut IV (bottom) relative to the raw spectrum (top).

Table 2.IV is a summary of the event rates in the signal window from the individual nuclides in the course of this analysis. The background in the signal window can be reduced by x~6 upto cut III and by x~8 in cut IV; the reduction can be somewhat larger, ~x10, if the α quenching is "tuned" to depress the low energy α's below the ^{14}C cutoff. The limiting factor on the internal background is thus $^{210}Pb \rightarrow ^{210}Bi$. The flattened background >1 MeV upto ~2 MeV in Fig. 2.4c is due to ^{228}Ac. The external background (see chapter XII) is estimated to be at about the same level. A live determination of the external component (see below) is thus necessary for further reductions. The final figure of 11/day in Table 2.IV for the internal background is used in Table 2.III.

The progress made so far in reaching design purities of the scintillator regarding U, Th and other impurities including Pb, sets the stage for substantial further gains on the internal backgrounds by *focusing specifically on Pb in TMB and PC.*

These analyses can thus lead to a reasonably complete spectral characterisation; a complex initial background spectrum from 28 different nuclear species is reduced basically to that of the shape of a single, simple β decay, that of ^{210}Bi. In the process, possibilities such as disequilibrium in the decay chains, surface contamination (presumably ^{210}Pb will be the dominant source) or the presence of other impurities of low energy radiations can possibly be inferred from these analyses of the background profile. We stress that the background tags discussed here are monitors of the stability of the background in Borexino, valuable for the search for time-varying neutrino signals from solar ^{7}Be.

Spectroscopy and Monitoring of External Background: Another component that can be identified in the Borexino data is the external background. Simulations of this component (chapter XII) based on the present shielding architectural design show that in a 6m F.V., it is <2 events/d in the signal window, well below range of the internal background. Outside the F.V. however, it increases exponentially to x600 at the acrylic

Table 2.IV Live Determination of Internal Background (Events/year in Signal Window (0.25-0.8 MeV); "High" Purity Scint.)

Imp.	Raw	Cut I (CE)	Cut II (PSD)	Cut III (SC)	Cut IV (U)
β+γ's					
Th-234	1	1	1	1	1
Pa-234	1412	1412	1412	1412	70
Pb-214	3321	3321	3321	166	166
Bi-214	219	11	11	11	11
Pb-210	0	0	0	0	0
Bi-210	1764	1764	1764	1764	1764
Ac-228	135	135	135	135	135
Pb-212	919	919	919	46	46
Bi-212	283	14	14	14	14
Tl-208	0	0	0	0	0
K-40	529	529	529	529	529
U α's- UnCorr.	6942	6942	1039	1039	1039
Corr.	10894	543	81	81	81
Th α's -Uncorr.	1200	1200	180	180	180
Corr.	4421	220	34	34	34
Total/Year	32044	17012	9442	5414	4099
Total/Day	88	47	26	15	11

wall 1.25m away. Thus it will overtake the internal background beyond ~40 cm from the edge of the F.V.. The radial dependence of the spectrum can be measured differentially. This is useful for two reasons: extrapolation back into the fiducial volume can help determine the spectrum of the external background component in the F.V. secondly, the smooth profile of the variation will show sharp increases near the acrylic shell due to possible surface activity. The locality of the activity, its spectral characteristic and the stability of these spikes are important diagnostics for a continual and global monitoring of the surface problem during Borexino operations.

References

[2.1] A. de Bari, R. S. Raghavan, W. Kelly and J. Fasset (To be published).

[2.2] W. Kelly and J. Fasset (To be published).

[2.3] R. Beukens and R. S. Raghavan (To be published)

[2.4] Sudbury Neutrino Observatory Proposal (1987).

[2.5] The procurement of this special glass for our experiment was possible by the cooperation of the SNO Collaboration.

CHAPTER III

NEUTRINO SIGNALS & SIGNATURES

3.1 Neutrino Detection Modes

Neutrinos can be detected in Borexino using a variety of reactions. These include:

•) neutrino-electron scattering which is sensitive to both electron and other types of flavours,

$$\nu + e \rightarrow \nu + e \tag{3.1}$$

•) inverse beta decay in ^{11}B nuclei, sensitive only to neutrinos of the electron type,

$$\nu_e + {}^{11}B \rightarrow e^- + {}^{11}C \; (\rightarrow e^+ + {}^{11}B) \tag{3.2}$$

•) inverse-beta decay in protons, sensitive only to antineutrinos of the electron type,

$$\bar{\nu}_e + p \rightarrow e^+ + n \tag{3.3}$$

With these reactions, neutrinos from the sun as well as from a laboratory radioactive source can be detected in Borexino. Table 3.I lists details of these reactions. A possible neutral current reaction on ^{11}B (applicable to neutrinos of all flavours) is not listed because its event rate is too low in the small size Borexino to be useful; this reaction will be of primary significance in the planned Borex detector with ~20 times the mass of Borexino. Table 3.I lists also the neutrino types that can be observed using these reactions, the possible signatures for identifying them and the event rates for solar fluxes predicted by the SSM. The analysis threshold of signals of these reactions in Borexino depends on experimental factors such as background vs. signal and the efficacy of

Table 3.I Neutrino Detection Reactions in Borexino

	Reaction (3.1)	Reaction (3.2)	Reaction (3.3)
SOLAR NEUTRINOS-LO ENERGY (^{7}Be, pep, ^{13}N, ^{15}O)			
Event Threshold (Analysis: MeV)	0.2	—	—
Neutrino Thres (MeV)	0.41	—	—
Signal Range (MeV)	0.25-1.5	—	—
Signature	Yearly Var. ($1/R^2$ Effect)	—	—
Fiducial Vol.	100 Ton	—	—
Event Rate SSM (0.25-0.8 MeV)	50/day (18000/yr)	—	—
SOLAR NEUTRINOS-HI ENERGY (^{8}B)			
Event Threshold (Analysis: MeV)	4.0	4.0	—
Neutrino Thres (MeV)	4.23	5.98	—
Signal Range (MeV)	4 - 14	4 - 12	—
Signature	—	Del. Coinc.	—
Fiducial Volume	240 ton	240 ton	—
Event Rate (SSM (4-12 MeV)	364/yr	222/yr	—
ANTINEUTRINOS--^{90}Sr SOURCE			
Event Threshold (Analysis: MeV)	0.2	—	1.02
Neutrino Thres. (MeV)	0.37	—	1.8
Signal Range (MeV)	0.2-2.2	—	1.0- 1.5
Signature	on-off	—	Del. Coinc.
Fiducial Volume	200 ton	—	200 ton
Event Rate (5 MCi @ 8 m)	56/day (0.2-0.8 MeV)	—	32/day
ANTINEUTRINOS—SUN ?			
Event Threshold (Analysis: MeV)	—	—	4.2
Neutrino Thres. (MeV)	—	—	5
Signal Range (MeV)	—	—	>4.2
Signature	—	—	Del. Coinc.
Fiducial Volume	—	—	200 ton
Event Rate	—	—	(20-100/yr?)

suitable signatures. The thresholds for reaction (3) for example, are different for the sun and the source mainly because the antineutrino event rates with the latter are far larger (>300 times) than those expected in some exotic scenarios from the sun. The signal/background considerations also play a key role in the selection of a suitable fiducial volume for the particular reaction.

3.2 *Low Energy Neutrino Spectroscopy*

The basic detection reaction for observing low energy ^{7}Be solar neutrinos in Borexino is ν-e scattering (reaction 3.1 above) in the scintillator with N_e=3.2x10^{31} electrons in the 100 ton FV. The reaction has no threshold, however we expect a practical low energy cutoff on recoil electrons at ~0.25 MeV. The ν_e-e scattering proceeds via both the charged and neutral currents, while ν_x-e is driven only by the neutral current. The total cross-sections for the two processes differ by ~5:1 at energies ~1 MeV. The differential cross-sections for ν_e and ν_x are given by [3.1]:

$$d\sigma_e / dT = \sigma_o \, [0.533 + 0.053(1 - \frac{T}{q})^2 - 0.168\frac{T}{q^2}] \qquad (3.4a)$$

$$d\sigma_x / dT = \sigma_o \, [0.073 + 0.053(1 - \frac{T}{q})^2 + 0.062\frac{T}{q^2}] \qquad (3.4b)$$

were σ_0= 88.08 x 10^{-46} cm^2, T is the kinetic energy of the recoil electron and q the incident neutrino energy, both in units of m_ec^2. A monoenergetic neutrino produces a recoil spectrum with a slight (almost) linear slope with a "compton" edge at: T_{max} = $2q^2/(1 + 2q)$. For the ^{7}Be solar neutrino line feature at 0.86 MeV, the edge is at 0.66 MeV.

Low Energy Signal Spectrum: The low energy signal <1.5 MeV is created by the monoenergetic ^{7}Be neutrinos and to a smaller extent, by continuous spectra from ^{13}N ($E_{\nu max}$ =1.2 MeV) and ^{15}O ($E_{\nu_{max}}$ = 1.7 MeV) and the line feature at 1.44 MeV due to the pep reaction in the sun. Fig. 3.1 shows a Montecarlo simulation [Appendix V] of low energy spectra in Borexino (100 ton FV). The signal events are the solid line histogram. They are the recoil electron spectra due to SSM fluxes[3.1] of ν_e's (higher spectrum) and the pure ν_μ signal (lower spectrum) due to complete conversion of a SSM flux (due to the MSW effect) [3.2]. The sharp rise at the lowest energies is due to pp neutrinos. They may not be visible in practice because of the possible presence of ^{14}C which may set a cutoff at ~0.25 MeV (dashed vertical line in Fig. 3.1). Above the cutoff, the signal is dominated

Table 3.II Low Energy Signal and Background in Borexino (100t FM)(Event Rates/day: High Purity Scintillator)

EVENTS	^{7}Be (0.25 to 0.8) MeV
SIGNAL (SSM)	50
SIGNAL (MSW)	10
BGD. (Int.radioactivity)	11
BGD. (Total Ext.)	<2

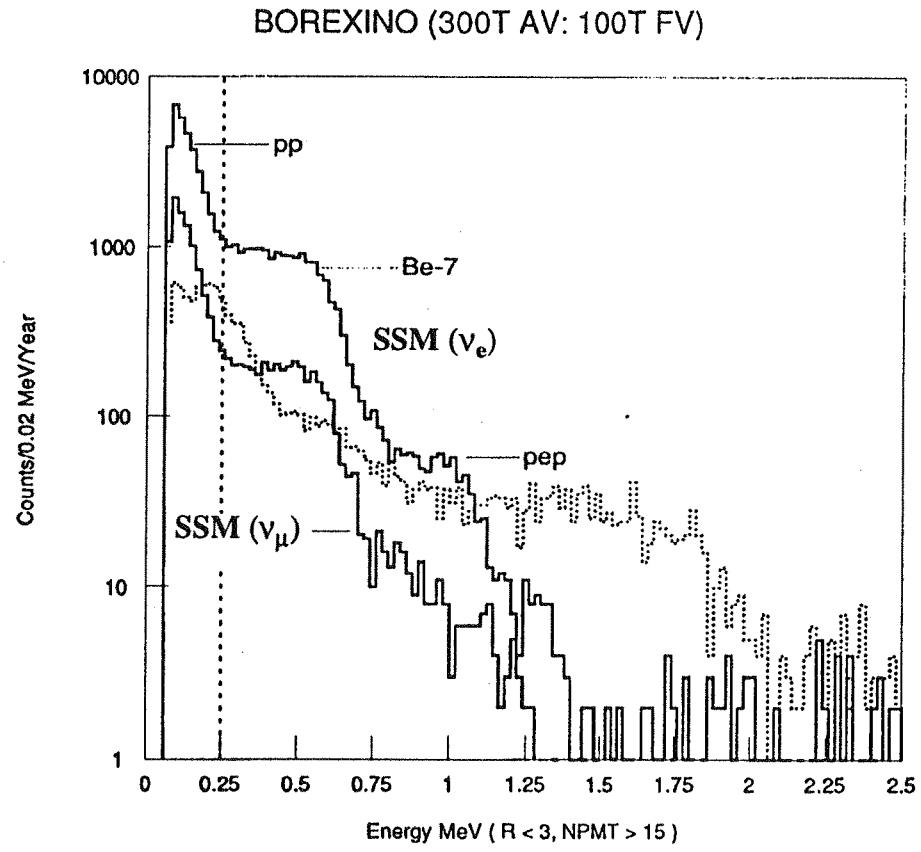

Figure 3.1 Simulated spectra of low energy signal (solid lines) and radioactivity background (dotted line) in Borexino (100 ton FV) The upper solid line is for SSM ν_e's and the lower, for SSM fluxes completely converted to ν_μ's (via the MSW effect).

by the ^{7}Be events in the signal window 0.25 to 0.8 MeV. As seen in Fig. 3.1, the typical energy resolution in Borexino is sufficient to define the scattering "edge" of the ^{7}Be neutrino line at ~0.7 MeV despite some smearing due to the presence of the ^{13}N signal events with an endpoint at ~0.85 MeV. The pep neutrinos, also monoenergetic (1.44 MeV), produce a scattering edge at ~1.2 MeV and a second plateau just above the Be edge. The SSM flux of ^{15}O neutrinos is nearly 3.5 times that of the pep's. They produce additional events ending at ~1.5 MeV. The observed signal in the "pep plateau" is thus 1.7 times the pep signal alone.

The background spectrum shown by the dotted profile in fig. 3.1 is due only to radioactivity in a high purity (10^{-16}g/g) scintillator, remaining after active cuts based on internal tags or external indicators (see § 2.4). The external background is not shown; it is small below 1.25 MeV. Table 3.II compares the signal and background rates.

Fig. 3.2 shows the low energy (signal + background) profile. The edge at ~1 MeV region is due to pep neutrinos. The dotted lines at the bottom of the figure represent the results of Montecarlo simulations of the external background due to radioactivity in the acrylic and other detector materials and the cave background. The cosmic ray induced background is negligible at these energies (see chapter XII). This background has not been added to the solid line profile. Its level can be depressed substantially relative to the internal background by choosing a 5.5m 80 ton FV where it can be reduced by a factor of 3 at the cost of only 20% of the signal.

Spectroscopic measurement of the ^{7}Be Flux: The simulated spectra in Fig. 3.2, show clearly that SSM -type fluxes can be measured directly by spectroscopic techniques for the case of the higher intrinsic purity of the scintillator because of the good signal/noise (~3.5 to 5). A good estimation of the relatively small background in the Be signal window is possible because the scattering edge and the plateau can be well demarcated (Fig. 3.2). However, even in this case, because the scattering signal is relatively non-specific, a signature directly connecting the scattering events to the sun is necessary (and possible) in Borexino.

However, if the purity is worse and backgrounds are significantly higher than in Fig. 3.1, a reliable spectroscopic flux measurement becomes difficult, less because of statistics but because the scattering edge feature is increasingly obscured. In this case, reasonable flux determinations are possible, based entirely on the direct solar signature.

Solar Signature for the ^{7}Be Neutrino Signal: The strategy in Borexino for reliable ^{7}Be neutrino observations in general under wide tolerances of scintillator purity is based on a

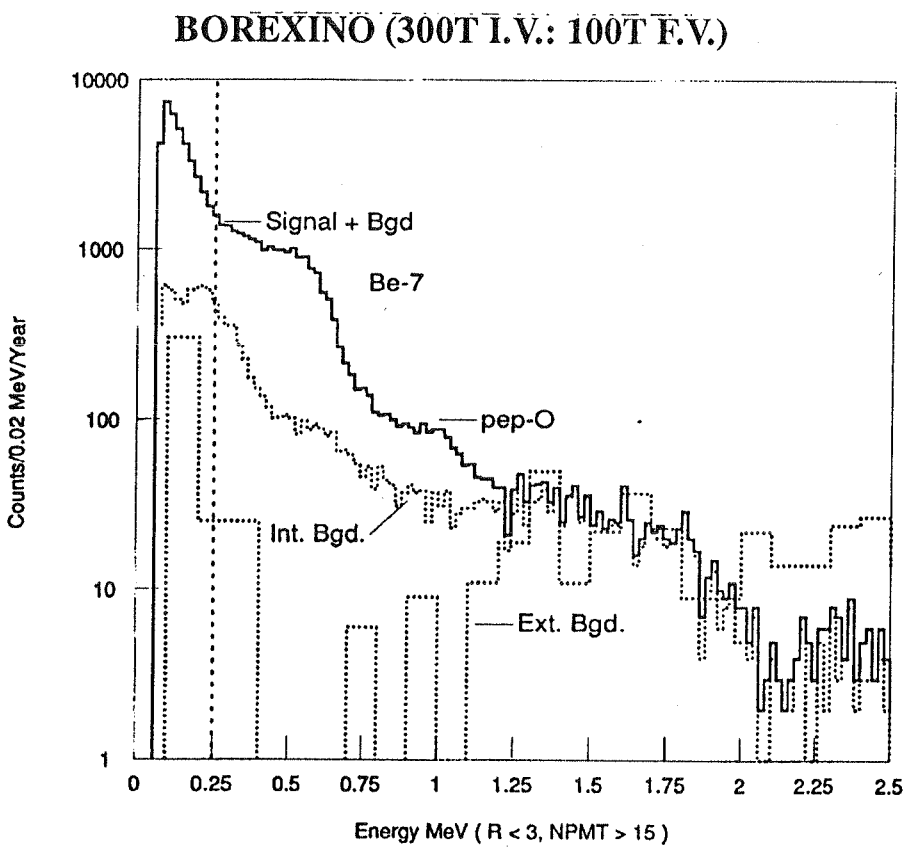

Figure 3.2 The solid line is the profile of the SSM ν_e signal plus the radioactivity background. The dotted curve is the radioactivity alone. The dotted histogram at the bottom is the external background.

Figure 3.3 Applicability of the $1/R^2$ Solar Signature for ^{7}Be ν flux measurement

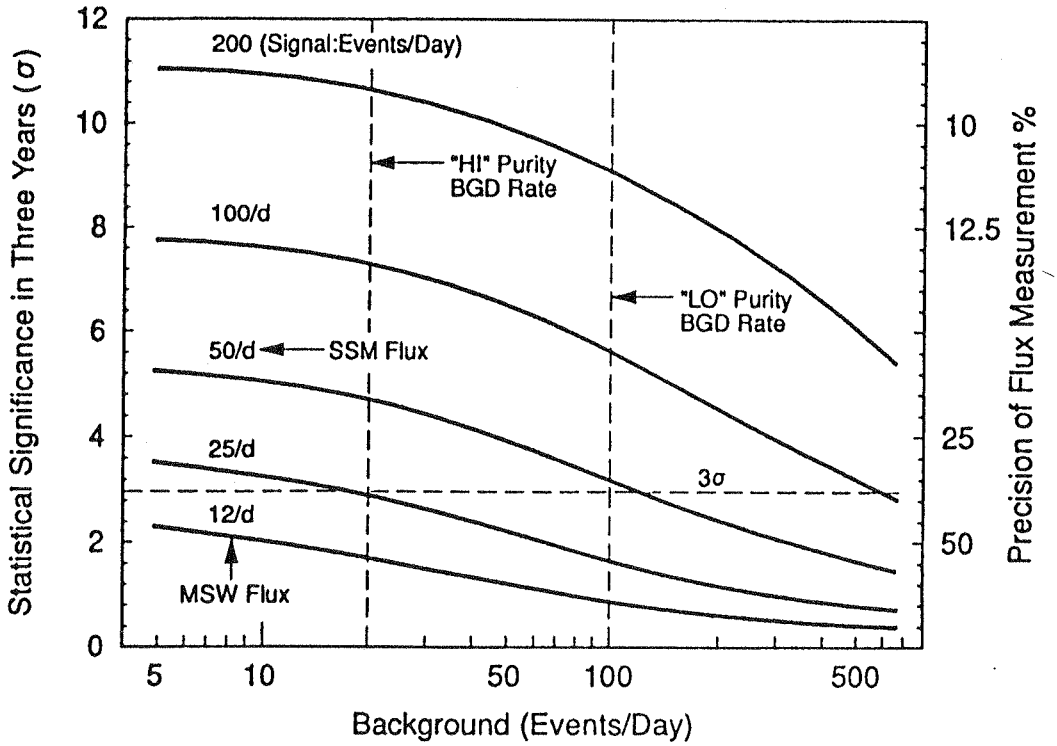

signature connecting the low energy signal explicitly to the sun. The reasonably high signal rates of the order of 50/day (9000 events/half year), opens the possibility of using the $1/R^2$ effect due to the eccentricity of the earth's orbit around the sun which creates a yearly rate variation of 3.5% and well-defined seasonal phases. Such an effect (observable only in the signal window), is intrinsic to a solar signal independent of the astrophysical or neutrino scenario. This variation can be observed directly by filtering out the time varying signal part of the observed events independently from the constant part of underlying background without the need to explicitly measure the background. This signature will assure solar origin of the measured result under all circumstances (especially in the case of an unexpected, higher than SSM signal) and prove that it is a real effect. In practice, variations of the background are not expected to be periodic. However, the temporal stability of the background over periods of the order of months can be monitored by the event rates in the energy regime >1.5 MeV, above the solar signal windows and by observing distortions in the spectral profile within the windows (arising e.g., from the Pb-Bi activity, see §2.4).

Application of the $1/R^2$ signature is limited by the signal rate as well as the signal/background ratio. The range of signal and background amenable to this strategy of flux measurement is illustrated in Fig. 3.3. It shows Montecarlo estimates of the statistical significance or equivalently, the fractional precision attainable for a flux measurement for a period of three years for various values of signal rates as a function of the (constant) background rate. The vertical dotted line at a background level of ~20/day typifies a high purity scintillator ($\sim 10^{-16}$g/g) and the dashed vertical line at 100/day, a low purity (10^{-15} g/g) scintillator.

In the major physics scenarios, complete neutrino conversion by the MSW effect predicts a signal of ~10/d in Borexino. An "astrophysical" solution of the SNP (see § 2.1) expects a rate of ~50/day. At a background of 100/d, the 1σ error incurred in a measurement of the time-varying part of the events, obtained in a $1/R^2$ analysis, would be ~13/d for a live time of three years. This implies that in the MSW case with the low flux, a solar signal would be measured at best as 10±13/d. The result can rule out an "astrophysical" scenario with a signal ~50/day high flux with at least (3σ) confidence, solely on the basis of this signature. An SSM type signal rate can be measured, e.g., as 50±15/day, resulting in a flux value determined with a precision of ~30%. Thus, with the help of the yearly variation solar signature, a significant measurement of the ^{7}Be neutrino flux can be made without the need to determine the nature or value of the background even with a background in the range ≤100/d in the signal window.

In the lower background regime with higher purity, the signal determination would entail a 1σ error of ~8/day; the physics distinction can be made at the ~5σ level and an SSM type flux measured to ~20%. In this case, however, better results are possible with direct spectroscopy because of the good signal/noise; the $1/R^2$ effect ensures the solar origin of the signal.

3.3 *^{8}B Solar Neutrino Spectroscopy*

The high energy ^{8}B neutrinos can be detected by two reactions both of which result in electron signals. These are ν-e scattering, reaction (3.1), which we considered above, and inverse β-decay of ^{11}B, reaction (3.2), the "charged current" (CC) signal. Experimentally, the basic ^{8}B signal is the the total signal (ν-e + CC) since cross-sections and spectral shapes for both channels are well-established. In principle, a signature is available specifically for the CC channel so that the two reactions can be separated.

Inverse β-decay of ^{11}B: This reaction (eq. 3.2) induces transitions from the ground state of ^{11}B in the TMB (80% abundance in natural boron) to that of ^{11}C and to a minor extent also to its excited levels at E_i= 2.0, 4.32 and 4.8 MeV. The CC nature of these transitions dictates that they detect only electron neutrinos ν_e. The thresholds for the ground and excited states are given by: $E_{th} = E_i + \Delta$ where Δ = 1.982 MeV, the ^{11}B-^{11}C mass-difference. In any of the transitions, an electron of energy $E_e = E_\nu - E_{th}$ is emitted. For the ground state transition, $E_e = E_\nu - \Delta$. For the excited states, a de-excitation γ-ray of energy E_i is also emitted and detected calorimetrically summed to the electron signal. Thus the total energy of the neutrino event is always $E = E_i + E_e = E_\nu - \Delta$. The inverse β energy spectrum of (0 to ~12 MeV) faithfully reflects the solar ^{8}B ν_e-spectrum arriving at the detector.

The event rates for this reaction can be calculated by the standard theory with known nuclear parameters [3.3]. The ^{8}B signal is weak in Borexino because of its small size. Thus, to maximize the signal, a larger FM is desirable. In the range of interest to ^{8}B neutrinos, >4 MeV, internal or external radioactivity creates only a weak background. Other possible background in this regime, such as high energy γ's from neutron capture and muon-induced activities in the FV (see chapter XII), are also expected to be relatively small. Thus a larger FV can be chosen for ^{8}B ν spectroscopy (LFV). We adopt a LFV of 8m dia. (0.50m buffer to the IV wall), containing 240 tons of scintillator with ~22 tons of

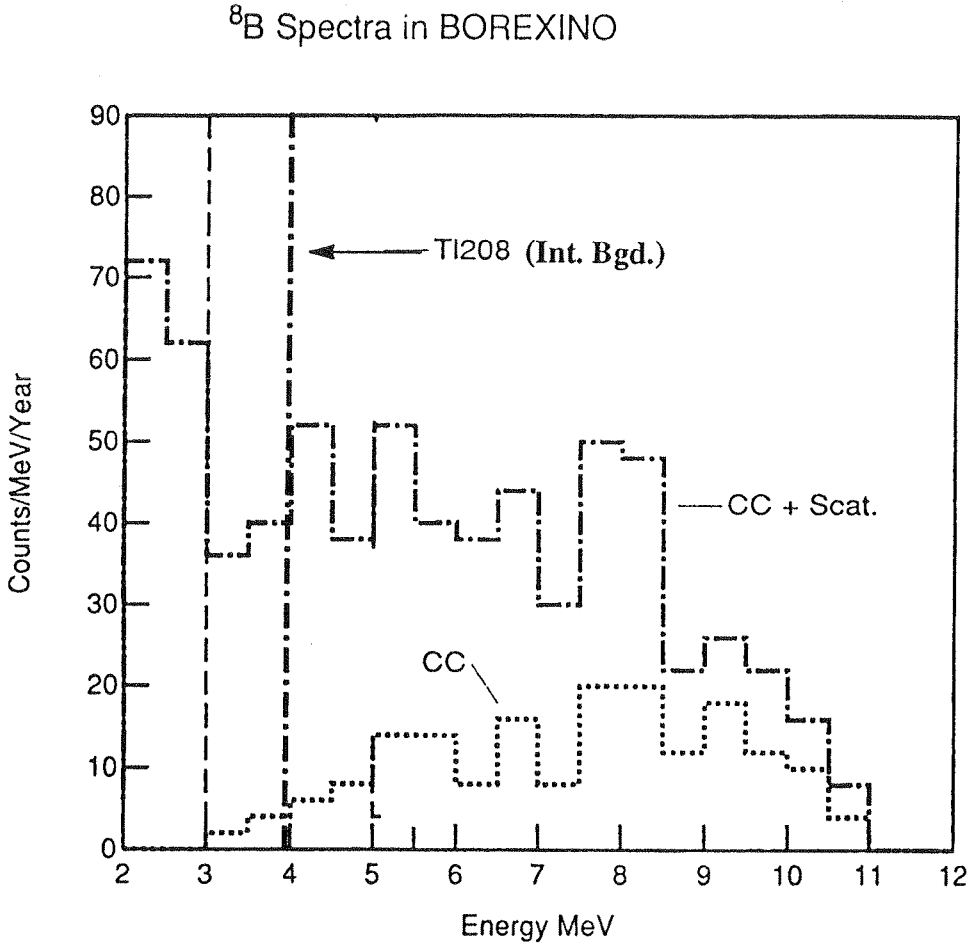

Figure 3.4 Simulations of High Energy Signal in Borexino. The signal rates + shapes are for an MSW scenario compatible with K-II results. The vertical line at ~9 MeV is limit of external background.

boron). In this case, even though the external background becomes ~100 times larger than in the 6m FV, the spillover in the high energy regime is small as shown by simulations in fig 3.4 for a high purity scintillator. The spectral shapes and event rates of ν_e and CC channels have been calculated for various input solar neutrino spectral profiles for the SSM as well as MSW scenarios allowed by the present experiments. Table 3.III gives event rates for the signal energy range >4 MeV for the SSM and a typical MSW scenario.

Fig. 3.4 shows, for example, the ^{8}B spectra observable in Borexino for the case of an MSW effect in the sun compatible with the K-II results. The total event rate >4.0 MeV in these spectra is ~268/y (cf. SSM rate = 586/y) as compared to the K-II signal ~90/y. The dot-dashed profile is the total signal (CC+e-ν) while the dotted one is for the CC only

Table 3.III ^{8}B *Signal Rates in Borexino (Events/year; E> 4 MeV; 240 t FV with 22t B)*

	CC($^{11}B \rightarrow {}^{11}C$)			(e-ν)	
Scenario	E_i (MeV)	B(GT)[a]	N_{CC}	N_{sc}	Total
SSM	0	0.345(8)	167		
	2.00	0.399(8)	18.5		
	4.32	0.480(9)	24		
	4.81	0.480(9)	12.5		
SSM	Total		222	364	586
MSW			92	176	268

[a]Measured CC matrix elements by Taddeucci et al, Phys. Rev. C42, 935 (1990).

(possibly separable by a CC signature, see below). The vertical lines show the flanks of the background profile due to external radioactivity (ending at ~3 MeV) and due to internal radioactivity (10^{-16}g Th/g) from the ^{208}Tl radiations (ending at ~4 MeV). The Tl activity is assumed to be 95% tagged (see § 2.4) by its correlated cascade.The low energy cut off of ~4MeV is the lowest among future detectors (>6 MeV) The spectral shapes at these energies contain vital information on possible new neutrino physics.

Signature for CC Signal: The CC signal can be discriminated, in principle, from the scattering signal because the CC transitions produce ^{11}C which is β^+ radioactive with a lifetime of ~20 min. Thus every CC transition should be accompanied by a positron of a calorimetric energy ranging from a minimum of 1.02 MeV (the positron annihilation signal) to 2 MeV (positron kinetic energy ~1 MeV) occurring at the same spatial location as the CC event. The overall trigger rates in the detector do not pose a problem in identifying this delayed coincidence despite the very long lifetime. However, a problem may arise from the convection in the liquid which may transport the ^{11}C to considerable distances and lessen the sharpness of the spatial coincidence. The rates dictate that the signature would be operable if the radius of search for the positron can be restricted to ~1.5m or less from the location of the prompt CC event of >4 MeV. Crude hydrodynamic estimates of convection do indicate that this condition could be satisfied in the LFV for the B signal, 25 cm away from the acrylic wall. However, since it appears impossible to guarantee this estimate at present, direct methods for controlling convection by temperature gradients are being considered.

3.4 *Antineutrino Spectroscopy (Solar Source)*

Sensitivity to $\bar{\nu}_e$'s in Borexino adds a unique dimension to its potential for a wide ranging search for new neutrino physics. A search for antineutrinos above terrestrial $\bar{\nu}_e$ (radioactivity, nuclear power reactors) energies as well as below them, has been suggested for various reasons from time to time. In the context of present solar neutrino results, antineutrinos are specifically predicted in certain scenarios (Majorana magnetic moments of neutrinos and neutrino decay) (§ 4.1, §4.3). Typical $\bar{\nu}_e$ signals in Borexino for these scenarios are in the range <100/year, thus needing high detection efficiency, a strong signature for background elimination as well as proof of the presence of a $\bar{\nu}_e$. Antineutrinos are not predicted by any solar model, thus observation of (solar connected) $\bar{\nu}_e$.'s would be of major significance.

Signature for Antineutrinos: The liquid scintillator contains a substantial amount of protons (10^{31}) in the FV (200 t). The presence of these free protons affords a high sensitivity to antineutrinos ($\bar{\nu}_e$) via the classic Cowan-Reines inverse β^+ reaction (eq. 3.3).

The neutron in (eq 3.3) can be detected efficiently by the slow-neutron reaction:

$$n + {}^{10}B \rightarrow {}^{7}Li + \alpha\,(2.3\ \text{MeV}) + \gamma\,(0.48\ \text{MeV})\ (94\%) \qquad (3.4)$$

The visible effect of this reaction is a signal of energy 0.48 MeV from the γ-ray (plus a small amount of energy (~50 keV) from the quenched pulse of the accompanying α particle). Because of the diffusion time for neutrons, they are observed with a delay time after the prompt pulse of the β^+. The mean "lifetime" of the delay time distribution is $\tau_n \approx 2\mu$sec. This relatively fast delayed coincidence of the β^+ with the 480 keV γ-ray of eq.3.4 provides a distinct signature which can eliminate random coincidences with the normal backgrounds including untagged cosmic ray muon induced neutrons (see chapter XII). Since 20% of B occurs as ^{10}B and the cross section of reaction (3.3) is ~4000 b, $\bar{\nu}_e$'s can be detected very efficiently. The $\bar{\nu}_e$ energy spectrum is given directly by the spectrum of the prompt β^+ signal (the visible energy $E_{\beta^+} = E_{\bar{\nu}_e}$ - 0.78 MeV).

In principle, antineutrino spectroscopy is possible in Borexino for a neutrino energy as

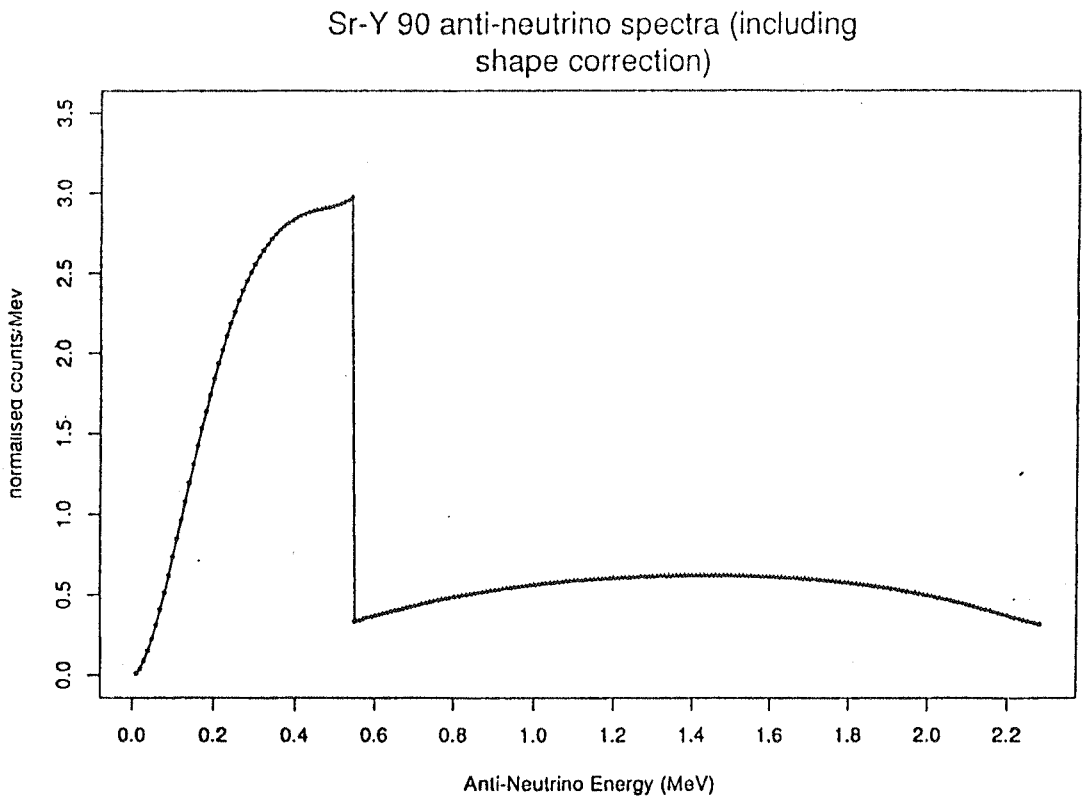

Figure 3.5 Neutrino spectrum from ^{90}Sr-^{90}Y unique forbidden β-decay chain.

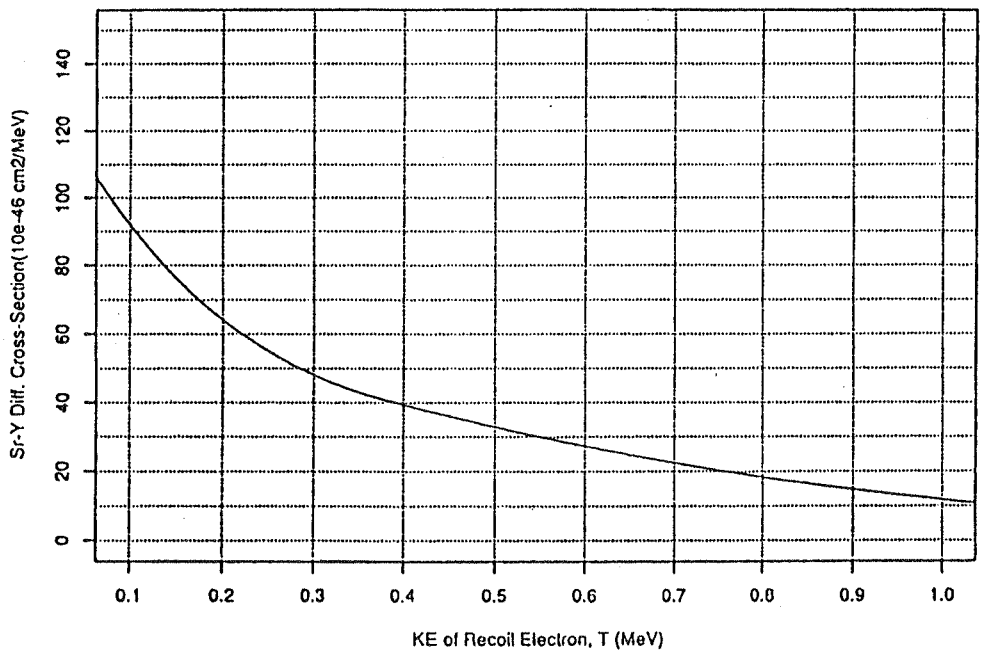

Figure 3.6 $\bar{\nu}_e$ -e scattering cross-section averaged over the ^{90}Sr - ^{90}Y source spectrum as a function of T, the kinetic energy of the recoil electron.

low as $E_{\bar{\nu}e}$=1.8 MeV, the threshold of reaction (3.3) since even a β^+ of zero kinetic energy can be observed by its annihilation energy of 1.02 MeV alone. Detection of antineutrinos below 3.3 MeV will however depend critically on the internal radioactivity, especially the long-lived ^{214}Bi activity whose delayed cascade emission can mimic the $\bar{\nu}_e$ signal. At higher energies, however, the only unsuppressible background is that of $\bar{\nu}_e$'s from terrestrial sources. Radioactivity in the earth produces $E_{\bar{\nu}e}$ <3.3 MeV while those from power reactors extend beyond 3.3 MeV with an intensity falling rapidly for $E_{\bar{\nu}e}$ >5 MeV (see Fig. 4.3). Above a cutoff energy of 5 MeV, solar antineutrino signals at rates as low as 20/year may be measurable in Borexino and specified as extraterrestrial from the observed energy distribution.

3.5 *Antineutrino Spectroscopy using ^{90}Sr Source*

Borexino will attempt observations in a new experimental regime. A number of checks and diagnostics of the operation of the detector and for the characterisation of the internal backgrounds in the experiment have been described. Each of the signal reactions has been invested with a signature, the main low energy signature connecting directly with the sun. As a final guarantor of the ability of the detector to observe neutrino signals and as an absolute, quantitative measurement of the cross section of neutrino scattering at the energies of interest to Borexino, we plan a calibration of the neutrino scattering signals in Borexino. We plan to investigate antineutrino electron ($\bar{\nu}_e$ -e) scattering using a laboratory radioactive source of ^{90}Sr - ^{90}Y, which emits antineutrinos [3.4]. Since there is no theoretical uncertainty between (ν_e-e) and ($\bar{\nu}_e$-e) scattering, this meets the calibration requirements fully. Besides its values as a calibration, this experiment has major physics implications, being the first exploration of this energy regime in neutrino scattering. An important advantage of the source measurement is its differential nature (source "on" - source "off") so that the background concerns are peripheral.

In addition to ($\bar{\nu}_e$-e) scattering, reaction (3.3), the Cowan-Reines inverse β-decay in protons, can also be observed with the ^{90}Sr source since it permits $\bar{\nu}_e$'s of energy >1.8 MeV, the threshold of this reaction. These events can be observed with the delayed coincidence signature discussed above. The ($\bar{\nu}_e$, p) channel allows a direct on-line calibration of the source strength, geometrical effects and target size.

Very strong (megacurie) antineutrino sources are far more accessible via fission-

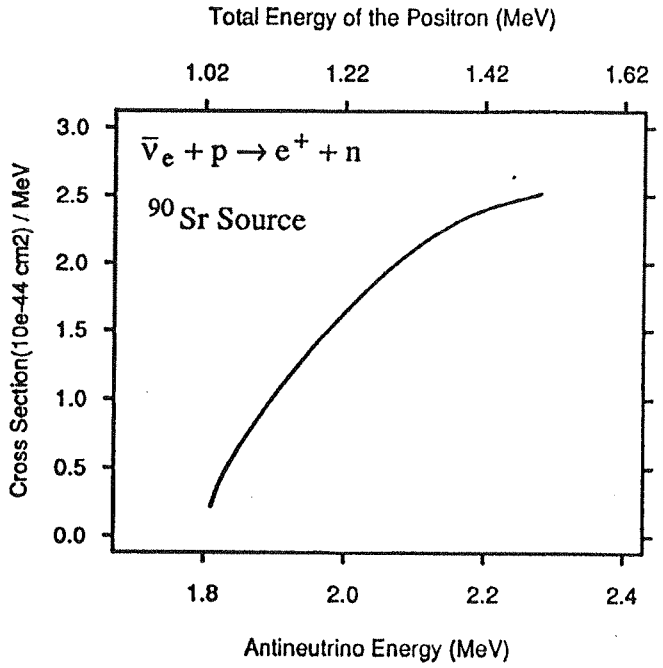

Fig. 3.7 Differential cross-section for ($\bar{\nu}_e p$) absorption average over the $\bar{\nu}_e$ spectrum emitted by ^{90}Sr-^{90}Y

Table 3.IV Antineutrino signal rates in Borexino for a 5 MCi ^{90}Sr source placed at 7 or 8 m from the centre of the detector

Reaction	Signal Rates/day	
	7m Geometry	8m Geometry
($\bar{\nu}_e$, e) (reaction 3.1) (T=0.2-0.8 MeV)	141	56
($\bar{\nu}_e$,p) (reaction 3.3) ($E_{\beta+(total)}$)=1.02-1.5 MeV)	80	32

products than neutrino sources (such as ^{51}Cr or ^{65}Zn). ^{90}Sr- ^{90}Y, a pure β emitter, is well suited since relatively inexpensive sources are already commercially available in excess of 5 MCi with established experience and procedures for safe handling, transport, storage and maintenance. ^{90}Sr ($T_{1/2}$ = 28yr , $E_{\beta max}$ =0.55 MeV) and ^{90}Y ($T_{1/2}$ = 64 hr , $E_{\beta max}$ =2.27 MeV) emits 2 $\bar{\nu}_e$'s /Sr decay at equilibrium. Both β decays are unique forbidden types with precisely calculable shapes; the $\bar{\nu}_e$ spectrum from this source is shown in Fig. 3.5. The precision of knowledge of the input neutrino spectrum is vital to an accurate measurement of the scattering cross section.

($\bar{\nu}_e$-e) Scattering Signals from ^{90}Sr: The $\bar{\nu}_e$ scattering cross-section as a function of the kinetic energy T of the electron recoil is shown in Fig. 3.6. The scattering cross-section averaged in the energy region 0.2 to 0.8 MeV, the usual low energy signal window in Borexino (most of the cross-section resides also in this bin), is calculated to be $\sigma_{\bar{\nu}_e}$ (0.2-0.8 MeV) = 21×10^{-46} cm^2 and in the window 0.2 to 2.3 MeV, it is σ_{tot} (>0.2 MeV) = 28×10^{-46} cm^2. Signals rates for a 5MCi source at representative distances from the centre of the Borexino detector are given in Table 3.IV. With a year's exposure, these signal rates can allow the $\bar{\nu}_e$ -e cross-section to be measured to a precision of a few percent. The physics significance of such a measurement for a possible neutrino magnetic moment is discussed in chapter IV and chapter V.

($\bar{\nu}_e$, p) Absorption Signal from ^{90}Sr: The $\bar{\nu}_e$ spectrum of fig. 3.5 was used to calculate the signal from reaction 3.3, the inverse beta-decay of the proton. Fig. 3.7 shows the results. The signal rate increases steeply from the threshold antineutrino energy of 1.8 MeV for reaction 3.3 to a cut-off at 2.3 MeV, the end point of the source spectrum. This results in a β^+ signal of a total energy (rest+kinetic) ranging from 1.02 MeV to 1.43 MeV. Even though these are low energies, the delayed coincidence signature is sufficient to observe them above background. Unlike possible $\bar{\nu}_e$ from the sun with signal rates ~100/year (see chapter 4) (and thus must be restricted to antineutrino energy >5 MeV to avoid terrestrial $\bar{\nu}_e$ background) the ^{90}Sr source signal can be observed even at these (<1 MeV) energies because the signal is ~10^4/year (see Table 3.IV). Further, the terrestrial background can be subtracted because this is a source-on-off experiment.

References

[3.1] J. N. Bahcall, Neutrino Astrophysics (Cambridge U. Press) 1989.

[3.2] S. P. Mikheyev and A. Y. Smirnov, Nuovo Cim. 19, 17 (1986).

[3.3] See ref. (1.18).

[3.4] A. Golubchikov, S. Prakhov and O. Zaimidoroga. Rapid Communication of JINR Dubna, 1991 (in press).

CHAPTER IV

NEW NEUTRINO PHYSICS - PROPOSALS AND TESTS

The experimental results on solar neutrinos to date have stimulated a rich field of testable theoretical proposals for possible new neutrino physics. In this chapter we review the leading ideas and their testability in future experiments, briefly pointing out the place of Borexino among these detectors. A detailed examination of the tests in Borexino is reserved for chapter V.

4.1 *Neutrino Mass and Mixing*

Flavour Conversion in Vacuum — "Just So" Neutrino Oscillations: If neutrinos have a non-zero mass (as allowed by extensions of standard electroweak theory), a general description is given by a triplet of mass eigenstates for the three neutral leptons which transform to the flavour-eigenstates of the three neutrino flavours e, μ and τ by a suitable mixing matrix. Important experimental consequences such as neutrino oscillations then follow as shown first by Pontecorvo in a series of beautiful papers [4.1]. He also pointed out the immediate relevance of these ideas to the SNP. The essential physics can be displayed by a simple two-flavour model with a mixing angle θ.

Neutrinos are generated as flavour eigenstates. In free space, a ν_e as emitted for example in nuclear β-decay, is a specific superposition of mass eigenstates. As the ν_e wave travels, its component mass-eigenstates propagate with different wave-vectors

(momenta) because of the different masses. Then, the overall mixture is not conserved during the propagation because of interference effects. After a distance equal to the "oscillation" length, the mixture corresponds to a different flavour-eigenstate, thus manifesting lepton number violation in a direct fashion. A solar ν_e detector e.g., then observes a signal rate that displays an oscillatory dependence on the distance R from the source (superimposed on the $1/R^2$ fall off). The oscillatory survival probability P_{ee} of the initial ν_e flavour is given by:

$$P_{ee} = 1 - \sin^2 2\theta \ \sin^2\left(\frac{\pi P}{\lambda}\right). \qquad (4.1)$$

The oscillation length $\lambda = \frac{4\pi E}{\Delta m^2}$ where E is the neutrino energy and Δm^2 is $(m_1^2 - m_2^2)$ of the two mass-eigenstates. Eq.(4.1) holds for a monoenergetic neutrino beam such as solar ^{7}Be or pep neutrinos; an averaging of E over their small energy widths (created e.g. by Doppler broadening) adds small corrections [4.2]. For continua like the ^{8}B neutrinos, the energy-average creates large effects [4.3].

The observable flux depends on the oscillation phase in eq. (4.1) (in addition to the mixing angle). Large depletions in the solar neutrino flux can occur if the phase is a

$$n + 1/2 = 6.07\left(\frac{1\text{MeV}}{E}\right)\left(\frac{\Delta m^2}{10^{-10}\text{e V}^2}\right) \qquad (4.2)$$

multiple of $\pi/2$, i.e. the earth-sun distance R = (n+ 1/2) λ with n=0,1,2.., or:

Given a reasonably large mixing angle θ, for small n, eq.4.2 shows that neutrinos of 1 MeV can be strongly depleted but ^{8}B neutrinos, with much longer λ's, are barely reduced. For large n, the oscillations are washed out, reducing fluxes at all energies to the minimum of 1/2 SSM flux (for 2 flavour mixing). There is however, a window of moderate n values (3-20) ("just so" oscillations [4.4]), in which it is possible to accommodate agreement with the results of all present experiments. Such constraints limit the possibility of vacuum oscillations to the parameter region of $[0.5 < \Delta m^2 < 2.5] \times 10^{-10}$ eV^2 and $\sin^2 2\theta > 0.7$ [4.5]. This scenario would, however, be ruled out if the Ga experimental results eventually stabilise at a signal of < 40 SNU.

Flavour Conversion in Matter – Wolfenstein Effect: Wolfenstein has shown that the propagation of neutrinos in matter is different from the above because of the neutrino-electron scattering [4.6]. The scattering process ($\nu+e\rightarrow\nu+e$) for ν_e is driven by the charged weak current as well as the neutral current whereas other flavours can scatter electrons only via the latter. Thus, ν_e's propagate in an effective potential which depends on the matter density. Transport in matter is then controlled not by λ, the vacuum oscillation length as above, but by the ratio of λ to the coherent forward scattering length $\lambda_M=2\pi/\sqrt{2}G\bar{\rho}$ where G is the Fermi coupling constant and $\bar{\rho}$ is the electron density. As a result, the superposition of mass eigenstates for a given flavour in matter becomes different. A "matter" mixing angle θ_M can then be defined as:

$$\tan 2\Theta_M=\frac{\tan 2\Theta}{1-(\lambda/\lambda_M)\sec 2\Theta} \tag{4.3}$$

The mixing is maximised to unity ($\theta_M\rightarrow\pi/4$) irrespective of the vacuum mixing θ, when a resonance condition is fulfilled:

$$\lambda/\lambda_M=\cos 2\theta \tag{4.4}$$

For a given neutrino energy and Δm^2, there is a particular matter density ρ_o at which

$$\rho_o = 13.2\cos 2\theta\left(\frac{\Delta m^2}{10^{-6}eV^2}\right)\left(\frac{1MeV}{E}\right) \tag{4.5}$$

this resonant enhancement of the mixing occurs:

Matter Effects in the Sun—Mikheyev-Smirnov-Wolfenstein Effect: Mikheyev and Smirnov [3.7] applied Wolfenstein's ideas to the case of the sun where the density varies monotonically from a high value (~150 g/cc) at the core to ~0 at the limb (see Fig. 1.2). They found that variability of the density produces dramatic results. A resonance density layer in the path of a neutrino created in the high density core can produce a complete conversion to a heavier flavour, e.g., $\nu_e\rightarrow\nu_\mu$. Instructive descriptions of this physics have been given by Bethe [4.8].

When the ν_e is created in the core region of density $\rho>\rho_o$, it is created essentially in

the higher or the "wrong" mass eigenstate ν_2 (in vacuum it is mostly the lighter mass eigenstate ν_1) because, in matter, the mixture of mass eigenstates for a given flavour is controlled by θ_M (see eq.4.3) and thus by the density (via λ_M). The flavour mixture corresponding to the eigenstate ν_2 changes continually across the sun because the density (and thus θ_M) changes. At the resonance layer it is an equal mixture of ν_e and ν_μ flavours. At the exit into vacuum, ν_2 is restored to its normal vacuum state of mostly the heavier flavour ν_μ. The emitted neutrino, on the other hand, will be *maintained in the "heavy" mass eigenstate* ν_2 if it passes through the sun adiabatically i.e. without inducing transitions between the states ν_2 and ν_1. The solar neutrino will then be emitted into the vacuum not as ν_e but as ν_μ, thus resulting in effect, in a nearly complete flavour conversion at the resonance layer. The ν_e survival probability is:

$$P_{ee} \approx \sin^2\theta. \tag{4.6}$$

Thus, P_{ee} is limited from zero only by the vacuum mixing angle θ: the *smaller* the natural mixing, more complete is the conversion (contrast with eq.4.1).

The condition for adiabaticity is that the physical width of the resonance be large compared to the matter oscillation length. For a 10 MeV neutrino this condition is satisfied in the sun for $\Delta m^2 \sim 10^{-4}$ eV^2 and $\sin^2 2\theta > 4\times10^{-4}$. For smaller masses and larger angles, the adiabaticity progressively breaks down and the conversion is increasingly partial.

In summary, the MSW effect can result in complete suppression of ν_e signals anywhere in the solar spectrum for $\Delta m^2 < 10^{-4}$ eV^2 and mixing angles as low as $\sin^2 2\theta \sim 10^{-4}$. A signature of the MSW effect is that the suppression is strongly *energy dependent.* Thus a major experimental consequence of the MSW effect is a spectral distortion of high energy neutrinos such as that from ^{8}B over the range 0-14 MeV.

The action of the MSW effect is illustrated in Fig. 4.1 by isosignal contours in the Δm^2 - $\sin^2 2\theta$ plane for two neutrino groups: the ^{8}B neutrinos of energy ~8-13 MeV (as seen in K-II) and the monoenergetic ^{7}Be neutrinos, as would be observed in Borexino. With the maximum density available in the sun, the highest Δm^2 value that can be probed by the MSW effect is ~10^{-4} eV^2, for which the high energy ^{8}B neutrinos are suppressed (essentially independent of angle). At smaller Δm^2, the suppression becomes non-adiabatic and depends more strongly on θ. The energy dependence of MSW effect is

illustrated by the ^{7}Be signal rates, which, because of an order of magnitude lower energy, are not suppressed unless Δm^2 happens to be proportionately lower. In the case of the Homestake and Ga experiments sensitive to ν groups at different energies, the MSW contours are more complex but clearly show the successive resonances at different Δm^2 due to the neutrino groups at high, medium and low energies.

Regeneration in the Earth: The MSW effect is reversible in reverse passage from vacuum into matter. Under certain conditions, a solar neutrino converted to a different flavour in the sun by the MSW effect, can be regenerated to its original flavour when it traverses earth matter.[4.9] [4.10] The earth densities vary from $\rho \sim 3$ at the crust to nearly 12 at the core. Eq.(4.5) shows that with such a density range, a 10 MeV neutrino has a chance of regeneration if Δm^2 is in the range of 5×10^{-5} eV^2 while a 0.86 MeV Be neutrino could reconvert if $\Delta m^2 \approx 4 \times 10^{-6}$ eV^2. To keep the matter oscillation length smaller than the track length in the earth, thus create a detectable effect, $\sin^2 2\theta > 0.05$. Experimentally, the earth effect can be dramatic since it results in an increase in the signal rate at night compared to that during the day when the neutrino is detected before entry into the earth. The "day-night" effect would undoubtedly be the most convincing demonstration of the

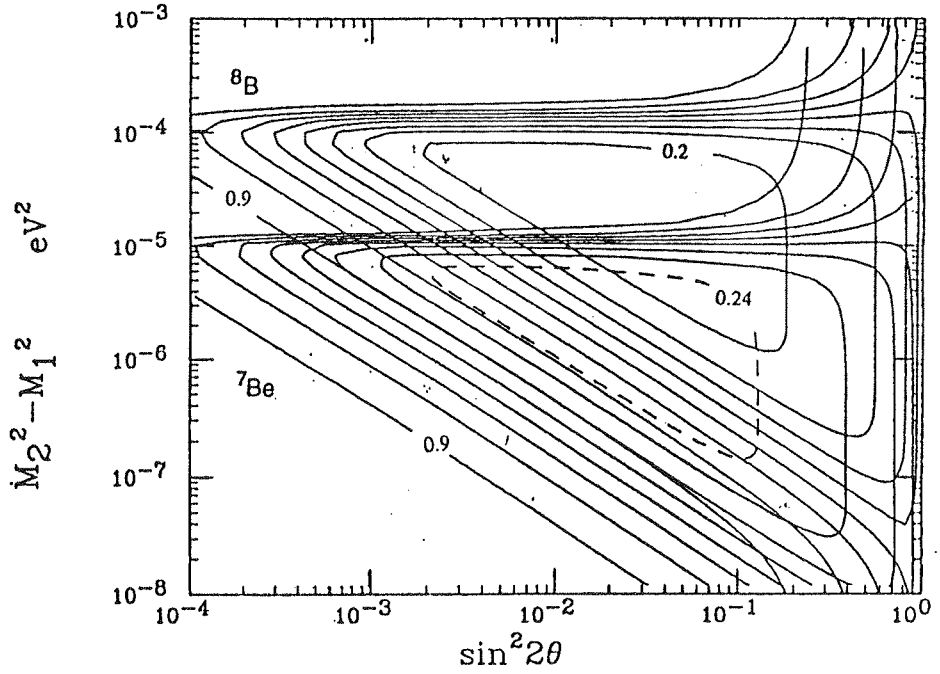

Figure 4.1 Isosignal MSW contours for K-II (^{8}B ν's) and Borexino (^{7}Be ν's). The observed signal is from electron scattering in both cases

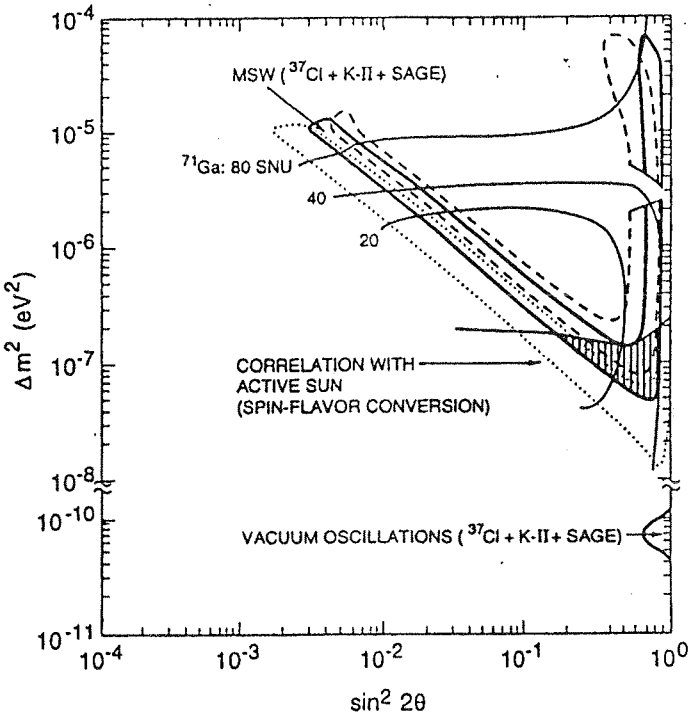

Figure 4.2 MSW parametric regions allowed by present solar neutrino experiments [ref. 4.11].

MSW effect. Observation of the effect for ^{7}Be neutrinos in real-time can lead, in fact, to an experimental determination of the neutrino parameters (chapter V).

Experimental Status of the MSW Effect: The solar neutrino results to date do not show conclusive evidence for the MSW effect; neither do they rule it out. The results do impose constraints on the neutrino parameters for which an MSW effect is still allowed. Fig. 4.2 summarises these conclusions. Taking the flux values from the three experiments (Table 1.II) and their sensitivities into account, the wish-bone like area enclosed by the solid line represents the parameter region still allowed for MSW effect at a confidence level of 90%. This statement is based on the acceptance of the SSM fluxes; the areas within the dashed line and the dotted line show how the allowed region shifts if the ^{8}B flux is increased or decreased by 30% [4.11]. The MSW contours of ^{71}Ga, also shown in Fig. 4.2, indicate the effect of future SAGE and GALLEX results on the allowed area. A small enclave at low masses allows vacuum oscillations (see above). The break in the vertical limb of the "wish-bone" is due to a negative search for a day-night effect by K-II.[4.12] In summary, the experiments appear to disfavour a purely adiabatic MSW conversion in the sun and tend to restrict the allowed range of Δm^2 to $<10^{-5}$ eV^2. It is worth stressing that these conclusions and the interpretations reached in Fig. 4.2 are based on the premise of time-averaged flux results from all experiments, in particular, that from

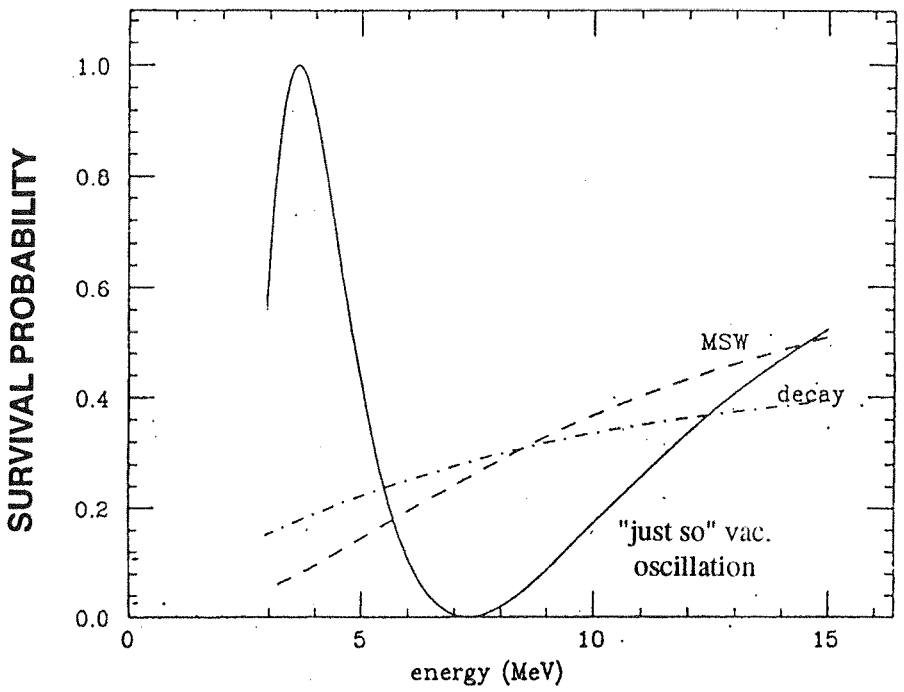

Figure 4.3 Spectral deviations of ^8B neutrinos caused by various effects: a) MSW effect; b) Neutrino decay; c) "Just so" vacuum oscillations [ref. 4.5].

Homestake. The claimed time-variation is tacitly ignored.

Tests of Vacuum and Matter Conversion: The allowed areas in Fig. 4.2 can be tested in future detectors by flux determinations as well as "appearance" effects.

- *The signal in the Ga detector* will be an early pointer of flavour conversion; for <80 SNU, standard astrophysical theory becomes definitely inadequate. In this Ga signal region, vacuum as well as matter conversion is viable. For <40 SNU only matter conversion via the MSW effect is viable, restricting Δm^2 to $<10^{-6}$ eV^2.
- *Neutral Current Detection of ^8B Neutrinos*: A measurement of the ^8B neutrino flux via the weak neutral current in comparison with the ^8B flux measured via charged current detection would probe directly the presence of flavour conversion in general since the neutral current is flavour blind. This test can be carried out only in SNO and in the planned BOREX detectors; it is relatively insensitive to neutrino parameters in the current regimes and it is ineffective if conversion takes place to "sterile" states.
- *High Energy Spectral Shape:* A more precise measurement of the spectral shape of ^8B

neutrinos than has been possible so far at K-II is valuable. A non-standard shape will, in general, be a clear indication of new neutrino physics. In the "vertical" part of the allowed MSW regime of fig. 4.2, no spectral shape change can occur. In the MSW non-adiabatic regime, the "slope", the lower energies are converted more efficiently; the shape is thus biased towards high energies. The shape distortion in this case is generally small, thus, a lower energy threshold and/or a higher signal rate will be necessary. High rates will be possible in SNO and Superkamioka and low thresholds in Borexino.

A shape distortion of these types is not unique to the MSW effect; it may arise also due to neutrino decay (§ 4.3) or from vacuum oscillations. This is illustrated in Fig. 4.3 which shows the spectral deviation of ^{8}B neutrinos for neutrino parameters typical of "just so" vacuum oscillations, with an oscillation length less than the earth-sun distance. In the flight to the earth, neutrinos of different energies have slightly different oscillation lengths, thus different survival probabilities. As seen in Fig.4.3, the distortion can be very strong below ~7 MeV. At the higher cutoffs (~8MeV) typical of K-II, the effect cannot easily be distinguished from the MSW effect especially with poor energy resolution. The lower cutoff in Borexino and its high energy resolution are uniquely suited for detecting this effect despite the lower signal rates. Note that the spectral shape in this scenario is time-dependent. Neutrino decay generally biases the spectrum toward higher energies because lower energy ν's have shorter lifetimes. Thus, as seen in fig. 4.3, this effect can create a shape distortion very similar to the non-adiabatic MSW effect.

- *Low Energies— Day-Night / Seasonal Variation of ^{7}Be ν_e Flux:* The allowed regions of the MSW effect in Fig. 4.2 predict a strong day-night effect for neutrinos ~1 MeV for $\Delta m^2 < 10^{-6}$ eV^2[4.11]. Well defined seasonal flux variations are predicted by the "just so" vacuum oscillations (eq.4.2 with n~3) in the small enclave at very low masses in Fig. 4.2. Observation of these effects requires, in practice, a monoenergetic neutrino at ~1 MeV. Thus experiments with real-time sensitivity at low energies which can observe the ^{7}Be neutrino line feature with reasonably high signal rates would be ideally suited to observe these compelling effects. Such observations can also lead to a determination of the neutrino parameters [4.11] (see chapter V).

To summarise, flavour conversion can be tested by high energy data from SNO and Superkamioka. Spectral distortions at high energies and striking time variabilities at low energies can be observed with particularly unique advantage in Borexino.

Magnitudes and Implications: If the solar neutrino flux is correlated with the solar cycle, most of the viable scenarios are based on a large neutrino magnetic moment μ_ν. The Standard Model predicts $\mu_\nu \sim 10^{-19}\,(m_\nu/1eV)\,\mu_B$. For solar scenarios, values of order $10^{-11}\,\mu_B$ are desired. The discovery of such a moment would thus clearly compel new physics beyond the Standard Model. Serious theoretical efforts are being made to explore new concepts leading to a large μ_ν combined with a small neutrino mass [4.13]. At present, laboratory measurements limit the value of μ_ν to $<4\times10^{-10}\,\mu_B$ [4.14] while astrophysical considerations place it at a much lower value, $<3\times10^{-12}\,\mu_B$ [4.15].

Dirac Moments—Spin Conversion: Originally advanced in general terms [4.16] these ideas have been revived, specifically from a new observation point of view, the time variation.[4.17]. Passage of Dirac neutrinos with a (diagonal) neutrino magnetic moment

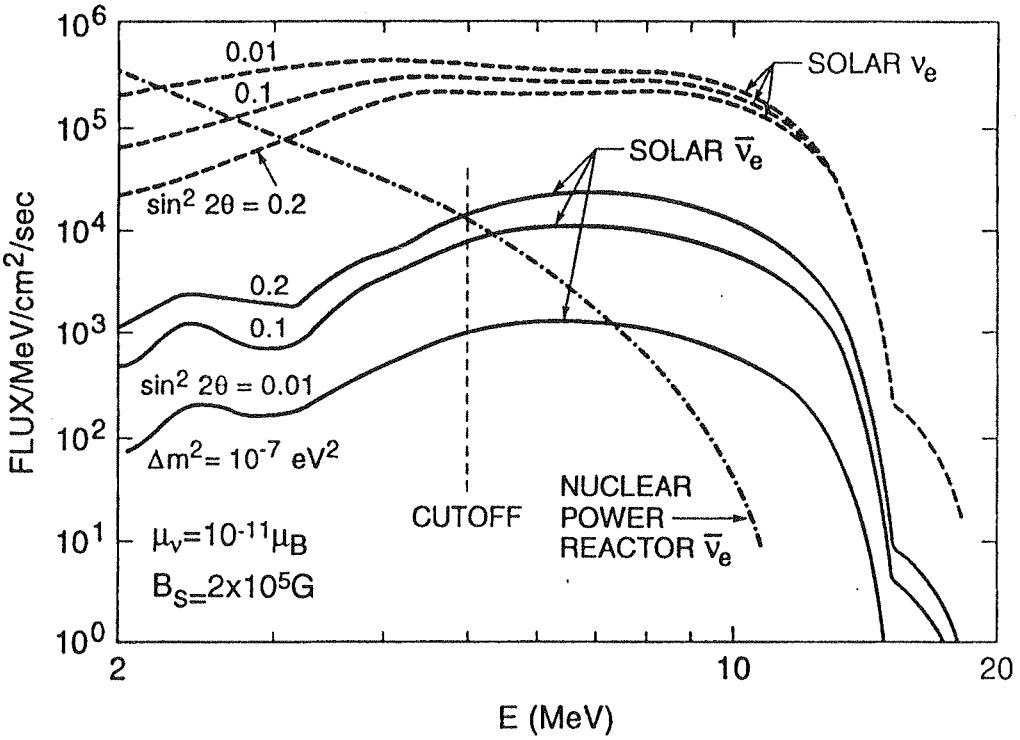

Figure 4.4 Solar antineutrino spectra from spin-flavour conversion of ^8B neutrinos in the sun (ref. 4.11). For comparison, the original neutrino spectrum is also shown. Note the profile of antineutrinos from terrestrial power reactors [ref. 4.23].

through distances of the order of the convection zone of the sun in the presence of a magnetic field, can induce a neutrino spin precession. This results in a right-handed neutrino. Since this object is normally considered sterile, hence undetectable at Homestake, a change in the neutrino flux would result. With a magnetic field correlated with the solar cycle, the neutrino flux could follow suit via this mechanism.

The implications of such a scenario can be summarised as follows: 1) A moment $\mu_\nu \sim 10^{-11}\ \mu_B$ together with a magnetic field of $\sim 10^4$ G in the convection zone of the sun and a field $\sim 10^6$ to 10^7G in the centre are necessary [4.17]. 2) This scenario is valid for $\Delta m^2 < 10^{-9}$ eV^2, thus, the MSW effect plays little role. 3) Besides the correlation to the solar cycle, a semi-annual variation of the ^{8}B flux is predicted, arising from the periodic swing of the solar field-axis relative to the ecliptic, which creates a "shutter" effect on the neutrino flux [4.17]. (This effect does not however, appear for the ^{7}Be or pp neutrinos because they are created in extended zones in the sun). The low signal rates in current experiments do not admit a clear conclusion in this respect. 4) The flux suppression during solar active periods is *energy independent.* Thus all detectors, in particular also K-II, should observe the same variation, in contradiction with its present results.

Majorana Moments – Spin-Flavour Conversion: A Majorana neutrino transition magnetic moment (with only off-diagonal elements), interacting with a solar magnetic field, converts both spin and flavour. This effect must therefore be considered in a coupled fashion with the MSW effect. The problem was first studied by Lim and Marciano [4.18] and independently by Akhmedov [4.19]. This interaction results in $\nu_e \rightarrow \bar{\nu}_{\mu(\tau)}$. Such an effect can be consistent with the Homestake time variation results for a solar magnetic field of $\sim 2\times10^5$ G in the convection zone during solar activity [4.20], as suggested by models derived from solar radius changes during solar activity [4.21]. A Majorana moment of $\sim 10^{-11}\ \mu_B$ is required. The neutrino mass parameter region relevant for this effect is $\Delta m^2 < 10^{-7}$ eV^2 as shown in Fig. 4.2. Mixing angles are limited to $\sin^2 2\theta > 0.05$ in order to be consistent with straight flavour-conversion in a *quiet* sun. In these periods the magnetic activity is supposed to decrease significantly, leaving only the MSW conversion in operation. The neutrino mass and especially the mixing angle range above are consistent with Homestake results during quiet sun periods.

Spin-flavour conversion is energy dependent; for example, it predicts little variation in low energy experiments such as Ga which, in any case, are required to have very low signal rates in the MSW ranges of this scenario (see fig. 4.2). However, it does require that a time variation somewhat similar to Homestake should have been observed at K-II as well.

Test for Spin-Flavour Conversion -Solar Antineutrinos: If spin-flavour transitions $\nu_e \rightarrow \bar{\nu}_\mu$ occur in the MSW parameter regime $\Delta m^2 < 2 \times 10^{-7}$ eV^2 and $\sin^2 2\theta > 0.05$ (see fig. 4.2), a testable consequence of the effect can be predicted [4.11]:the appearance of solar antineutrinos on earth via the process: $\nu_e \rightarrow B_{sun} \rightarrow \bar{\nu}_{\mu(\tau)} \rightarrow$ Vac.Osc.$\rightarrow \bar{\nu}_e$

A key point in the above process is the relatively large mixing angle allowed by this scenario, which allows a reasonable conversion rate for $\bar{\nu}_\mu \rightarrow \bar{\nu}_e$. Unlike "just so" oscillations considered in §4.1, the mass range is higher, thus the oscillation lengths are much smaller than for that case. The result is an overall reduction of the antineutrino flux without a spectral distortion. The resulting $\bar{\nu}_e$ spectra (shown in fig 4.4) thus resemble the original ^{8}B spectra.

.Antineutrinos are not predicted by any astrophysical model. At sufficiently high energies, ($E_\nu > 5$ MeV), those of terrestrial origin (a fundamental background) offer little interference. An estimate of the terrestrial background ν_e spectrum [4.22] is shown in Fig.4.4. In the viable parameter regime, typically a few percent of the ^{8}B ν_e's can be converted to $\bar{\nu}_e$'s [4.11]. Recently, an upper limit of the $\bar{\nu}_e$ flux from the sun has been set at ~6% of the ν_e flux as seen in K-II [4.23]. Experimentally, even such low fluxes of $\bar{\nu}_e$'s can be clearly detected by proton targets in solar neutrino detectors carefully designed for low-energy studies. The $\bar{\nu}_e$ spectrum (Fig.4.4) predicted above to be very similar to the spectrum of ^{8}B ν_e's, provides a strong signature. Also, the $\bar{\nu}_e$ signal should switch on and off with solar activity, thus providing final proof of the basic scenario of this effect.

Antineutrinos can be detected with a sensitive delayed coincidence signature in Borexino (see Chapter III).

Neutrino Magnetic Scattering by Electrons: The principal difficulty with the magnetic moment scenarios above is that they all predict similar effects in K-II and Homestake and thus fail to explain the discrepancy. So far, the effect of a large μ_ν in the solar interior was considered. Recently the magnetic moment idea has been taken a step further and its effect in the *detector* has been examined [4.24].

A neutrino magnetic moment can affect the scattering signal in K-II by adding a new scattering component (via EM coupling) to the normal "weak" scattering (via W's and Z's). In contrast to the Homestake signal, the magnetic scattering signal is independent of whether the neutrino is normal (left-handed) or sterile (right-handed). In the quiet sun period when all neutrinos are presumably normal, the solar neutrino flux is given wholly by the Homestake result; the ^{8}B part of it induces the K-II signal by (weak + magnetic) scattering. When the solar activity rises, a large part of the flux is converted to sterile

right-handed neutrinos: the Homestake signal is reduced because the normal flux is reduced. At K-II however, the signal would be nearly constant because the magnetic scattering from the total flux (normal + sterile) remains the same; only the "weak" scattering part is reduced. This idea leads to the following bounds for the value of μ_ν: $4<\mu_\nu<9.3\times10^{-10}\ \mu_B$ (95% c.l.).[4.24] The lower bound is just within the present limit on μ_ν [4.14] [4.25]. The central argument of this scenario, applied originally to spin conversion scenarios, [4.24] applies also to spin-flavour conversion (Majorana) [4.26].

Tests for Neutrino Magnetic Scattering: The significant feature distinguishing μ_ν scattering from weak scattering is the dependence on electron recoil energy [4.25]:

$$\frac{d\sigma}{dT} = \mu_\nu^2 \frac{\pi\alpha^2}{m_e^2}\left(\frac{1}{T} - \frac{1}{E_\nu}\right) \tag{4.7}$$

where E_ν is the neutrino energy and T is electron recoil kinetic energy. The recoil electron spectrum rises rapidly at low energies (unlike the flat profile of weak ν-e scattering). Consequently, the cross-section is larger, the lower experimental minimum cutoff on the recoil energy. For the values of μ_ν estimated above, the effective scattering cross-section can be several times larger than that due to weak scattering alone. Thus a solar neutrino experiment spectroscopically observing low energy neutrinos (e.g. ^{7}Be) by ν-e scattering with a low threshold will reveal an apparent flux much larger than that seen by a detector such as Ga, which observes the same Be neutrinos via inverse-beta decay. In other words, a severe incompatibility of the signals in Borexino and the Ga experiments, measuring same neutrinos by scattering and absorption will provide compelling evidence for neutrino magnetic scattering. Furthermore, the recoil spectral profile in scattering provides a "magnetic" signature by the 1/T recoil energy dependence.

The above test uses solar ν_e-e scattering. In principle, $\bar{\nu}_e$-e scattering with a smaller "weak scattering" background is more sensitive to the presence of magnetic scattering. Such a possibility, investigated so far with reactor antineutrinos, can be significantly improved upon by using a laboratory $\bar{\nu}_e$ radioactive source and a low energy neutrino detector in an underground location. Borexino is the only detector in which such tests can be carried out. Low energy ν-e scattering of solar neutrinos as well as $\bar{\nu}_e$-e scattering of antineutrinos from a calibration radioactive source can be investigated with sufficient precision and significantly lower the present experimental limits on μ_ν to approach the stringent limits suggested by astrophysical considerations.

4.3 *Neutrino Decay*

Solar neutrinos decaying in flight is an early suggestion to solve the SNP [4.27]. If this is the reason for the deficit of ^{8}B neutrinos, larger flux deficits will occur at lower energies because softer neutrinos in general will have shorter lifetimes due to time dilation. This prediction is indeed consistent with present experimental results. The spectral deviations of decaying ^{8}B neutrinos can be very similar to that of the MSW effect in the non-adiabatic regime [4.5.] Fig. 4.3 which compares the spectral survival probability expected from vacuum oscillations, non-adiabatic MSW conversion and ν-decay shows that the first two scenarios cannot be distinguished from ν-decay with the results available so far. Thus, a direct means to confirm (or deny) the presence of neutrino decay is necessary. The only possibility so far, is the detection of antineutrinos emitted in the decay process, as first proposed in [4.28].

Neutrino decay is an intrinsic process determined by the mass and thus by the *MASS eigenstates*. The most viable mode is given as:

$$\nu_2 \rightarrow \bar{\nu}_1 + \varphi \qquad (4.8)$$

where ν_2 is the heavy mass eigenstate, $\bar{\nu}_1$ the lighter mass and ϕ is a hypothetical, invisible, pseudoscalar boson called the Majoron. The process is governed by a coupling constant g whose value is limited by data on leptonic K decays. The recent LEP results on the Z_0 width have limited but not eliminated the range of theoretical possibilities for constructing the Majoron [4.29].

If the electron neutrino is a relatively pure light mass state, data from supernova SN1987a set stringent limits on the neutrino lifetime and remove decay as a factor in the SNP. However, if the electron neutrino is a mixture of light and heavy species, the heavy mass admixture can still induce decay with a lifetime comparable to the solar neutrino flight time [4.30]. Thus,

$$\nu_e \text{ (mixed)} \rightarrow \bar{\nu}_e \text{ (mixed)} + \varphi \qquad (4.9)$$

For a decay scenario to be the underlying factor in the SNP, the allowed mixing range is limited to large mixing angles as shown in Fig. 4.5.

If the MSW effect is present, it can induce neutrino decay even if the mixing angles are very small [4.28], because the relatively pure, stable ν_e (ν_1) is flavour-converted to a ν_x which consists mostly of the heavy mass eigenstate (ν_2).This state can then decay by

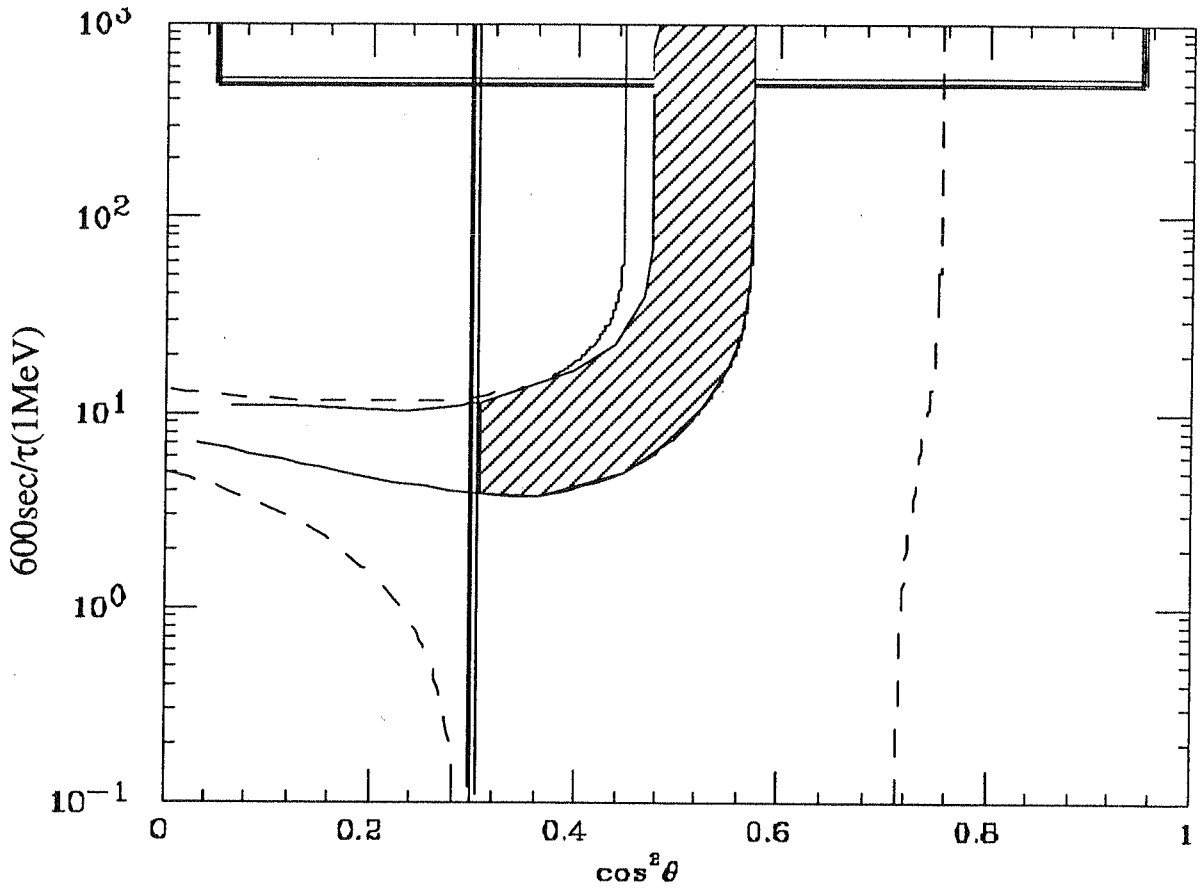

Fig 4.5 Mixing regime (hatched area) relevant to the SNP by SN1987a, reactor neutrino experiments and 2σ limit on results from Homestake and K-II (from ref. [4.31])

eq. (4.8). The "MSW-catalysed" decay can thus be written:

$$\nu_e \rightarrow \text{MSW} \rightarrow \nu_x \rightarrow \bar{\nu}_e + \varphi \qquad (4.10).$$

In this case, the factor relevant to the SNP is the MSW effect, not ν decay. However, the process (4.10) offers a new and elegant means for investigating the fundamental question of the intrinsic stability of the neutrino via the MSW effect.

Both processes (4.9) and (4.10) can be directly detected by the emission of antineutrinos from the sun. Because of the helicity change in eq. (4.8) the energy of the antineutrino is considerably degraded relative to the initial neutrino. Fig. 4.6 shows the degraded spectrum of antineutrinos from neutrino decay. Since antineutrinos can be emitted also from spin-flavour conversion (§4.2, see Fig. 4.4) a distinction must be made between the two scenarios. This can be achieved by means of the spectral shape of the

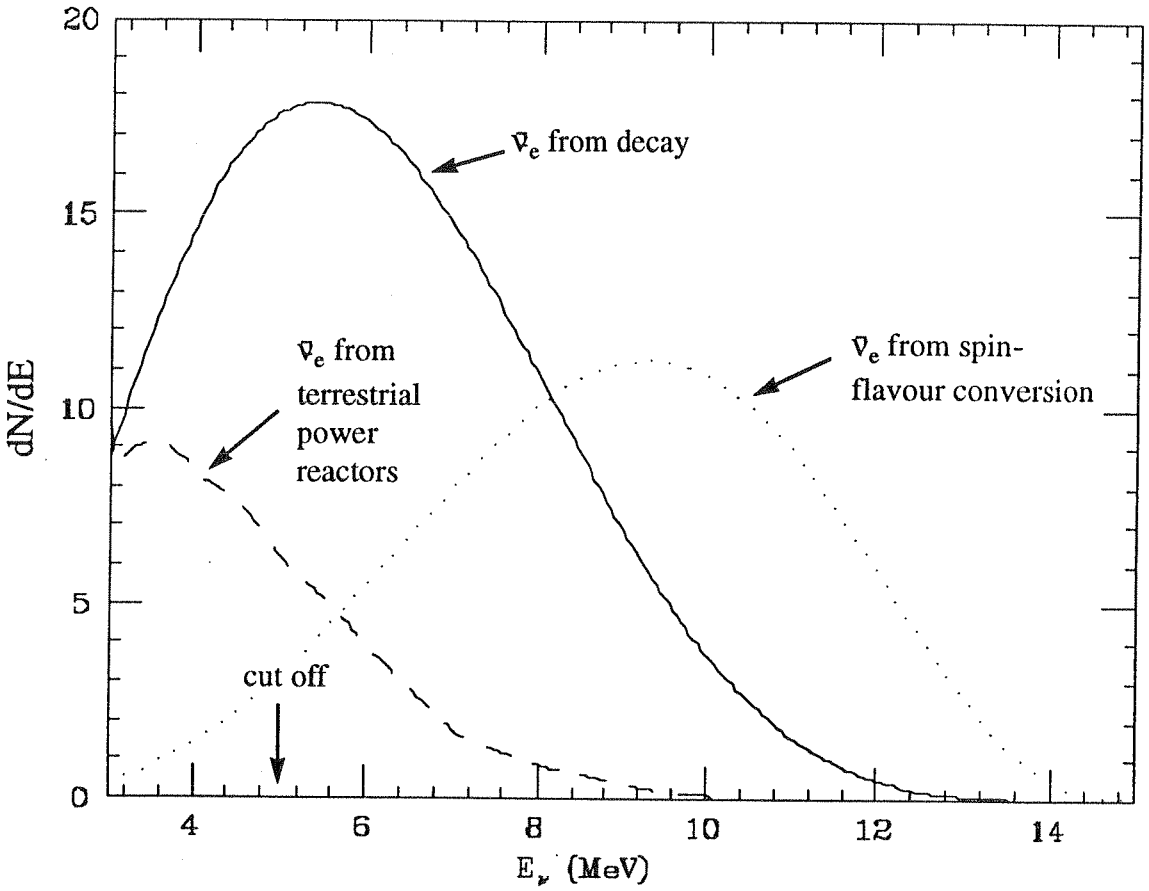

fig. 4.6 Antineutrino spectra from ν-decay compared with that from spin-flavour precession and the irreducible $\bar{\nu}$ background from power reactors on the earth.

antineutrinos.As shown in Fig. 4.4 and comparatively in Fig. 4.6, the spectra for the two scenarios are quite different, the spin flavour spectra being harder and resembling the original spectrum of ^{8}B neutrinos while that from neutrino decay is softer and peaked at lower energies. A minimum cut-off at a neutrino energy of 5 MeV will minimise the fundamental terrestrial background (also shown in Fig. 4.6) of antineutrinos even for the softer antineutrino spectrum from decay.

Of the prospective detectors, Borexino has the best chance to observe these processes because of its sensitive antineutrino signature (Chapter III).

References

[4.1] B.M. Pontecorvo, Sov. Phys. JETP 7, 172 (1958); Z. Maki, M. Nakagawa and S. Sakata, Prog. Theor. Phys. 28, 870 (1962); B. M. Pontecorvo, Sov. Phys. JETP 26, 984 (1968).

[4.2] S. Pakvasa J. Pantaleone, Phys. Rev. Lett. 65, 2479 (1990).

[4.3] J. N. Bahcall and S. Frautschi, Phys. Lett. 29B, 623 (1969).

[4.4] S. L. Glashow and L. M. Krauss, Phys. Lett. B190, 197 (1987).

[4.5] A. Acker, S. Pakvasa and J. Pantaleone, Phys. Rev. D43, 1754 (1991); V. Barger, R.J.N. Phillips and K. Whisnant, Phys. Rev. Lett. 65, 3084 (1990).

[4.6] L. Wolfenstein, Phys. Rev. D20, 2634 (1979).

[4.7] See ref. 3.2.

[4.8] H. Bethe, Phys. Rev. Lett. 56, 1305 (1986).

[4.9] M. Cribier et al, Phys. Lett. B188, 168 (1987).

[4.10] A. J. Baltz and J. Weneser, Phys. Rev. D37, 3364 (1988)

[4.11] R. S. Raghavan, A. Balantekin, F. Loreti, A. J. Baltz, S. Pakvasa and J. Pantaleone, Phys. Rev. D (In Press).

[4.12] K. Hirata et al, Phys. Rev. Lett. 65, 1297 (1990).

[4.13] K. S. Babu and R. Mohapatra, U. Maryland Report UMD-PP-91-100 (1990).

[4.14] P. Vogel and J. Engel, Phys. Rev. D39, 3378 (1989).

[4.15] G. Raffelt, Phys. Rev. Lett. 64, 2856 (1990).

[4.16] A. Cisneros, Astrophys. Sp. Sci. 10, 87 (1971).

[4.17] M. B. Voloshin and M. Vysotski,L. B. Okun, Sov. Phys. JETP 64, 446 (1986); 65, 209(E) 1987; M. B. Voloshin and M. Vysotski, Sov. J. Nucl. Phys. 44, 544 (1986).

[4.18] C. S. Lim and W. Marciano, Phys. Rev. D37, 1368 (1988).

[4.19] E. Akhmedov, Sov. J. Nucl. Phys 47. 689 (1988).

[4.20] A. B. Balantekin et al, Phys. Rev. D41, 3583 (1990); H. Minakata and H. Nunokawa, Phys. Rev. Lett. 63, 121 (1989); E. Akhmedov, Sov. Phys. JETP 68, 690 (1989).

[4.21] A. S. Endal, S. Sofia and L. W. Twigg, Ap. J. 290, 748 (1985).

[4.22] P. Lagage, Nature 316, 420 (1985).

[4.23] R. Barbieri et al, Phys. Lett. B259,119 (1991).

[4.24] A. Suzuki, M. Mori. K. Numata and Y. Oyama,Phys. Rev. D43, 3557 (1991).

[4.25] A. V. Kyuldjiev, Nucl. Phys. B243, 387 (1984).

[4.26] S. Pakvasa, Proc. 25 ICHEP, Singapore (Word Scientific) Vol I p698, (1991).

[4.27] J. N. Bahcall, N. Cabibbo and A. Yahil, Phys. Rev. Lett. 28, 316 (1972); S. Pakvasa and K. Tennekone. Phys. Rev. Lett 28, 415 (1972).

[4.28] R.S. Raghavan, X.G. He and S. Pakvasa, Phys. Rav. D38, 1317 (1987)
[4.29] Z. Berezhani and A. Smirnov, Univ. of Ferrara Preprint Infn-91-06
[4.30] J. Frieman, H. Haber and K. Frecse, Phys. Lett. B200, 115 (1988)
[4.31] The major part of the §4.3 is based on an internal report of: Z. Berezhani, G. Fiorentini, M. Moretti, A. Rossi, Physics Dept and INFN Section, University of Ferrara.

CHAPTER V

PHYSICS PROGRAM OF BOREXINO

The question of whether the explanation for the results of present solar neutrino experiments is based on astrophysics or new neutrino physics is yet experimentally unresolved. For neutrino physics, the focus is on the search for compelling evidence for flavour conversion. The discussion in Chapter 4 makes it clear that besides these major motivations, the field has exposed the close relevance of solar neutrino research to a wide range of questions which bear on practically all the unknown intrinsic properties of the neutrino: mass, mixing structure, magnetic moment, Majorana character and stability.

The dimensions of the basic experimental sensitivities of Borexino were described in Chapter 3. New tools such as real-time counting of ^{7}Be neutrinos, sensitivity to flux variations with time and to antineutrinos and the possibilities opened by (ν -e) scattering at low energies offer new ways to attack not only the main questions posed above but to clarify a much wider range of neutrino physics aspects.

While the primary focus is on solar neutrinos, Borexino is basically a counting detector with a relatively large mass, capable, for the first time, of observing rare low energy nuclear events with superior energy and spatial resolution under conditions of ultralow background. This unique combination of assets encourages new approaches to a few outstanding problems in "laboratory" neutrino physics as well.

Table 5.I summarises six independent experimental probes available in Borexino, the observable targeted by each and the physics questions under test. In the following sections, we examine the sensitivities of these probes, the possible outcomes in the various scenarios and their physics significance.

In the area of solar neutrinos, the viability of some of the physics scenarios may be reassested by the final results of the Ga experiments. The Ga signal rate predicted in each

Table 5.I Experimental Probes in Borexino and their Physics Foci.

Experimental Probe	Observable	Physics Tested	Compatible Ga Signal (SNU)
SOLAR NEUTRINO PHYSICS			
1. Low Energy Signal (^{7}Be (ν -e) Scatt.)	Signal Rate (0.2-0.8 MeV) ^{7}Be ν Flux	SSM (50/d) OR MSW (10-20/d)	>100 <80
		Mag. ν Scatt.?	Conflict w. Borexino
	Spectral Shape of Recoil e^-	Mag. ν Scatt	"
2. Temporal Variation (^{7}Be Signal)	Yearly ($1/R^2$)	Solar Origin of Signal— ^{7}Be Flux (SSM) (Bgd. Indep.)	>100
	Day -Night	MSW Effect, (ν Parameters.)	<40
	Seasonal	"Just So" Vac. Oscillations, (ν Parameters.)	45-80
3. High Energy Signal (^{8}B ν-e, CC)	Spectral Shape (4-12 MeV)	MSW Effect OR ν Decay OR "Just so" Osc.	<80 <30 45-80
4. Antineutrinos [($\bar{\nu}$, p) Delyd. Coinc.] ($E_{\bar{\nu}e}$ >5MeV)	Normal (^{8}B) Shape	Spin-Flavour Conv. (Majorana ν+ ν Mag. Mom. + Solar Mag. Field)	<40
	Degraded Shape	ν Decay (Strong Mixing)	<30
		MSW+Decay (Weak Mixing)	<80
LAB. NEUTRINO PHYSICS			
5. ^{90}Sr $\bar{\nu}$ Source (On-Off)	$\bar{\nu}$-e Scatt. (0.2-0.8 MeV) [($\bar{\nu}$, p) normalisation]	New Limit on μ_ν (2.10^{-11} μ_B)	
6. Xe gas dissolved in Borexino Scint. (2 ton Xe; On-Off)	Ultralow bgd. spectroscopy <2.5 MeV>	Deep Search for ν-less ββ-decay in ^{136}Xe	

case is thus also listed as a "road map" to the various experimental possibilities. If the final value of the Ga signal stabilises around the central value of 20 SNU observed so far in the SAGE experiment [1.7], Table 5.I shows that Borexino will have a wide-ranging role in decisively clarifying the nature of most of the intrinsic neutrino properties.

In such a case, barring very radical scenarios for a low pp flux, the only alternatives for explaining the combined data from Homestake, K-II and SAGE would be ν decay or the MSW effect. Both scenarios can be decisively tested in Borexino by "appearance" type effects (independent of background and observable with a relatively high tolerance on scintillator radiopurity) such as: solar antineutrinos in the case of ν decay and a dramatic day-night flux variation for the MSW effect. Such a detailed and direct distinction is possible only in Borexino.

The observation of a day-night effect in particular would lead to a determination of the neutrino mass and mixing parameters as well as the astrophysical fluxes of the ^{7}Be and ^{8}B solar neutrinos. Such complete results, possible only in Borexino, will have a major impact on both neutrino physics and solar astrophysics.

5.1 *Solar neutrino physics*

5.1.1 *Low Energy Signal Rates*

A basic source of information that can point out broad physics directions is the low energy neutrino signal rates and spectra observable in Borexino. Fig. 5.1 shows theoretical spectra of low energy ν-e scattering signals in Borexino, calculated for several scenarios: the standard model of the sun/neutrino, the MSW effect and neutrino magnetic moments. All these spectra assume SSM fluxes. The main plateaux arise from the ^{7}Be neutrino line and the weaker tails at higher energies from pep, O and N neutrinos from the sun. The lowest event rate, ~10/d (E_e=O.25-0.8 MeV), occurs for the MSW case with nearly complete conversion of ^{7}Be ν_e to $\nu_{\mu(\tau)}$.A large signal of ~50/d ("weak ν_e" in fig. 5.1) occurs for the SSM ν_e flux. In these curves the "weak" scattering shape of the recoil electron profile is preserved. In §3.1 we discussed the strategy of the $1/R^2$ solar signature for measurement of ^{7}Be ν fluxes (especially for high backgrounds).

The two highest curves in Fig. 5.1 illustrate the strong signal enhancement expected from the added magnetic scattering for 1) the most stringent laboratory limit on μ_ν [4.14]

[4.25] and 2) for the lowest value of μ_ν needed to explain the constancy of the K-II signal [4.24]. The resulting signal rates in Borexino are ~120/d and ~420/d. The spectral shape of the recoil electrons in these cases is different because of the characteristic 1/T dependence on the recoil energy T for magnetic scattering (eq.4.7). With the large signal rates, the shape can be measured and distinguished from the "weak" scattering shape. It is particularly important to clearly demonstrate the solar origin of the signal in these cases where the signal is *larger* than the predictions of the SSM. It is here that the $1/R^2$ yearly variation signature is likely to be of decisive value.

Taken by itself, a Borexino signal rate of 10/d (or lower for smaller solar outputs) is required if the MSW effect is the operative scenario. On the other extreme, Borexino rates higher than SSM rates will be clear pointers to a significant non-standard effect. Taken together with results of Ga detectors, especially a low signal there, only the lowest signal profile in Fig. 5.1 would be consistent, strongly pointing either to MSW conversion or neutrino decay. A Borexino signal substantially higher than this minimum (in conflict with the Ga signal) would already point to a major neutrino effect—e.g. magnetic scattering. Thus, the data on signal rates at these energies could basically clarify the main directions of the operative physics or astrophysics and set the stage for further investigations in Borexino. In the case of an SSM type scenario, a measurement of the ^{7}Be neutrino flux would be the major result from the low energy signal rate alone.

5.1.2 *Temporal Flux Variations at Low Energies*

These variations are of 3 kinds: yearly, day-night and seasonal. The $1/R^2$ yearly time variation, independent from physics or astrophysics, is the basic signature of solar origin of the signal. Other types of time variations would however, generally imply the presence of new neutrino physics. Because of the *monoenergetic* nature of ^{7}Be neutrinos, the day-night or seasonal variation is a sensitive and direct indicator of flavour conversion in a major part of the presently allowed neutrino parameter regimes. Such type of data will be one of the main outcomes of Borexino. The $1/R^2$ variation and its practical applicability was treated in Chapter 3. Here we consider the day-night and seasonal effects.

The Day-Night Effect: The MSW fit to the present data (Fig. 4.2) suggests that Δm^2 is likely to be $<10^{-5}$ eV^2 and predicts that neutrinos <1 MeV, thus also ^{7}Be neutrinos, would be nearly completely converted in the sun (see fig. 4.1). The matter densities on the earth

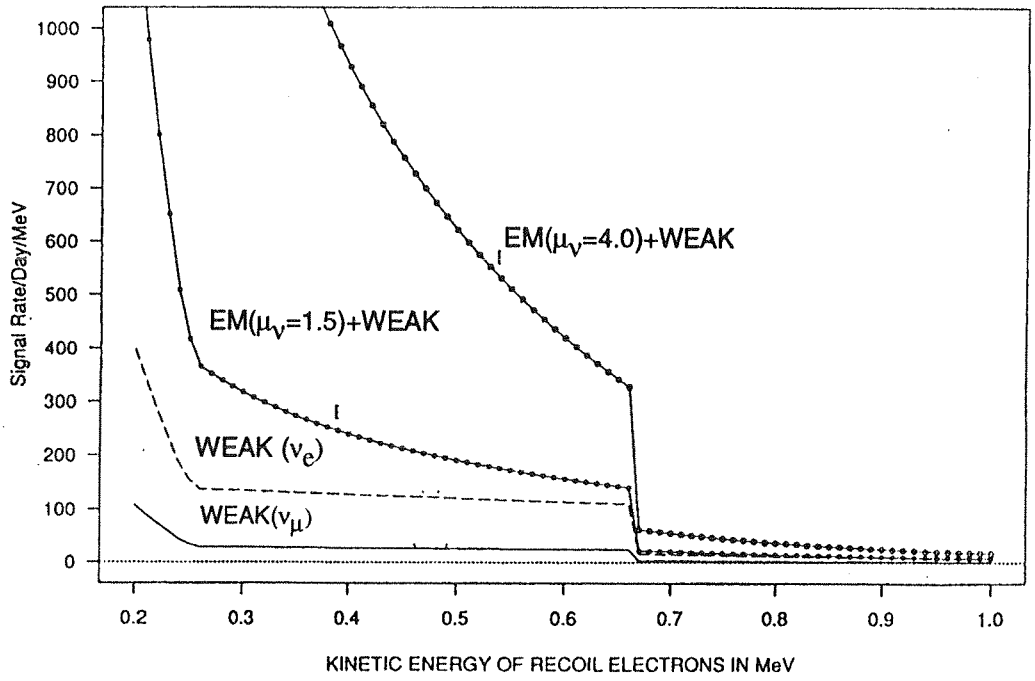

Figure 5.1 Low energy signal profiles in Borexino for different neutrino scenarios

Figure 5.2 Day-Night effect and seasonal variability of neutrino track in the earth.

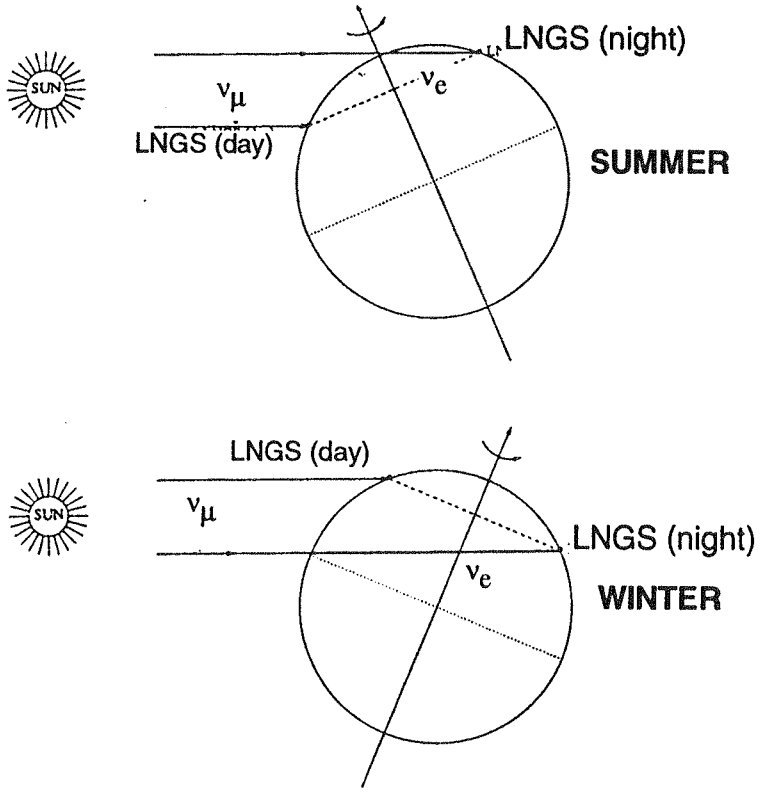

are such that, in this case, resonant reconversion in the earth could occur (see §4.1, eq.4.5). Such an effect creates an increase in the signal rate during the night compared to that during the day. The reconversion probability and thus the event rate excess $\Delta(T)$=[N(earth)-N(no earth)] is basically determined by 3 independent factors [4.11]:

$$\Delta(T) = N_7 (\varepsilon_e - e_\mu) (1 - 2P_S) [1-P_E(T)] \qquad (5.1)$$

where N_7 is the astrophysical flux of ^{7}Be ν_e's, and $(\varepsilon_e - \varepsilon_\mu) \approx 0.8\varepsilon_e$ where ε_e, ε_μ are the ν_e, ν_μ detection probabilities (via electron scattering). P_S is the ν_e fraction in the incident beam and depends only on ν parameters and solar data (in this regime, $P_S \approx 0$ for Be neutrinos). $[1-P_E(T)]$ is the reconversion probability in the earth, determined only by the neutrino parameters and the neutrino track through the earth.

The MSW resonance density for the ^{7}Be ν_e-line is: $\rho_o \approx 15.3 \cos 2\theta \, \Delta m^2$ (10^{-6}eV^{2}units). Densities ρ for neutrino tracks at Gran Sasso, Italy, ranging from $\rho \sim 4$ (summer) to ~10.5 g/cc (winter) [5.3], imply maximum reconversions for $\Delta m^2 \sim 4$ to 7×10^{-7}eV^2. Thus, essentially the entire lower half of the MSW "wish-bone" in Fig. 4.2 can be experimentally scanned by the earth regeneration effect.

The tilted rotation axis of the earth and its relative orientation to the sun results in a well defined experimental mechanism for a systematic scan search of the MSW effects. The variability of the neutrino track through the earth is illustrated in Fig. 5.2. The tracks in summer are shallow and short and those in winter long and probe the deep into the earth. Fig. 5.3 shows the day-night effect Δ directly as the event rate difference in the Borexino signal for 12 hours of live-time each "with" and "without" the earth interposed in the neutrino path. The three panels show Δ contours in the plane of the neutrino parameters for three different seasons, sampling three different slices of the track distribution through the earth [4.11]. They illustrate the shift of the Δ pattern with the track pattern.

Tomographic Analysis of the Day-Night Effect -Determination of ν Parameters: The track distribution available for the neutrino in the period of a year depends on the geographic latitude of the detector which limits the maximum angle of the track relative to the horizon. For a given location, the track T of a given angle produces a definite amount of flavour reconversion. Thus, $\Delta(T)$ can be calculated for each set of neutrino parameters as a function of the track angle.

In a real-time detector, the solar time of the event uniquely fixes the neutrino track T. Thus, experimentally, the variation $\Delta(T)$ can be tomographically reconstructed from the

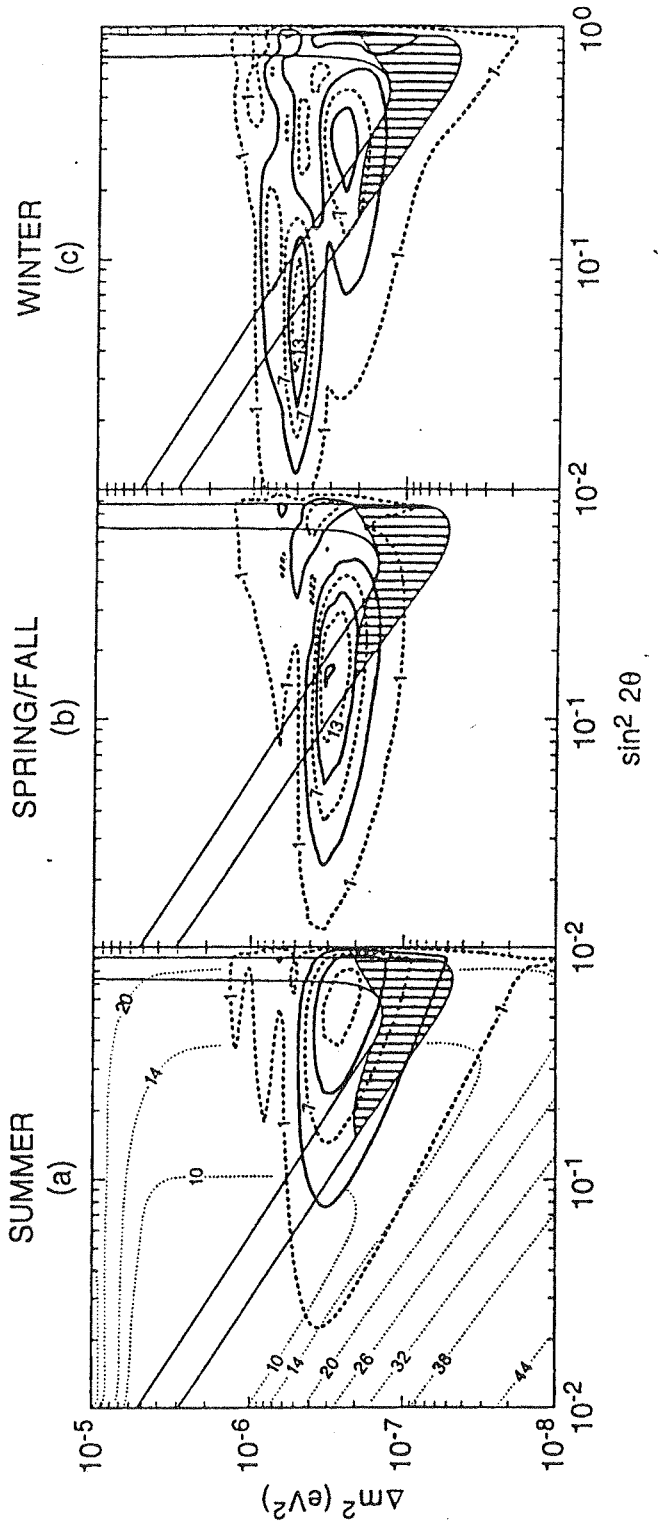

Figure 5.3 Contours of the day-night excess in the neutrino parameter plane for different seasons (from [4.11])

data. Figs. 5.4 (a-c) explicitly show a theoretical tomographic analysis [4.11] of the variation of the day-night excess Δ as a function of the track angles available at Gran Sasso. Each curve is calculated for pairs of neutrino mass/mixing parameters, sampling points in the wish-bone allowed region of the MSW effect. Table 5.II summarises the neutrino parameters for each curve in fig. 5.4.

Beginning at the upper left corner of the MSW "wishbone" (Fig. 4.2), $\Delta m^2 = 0.79 \times 10^{-6}$ eV^2, and moving down the diagonal in curves 1 to 3 in the top panel of Fig. 5.4, $\Delta(T)$ is very small for most of the tracks until one reaches angles $>60^o$, deep into the earth. Thus for this range of parameters, a substantial day-night effect will be seen only in winter months. The winter effect becomes dramatically large as the parameters approach those of curve (3). As Δm^2 becomes slightly smaller, the smaller earth densities probed by smaller angles begin to be effective and the day-night effect at most smaller angles also jumps substantially (curve 4) while that at high angles drops to smaller values. Continuing along the MSW diagonal (middle panel) $\Delta(T)$ changes systematically from large effects at smaller angles (i.e throughout the year) and small effects for the high angle winter tracks (curve 1) and reverses to the opposite tendency until, in curve (4), the effects approach smaller magnitudes in both the low and high angle regimes. In the vertical limb of the MSW map (lower panel) the angular dependence changes into patterns with new maxima at intermediate angles. Finally, in curve (4), a smooth oscillating pattern, characteristic of MSW solutions of various lengths through an approximate uniform medium (earth's mantle) is predicted.

Table 5.II Neutrino parameters of curves for $\Delta(T)$ in Fig. 5.4

Panel	Curve no.	Δm^2 10^{-6} (eV^2)	$Sin^2 2\theta$
Top	1	0.79	0.063
	2	0.63	0.079
	3	0.5	0.1
	4	0.4	0.13
Middle	1	0.32	0.16
	2	0.2	0.25
	3	0.13	0.4
	4	0.079	0.63
Bottom	1	1.0	0.71
	2	0.5	0.71
	3	0.25	0.71
	4	0.13	0.71

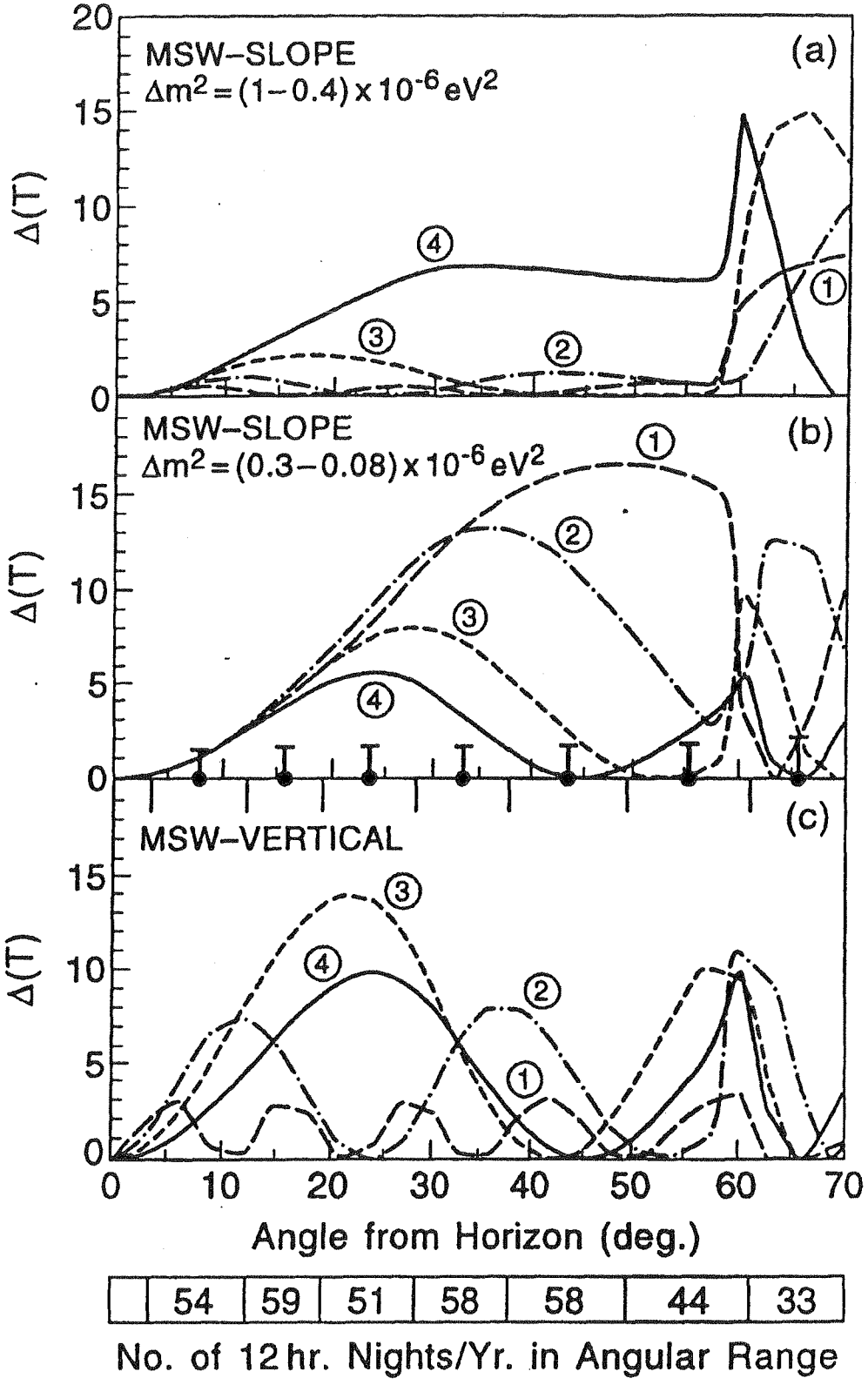

Figure 5.4 Tomographic variation of Δ with neutrino track angle for different neutrino parameters in the allowed region [ref. 4.11]. The relevant ν parameters are listed in Table 5.I. The error bars in the middle panel represent the statistical error (1σ) expected in a measurement of Δ(T), assuming a background of~100 events/day in the signal region (corresponding to a scintillator radiopurity of 10^{-15} g/g.).

The essential point of Fig. 5.4 is that the day-night effect can lead to a direct determination of the neutrino parameters in the region allowed by present experiments. The tomographic track dependence of the day-night effect $\Delta(T)$ is characteristic of the value of ($\sin^2 2\theta$, Δm^2). The numerical values of $\Delta(T)$ in Fig. 5.4 were obtained using the detector parameters, ν-e scattering cross sections as well as N_7, the astrophysical ^{7}Be SSM flux. However, experimentally, the neutrino parameters are determined directly from the tomographic shape. Thus these results are independent of the SSM.

Determination of Astrophysical Fluxes: The known neutrino parameters and data on solar densities can now be used to estimate P_S in eq. 5.1, the percentage of ν_e flavour in the neutrinos leaving the sun. For most of this regime, P_S is nearly zero. Thus the remaining scale factor N_7, the astrophysical flux of ^{7}Be neutrinos in the sun, can be determined by comparing the measured value of $\Delta(T)$ at any given T to that calculated using the MSW theory and the earth density profile characteristic of that track T.

Finally, from the measured value of the ^{8}B flux, e.g. from K-II or Borexino and the neutrino parameters determined above, the astrophysical flux of ^{8}B neutrinos is also determined. Thus both neutrino physics and astrophysics aspects of the solar neutrino problem can be experimentally defined in a complete manner.

Detectability of the Day-Night Effect: These determinations require only the rates and changes of rate of the excess events at night-time, the excesses occurring only in the ^{7}Be ν signal window. An explicit spectroscopic separation of the signal from background in the detector is thus not imperative as long as the background is reasonable. The maximum possible excess effect is Δ ~18 in the case when complete regeneration occurs in the earth, i.e., the "earth off" signal rate is ~6 events/12 hour period (during day time), increasing dramatically to ~24 events/12 hours with the "earth on" (i.e. during night times). Fig. 5.4 shows that typically, effects with $\Delta > 3$ occur for at least some part of the angular range for most of the ν parameter range considered here.

From the measurement point of view, the "earth on" lifetime is not equal at each angle and must be taken into account in the counting statistics estimates. The box at the bottom of Fig. 5.4 gives the number of 12-hour nights possible at the LNGS location for each angular bin. Low angles have the longest "earth-on" lifetimes while the high angles have the shortest. An angle resolved, differential measurement of the $\Delta(T)$ pattern (necessary for determining neutrino parameters) is possible if the statistical error in the measured value of $\Delta(T)$ in each bin (determined by the background and thus the radiopurity of the scintillator) is sufficiently small. In the middle panel,. the statistical accuracy estimated

for $\Delta(T)$ in each angular bin is shown for a background of 100 events/day in the signal range of 0.2-0.8 MeV, corresponding to a low purity scintillator with 10^{-15} g/g. It is seen that even for this low purity, the fluctuations can be small enough to essentially distinguish the variation of the $\Delta(T)$ pattern with the neutrino parameters.

Seasonal Flux Variations: The monoenergetic nature of ^{7}Be neutrinos and the seasonal variation of the earth-sun distance enable the application of the "text-book" method of detecting "just so" neutrino oscillations in vacuum (§4.1) by measuring signal rate vs. travel length of isotropically emitted neutrinos. The ^{7}Be signal rate should display seasonally periodic changes, directly probing the neutrino oscillation effect as the earth moves back and forth relative to the sun. The viable parameter region for this effect is $\Delta m^2 < 10^{-10}$ eV^2 and $\sin^2 2\theta > 0.7$, which results in a small number of oscillations for ^{7}Be neutrinos (eq.4.12 with low n). Thus, even a small variation in the earth-sun distance can produce sizable flux variations as shown for a few representative parameter choices in

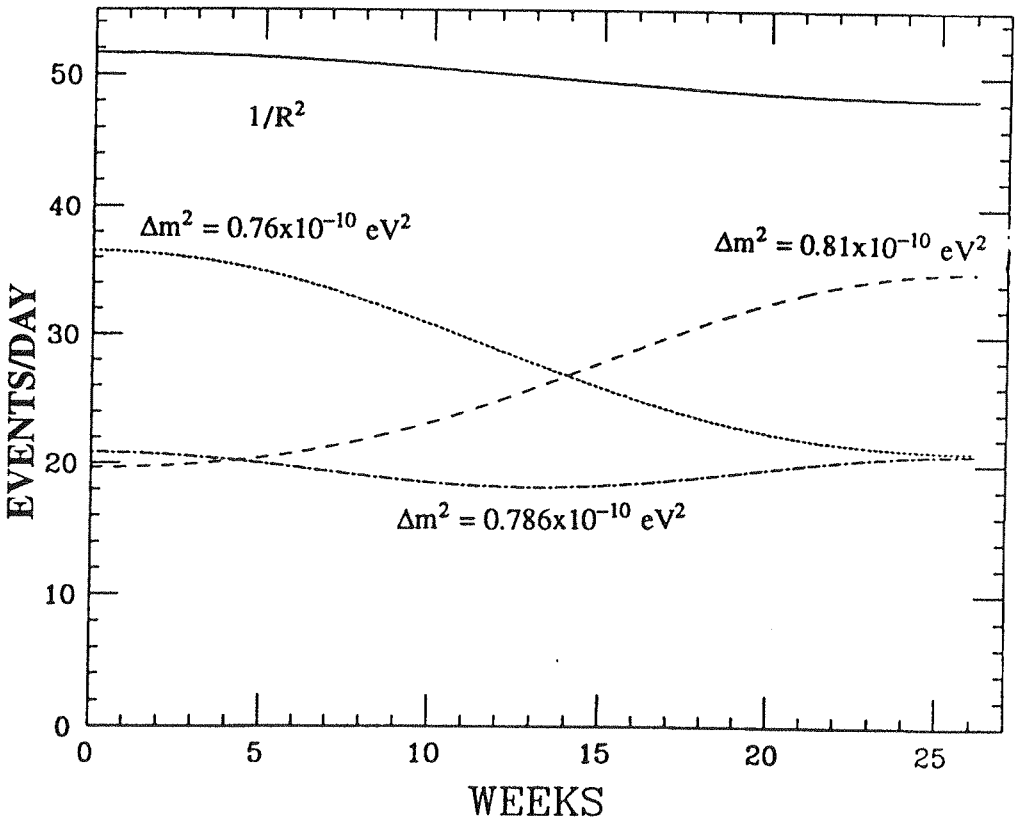

Figure 5.5 Seasonal variation of the ^{7}Be signal via "just so" vacuum oscillations. Shown for comparison is also the $1/R^2$ effect arising from the earth's motion only

Fig. 5.5. The effects can be large compared to the 3.5% variation due to the $1/R^2$ effect, also shown in fig 5.5. As seen there, the amplitude, phase and period of seasonal effects due to "just so" oscillations can be very different from the $1/R^2$ effect. Also they are much more sensitive to neutrino parameters than in the case of MSW matter conversion above. Observation of the seasonal effect due to vacuum oscillations will locate these parameters within a narrow range.

Flux variations from day-night and seasonal effects can be relatively easily separated due to the wide differences in periods. Also, the present allowed parameter regimes predict that the day-night and the seasonal rate variations can occur only mutually exclusively.

The search for seasonal flux variations must involve, as a rule, both the $1/R^2$ effect and vacuum oscillations. The $1/R^2$ effect is completely predictable in amplitude and phase, thus the analysis should search for the presence of extra variations with different amplitudes and phases. The specified phase and periodicity of these effects underscores the possibility of minimising systematic errors by observations over two to three years with several periods, particularly in the case of small effects. This generally requires reasonably stable detector operations with sensitivities and calibrations monitored continuously on-line. The possibility of such facilities in Borexino were discussed in §3.1. The stability of the operational background in turn, can be monitored by the low energy spectrum 1.5 to 3 MeV, beyond the energy window of the Be solar neutrino signals (see Fig. 3.2).

5.1.3 *The High Energy Signal- Spectral Shapes of ^{8}B Neutrinos*

Distortions of the spectral shapes of ^{8}B neutrinos cannot arise from known astrophysical effects [5.1]. They can arise in general, only from neutrino physics effects. Shape determination will be carried out to high precision by all the large experiments, SUPERKAMIOKA, SNO, and BOREX. Despite the smaller target mass, such a measurement is possible also in Borexino, the main advantage being a cutoff energy lower than that in Cerenkov detectors in general (4MeV in Borexino vs. 7.5 MeV at K-II). The (CC+e-ν) signal event rate above 4 MeV is 586/year (SSM flux) in the enlarged Borexino FV with 240 t scintillator (see §3.3). Typical rates in the MSW scenarios are 180 to 270/year compared to the present K-II rate of ~90/year (see Table 3.III).

The shape of the ^{8}B spectrum can be distorted by three causes known so far: a) MSW

effect; b) neutrino decay (§4.3) and c) "just so" vacuum oscillations (§4.1). Recall (Fig. 4.3) that a) and b) and to some extent c), can produce similar distortions at the high energy tail of the ^{8}B spectrum and be compatible with K-II data. At lower energies, the deviations diverge; large shape deviations (even "zero") can be caused by vacuum oscillations and thus observed readily in Borexino thanks to the lower cutoff (but probably not elsewhere). The effect can be cross-checked by a concurrent seasonal variation of the ^{7}Be flux (§5.12). We discuss here the detectability of the smaller shape distortion effects typical of the non-adiabatic MSW effect in the allowed regime.

The (CC+ ν-e) Signal: The MSW parameter region of Fig.4.2, has two main branches, the "slope" and "vertical" regions. In the vertical part of the MSW map, no spectral distortions are produced. Only the slope, the non-adiabatic MSW effect, is sensitive to the neutrino energy and thus can affect the spectral shape. The distortion produced, however, is small and cannot yet be seen at K-II.

The theoretical ^{8}B solar ν_e spectra and the corresponding signal spectra (for a LFV of 240 tons and a lifetime of 2 years) for the inverse beta-decay (CC) on ^{11}B and the ν- e scattering channels in Borexino were calculated for neutrino parameters at 16 points distributed in the MSW wish-bone area. The spectral shapes were distorted compared to the standard shape (in the "slope") but the shape distortion was nearly the same along isosignal MSW contours along the entire slope region. The shape changed significantly only across the band (which involved also a change in the signal rates). These theoretical spectra were used to reconstruct practical spectra observable in Borexino using our standard Montecarlo codes (Appendix V). The relative shape was analysed by normalising the reconstructed spectra at different points in the MSW regions by that corresponding to the standard no-MSW incident spectrum in a manner similar to that followed at K-II [5.2].

Figs. 5.6 (a-b) shows typical results of spectra normalised to the standard shape for (Δm^2, $\sin^2 2\theta$) pairs of (10^{-5} eV^2, 3×10^{-3}) (5.6a) and (4×10^{-6} eV^2 ,0.77) (5.6b). Fig. 5.6c shows for comparison, results from K-II for a live time of 2.85 years [5.5]. The MSW/SSM ratio data in Fig. 5.6a show that a standard shape for ^{8}B neutrinos, i.e. energy independence of this ratio (dashed line), could be ruled out at >95% confidence. The data in Fig. 5.6b, are consistent with a standard shape as expected in the "vertical" MSW regions. Thus, the non-adiabatic MSW effect can be detected at these levels of significance in the entire sloped part of the MSW "wish-bone" of Fig. 4.2. This is especially valuable as an MSW indicator in the "slope" region with $\Delta m^2 > 10^{-6}$ eV^2, where ^{7}Be neutrinos are not expected to show a day-night effect.

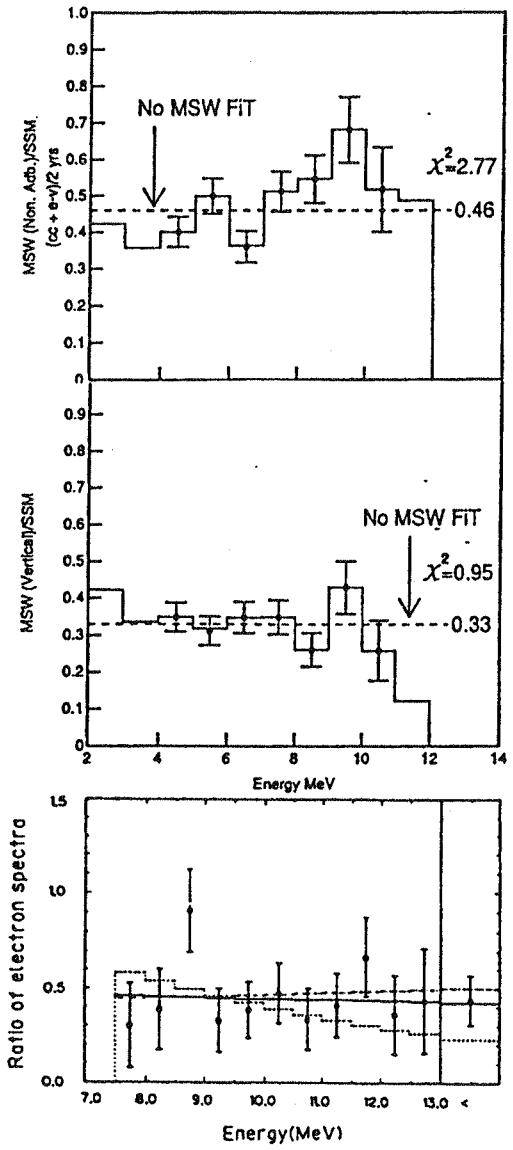

Figure 5.6 Ratio of MSW/SSM ^8B neutrino spectra (CC+ν-e) from simulated reconstruction in Borexino ("life time" 2 yrs). a) MSW "Slope" region (deviation predicted); b) MSW "Vertical region (no effect predicted). The ratio data were fitted to the "no effect" (dashed line); the χ^2 and the fit flux fraction are shown. c) Comparative data (2.85 yrs) from K-II [5.2].

The CC Signal: Deeper insight into shape effects may be possible by isolating the CC signal via its signature (§3.2). The CC shapes display a larger distortion in general and thus detectable even with the inherently lower statistical quality of the data. Further, the rate ratio CC/ν-e is fixed at all energies; thus it can be used as an important fit constraint in the search for shape effects and for minimising systematic errors.

5.2 *Solar Antineutrinos*

5.2.1 Spin-flavour Conversion in the Sun

Antineutrinos from the sun may be observed if spin flavour conversion takes place in the magnetic fields of the solar convection zone (§4.2)[4.11]. The $\bar{\nu}_e$ spectrum due to spin

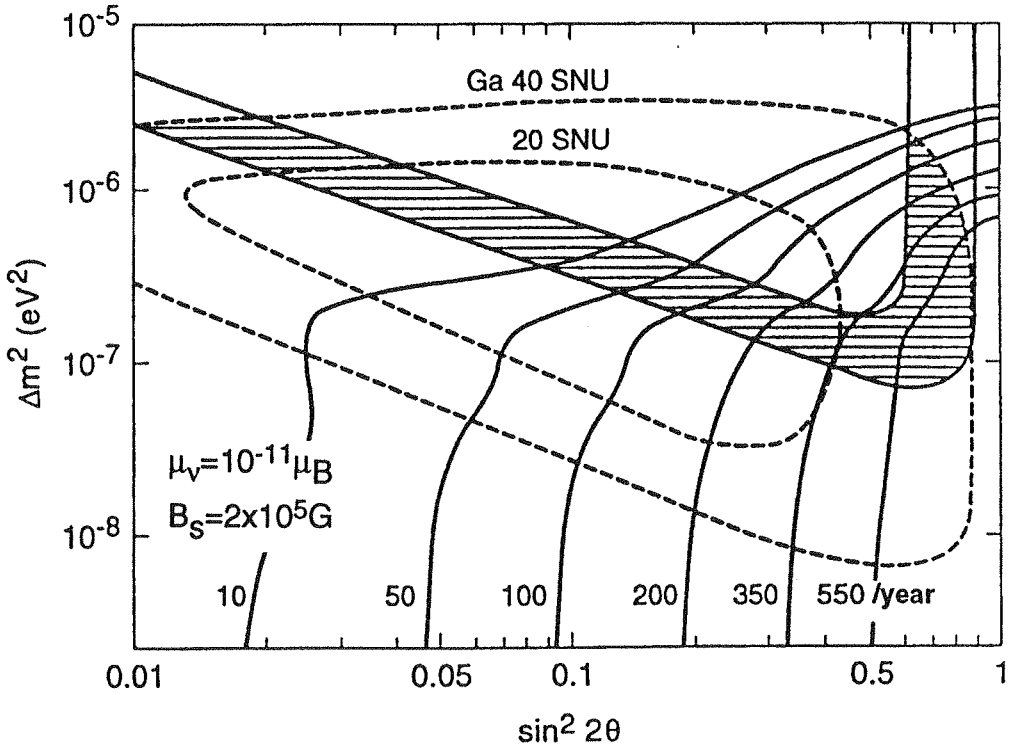

Figure 5.7 Antineutrino rates in Borexino via spin-flavour conversion in the sun [ref. 4.11]. The MSW allowed region and some Ga signal contours are also shown.

flavour conversion has been calculated (Fig. 4.4) as a function of the neutrino parameters for the relevant region ($\Delta m^2 < 2x10^{-7}$ eV^2). Using these spectra, the $\bar{\nu}_e$ signal rates for $\bar{\nu}_e$ energies >5 MeV have been calculated as a function of the neutrino parameters. The restriction to >5 MeV minimises possible background due to terrestrial $\bar{\nu}_e$ background (see Fig. 4.4). The results show (see Fig. 5.7) that a sizable signal of antineutrinos, from ~10 to 600 events/year, may be observable the rate being high near Cabibbo angle. For $\Delta m^2 < 10^{-7}$ eV^2, the $\bar{\nu}_e$ signal can be of the order of or typically larger than the solar ν_e signal even though the $\bar{\nu}_e$ flux is a small fraction of the ν_e.flux because of the difference in cross-sections. The $\bar{\nu}_e$ flux and the shapes predicted in Fig. 4.4 can be measured using the specificity of the delayed neutron coincidence signature (§3.4).

The above estimates of signal rates are based on a magnetic field of $2x10^5$ G in the convection zone and a value of $\mu_\nu = 10^{-11}\ \mu_B$. These choices produce effects consistent with the time variation at Homestake. For a magnetic moment as small as $\mu_\nu = 5x10^{-13}\mu_B$, for the same solar field as above, an antineutrino signal rate of 20 to 80 events/year can be expected. Even the lower rate is detectable in Borexino. Thus, whether spin-flavour precession is the cause of the Homestake variation or not, Borexino can set a stringent intrinsic limit for this process in the sun.

5.2.2 *Neutrino decay*

The second means by which antineutrinos can be emitted from the sun is by neutrino decay (§4.3).The process is governed by eq.(4.9) (straight decay, strong mixing), eq.(4.10) (MSW+decay, weak mixing). The crucial signature defining the antineutrino signal as due to ν decay is a $\bar{\nu}_e$ spectrum biased markedly towards lower energies (see Fig. 4.6).

The probability of the "straight decay" process is limited by 1) the range of mixing angles allowed the SN1987a data and 2) by direct experimental limits on the minimum neutrino lifetime. The lifetime itself is governed and limited by the Majoron coupling constant g, set by data on K-decay: $g^2 < 4.5x10^{-5}$, independent of the mixing angle (see discussion in [4.28]). With information on g, the following relation applies [4.28]:

$$\tau\,(10\ \text{MeV}) = 3.3x10^{-7} / g^2\,\Delta m^2\,(\text{eV}^2)\ \text{sec.} \qquad (5.2)$$

Within the constraints 1) and 2) above, the probabilities of the straight decay process

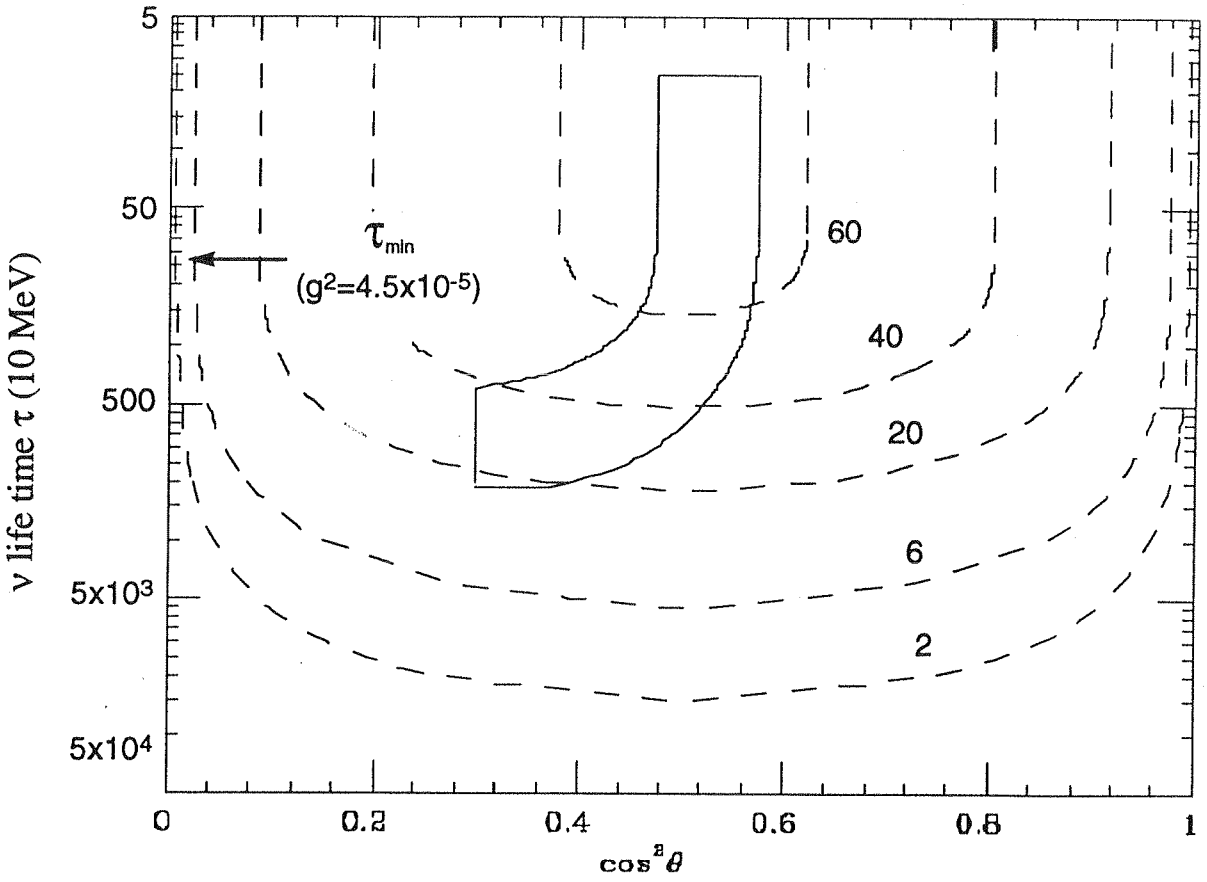

Fig. 5.8 Solar antineutrino rates in Borexino (200t FV) from ν-decay (strong mixing) according to eq.(4.9); 100t F.V., 2 years of data acquisition.

Fig. 5.9 Solar antineutrino rates in Borexino (200t FV) from (MSW+ν decay) (weak mixing) according to eq 4.10. A positron kinetic energy T^+=1.5 MeV corresponds to $E_{\bar{\nu}_e}$=3.3 MeV. The indicated terrestrial $\bar{\nu}_e$ (power reactor) rate limit applies to T^+=1.5 MeV [4.28].

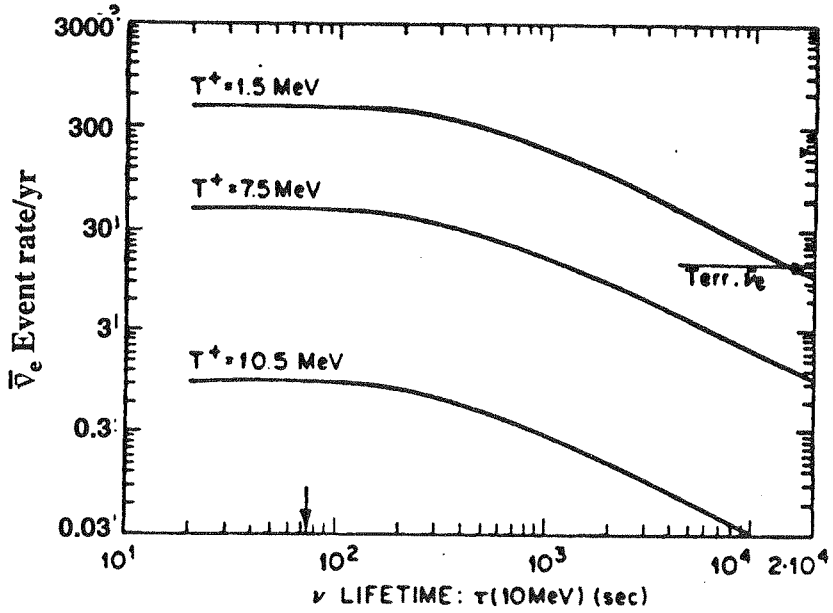

(eq. 4.9) can be calculated to yield the spectrum and intensity of antineutrinos arriving on earth and thus also the $\bar{\nu}_e$ signal rate in Borexino. This is shown in Fig. 5.8 in the lifetime-mixing plane [4.31]. The enclosed area in the center defines the parameter region allowed by constraints 1) and 2). The antineutrino signal in Borexino ranges from ~20 events/yr to >~60/yr near the lower limit on the neutrino lifetime in fig. 5.8. Observation of these antineutrino rates is within the design range of the detector (see discussion in §5.21 and §3.4 for remarks on the expected backgrounds). The range of $\bar{\nu}_e$ rates in Fig. 5.8 defines an observable lifetime range of ~100-1000 sec. By eq. (5.2) and the above limit on g^2, the applicable range of Δm^2 is ~0.7×10^{-4} to 7×10^{-6} eV^2. By definition of this decay process, the viable mixing angle must be large, $\sin^2 2\theta$ approaching ~1.

Fig. 5.9 shows calculated antineutrino rates for the MSW+decay process (eq. 4.10). In this figure, the rates are given for various lower thresholds on the kinetic energy T^+ of the signal positron. The corresponding incident neutrino energy is given by $E_{\bar{\nu}_e} = T^+ + 1.8$ MeV. The standard cutoff of 5 MeV for the antineutrino energy adopted here (see §3.4) signifies a T^+ of 3.2 MeV. The signal rates for MSW+decay are in general higher than those predicted for the straight decay. The observable lifetime range of 100- ~2.10^4 sec (see Fig. 5.9) then corresponds (via eq. 5.2) to Δm^2 in the range ~0.7×10^{-4} to $3.5 \times 10^{-7} eV^2$ and allows mixing parameters $\sin^2 2\theta \ll 1$. The MSW+decay process is thus observable in Borexino for most of the MSW parameter range allowed by present experiments (Fig. 4.2). The antineutrino channel in Borexino thus introduces a sensitive tool for the search for the instability of the neutrino over a wide range of mass and mixing parameters via the MSW+decay mechanism.

5.3 *Laboratory Neutrino Physics*

5.3.1 ^{90}Sr $\bar{\nu}_e$ Source Experiment. -Deep search for ν Magnetic Moment [5.3]

The fundamental aim of this experiment is a determination of the low energy $\bar{\nu}_e$-e scattering cross section with a laboratory antineutrino source.This process has not so far been investigated either for neutrinos in the sub-MeV regime or by observation of recoil electrons at very low energies. The present experiment aims at both. These plans will be initiated after the initial phases of Borexino operation. The source experiment will have a dual purpose: it will serve as a calibration of the solar neutrino signal in Borexino, (considered in §2.4) and the data will also be analysed for the presence of μ_ν.

Neutrino magnetic moments can be sensitively investigated by ($\bar{\nu}_e$-e) scattering (with a lower "weak" scattering "background" than with ν_e-e scattering) using a strong radioactive source of antineutrinos. The presence of a magnetic moment adds a new component to the scattering cross section (see §4.2). Sensitivity to low electron recoil energies and a well-defined antineutrino source spectrum are key requisites. As mentioned in §2.4, these requirements are fulfiled with a radioactive source of ^{90}Sr-^{90}Y. Set at a distance of ~8 m from the center of the detector, a 5 MCi source will produce a signal rate of ~56 events per day in the signal region of 0.2-0.8 MeV (see §3.5). The background in this signal window can range from a low of ~20 events per day (high purity 10^{-16} g/g scintillator and 10/d MSW signal from Sun) to a high of ~150/day (low purity 10^{-15} g/g scintillator and a SSM solar signal of ~50/day). These signal and background figures indicate the following estimates: for a "source on" live time of 100 days and a longer (normal) lifetime, 400 days with "source-off", the ($\bar{\nu}_e$-e) scattering cross-section can be determined with a 1σ error of 3% for the high background case and <2% for the low background case.

Fig. 5.10 shows the $\bar{\nu}_e$-e scattering cross section for "weak" scattering compared to magnetic scattering with a $\mu_\nu = 1.5\times10^{-10}\ \mu_B$, a value smaller than the most conservative limit on the moment at present [4.14] [4.24]. The presence of such a moment can be easily detected in Borexino. The signal enhancement due to magnetic neutrino scattering as a function of μ_ν is shown in Fig. 5.11. This curve indicates that with a precision of a few percent of the scattering cross section, an upper limit of $\mu_\nu \leq 2\times10^{-11}\ \mu_B$ can be set in Borexino, a factor ten below present laboratory limits and in the range of interest for μ_ν effects on solar neutrinos. An important normalisation of the scattering data can be applied with the help of the ($\bar{\nu}_e$,p) events observable at the same time (see Table 3.IV). These events are specified by (e^+-n) delayed coincidence signature (§3.4). This facility automatically calibrates the $\bar{\nu}_e$ flux incident on the detector and eliminates the need for determining the source strength or the geometrical factors of the experiment.

5.3.2 *Deep Search for Neutrinoless ββ Decay in ^{136}Xe in Borexino* [5.3]

This nuclear process has been the subject of experimental and theoretical study for more than two decades and, at present, more than 30 experiments are applied to this problem. A decay of this type involving [A(Z) -> A(Z+2) + 2 β] occurring without neutrino emission is revealed by the appearance of 2 beta-particles carrying the total

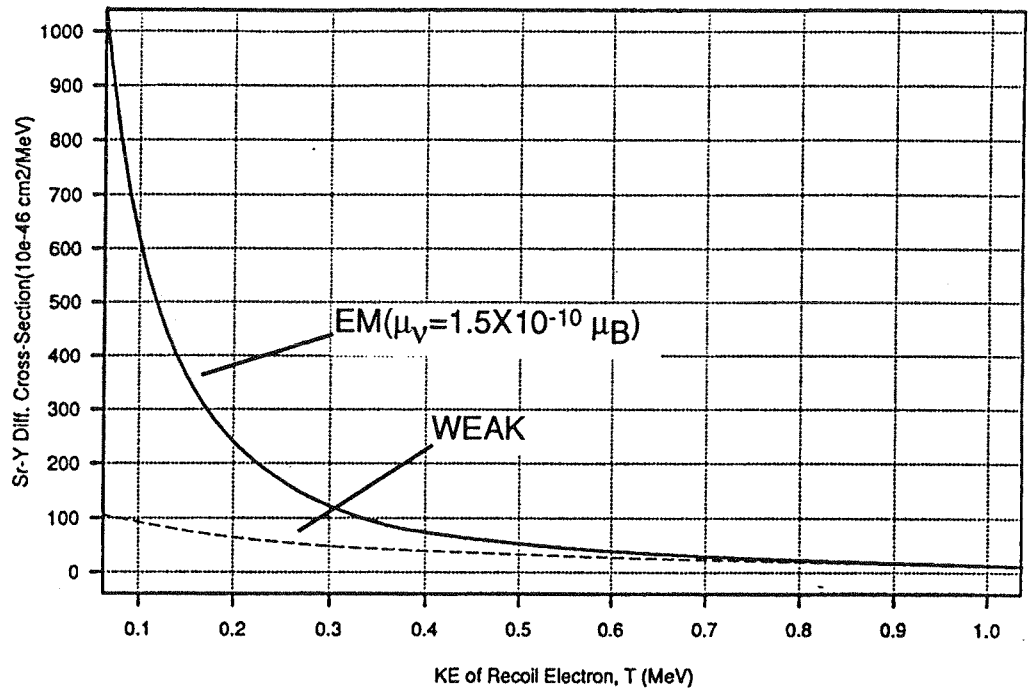

Figure 5.10 Comparison of the "weak" and magnetic $\bar{\nu}_e$- e scattering cross section (with μ_ν = 1.5x10^{-10} μ_B) as a function of the electron recoil kinetic energy T.

Figure 5.11 Enhancement of $\bar{\nu}_e$-e scattering signal as a function of neutrino magnetic moment.

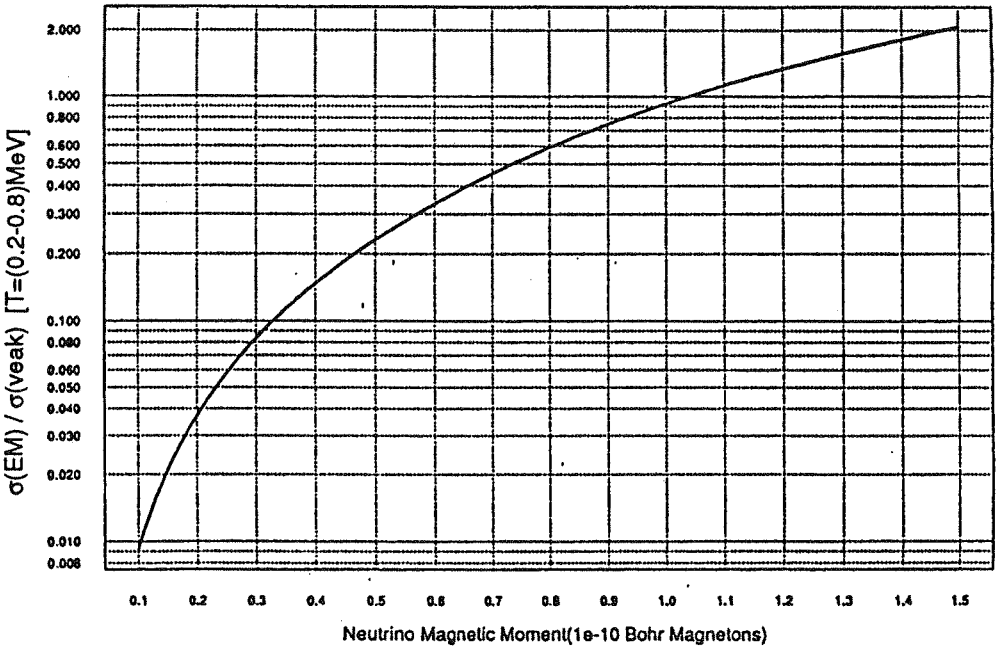

decay energy, which thus appears as a monoenergetic peak in a calorimetric detector. Such a signal is a unique signature for the presence of a flavour-mixed (massive) Majorana neutrino. The rate for this process is determined, among others, by the mass of the Majorana neutrino. The present upper limit for the halflife of such a decay of ^{76}Ge is $>1.2\times10^{+24}$ y (90%c.l.) [5.4], implying a neutrino mass $\langle m_\nu \rangle < 2.4$ - 4.7 eV [5.5]. The long lifetime obviously requires a large target mass (preferably acting as its own detector) and a very low background. In the above case, a 7 kg source of ^{76}Ge in a high-resolution Ge detector was used with a measured background of 1.2/keV/kg/yr @ 2 MeV. In another case, that of ^{136}Xe, a recent experiment [5.5] has set a limit on $\langle m_\nu \rangle$ of 3.3 - 5 eV, with a ^{136}Xe source mass of 3.5 kg in a time projection chamber operating with a background of 10^{-2}/keV/kg/year. For a substantial extension of the lifetime limit and thus reduction of the limit on $\langle m_\nu \rangle$ (the lifetime varies as $\langle m_\nu \rangle^{-1/2}$), an altogether new approach may have to be considered, employing ton size target masses and a corresponding reduction in the background at the same time.

The design of Borexino is optimized in just these directions. Fig. 3.2 shows that in the 2-2.5 MeV region, the estimated background is about 10/20 keV/100tons/yr in the standard FV. The operating background in Borexino is thus 5×10^{-6} /keV/kg/yr, more than 5 orders of magnitude below the Ge experiment and more than 3 orders of magnitude below the Xe experiment. It is thus relevant to examine if Borexino can be applied advantageously to a deep search for this process.

Consider the application of the double β-decay of ^{136}Xe problem in Borexino. This case offers many favourable advantages, chiefly a satisfactory solution of the problem of incorporating the double β-decay source in the detector. It is well-known that noble gases (especially the heavier elements) have a high solubility in organic liquids, e.g. the solubility of Xe in benzene is 2.2 wt % at 15 °C. That in the Borexino liquids is yet undetermined, but the systematics of solubility data suggest assuming a value of 2%. This implies a source mass of 2 ton of Xe, i.e. 8.8×10^{26} atoms of ^{136}Xe in the FV of Borexino.

The use of Xe has many other important merits. Xe, an inert gas, is probably the ideal dopant in the liquid scintillator since it can be incorporated into the scintillator with the least detriment to the scintillation or the optical or other properties of the detector. Xe can be obtained with a high degree of purity since other radioactive gases such Rn and gases such as Kr and Ar with trace radioactivities can be removed because of the convenient differences in the boiling point of Xe compared to them. (The radiations of ^{39}Ar and ^{85}Kr are also <0.7 MeV, well below the region of interest at 2.5 MeV).

The background @ <2.48> MeV (the$\beta\beta$ peak position) over a width of 200 keV, the FWHM typical for this energy in Borexino, is given from Fig. 3.2 as 100 counts/year. Unlike previous $\beta\beta$ decay experiments the Borexino-Xe approach enables a source on—source off procedure. Thus, in a 2-year measurement, the 90% c.l. upper limit on a possible peak at the double β-decay energy is $1.6(400)^{1/2} = 32 = 16$ counts/year. With a 100% detection efficiency, this background rate, with a source of 8.8×10^{26} ^{136}Xe nuclei, implies a 90% c.l. upper limit on the halflife of about 3.8×10^{25} years. This represents an extension of the present ^{136}Xe ν-less double β half-life result [5.5] by a factor of 150. Thus, in a 2-yr measurement in Borexino, the limit on $\langle m_\nu \rangle$ can be reduced by a factor 12, to $\langle m_\nu \rangle < 0.3$ eV, well below the lowest value aimed at in any current or planned experiment [5.6].

References

[5.1] J. N. Bahcall, Institute of Advanced Study Preprint (1991).

[5.1] K. Hirata et al, Phys. Rev. Lett. 65, 1297 (1990).

[5.3] R.S. Raghavan, Proc. 25 Int. Conf. High Energy Physics (Singapore 1990) (World Scientific) (1991) p. 482.

[5.4] D. O. Caldwell et al, in Proc. XIV EPS Conf. on Nucl. Phys. Bratislava (1990); J. Phys (G), to appear.

[5.5] H. T. Wong et al, Phys. Rev. Lett. 67, 1218 (1991).

[5.6] See M. Moe, Nucl. Phys. B (Proc. Suppl.) 19, 158 (1991); (In this review the $<m_\nu>$ limit from [5.4] is quoted as 1 eV, instead of 2.4 eV as cited by [5.5]. Our statements are based on the framework of [5.5]. For valid comparisons with our statements, Moe's projections of best future $<m_\nu>$ values must be accordingly increased by a factor of 2.4.)

PART II

TECHNIQUE

Chapter VI

THE DETECTOR

6.1 *General Description*

The basic design of the Borexino detector is simply described: A central spherical volume of liquid scintillator will be observed by a large number of concentrically distributed phototubes. An overall shielding architecture (consisting of two major parts, water and an external solid shield) protects the scintillator volume from background radiations from the rock as well as contamination in the shielding and container materials. The cardinal aspects of the design are: detection of the scintillation signal (determining the fiducial target volume (F.V.) and the optical coverage of the emitted scintillation light, thus also the number of phototubes (PMT)/reflector units and the radius of the PMT surface), the shielding architecture (determining the dimensions of the containment vessels for the scintillator and other shielding liquids as well as the external shielding structure) and finally, interwoven in the above, radioactive purity aspects of all materials other than the liquid scintillator. We consider in turn, the physical and dimensional aspects, the shielding logic and the design of the individual components of the detector.

Dimensional and Physical Aspects: The overall size of Borexino is decided by two basic dimensions: a) The target volume will be 100 tons scintillator, thus with a density of ~0.9, this results in F.V. sphere of 6m diameter; b) It is necessary to arrange a total shielding depth of ~5 mwe to protect the F.V. from the rock backgrounds. For water as the main shielding medium this implies, e.g., a total diameter of 17m for the detector sphere. Details of the detector (in the two main design options under present consideration) are arranged by these two limiting dimensions. The simpler design (A) is basically the above, with water as the only shielding agent. Design (B) incorporates a hybrid shield design with water and low background concrete. We compare the compromises involved in the two design options

later.

Table 6.I lists the physical specifications of designs A and B. The individual components of the detector are: 1) the inner container vessel (I.V.) holding the liquid scintillator. Its total mass is ~300 tons, thus the diameter of this vessel is 8.5 m, the outer 1.25m serving as the last shielding buffer for the F.V. also with respect to the shielding water and the inner container material. The container is made of teflon laminated acrylic, the transparency of which permits observation of the scintillations. 2) The PMT array placed at the diameter of 12.5m.

Designs (A) and (B) diverge beyond the above common features. In (A) (fig. 2.1), the scintillation vessel is completely submerged in a containment tank of diameter 17m filled with water. The water provides the final ~4m shielding from the rock ambience. In this design, the PMT/reflector array is thus immersed in water. In (B) (fig. 6.1) the containment

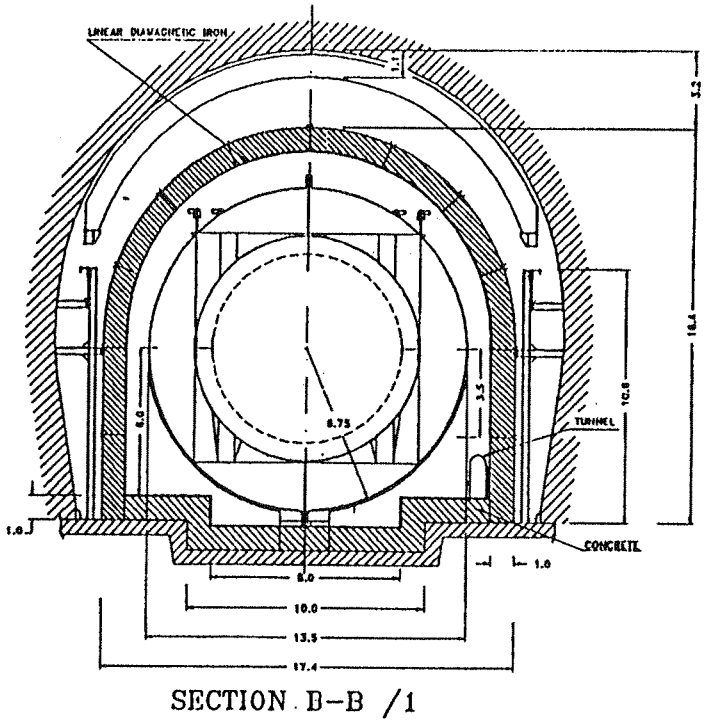

Figure 6.1. General overview of the detector configuration for the solution B.

tank is smaller, of diameter 13.5 m. The PMT's are operated in air, placed on the outside surface of the tank, viewing the scintillation volume via sealed optical windows. The

Table 6.I. Specifications for Borexino Conceptual Designs (A) and (B)

COMMON		
Fid. dimension (Low Energy)-FV	6m d	
Fid. dimension (High Energy)-LFV	8 m d	
Fid. Mass (Low Energy)	100 t	Liquid Scintillator (density 0.9g/cc)
Fid. Mass (High Energy)	240 t	"
Inner Vessel (I.V)	8.5 m d (Sph.) 2.5cm thick	Laminated Acrylic
Mass of Acrylic Shell	5t	
Total Scint. Mass	300 t	
DESIGN (A)		
Containment tank	17m d x 17m (Cyl.) 1.-2.5 cm thick	Plastic Lined Iron or Steel
Safety tank	92t	Carbon steel
Mass of Tank	139t	
Mass of Shield Material	4 kton	Water
PMT Radius	6.25m	Support Frame – Stainless Steel
PMT	1660	PMT/Reflectors in Water
DESIGN (B)		
Containment tank	13.5m d (Sph.) 2.5-3.cm thick	Stainless Steel
Mass of Tank	118t	
Shield I – Mass	1 kton	Water
Shield II		Sulfurcrete (1m thick)
Mass of Shield II	3kton	
PMT Radius	6.25m	Outside Tank Surface/Optical Window
PMT	1660	PMT in air/ Reflectors in water

reflectors are placed in the water inside the tank and aligned with the optical windows.

Since the water shield is insufficient, the rest of the shielding is made up by an extra (1m thick) concrete structure beyond the tank. Table 6.I summarises the dimensions.

Designs (A) and (B): The two different designs under consideration are currently under evaluation from many points of view, mainly three: operational safety, cost and experimental conveniences. Overall, the simplest design is that of design (A) both from construction and cost. The design (B) is more expensive but does allow safe maintenance and disposal of liquids in the case of catastrophic failure and affords the convenience operating PMT's in air.

6.2 *Shielding Logic – Material Purities*

The architectural detail in the above designs is dictated by the fact that the shielding from the rock involves large layers of materials with finite radioactive contamination which itself must be shielded. Thus the underlying logic dictates that closer to the central volume, the higher the bulk radiopurity of the material. An additional consideration is the significant background radiations from radioactivity in the PMT's and in other constructive materials (acrylic and steel). Our design input criteria require that the purities of these large-scale materials can be high but demonstrably obtainable in the large-scale at reasonable cost. The output result desired is that the background from external sources is significantly lower than that due to the radioactivity of the scintillator itself.

Table 6.II summarises the radioactivity contents of components of Borexino, measured in samples and assumed in the simulation studies of the external background as representative. The rates of background from the rocks in LNGS (hall C) are given in Table 12.XI. The background and purity assumptions listed in Table 6.II are thus reasonably conservative. The results of simulations (see chapter XII) show that with these assumptions and in the shielding architecture adopted, the external background in the F.V. in the low energy signal region is likely to be only 20% of the internal scintillator background at the highest level of design radiopurity i.e. $\sim 10^{-16}$g/g.

A principal device in achieving this result is the design of a generous buffer shield of upto 1.25m of the scintillator itself, definable by analysis software for low energy events. The thickness of this buffer shield can be decreased to only 0.25m for high energy

neutrino spectroscopy of the much weaker ^8B signal for which external background leakage into the F.V. is much smaller.

We stress that the impurity levels taken into account in the above refer to bulk purities. We intend to operate counting test facilities (See Appendix VI and Vol. III) to make batch quality control on the specifications. The fluctuations expected in the purity specifications

Table 6.II. Purity Specifications for Borexino Components

Material	Demonstrated* U/Th [(x)10^{-y}g/g] (x)y	Assumed (U/Th/K) [(x)10^{-y}]g/g) (x)y
Acrylic	(11)13/(3)13**	12/12/10
Water	(5)14/(7)14	13/13/11
Steel	(5)9/(5)9	8/8/6
PMT$^{\$}$	(5)8/(1)7/(2)4	(5)8/(1)7/(2)4
Sulfurcrete	8/8**	8/8/6

**Measured by Borexino Coll. except for ** from SNO Proposal – MARKII – 1989.*
$^{\$}$The total radioactivity of 1 PMT (Thorn Emi 9351/with the 8426 Schott glass) is 49μg of U, 96μg of Th and 0.21 g of natural K [36μg of U, about the same for Th, 0.16 g of natural K are due to the glass bulb].

are, at present, undetermined. This problem could be important essentially for the acrylic container vessel since this is the closest to the F.V. In case the acrylic purity is a problem, we have in reserve a modified design. The acrylic vessel is made larger, say of diameter 9m while the active scintillator diameter is contained at the 8m mark by a thin septum of teflon (Tedlar) film floating in a buffer of high-purity inactive organic liquid (say pseudocumene) of nearly the same density . Thus the background of the acrylic can be drastically cut, replaced by the much smaller one due to the teflon film.

6.3 *Detector Components*

Acrylic Vessel (designs A and B): The material for the I.V. should satisfy several requirements: optical transmission, structural strength and chemical compatibility to the scintillator. A satisfactory combination of these properties appears possible by acrylic laminated by a thin (~few 0.1mm) layer of teflon (Tedlar: Dupont polyvinylfluoride). The

lamination procedure is well established, and the compatibility of the laminated acrylic to the forming and bonding procedures required for construction of the vessel have been shown to be excellent. The laminate preserves the transparency of the acrylic and laminate itself is chemically inert to the scintillation liquid components. Accelerated aging tests of containers made by bonding laminated acrylic forms and filled with the component liquids of the Borexino liquid scintillator are in progress.

A preliminary design of the acrylic vessel, of wall thickness 2.5cm and its suspension in the water environment of the detector and the engineering feasibility of this design in the framework of the mechanical designs of the water containment structure have been made (see Appendix II). Basically, the design calls for the I.V. to be suspended inside the water tank by high-strength polymer ropes (Kevlar) arranged for buoyant and suspended configurations. Possible construction scenarios which emphasise ultra-clean environments and methods have been proposed (Appendix II).

Water tank (design A): Referring to the design A, all the detector is immersed in a large cylinder, filled of purified water. The container material is stainless steel, with a variable thickness from the b0ttom (2.5 cm) to the top (1 cm). The roof is conical and is also made with stainless steel, 0.5 cm thick. Due to the aggressiveness of the ultrapure water, perhaps the internal wall will be coated by a protected layer. A second external tank of carbon steel, will assure the total containment of the water, in case of cracking of the first one. A preliminary design with the stress analysis has been already carried out (see Appendix Ib).

External PMT's framework (design A): Again referring to the design A, the PMT's and the reflectors, coupled to them, are supported by a geodesic steel framework. It consists of faceted spheres, connected one-another by steel tubes; six tubes and reflectors are screwed to each sphere (Appendix Ib).

External vessel (design B): In the design B the containment of the shielding water is assured by a stainless steel spherical vessel, with variable thickness from the bottom (3.0 cm) to the top (2.5 cm). Its radius is fixed at 6.75m, to allow a water buffer large enough to shield the steel radioactivity.

The external vessel works also as support for the ~1650 PMT's which are mounted within the sphere, 0.5m far from the internal surface. A smaller distance from the centre of the detector assures a better light collection coverage, while the PMT's radioactivity is shielded enough by the reduced water buffer. The photomultiplier supports consist of hollow cylinders which cross the sphere steel. At the internal side an acrylic window is

mounted to assure the optical contact; it supports the reflector which is conceived as a barrel, 0.5m long (see Chapter VIII). A conceptual design of the external vessel, which includes also the stress analysis, is summarised in the Appendix Ia.

External shielding: The external shielding is installed as shown in Fig. 6.1; it is formed by a vaulted roof laid on four side walls, with an access door. It consists of blocks of sulfurcrete, 1m thick. Two mechanical solutions have been studied and they are presented in the Appedix Ia. In the two bottom sides of the detector two escaping tunnels in the external shielding are planned (Appendix Ia).

Auxiliary systems: The TMB, when produced in the plant, is immediately stocked in 16 steel tanks, ~7m height and 2.4m of diameter, which are transported to the Gran Sasso and placed one upon another. The pseudocumene is stocked in one similar tank and both the liquid are mixed in a proper device to produce the scintillator and before they will be sent in the inner vessel through a filling apparatus. The stock tanks, connected each to other, represent also a backup vessel which can be used if the internal vessel has to be discharged for some reasons. A system is also installed, which cleans-up the Gran Sasso water and fills the vessel. This system provides also a continuous purification of the water, avoiding also impurities due to biological activity (Appendix Ia).

Chapter VII

THE LIQUID SCINTILLATOR

7.1 *Scintillation Properties*

The most important properties of the scintillator for the Borexino experiment are the light yield and the bulk absorption, besides obviously its possibility of radioimpurity cleaning up.The timing of the light response and the pulse shape discrimination properties (PSD) (i.e. the ability to discriminate alpha vs electron) are additional characteristics of vital importance, the former because it mainly determines the spatial resolution achievable in the detector, the latter since it provides a powerful technique to tag and remove a large fraction of non correlated background events.The activity of R&D on the scintillator, carried out in collaboration with Bicron Corporation, has demonstrated that it is largely possible to fullfill the requirements of the experiment.

7.1.1 *Typical composition, physical/chemical properties*

All the liquid scintillators evaluated during the R&D phase are based on a pseudocumene and trimethylborate (TMB) mixture with the TMB at the two concentrations levels of 80% and 90% by volume. Two primary scintillation fluors, butyl-PBD and PPO are included at two concentrations. The purpose of these components is to

enhance the light yield.The concentration of the wavelength shifter, bis-MSB, has been incorporated at the fixed level of 0.2 g/l. It provides the shifting of the wavelength of the scintillation light towards the blue region of the visible spectrum, where the maximum sensitivity of the tubes is located. In most of the samples naphthalene, at two concentrations levels, has been included to increase PSD properties.The chemical and physical properties of the TMB, a compound with ~10% of boron content, and of the

Table 7.I TMB and Pseudocumene: chemical and physical properties

	TMB	PC
Formula	$B(OCH_3)_3$	$C_6H_3(CH_3)_3$
Molecular weight	103.92	120.20
Boron Content	10.3 wt%	
Color and form	Colorless clear liquid	Colorless clear liquid
Specific gravity	0.926 (25 C)	0.889 (-44 C)
Kinematic Viscosity	0.3cs (25 C)	
Melting point	-29 C	-44 C
Boiling point	68.7 C	168 C
Flash point	28 C	48 C
Moisture sensitivity	high	insensitive

pseudocumene, a standard aromatic liquid scintillator, are reported in Table 7.I. In Table 7.II the nine mixtures taken into consideration and tested, are listed.

7.1.2 *Photon yields*

The light yield of all the mixtures was evaluated.

The results reported in Table 7.III show that at least some of them exhibit a photon yield high enough (>5000 ph/MeV) to satisfy the minimum requirements for Borexino operation.

Table 7.II Typical compositions

A-1 6 g/l b-PBD 0.2 g/l bis-MSB 10% v/v Pseudo 90% v/v TMB	A-2 6 g/l b-PBD 0.2 g/l bis-MSBB 20% v/v Pseudo 80% v/v TMB	
B-1 6 g/l b-PBD 0.2 g/l bis-MSB 30 g/l Naphthalene 7% v/v Pseudo 90% v/v TMB	B-2 6 g/l b-PBD 0.2 g/l bis-Msb 30 g/l Naphthalene 17% v/v Pseudo 80% v/v TMB	B-3 6 g/l b-PBD 0.2 g/l bis-MSB 50 g/l Naphthalene 15% v/v Pseudo 80% v/v TMB
C-1 12 g/l b-PBD 0.2 g/l bis-MSB 30 g/l Naphthalene 7% v/v Pseudo 90% v/v TMB	C-2 12 g/l b-PBD 0.2 g/l bis-MSB 50 g/l Naphthalene 15% v/v Pseudo 80% v/v TMB	
D-1 6 g/l PPO 0.2 g/l bis-MSB 30 g/l Naphthalene 7% v/v Pseudo 90% v/v TMB	D-2 12 g/l PPO 0.2 g/l bis-MSB 30 g/l Naphthalene 17% v/v Pseudo 80% v/v TMB	

7.1.3 *Timing*

The time profile of the scintillation light pulse has been studied using a time correlated single photon counting technique, allowing statistical sampling and reconstruction of the decaying multiesponential tail of the scintillator response. Measurements were performed using gamma rays and alpha excitation, to study both timing and pulse shape discrimination properties. For reference purpose measurements taken on the mixtures D2

for both excitation are reported in fig. 7.1. Details on the measurements carried out on all the mixtures and on the analysis carried out on the results to evaluate the capability

Table 7.III Scintillation light yield

Scintillator sample	Light Output (%) Anthracene	Scintillation Photon/MeV
A1	20%	2941
A2	35%	5147
B1	26%	3824
B2	40%	5882
B3	42%	6176
C1	25%	3676
C2	41%	6029
D1	24%	3529
D2	33%	4853
Anthracene	100%	14706

in identifying the alpha particles are described in the Chapter X and in the Appendix III. From this analysis it emerges that it is possible to identify three exponential components in the decaying tail of the scintillator. The first of these, the so called fast component, that practically is the only one determining the timing features of the scintillator, is virtually independent from the type of excitation, as theoretically expected, and ranges from a minimum of 2.4 ns to a maximum of 3.8 ns. The span of the measured values of this parameter is well within the range required for the feasibility of the experiment.

7.1.4 *Pulse shape discrimination*

The well known pulse shape discrimination properties of the liquid organic scintillators is related to the different excitation and ionisation processes induced in the liquid by heavy ionising particles, like alphas, with respect to those typically produced by electrons. As widely illustrated in the literature [7.1], this difference produces two

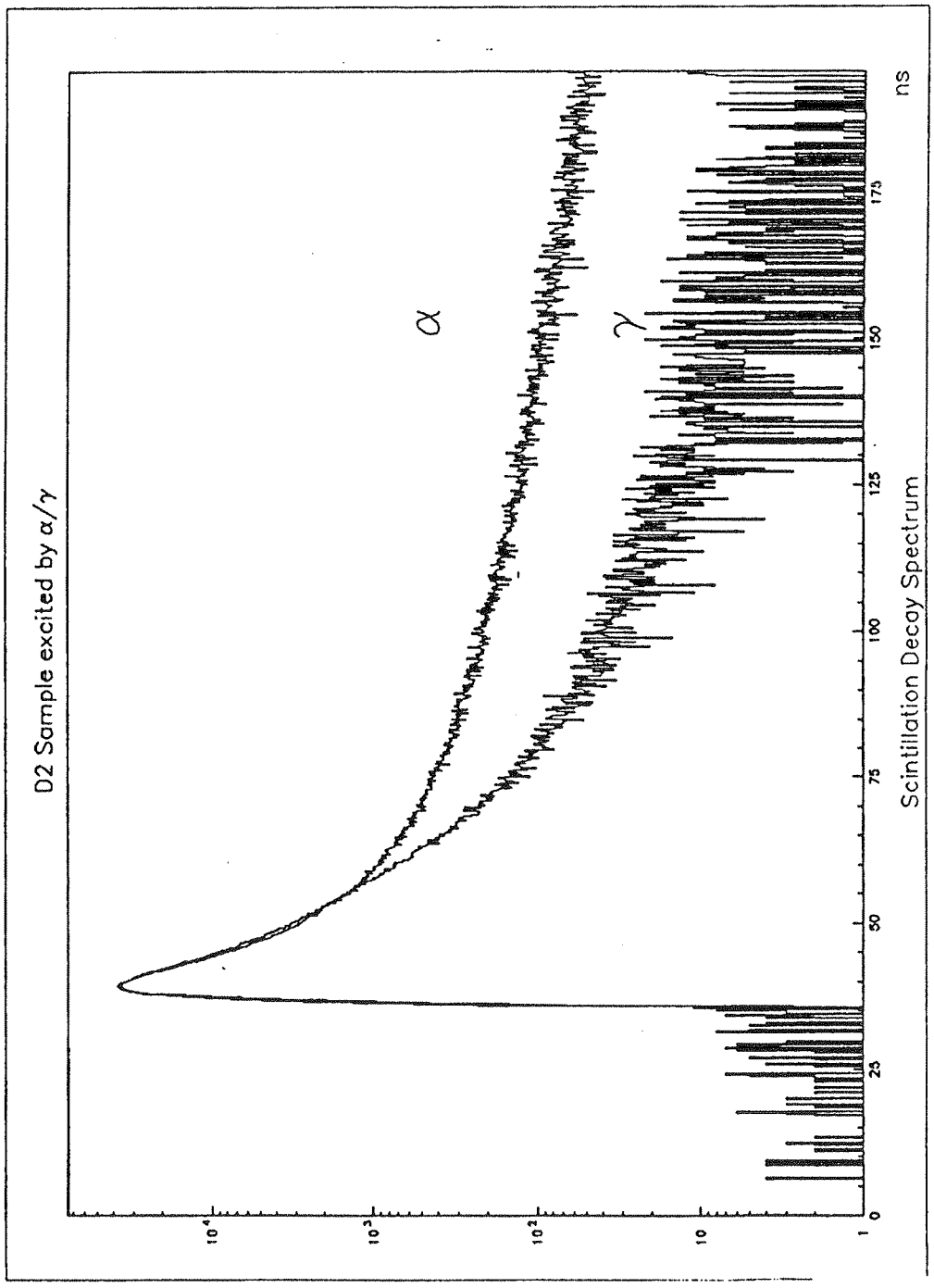

Figure 7.1 Time profile of the scintillation light for the D2 mixture excited by α and γ.

effects closely related each other: first, the total amount of light released for unitary energy deposit is smaller for an alpha than an electron (this effect is often related as alpha quenching), and second the light emitted in the delayed long decay components of the scintillation pulse is proportionally higher for alphas than for electrons.This latter feature is clearly visible in the experimental curves reported in fig. 7.1, where measurements taken with alpha and gamma excitation are overlapped, after normalization at the peak. The higher delayed alpha induced tail is strongly evident from this figure. The level of alpha vs electron discrimination achievable with these scintillators is described in §10.4 and in the Appendix III.

7.1.5 *Light quenching for heavily ionising particles*

In the literature the quenching factor is usually assumed to be 1/10 [7.1], that

Table 7.IV Alpha quenching

Nuclide Uranium series	Alpha Energy (Mev)	Effective Alpha Energy (MeV)
U-238	4.2	0.18
U-234	4.75	0.25
Th-230	4.65	0.22
Ra-226	4.8	0.25
Rn-222	5.5	0.35
Po-218	6.0	0.40
Po-214	6.9	0.55
Po-210	5.3	0.32
Thorium series		
Th-232	4.0	0.18
Th-228	5.4	0.34
Ra-224	5.55	0.35
Rn-220	6.29	0.42
Po-216	6.78	0.54
Bi-212	6.1	0.41
Po-212	8.8	0.9

practically means that an alpha is supposed to produce as much light as that originated by an electron whose energy is ten times smaller. However, it must be pointed out that this effect is not constant but exhibits a not neglible dependence on the alpha energy: the quenching factor (expressed as the ratio of the effective to the true energy) is an increasing function of the alpha energy. Direct measurements on the scintillators, which will be used in Borexino, are not yet available, but some reasonable guess can be derived from published data related to similar organic liquid scintillators. For this purpose in Table 7.IV the data desumed from [7.2], related to the NE 213 liquid scintillator, are reported.

These data concern the quenching of the alpha particles emitted from radioisotopes in the U and Th series, i.e. those actually producing most of the background events in the detector. From these data it emerges that the quenching factor strongly increases from an initial value of about 1/23 for the lowest energy alpha up to about 1/10 for the highest energy one. Direct measurements of the light quenching are now in progress at various energies ranging from 4 to 9 MeV.

Table 7.V Optical properties

	L [m]	A [m]	n
TMB	60	25	1.37
PC	13	8	1.53
TMB(80%)+PC(20%)	23	14.5	1.41
WATER	230	60	1.34

7.2 *Optical properties*

The most important optical parameters which can influence the light propagation inside the liquid scintillator and the light collection have been measured. The obtained values for pure TMB, pure Pseudocumene and a mixture of them (~ 80 % TMB + 20 % PC) are reported in Table 7.V. First column lists the scattering mean free path L (meters) and the second one the absorption length A (meters) and the third one the refraction index n. All these values refer to a wavelength of 420-430 nm, i.e. that corresponding to th light

emitted by the scintillator.

The attenuation length in TMB was observed for many months and little deterioration was observed in the optical trasparency of this fluid. Fig. 7.2 shows these results.

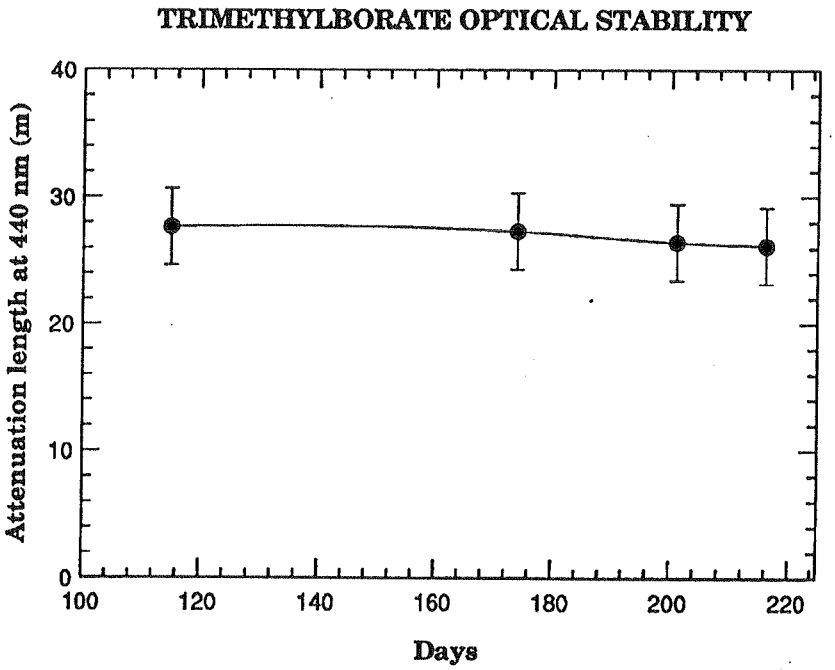

Fig. 7.2 Stability in time of TMB attenuation length.

References

[7.1] J.B. Birks, "The Theory and Practice of Scintillation Counting", Pergamon Press, 1964

[7.2] V.V. Verbinski et al., "Calibration of an Organic Scintillator for Neutron Spectroscopy", Nucl. Instr. and Meth. 65 (1968) 8 - 25

Chapter VIII

SIGNAL DETECTION

8.1 *General frame*

In Borexino the detection of the signal produced by the liquid scintillator is assured by about 1650 PMTs, which are installed 6.25 m far from the centre of the detector (see Chapter VI). The PMTs are coupled with reflectors, which work as light guide; they assure a total coverage for the light collection of about 50%.

A big effort has been made to choose the photomultiplier. The selection has been carried out taking into account PMTs already on the market and prototypes still in developing phase, in strict collaboration with various manufacturers. Extended test measurements have been done: on the 8" Thorn Emi 9351 and Hamamatsu R4558; on the 9" Philips XP1082; on the 10.4" Burle C83061E; on the 20" Hamamatsu R1449, R3600, R1449Z. Various parameters were analysed with special attention to those which are expected to have an important impact on the Borexino performances (see §8.2).

The choice of the photomultiplier allowed our collaboration to order the glass bulbs to the Schott enterprise and then to use for them the special glass 8246, which presents a very good radiopurity level (see Chapter VI).

8.2 *Guideline parameters adopted for the tube selection*

The thorough analysis of the impact of the tube characteristics on the overall detector performances has leaded to the identifications of eleven parameters significantly affecting

the operation of Borexino. Six of them are considered of high priority, while the remaining five are of minor importance. In the following the two groups of parameters are listed, with some comment regarding their role in the frame of the experimental environment.

a) Low priority parameters

1 - Maximum achievable gain

The maximum attainable gain is important since it is one of the factors concurrently limiting the detector sensitivity.

2 - Typical dependence of gain vs. high voltage

This functional relation leads to the coarse identification of the voltage range for which the tubes work at the operating gain of 10^7. It is important, for the reliable operation of the tubes, that such a gain be achievable with a not too high value of the applied voltage.

3 - Anode pulse rise time, fall time and FWHM

The design of the trigger system depends upon these parameters. A fast, narrow output pulse with limited rise time, processed by a fast trigger electronics, is such to produce a precisely timed trigger signal.

4 - Photocathode and anode uniformity

The uniform anode and photocathode responses to single spot excitation is not important in the Borexino operation. However they are a valuable indication of the quality of the tube since they reflect the degree of accuracy in the deposit of the photocathode layer and in the realisation of the input optic stage.

5 - Maximum non destructing vibration level

The maximum vibration level (at 15 Hz) a tube is able to tolerate is an indication of its global reliability, and is important anyway for an experiment expected to run during several years.

b) High priority parameters

1 - Photocathode quantum efficiency

The quantum efficiency value, in particular at 420 nm where the scintillation light is sharply peaked, determines the main features of the detector. Indeed the spatial resolution, the time resolution and the signal threshold rely critically on this parameter.

2 - Single photoelectron transit time spread

This characteristic influences directly the spatial resolution in the event reconstruction, and also the overall uncertainty in the definition of the fiducial volume.

3 - Pre and late pulsing

Pre and late pulsing are the numerical quantification of the transit time deviation from an ideal gaussian shape. It must be pointed out that pronounced non gaussian tails can affect negatively the possibility, provided by the pulse shape discrimination properties of the scintillator, to distinguish e^- and alpha induced signals.

4 - Afterpulses

Afterpulses as well can limit the achievement of acceptable performances for e^- and alpha identification, because they can mimic the delayed signals expected from alpha particles. Since the possibility to identify e^- vs α is based on the pulse shape analysis within the time region 50 - 500 ns (see Chapter X), the presence of afterpulses in this interval is of high importance.

5 - Dark count rate

The dark count rate determines the minimum number of coincident tubes, chosen for the threshold definition, that can keep within a reasonable limit the random trigger rate. Moreover, it can also contribute to reduce the percentage of alphas identification, since the random anode dark pulses, if too numerous, would destroy the different timing patterns of electron and alpha signals.

6 - Single photoelectron pulse height resolution

A well defined peak in the single electron response is useful, since it assures a precise threshold setting and a careful stability control of the tube performances during the detector's operation.

8.3 *Choice of the Thorn Emi 9351*

The comparative evaluation of the candidate tubes, based upon the parameters listed above, has been carried out by measuring samples of the different photomultipliers and by comparing the minimum guaranteed values as specified by the manufacturers.

These two concurrent evaluations have leaded to the selection of the Thorn Emi 9351.

The direct measurements performed by members of the collaboration, in particular, have demonstrated that this tube is the best for what concerns the dark noise rate, the afterpulsing, and the pre and late pulsing, while the width of the transit time distribution is at the same level of the Burle and Philips tubes (that of the 8" and 20" Hamamatsu tubes is slightly larger). Furthermore, the pulse height resolution of the single electron

response is very good, inferior to the excellent one featured by the Burle thank to the high gain gallium phosphide first dynode, but superior to those of the remaining phototubes.

Among the other parameters for which only the specifications provided by the manufacturers have been assumed as reference, it is remarkable the value of the quantum efficiency, typically as high as 30% at the peak wavelength, the highest among the PMTs taken into account. Moreover, the tube shows a remarkable performance for the maximum non destructing vibration level, slightly less than the Philips but better than the others. For the remaining parameters all the devices are at the same level.

The results of the magnetic field sensitivity test, described later and more in detail in the Appendix IV, have shown that, even though this tube is affected by an external magnetic field more than the Hamamatsu and the Philips ones, a limited suppression factor of the order of five of the Earth's field is enough to virtually avoid significant degradation of its performances. Finally, also cost considerations have been taken into account in the choice. The Thorn Emi phototube represents the best trade off between price and performances. In this Chapter the main performances of the selected tube are presented and discussed.

8.4 *General features of the Thorn Emi 9351*

The photocathode of this semi-hemispherical tube has a radius of curvature of approximately 11 cm, a minimum useful photocathode diameter of 19 cm, and thus a minimum projected photocathode area of 280.3 cm^2. The half angle subtended by the curved photocathode is about 72 degrees. The weight of the whole tube is around 900 g, of which 800 g is glass. The photocathode material is of the bialkali type (CsKSb), characterised by the highest yield in the blue region of the visible spectrum. The linear focussed multiplier consists of 12 dynodes. The emissive surface of the dynodes is of the same type of that of the photocathode.

8.4.1 *Quantum efficiency*

The typical dependence of the quantum efficiency vs. wavelength as provided by the

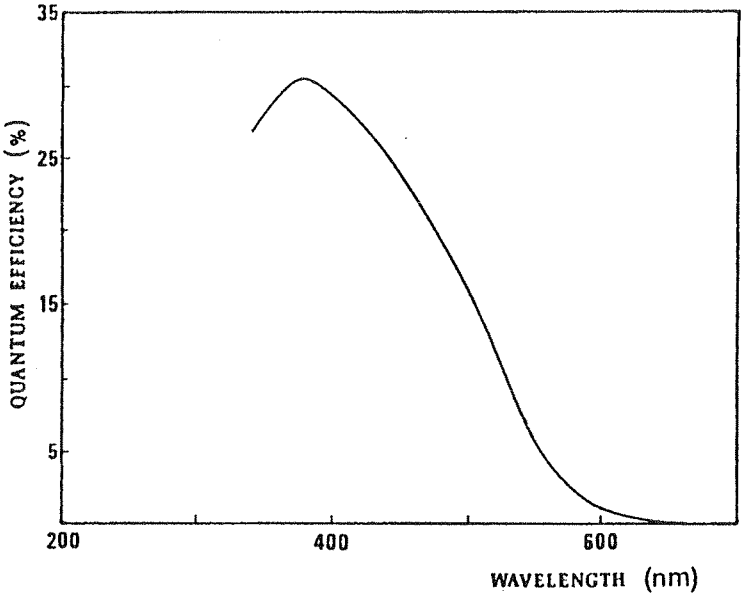

Figure 8.1. Typical plot of quantum efficiency vs. wavelength for the tube Thorn Emi 9351

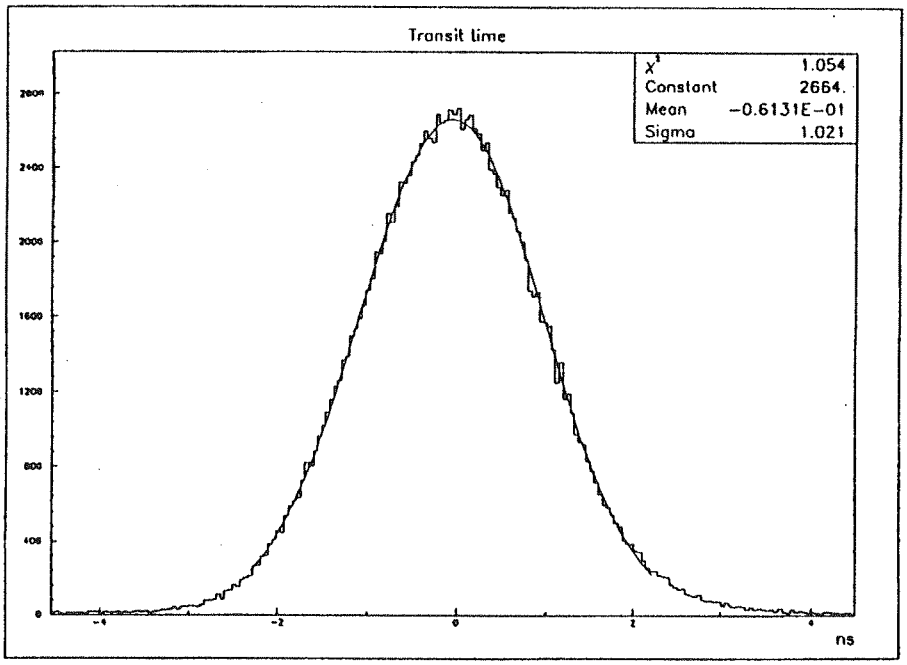

Figure 8.2. Transit time distribution of the tube serial number 1020

manufacturer is reported in fig. 8.1. From this figure it emerges clearly the high value of this parameter, that can attain a peak value as high as 30%.

8.4.2 *Single photoelectron transit time spread*

The transit time spread measurements have been carried out with an experimental set-

Table 8.I Transit time spread (σ) of the three samples of the Thorn Emi 9351 tube.

Serial number	WIDTH
1020	1.02 ns
1021	0.99 ns
1022	1.10 ns

up based on a Hamamatsu PLP-01 picosecond light pulsar, emitting light at a wavelength of 410 nm. In Appendix IV the experimental details are thoroughly reported. The measurements have been done for single photon and full photocathode illumination conditions.

Three samples of the tubes have been tested, obtaining similar results. For reference purpose the measured transit time distribution of one of them is shown in fig. 8.2. In Table 8.I the widths of all the three distributions are listed. The width of the experimental curve is the sigma of the gaussian fitted on the central portion of the curve itself. The estimated uncertainty on these measures is of the order of 0.05 ns.

These results clearly show that the Thorn Emi 9351 tube has a very low transit time spread.

Table 8.II Pre and late pulsing occurrence for the Thorn Emi 9351

Serial number	Pre pulsing	Late pulsing
1020	0.5%	1.3%
1021	0.3%	1.7%
1022	0.6%	1.2%

Figure 8.3. Pre and late pulsing of the tube serial number 1020

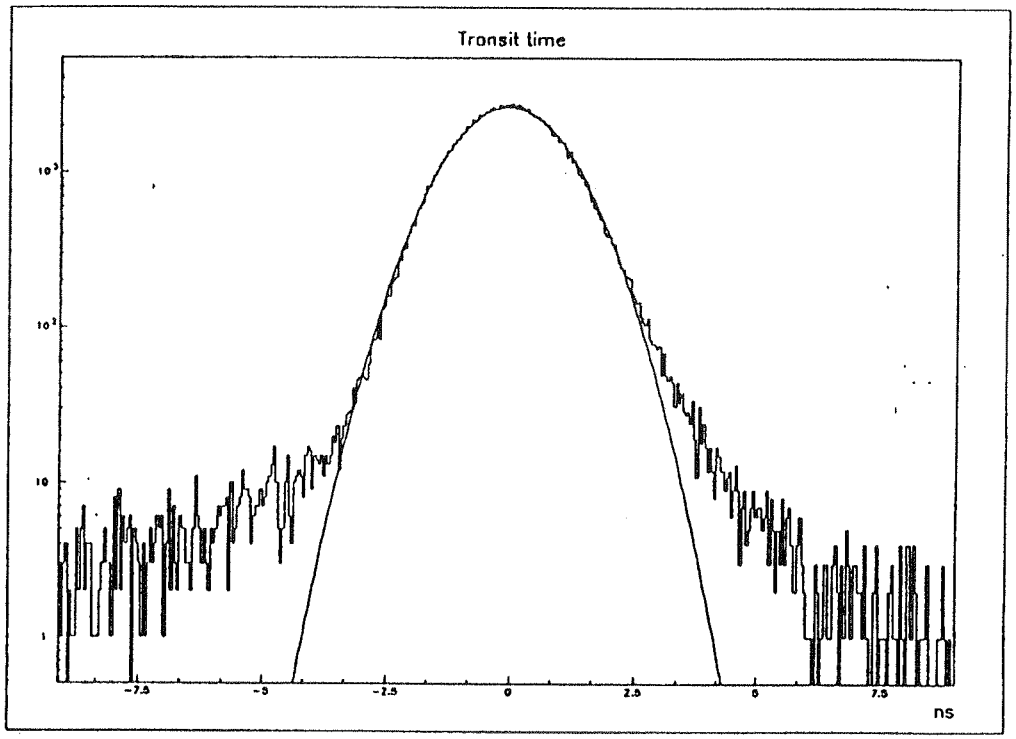

8.4.3 *Pre and late pulsing*

The three measured distributions have been analysed to derive the degree of deviation from an ideal gaussian shape, numerically expressed by pre and late pulsing. From the log plot of the distribution already shown in fig. 8.2 the right and left tails appear to be very limited (see fig. 8.3). The pre and late pulsing are expressed as the ratio between the total number of extra counts in the tails, (the differences between the counts in the tails of the experimental distribution and that in the best fitted gaussian) and the counts in the $\pm$ 3 σ region of the fitted gaussian. The span of the tail ranges is conventionally assumed equal to 20 σ;their starting points coincide with the instants where the experimental curve begins to deviate from the fitted gaussian. This evaluation is carried out after the background estimation and subtraction. The result of the analysis for the three measured tubes is summarised in

Table 8.II.These data demonstrate the excellent gaussian like tails of the transit time distribution of the selected tube.

Table 8.III Afterpulse of the Thorn Emi 9351

Time interval	4ns - 30 ns	30 ns - 100 ns	4 ns - 900 ns	50 ns - 3 μs
Afterpulsing prob.	2.9 ± 0.1%	0.15 ± 0.02%	3 ± 0.1%	0.4 ± 0.1%

8.4.4 *Afterpulses*

Afterpulsing analysis has been done in four time intervals, after the main pulse, ranging from 4 ns to 30 ns, from 30 ns to 100 ns, from 4 ns to 900 ns, and from 50 ns to 3 μs. The results are in the Table 8.III. The measurements concern afterpulses following single photoelectron main pulses, with a threshold at 0.1 pe. It is worthwhile to remind that the probability of afterpulses occurrence is an increasing function of the size of the main pulse. These measurements show the good performances of the tube regarding this parameter.

Table 8.IV Results of the single electron response measurements carried out on three different tube samples. P/V is the peak to valley ratio of the single electron response distribution. The width in the third column is the ratio between σ and the mean value of the best fit gaussian.

Serial number	P/V	WIDTH
1020	2.2	39.4%
1021	2.8	39.8%
1022	2.3	51.4%

8.4.5 *Dark counts*

The measurements of the dark noise rate performed on two tube samples, at an ambient temperature of about 20 °C have given very low results (counting rates in the

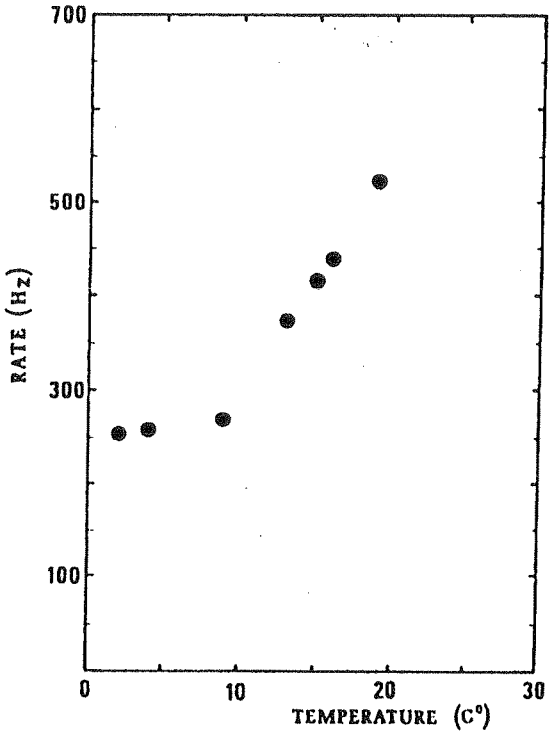

Figure 8.4. Dependence of the dark count rate vs. temperature.

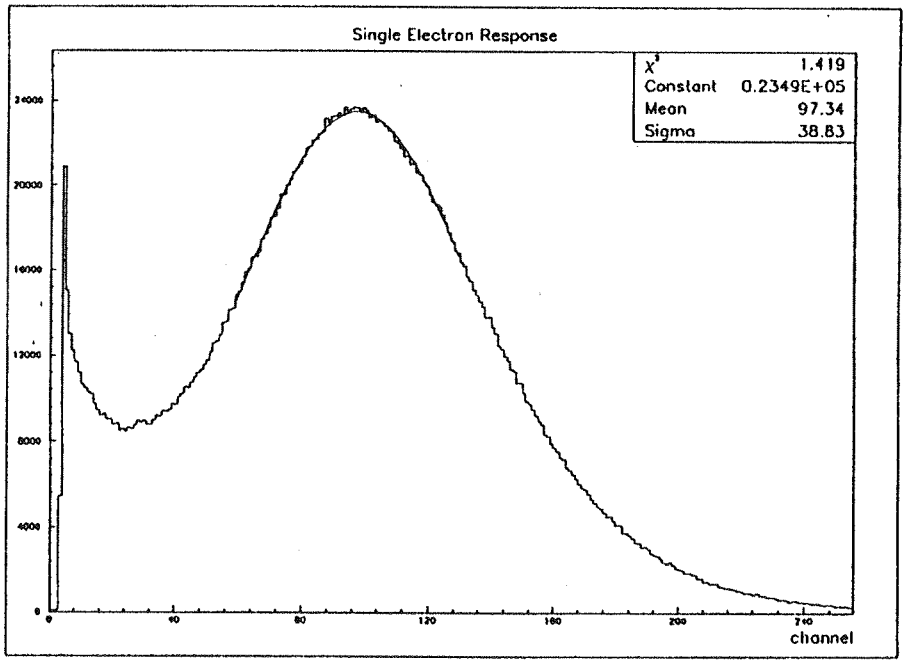

Figure 8.5. Single photoelectron response of the tube serial number 1021

interval 650 - 700 Hz). The tests were carried out with a discriminator threshold set at 0.2 pe, and after more than a week of operation in complete darkness. Such values are surely low enough to not interfere with the detector's operation. Nevertheless, a third tube sample has been measured at several temperatures, to test the dark rate dependence on the temperature. A dramatic reduction of the noise rate can be achieved by decreasing of few degrees the working temperature of the photomultipliers (see fig. 8.4).

8.4.6 *Single electron response*

The tube features an excellent pulse height resolution of the single electron response (see fig. 8.5). The results of the measurements done on three tube samples are summarised in the Table 8.IV.

8.5 *Magnetic field sensitivity*

In order to understand the degree of shielding needed to avoid effects of the Earth's magnetic field on the tube operation, magnetic field sensitivity tests have been performed. To this purpose a tube sample has been exposed to a field generated by a double set of Helmoltz coils, whose direction was set by turns parallel to the three main axis of the tube. The axis directions are defined in fig. 8.6. The single electron responses for an applied field of 500 mG are shown in figs. 8.7, 8.8 and 8.9. While for field directions parallel to the x and z axis the impact on the single electron response is practically negligible, for y axis the degradation of the distribution is evident. However, if such a field is reduced to 100 mG its influences becomes negligible (see fig. 8.10).

Similar conclusions can be desumed if we study the influence of the field on the transit time curves. Indeed, while the transit time does not show appreciable effects when the field direction is parallel to the x and z axis, the width of the distribution measured for a 500 mG field parallel to the y axis is degraded of 20% (1.2 ns against 1 ns obtained with zero field) and its overall shape is distorted (fig. 8.11). Nevertheless, in this case as well the influence on the distribution is negligible if the field is reduced to 100 mG.

Finally, in fig. 8.12 the relative count rate variation for applied fields parallel to the

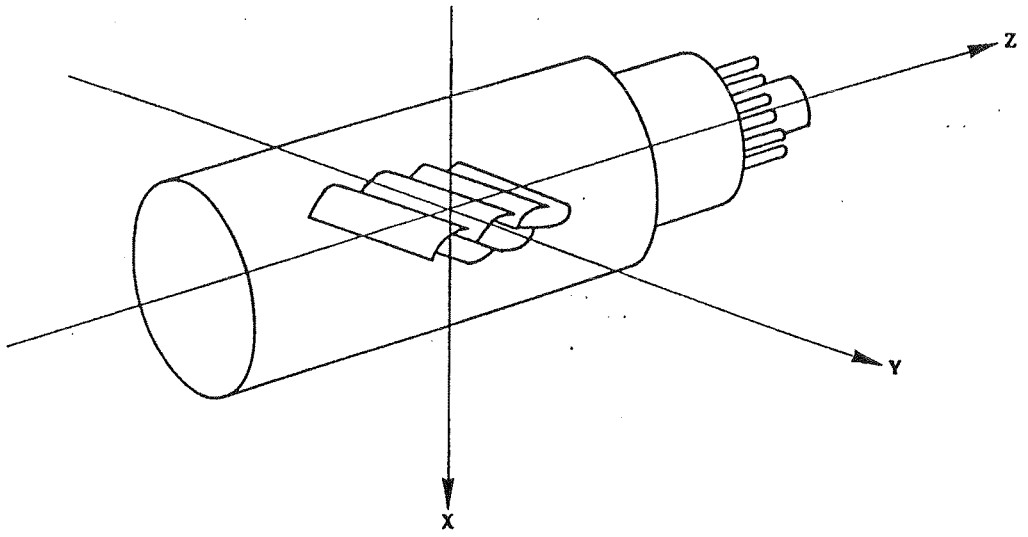

Figure 8.6. Definition of the x, y and z axis for a phototube with linear focussed dynode chain.

three axis, with values ranging from 0 to 500 mG, is reported. For the more sensitive y axis the observed variation is of about 50%, while for the other two the count rate drop is much less pronounced. The curves in this figure show that the loss in counting rate is very limited for field values not exceeding 100 mG. Hence the comparison of all these results points out that below 100 mG the impact of the magnetic field on the performances of the tube is virtually negligible. Thus a suppression factor of the Earth's magnetic field of the order of five is enough to avoid any kind of detectable malfunction.

8.6 Light reflectors

In the detector assembly the photomultipliers will be located at a distance from the centre of 6.25 m. Thus, considering the ratio between the total cathode area and the surface of the sphere whose radius is 6.25 m, it comes out that the physical coverage assured by the cathodes alone is around 10%. Reflectors coupled with the PMTs increase the effective coverage up to 50% (see fig. 8.13 and Appendices Ia and Ib).

The conceptual design of the reflector, whose optimisation has been performed

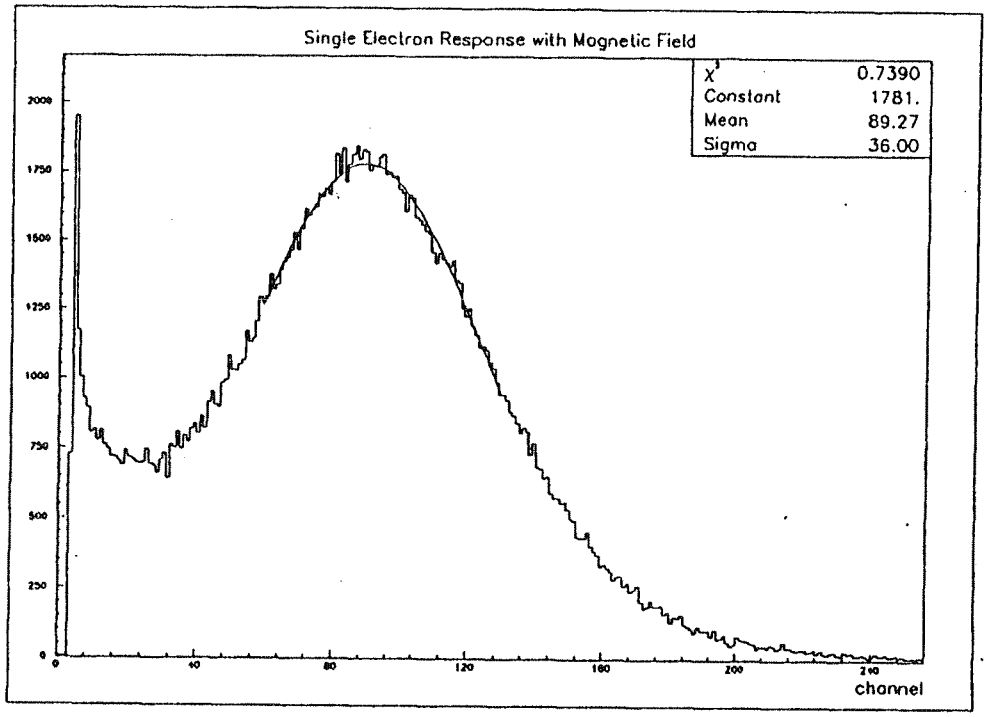

Figure 8.7. Single electron response of tube for an applied magnetic field al 500 mG parallel to the x axis.

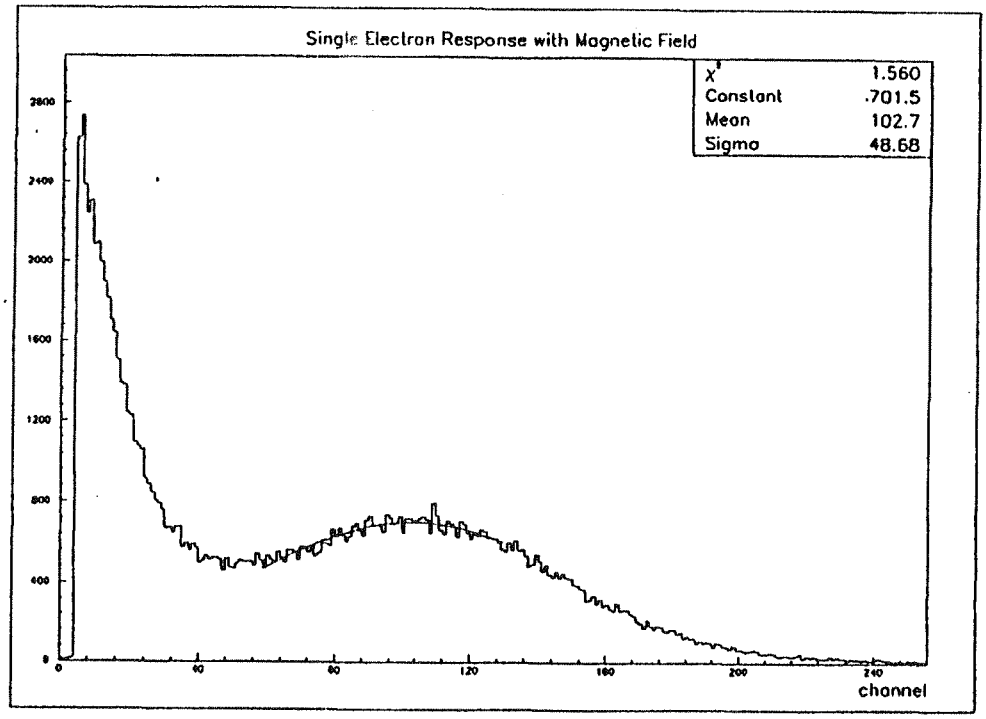

Figure 8.8. Single photoelectron response of the tube for an applied magnetic field of 500 mG parallel to the y axis.

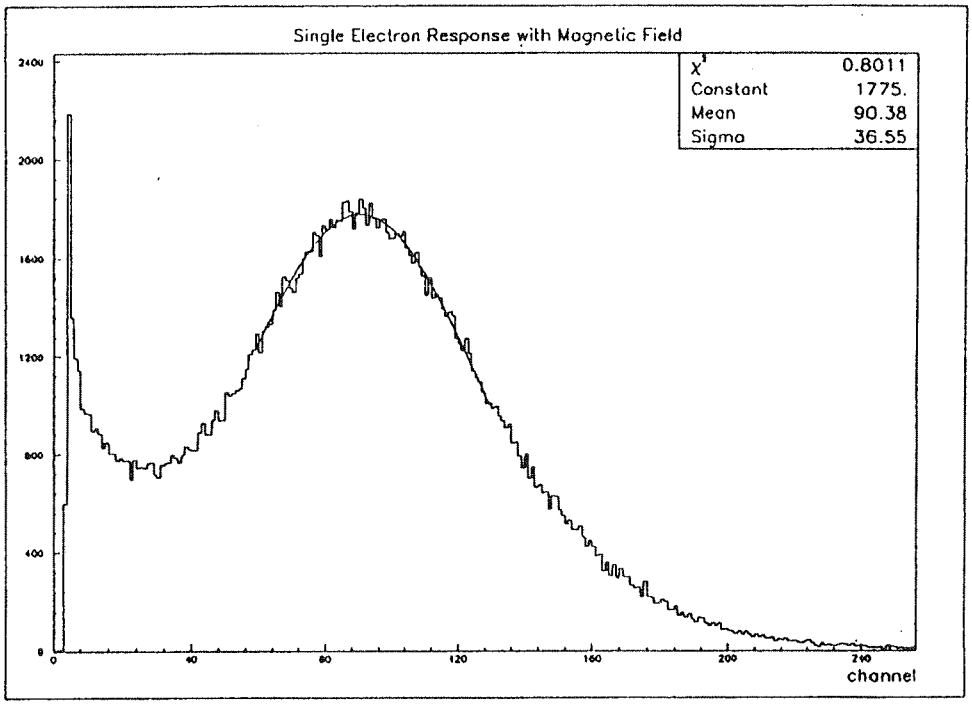

Figure 8.9. Single photoelectron response of the tube for an applied magnetic field of 500 mG parallel to the z axis.

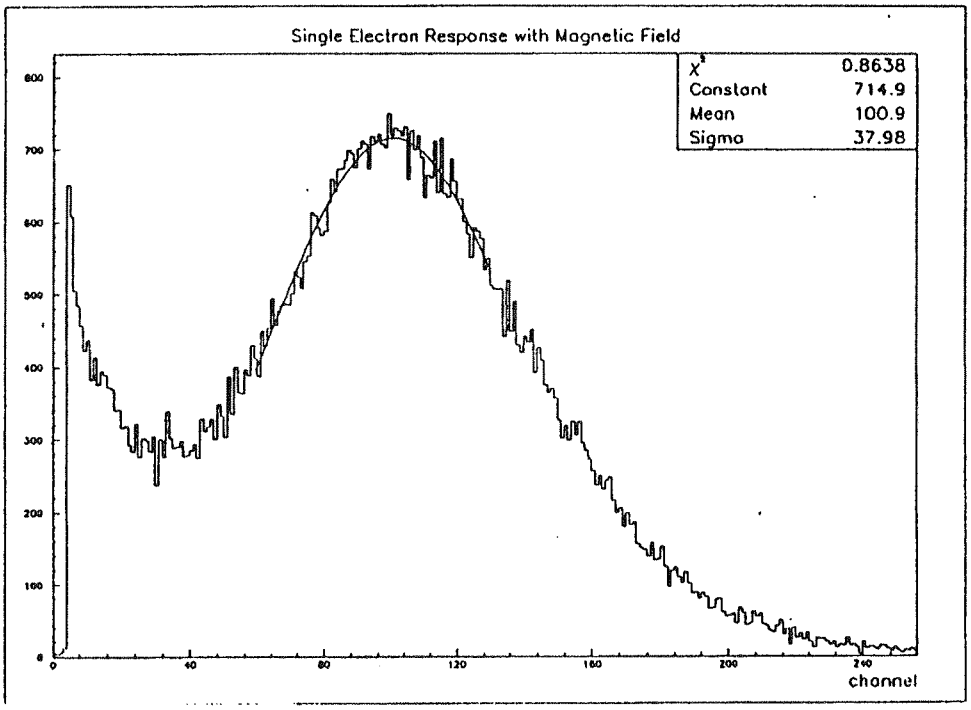

Figure 8.10. Single photoelectron response of the tube for an applied field of 100 mG parallel to the y axis.

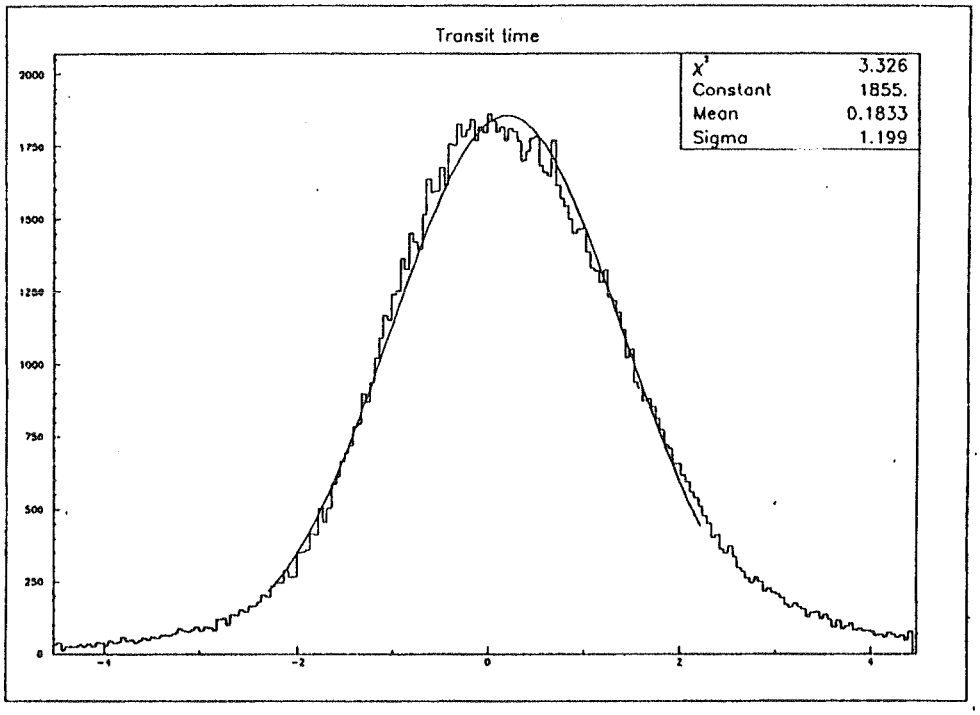

Figure 8.11. Transit time spread for an applied magnetic field of 500 mG parallel to the y axis.

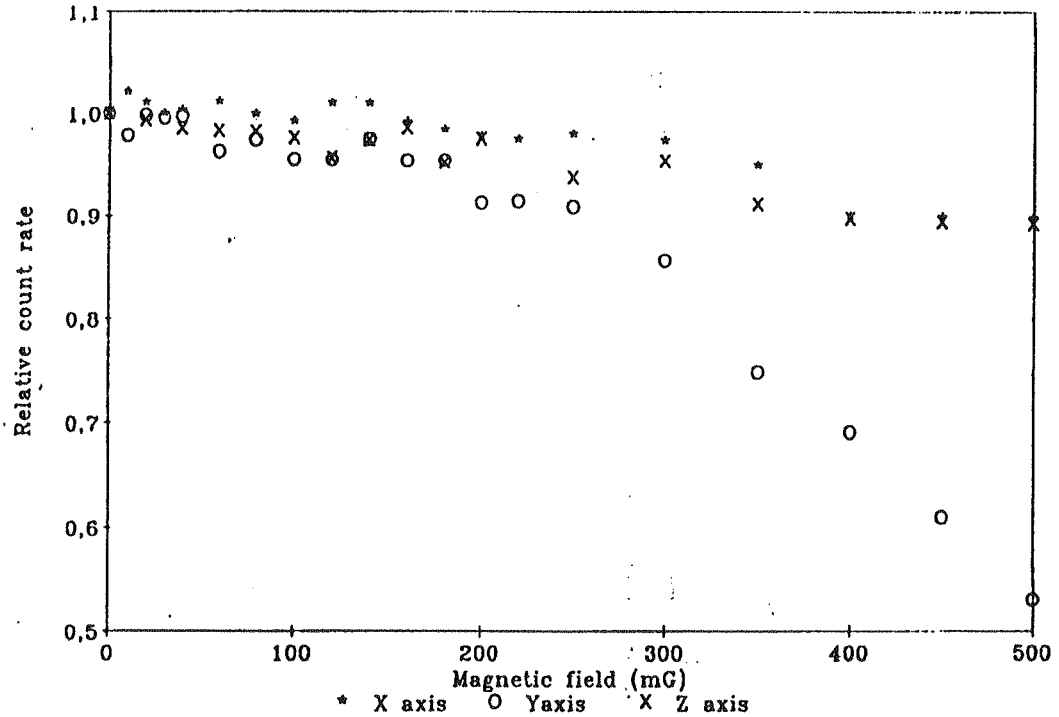

Figure 8.12. Relative counting rate variation as function of an applied magnetic field.

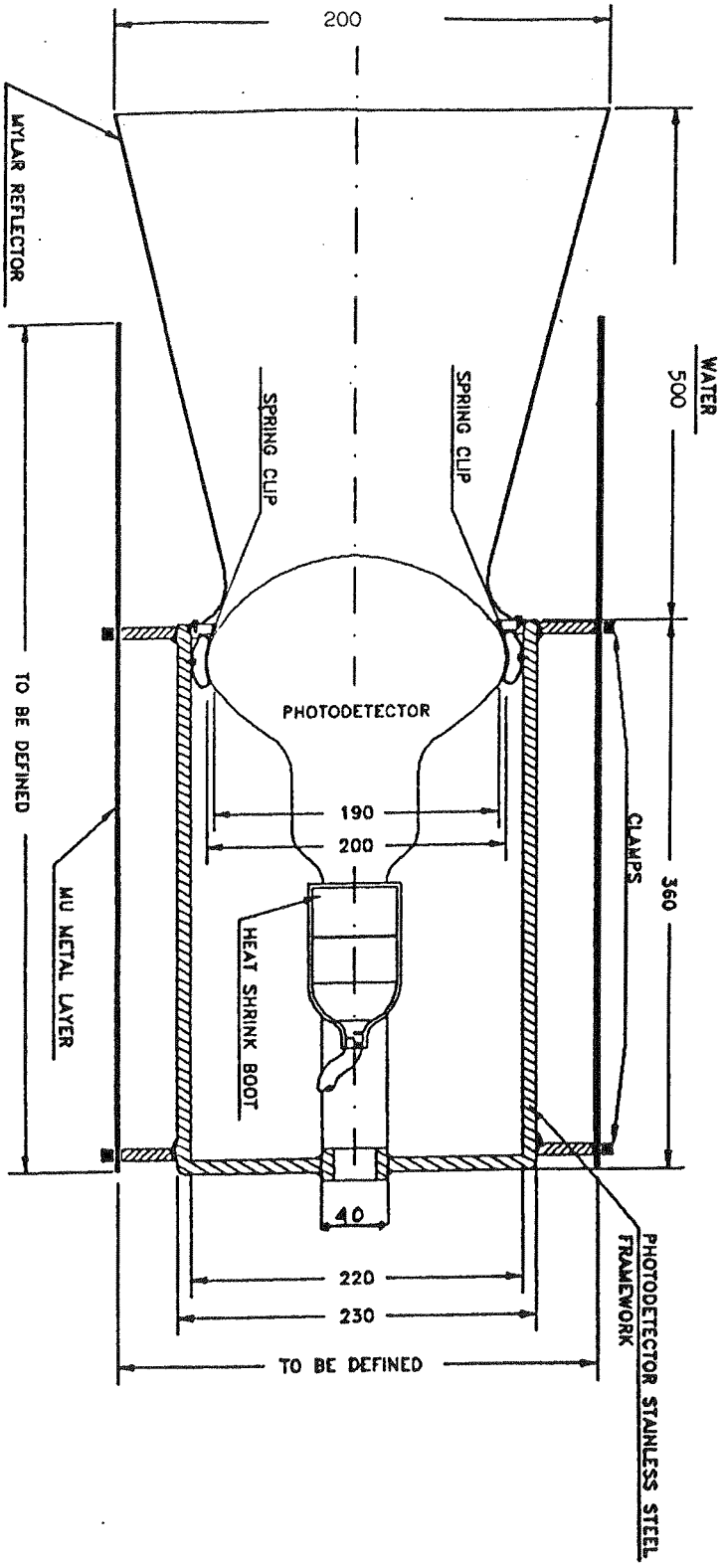

Figure 8.13. Preliminary design of the reflector-PMT coupling (dimensions are in mm)

through a detailed calculation described in the Appendix V, is based on three alternative geometries: parabolic, half barrel and cone. In all cases the radius of the exit surface is 9.5 cm, to match the photocathode active area; that of entrance surface is 2.1 times larger, i.e. around 20 cm, and the length is 50 cm.

Although an engineering design for this component is still not available, however it is very likely that its actual implementation will be done evaporating a thin aluminum reflective layer onto a mylar substrate. A thin protective coating deposited on the aluminium layer must be foreseen, to prevent the attack of the ionpure water to the reflecting surface.

Chapter IX

FRONT-END AND READ-OUT ELECTRONICS

9.1 *Introduction*

In the previous sections we have described the backgrounds that have to be kept under control. Together with the requirement of high purity for the liquid scintillator and the materials employed we also have a strategy to *monitor* the activity of the radioactive chains of ^{238}U and ^{232}Th. Examples of the delayed coincidences may be classified in time ranges as follows

Isotopes	type	half life	chain	classification
^{212}Bi - ^{212}Po	β–α	300 ns	^{232}Th	fast
^{214}Bi - ^{214}Po	β–α	160 μs	^{238}U	medium
^{220}Rn - ^{216}Po	α–α	150 ms	^{232}Th	slow

The delayed coincidences indicated in the Table, although very important, are only representative of the different time scales foreseen. For example the antineutrino detection capability of BOREXINO is based on an e–α delayed coincidence with half life of approximately 1μs. This coincidences is to be classified as fast (see Chapter II).

In the following sections we present the lines along which the Borexino readout system has been designed and we will show that a solution exists for each of the class of coincidences indicated. The problem of the delayed coincidences has been emphasised here because they set fundamental contraints to the final design of the read-out system. There are however other aspects of the system that have to be kept in mind:

– Energy measurement: this is basically achieved by counting the number N of PMTs

hits. In the energy range of interest, the probability of multiple hits on the same PMT is negligible and the resolution of the energy measurement is given by the Poisson distribution of N.

- The position is reconstructed using the time of arrival of each detected photon. Given the limitations of the PMT transit time jitter and the scintillator decay time, the timing error introduced by the read-out system can be of the order of 0.5 ns. This figure includes both the threshold time jitter due to the discriminator and the digitiser error.
- For an easy and stable operation of the detector the read-out system must contain a *fast* system to monitor the stability of the PMT gain/threshold.

9.2 *Basic Electronics Considerations*

Front end electronics. The Borexino PMTs will work in the *single electron counting* mode. As a consequence very low pulse height are foreseen at the anode output and the use of a fast amplifier is planned. The amplifier is followed by a discriminator. The block diagram of the front end electronic is shown in fig. 9.1.

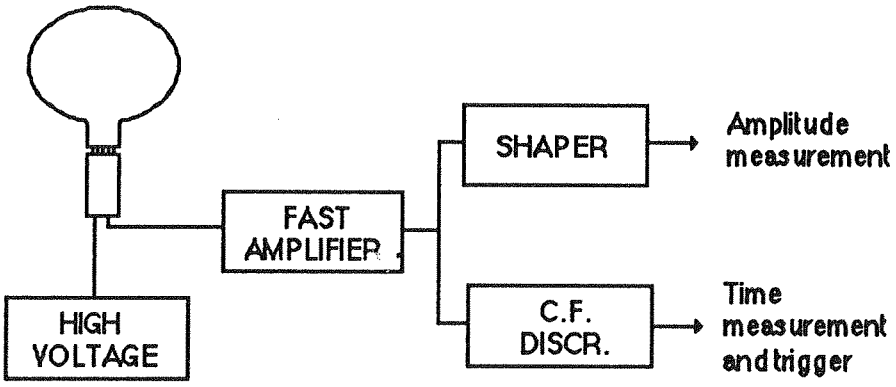

Figure 9.1 Front end Electronics

At the present stage of the project we have not yet decided whether to use a *constant fraction discriminator* or a simple *threshold discriminator*. The overall requirement is that the amplifier/discriminator component introduces a time jitter less than ~ 0.3 ns. For the threshold monitoring, an *amplitude measurement* section of the system is foreseen; later in this section a possible solution based on FADC will be discussed; in order to use a medium speed FADC, a shaper will provide the signal time stretching needed.

Trigger. Borexino consists of approximately 1650 photomultipliers. A typical event

will consist of several *simultaneous* signals (of the order of 30 for a 200 keV electron) from the PMTs. The concept of simultaneity needs some explanation: since the position of the event is randomly distributed within the detector, the time of arrival of the photons to the different PMTs will be different (this difference allows the position measurement). Another source of time spread is due to the decay time of the scintillator light for events consisting of α particles.

Signals from different PMTs will be considered *simultaneous* (and will be grouped in an *event*) if they occurs within a time window ΔT_{sim} . As an indication we can assume ΔT_{sim} = 50 ns. To trigger the read-out we will require that at least *n* (of the order of 10) PMTs give simultaneous signals. The simplified timing of the trigger and readout is shown in fig. 9.2. Upon arrival of a trigger, the pulse timing and the pulse amplitude of all the hits within a time window ΔT_{rec} are recorded; each hit will have a precise time of arrival measurement *within* the recording window: they will be grouped as *an event* in the offline analysis.

The measurements relative to single hits within the window can be implemented to be almost deadtimeless and the system dead time can be concentrated at the end of this window where the transfer to a *large capacity* event buffer takes place. Recording to a

Figure 9.2 Timing Outline of the Trigger, Measurement and Fast data transfer Aspects

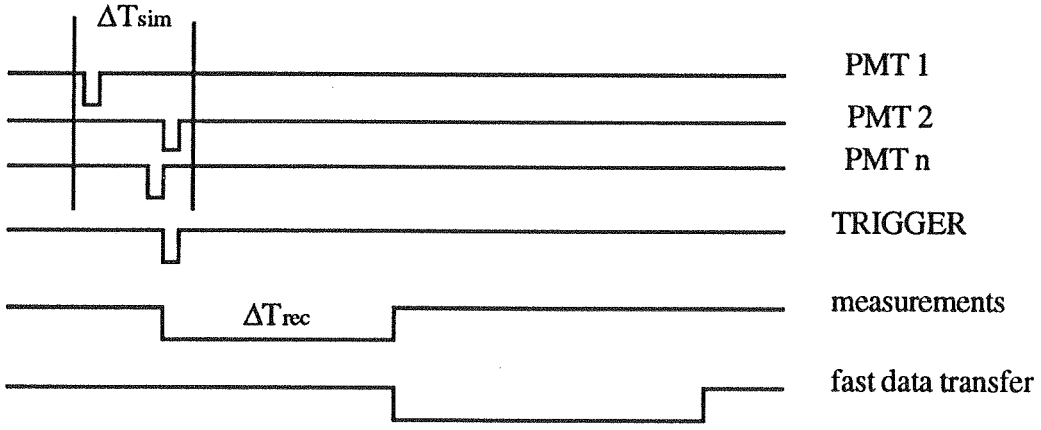

permanent storage will be done by the computer DAQ in an asynchronous way with

respect to the trigger.

The length of the window ΔT_{rec} must be determined having in mind the *fast* delayed coincidences: since at the end of the recording window the *slower* process of data transfer to an event buffer takes place, the window ΔT_{rec} must be long enough to provide the maximum efficiency for the delayed coincidences of interest, let us say 4 - 5 times the half life of longest lived process classified as *fast*. For the processes mentioned in the introduction, we obtain 1.5μs for the ^{212}Bi - ^{212}Po or 5μs for the antineutrino signature.

The data transfer to the event buffer at the end of the ΔT_{rec} window requires some caution. In fact this is the place where the potentially dangerous dead time of the system is located. A too large dead time here could spoil the time correlation capabilities of BOREXINO with respect to the class of *medium* delayed coincidences. To clarify better this point, we consider the time needed for the fast data transfer to an event buffer to have an estimate of the dead time of the system.

The time needed for the data transfer to an event buffer is determined by several factors:

- number of hits recorded: it is given by the sum of the hits due to a true energy release (150 hits for a 1MeV energy release) plus the background hits. Assuming a dark current of 5KHz, 2000 PMTs and a window ΔT_{rec} = 5μs we obtain 50 for the background and 200 for the total number of hits.
- number of words to transfer: this parameter depends on the detailed structure of the time digitiser. For the time being we assume 1 word. If more words per hit will be transferred, we can obtain the same data transfer capabilities implementing some degree of parallelism, if needed.
- speed of the fast data transfer: just to have an order of magnitude we assume 100ns/word having in mind that faster data transfer can be obtained if needed or employing faster electronics or implementing the necessary degree of parallelism in the data transfer.

With the numbers quoted above we obtain 20μs in order to transfer 200 words. This number gives the order of magnitude of the dead time; it can be easily reduced to 10 or 5μs, and we see that this solution is adequate to register with high efficiency also the *medium* delayed coincidences: we see that for the ^{214}Bi - ^{214}Po delayed coincidence (160μs half life) a system dead time of 5μs induces a lost of efficiency of only 2%.

The event buffer will be subsequently read-out by a computer. The asynchronous read-

out of the event buffer solves also the problem of the *slow* delayed coincidences. The efficiency (due to read-out system) on the correlation ^{220}Rn - ^{216}Po will be very high; only at extremely high (unforeseen) trigger rates the system would fail.

Finally few words on the trigger processor itself which is still in design: the basic requirement on the processor is the capability to provide a majority signal in a given time window out of 1650 PMTs. We are evaluating different solutions to choose the more convenient one; anyway this design does not involve basic difficulties.

The time digitiser. The scheme presented in the previous section is based on the assumption that a precise time (as well as amplitude) measurement is possible with virtually no dead time. In this section we will present a possible solution.

Precise time interval measurements are usually done by charging a capacitor with a constant current generator for a time interval defined by a *start* and a *stop* signal. The capacitor is charged and the voltage across it is proportional to the time interval to be measured. The capacitor is then slowly discharged at constant current and the time needed for the discharge is measured; the discharge time is still proportional to the capacitor voltage and also to the charging time interval. This method can be very accurate: slower the discharge, better the accuracy but at the cost of a large dead time.

A very simple and elegant way to implement the time of arrival measurement could be achieved by the use of a very fast counter driven by a clock. Upon arrival of a pulse from a PMT, the current value of the counter could be recorded. The disadvantage of this approach is that very fast electronics is required since we want subnanosecond precision. However recently a very interesting solution (mostly based on counters than on capacitor discharge) for the time measurements has been proposed by Lecroy Corp. We are carefully evaluating this possibility since it seems that, due to use of ASIC technologies, the Lecroy solution could be cost effective.

The method we propose here, similar to the scheme used in a different experiment [9.1], makes use of a technique still based on the charging of a capacitor with a constant current but, to reduce the dead time, the slow discharge is avoided and the voltage across the capacitor is measured by using a flash ADC. The basic idea is illustrated in fig. 9.3. The pulse timing within the recording window is made with a vernier technique. A coarse measurement is based on clock tick counting, the time vernier is carried out with a fast time to amplitude conversion. The time interval between the TRIGGER signal (the trigger) and the HIT signal (the individual PMT signal) is given by

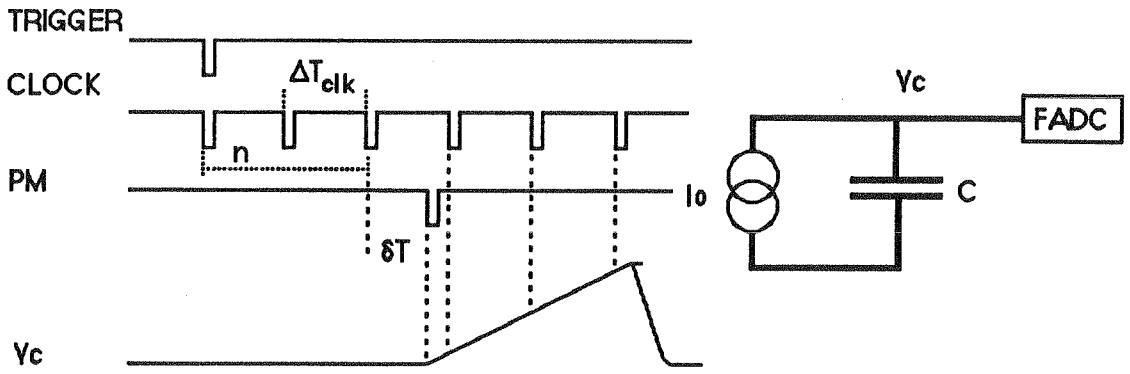

Figure 9.3 Time measurement

$$\Delta T = n\,\Delta T_{clock} + \delta T$$

where n is the number of clock pulses between the TRIGGER and the HIT, ΔT_{clock} is the clock period and δT is the time between the last clock pulse and the HIT (PMT pulse).

The number n can be easily measured with a counter while the time δT can be measured with high precision using the capacitor method. The current generator is started by the PMT signal. The voltage across the capacitor V_c rises for a time of about 75ns, and during this period is continuously sampled by a Flash ADC driven by the same clock, whose period is 32ns. The maximum voltage across the capacitor is given by

$$V_{c\text{-}max} = I_0\ 75\ \text{ns}\ /C.$$

Sampling the voltage ramp with the FADC and evaluating the intercept of this ramp with the baseline allows the measurement of the quantity δT. Using a clock of 32ns and an 8-bit FADC a precision of about 0.5ns can be achieved.

The deadtimeless operation of the system can be achieved by storing the sampled voltage in a fast RAM 8-bit memory. Finally, once the current generator has been stopped, the capacitor can be quickly discharged and the system is ready for a new

measurement; in this way the dead time per channel is 75ns plus only the time needed to reset the voltage across the capacitor at the end of the measurement (~30 - 40ns). Notice that this is the dead time *per channel* and not the *system* dead time since the probability of a multiple hit *on the same channel* is very low. This process can continue for all the duration of the the *recording* window ΔT_{rec} defined in the previous section. The only requirement is that the RAM memory be adequately large.

The other parameter needed for this measurement, the number of clock pulses previously introduced *(n),* can also be recorded in a fast RAM. Once the system is started by the trigger, the number of clock pulses is counted by a binary counter; every time a PMT pulse is detected the current value of the clock pulse number can be transferred to the RAM. The data temporarily stored in the RAM will be transferred to an event buffer at the end of the recording window ΔT_{rec} and later on asynchronously recorded on a permanent storage device. In the previous section we gave an estimate of the dead time assuming 1 word per hit. We see here that with a solution like the one illustrated we end up with a larger number of data per hit: 4 - 5 8-bits samples of the voltage V_c plus one 8-bits word for the clock counter. However with a data bus width of 32 bits we end up with 1.5 words per hit and the orders of magnitude given in the previous section are still valid.

The amplitude measurement. In the introduction we have pointed out that for the events of interest (neutrino interactions or natural radioactivity of the detector) the energy release measurement is easily obtained by counting the number of fired PMTs. There is however at least one other reason that strongly suggests to implement a pulse height measurement for each channel: PMT gain / threshold stability. In fact, since the experiment is a low background experiment, we must foresee a method to monitor the gain of the PMTs and the stability of the threshold that be independent from the data itself. For this reason we propose to use the dark current of the PMT and in particular the position of *single electron peak* or the position of the *valley* to monitor the gain variations of the PMT. The selection of the PMT model for Borexino has been particularly influenced by this criterion (Chapter VIII). The pulse amplitude measurement can be included very easily in the scheme previously described. A timing diagram of the full system is described in fig.9.4. The fast pulse from PMT processed by a shaper (as shown in §9.2) can be sent to another flash ADC. The amplitude measurement can be triggered by the digital signal of the given channel: in this way we can easily correlate the value of the threshold with the noise spectrum of the given PMT monitoring the value/stability of the threshold in a very effective way. The read-out of the FADC can be done in two different ways:

– The sampled voltages can be temporarily stored in a RAM bank and then transferred

to the event buffer together with the time measurements. This mode can be called *normal* data taking and can be useful in case of phenomena with very large energy release (muons for example) such that *multiple* hits on a given PMT occurs with high probability.

– The sampled voltages can be used to fill 256 word *histogram* dedicated to a single channel. This data taking mode can be called *monitoring*. It will allow us to implement a *Multichannel Analyser* for every PMT providing a very fast monitoring of the dark noise of the PMTs: with the foreseen speed of the system *all* the dark noise pulses of the PMTs will be analised and entered in the histogram in real time. The system illustrated is very flexible. It can be used quite easily for every other calibration task together with the dedicated hardware, light sources for example.

Data Acquisition. The system described so far will pose no particular problem for the data acquisition: the event rate foreseen is extremely low and the average event size, as pointed out in the previous section, will be of the order of 1KB. The use of an event buffer will allow to handle quite high *peak rates*, limited only by the transfer speed from the digitizers to the event buffer, making BOREXINO able to record *bursts* of events like neutrinos from stellar collapses without particular requirements on the data acquisition system itself. We plan to use the *CAMAC* standard for all the *slow control* functions like HV control, threshold setting and so on and we will relay on existing DAQ products (CERN, FERMILAB, ...) to build our readout system.

Conclusions. In fig.9.5 a block diagram of the full system is shown. The system as presented could be a reasonable solution for the Borexino electronics. The most critical part of the system is the time digitiser since this is the part where potentially dangerous dead time can come from. The solution proposed should allow to solve the problem of dead time with respect to the delayed coincidences. However interesting proposals come from the industry that open the possibility for a commercial and cost effective solution (at least for the digitiser section).

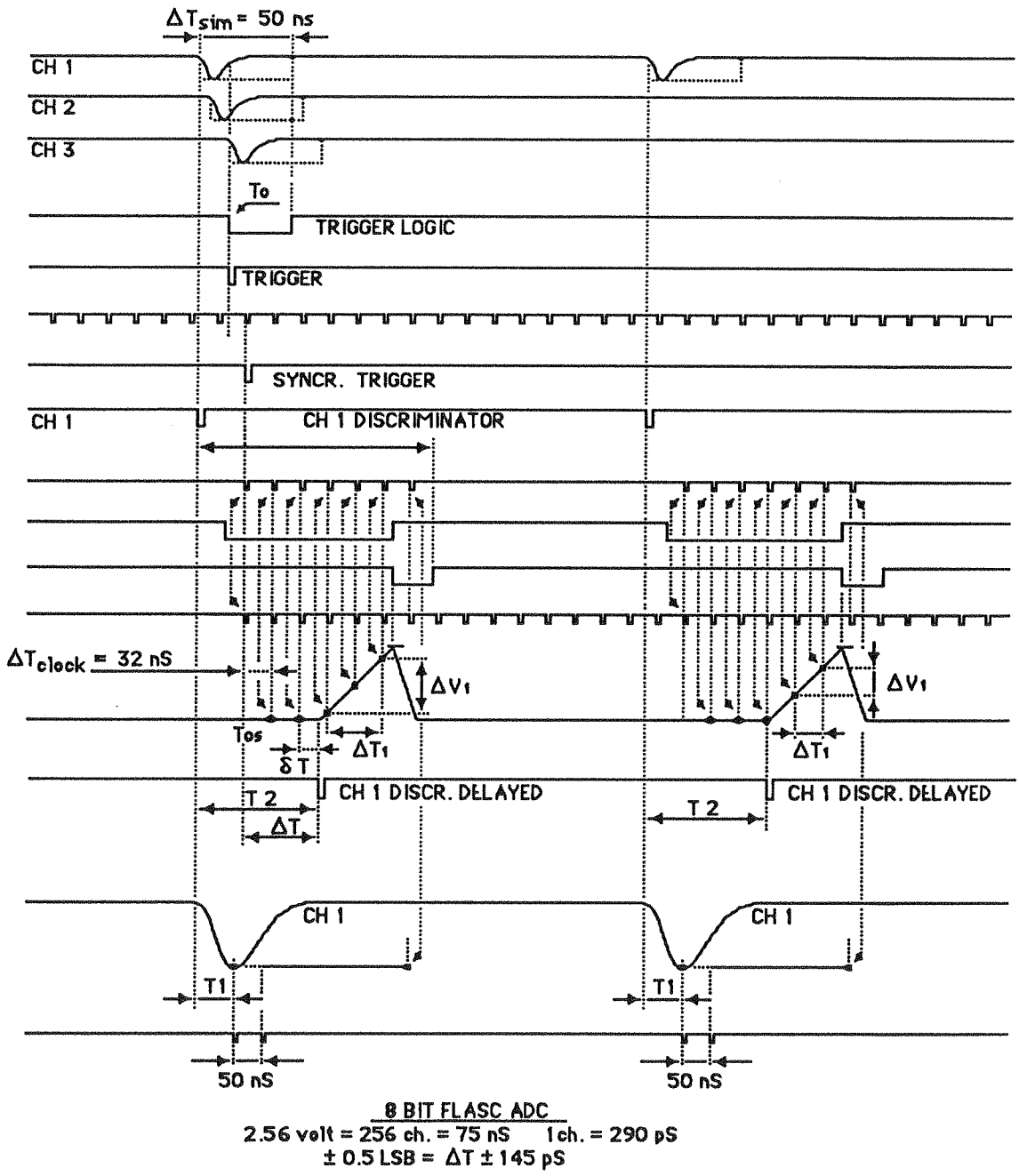

Figure 9.4 Timing diagram for the borexino electronics

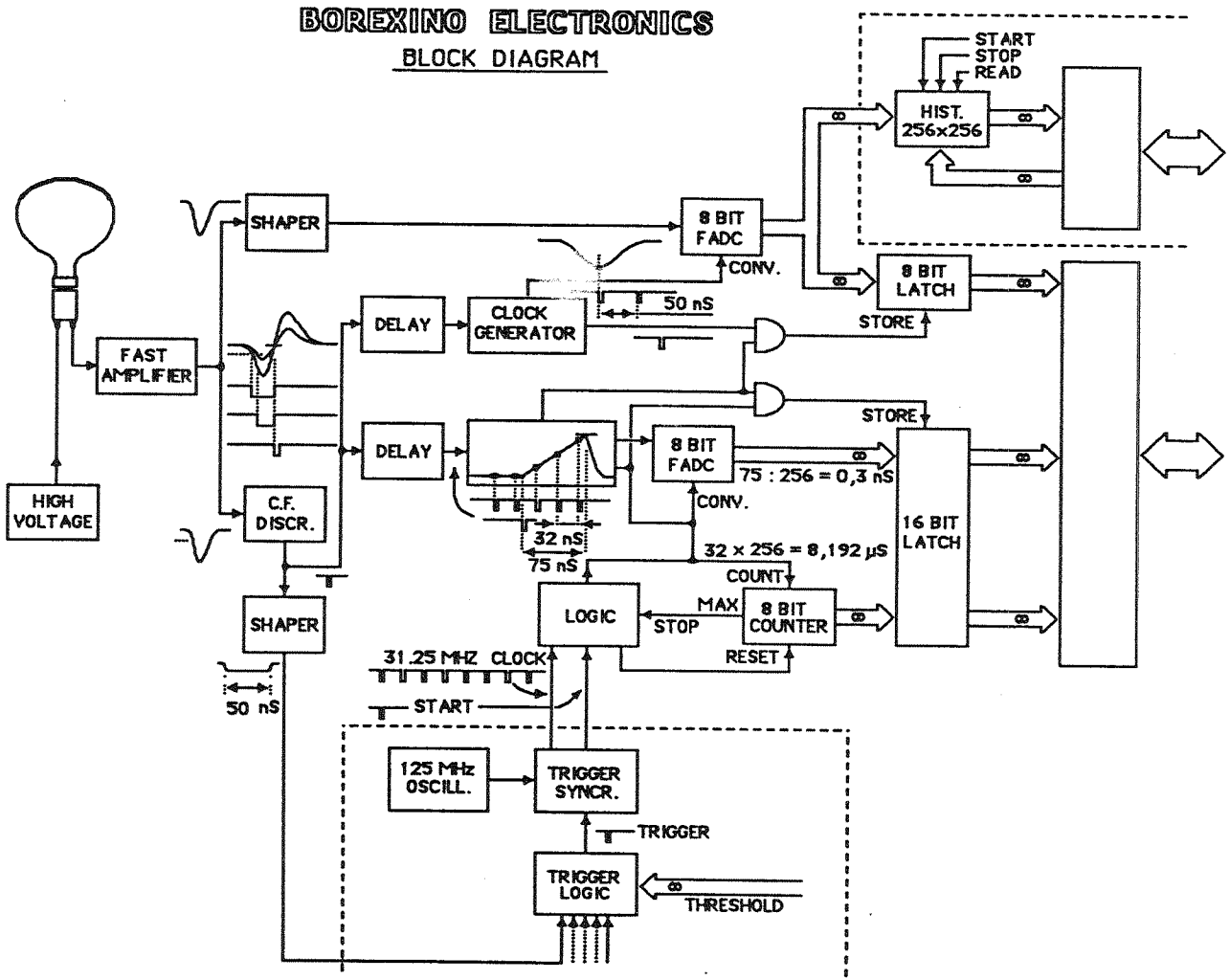

Figure 9.5 Block diagram

References

[9.1] Front end electronics system proposed for a neutrino detector at LAMPF by Vern Sandberg

Chapter X

SIGNAL RESPONSE

10.1 *Event simulation*

The optimization of the parameters of Borexino has been done by means of a very refined simulation code and a full reconstruction program (see Appendix V). The event simulation and processing proceed along the following guidelines. An event produced by charged particles consists of one or more energy deposits. One may consider that the energy deposits are point-sized. (If an energy deposit has extension, one may divide it into smaller parts in such a way that the extension of each part is negligible.) Each energy deposit is characterised by the time when the energy is deposited, by the space coordinates of the energy deposit and by the deposited energy. The energy deposits are processed one by one.

The number of scintillation photons produced by each energy deposit is determined. They are emitted isotropically. Each emitted photon is tracked from the place where it is produced to the place where it is absorbed or detected. The photon may be scattered and absorbed along its path, reflected and refracted on the acrylic wall of the inner vessel. If the photon is detected its contribution to the photomultiplier tube (*PMT*) signals is determined. A detected photon is characterised by the time when it is detected and by the place (*PMT* position) where it is detected (see Appendix V.). Even if the various parameters of the detector are discussed in other Chapters (VI, VII, VIII), we prefer to summarise here (Table 10.I) the parameter values used in the simulation and reconstruction programs.

Table 10.I. Parameters of the event simulation and reconstruction program.

Parameters of the Borexino Detector	
Liquid Scintillator (sample D2 see Table 7.II)	
Refractive index of *TMB* (n)	1.4
Attenuation length	14.5m
Scintillation photon yield	4853 photons/MeV
Light scattering mean free path length	25m
EMI 9351KB Photo Tubes:	
Number of *PMT*'s	1658
PMT photocathode radius (R_1)	0.095m
PMT photocathode curvature (R_2)	0.110m
PMT time jitter (σ)	1ns
PMT quantum efficiency (q)	20%
Practical coefficient	0.6
Parabolal-Shaped Light Guide:	
LG minimum radius ($R_{min}=R_1$)	0.095m
LG maximum radius ($R_{max}=2.1R_{min}$)	0.1995m
LG length	0.5m
LG reflection coefficient	0.9
Detector Dimensions:	
Inner Vessel (*IV*) diameter	8.5m
Fiducial Volume (*FV*) diameter	6m
Distance of *PMT*'s from centrum	6.25m
Distance of *LG* entrance from centrum	5.75m

10.2 *PMT Signals*

The photons produced by an event in the sensitive volume of Borexino generate *PMT* signals. The *PMT* signals provide information on their number and on the times when the *PMT*'s detect the photons (time signals). The time when a *PMT* detects a photon depends:

1) on the time when the photon was produced, 2) on the time of flight of the photon from its birth-place to the *PMT* and 3) on the *PMT* time jitter. The number of detected

photons and the number of *PMT*'s, which give a signal, depend on the deposited energy and on the space coordinates of the energy deposit (Table 10.II). In the simulation the events were uniformly distributed in the fiducial volume of Borexino.

Table 10.II. The number of detected photons and the number of PMT's which give a signal.

Photo electrons and PMT's per event		
Energy (MeV)	p.e./event $\pm \sigma$	PMT's/event $\pm \sigma$
0.05	9.3 ± 3.0	9.3 ± 3.0
0.1	18.8 ± 4.2	18.6 ± 4.2
0.2	36.8 ± 5.8	36.1 ± 5.6
0.5	93.6 ± 9.2	89.4 ± 8.5
1.0	188.2 ± 14.0	171.8 ± 12.1
2.0	375.8 ± 20.3	315.5 ± 16.3
4.0	750.3 ± 30.3	545.5 ± 28.0
5.0	939.0 ± 35.5	639.3 ± 33.4
6.0	1125.0 ± 38.8	723.7 ± 41.4

10.3 *Event Reconstruction*

The space-time coordinates of an event and the deposited energy are reconstructed from the *PMT* signals generated by the event.

1) The space-time coordinates of an event are calculated with the maximum likelihood method from the *PMT* time signals (vertex reconstruction). In fig. 10.1 the Δr vertex error is displayed for 100keV, 500keV, 2MeV and 5MeV point-sized energy deposits, respectively. In fig. 10.2 the errors of the coordinate reconstructions of 500keV electrons are shown. The extended events (showers, muon tracks, ecc) consist of more than one point-sized energy deposits (see §10.1). The event reconstruction program finds the weighted position of the energy deposits of an extended event. The weight of each energy deposit dependence on the deposited energy and on the time when the energy is deposited.

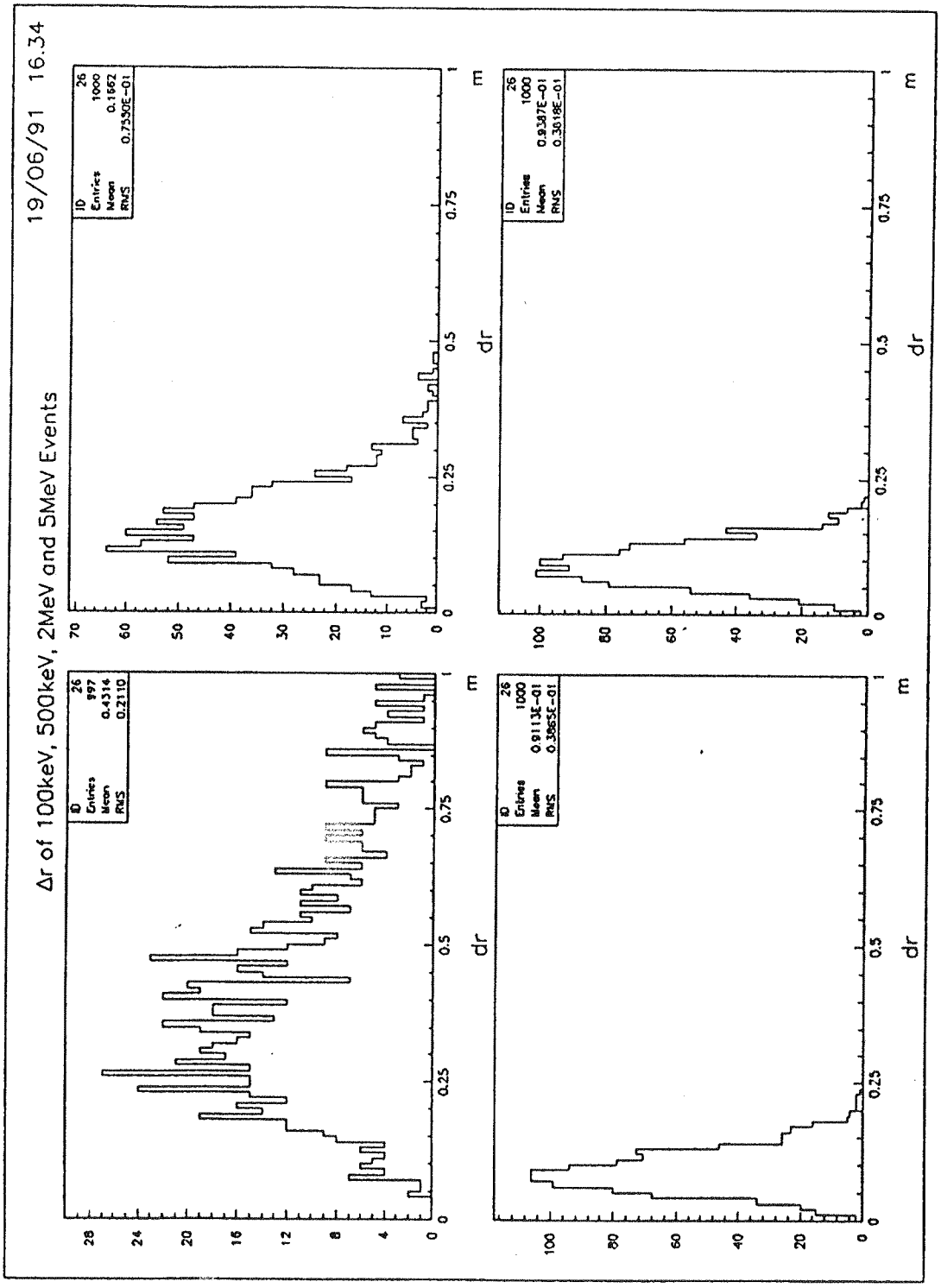

Figure 10.1. The Δr vertex error of the event reconstruction. The 100 keV, 500 keV, 1 MeV and 5 MeV point-sized energy deposits were distributed uniformly in the fiducial volume.

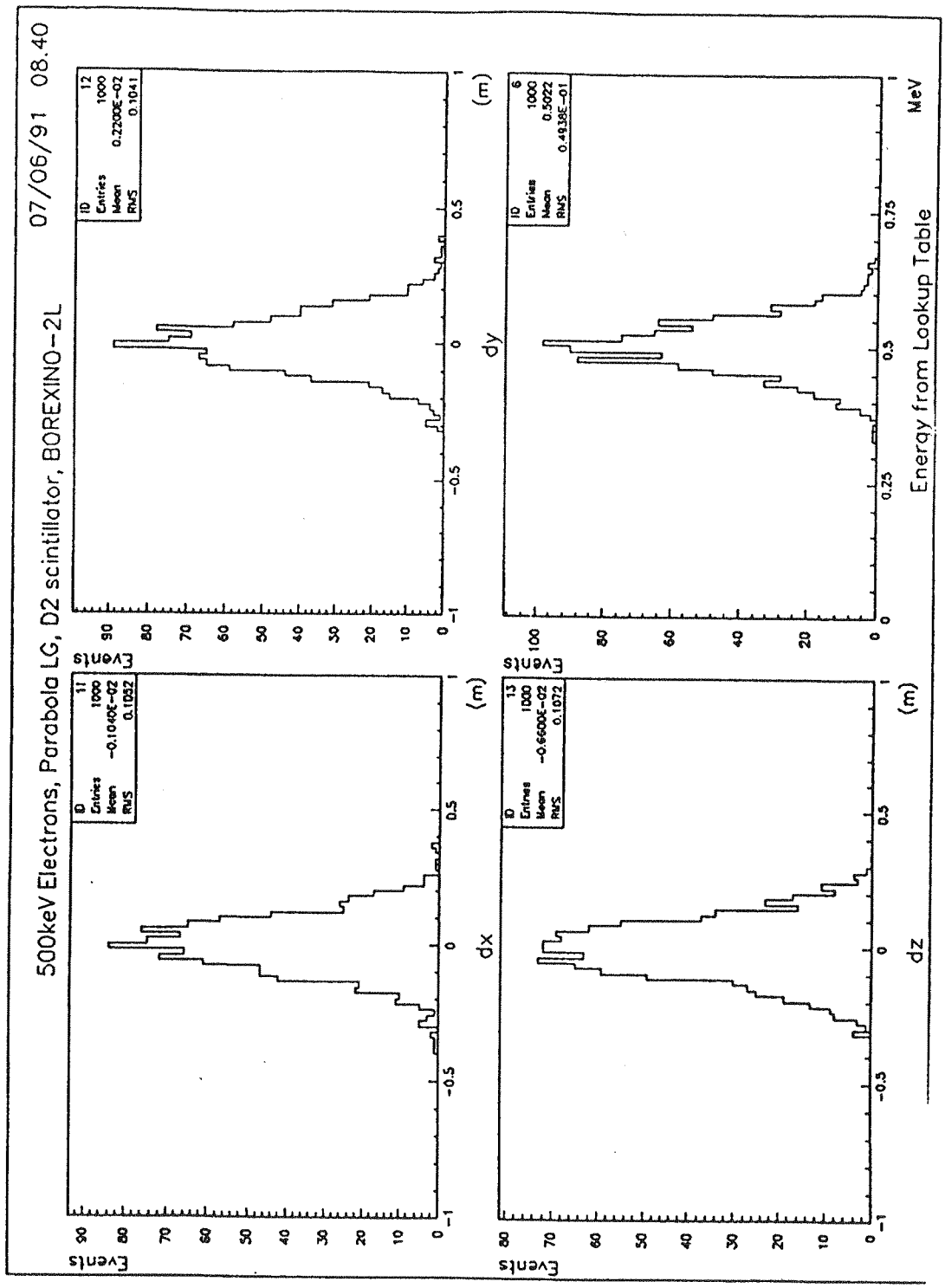

Figure 10.2. Spatial and energy resolution. The 500 keV point-sized energy deposits were distributed uniformly in the fiducial volume.

2) The energy deposit is determined by means of a look-up table. The number of *PMT* pulses depends on the space coordinates of the energy deposits and on the deposited energy:

$$N_{PMT} = f(\vec{r}_e, E),$$

where E is the deposited energy, $\vec{r}_e$ is the space vector of the energy deposit and N_{PMT} is the number of *PMT* pulses.

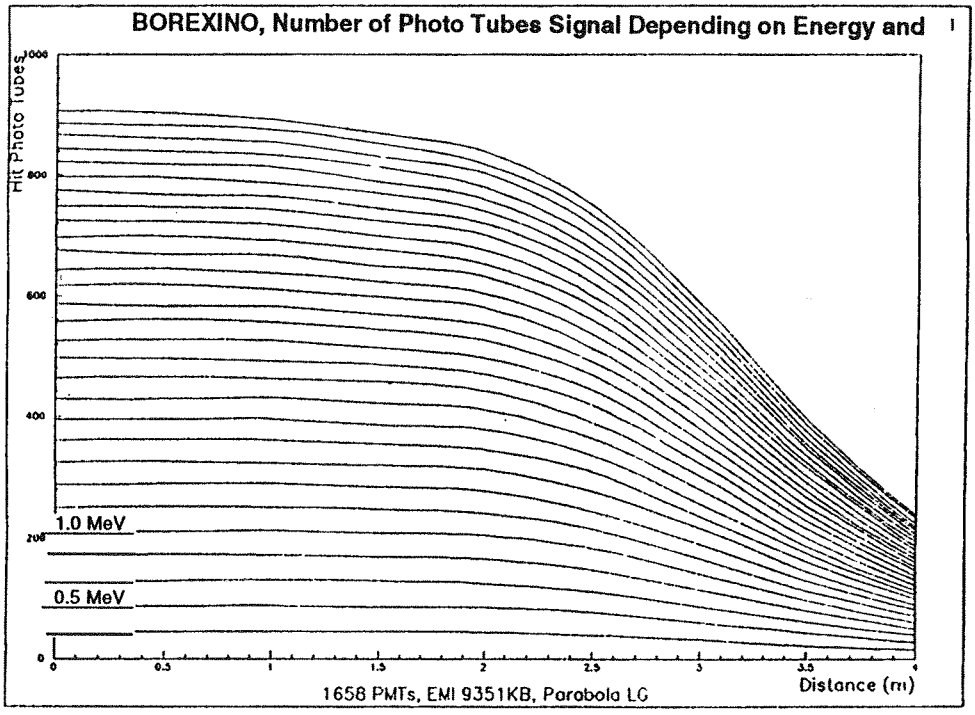

Figure 10.3. Number of hit PMT's vs. the distance between the energy deposit and the detector centre for different energy losses.

One may construct the table

$$E = T(N_{PMT}, \vec{r}_e)$$

(fig. 10.3) and determine the deposited energy knowing the number of *PMT* pulses and the reconstructed space coordinates of the energy deposit. The result of the energy reconstruction is shown in fig. 10.4. The simulated events have deposited 100keV, 500keV, 1MeV and 2MeV energy in the liquid scintillator and they were distributed uniformly in the fiducial volume.

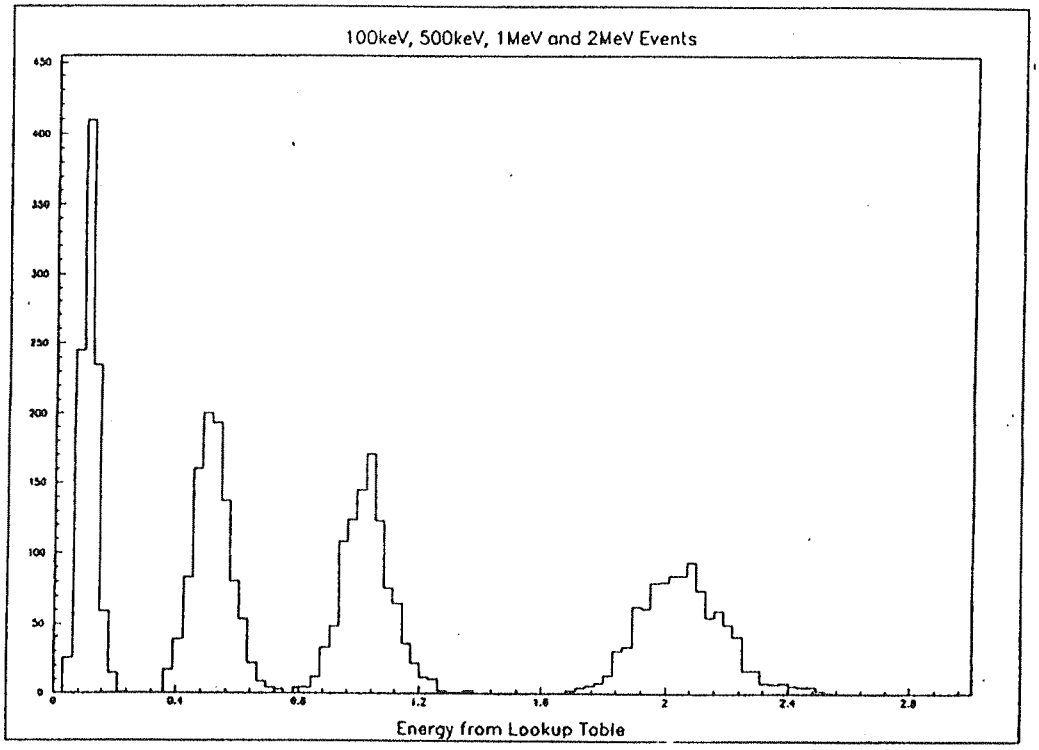

Figure 10.4. Energy resolution. The 100keV, 500keV, 1MeV and 2MeV point-sized energy deposits were distributed uniformly in the fiducial volume.

10.4 *Spatial and Energy Resolution*

The parameters of the event (time, position, energy etc.) are reconstructed from the *PMT* signals. The accuracy of the vertex reconstruction is limited by the error of the time signals. In the Borexino detector the typical value of σ for a single measurement is about *1m* due to the *PMT* time jitter, the scintillation decay, the light scattering and the refraction and reflection on the acrylic wall of the inner vessel. So *100* measurements are needed to reduce this error to *10cm*. The Borexino resolutions are shown in Table 10.III. For more details see Appendix V.

10.5 *Particle Discrimination*

The scintillation decay of the *TMB* loaded liquid scintillator is different for excitations

Table 10.III. Spatial and energy resolution in the BOREXINO detector

Spatial and Energy Resolution		
Energy (MeV)	ΔR (σ (cm))	ΔE (σ (keV))
0.05	71.6	16.0
0.1	52.3	23.6
0.2	35.2	32.0
0.5	18.3	50.1
1.0	12.9	76.5
2.0	9.9	120.1
4.0	9.7	189.6
5.0	10.2	227.9
6.0	10.3	226.2

produced by α particles and electrons. One may use this fact to discriminate α particles from gamma rays and electrons. Various *TMB* loaded liquid scintillators have been tested (see Table 7.II). The analysis of the measured spectra has shown that the best approximation of the decay spectra is given by the sum of three exponentials (figs. 10.5 and 10.6).

A careful analysis was carried out to select the best liquid scintillator sample for the α separation (see Appendix III); the analysis has shown that the *D2* sample is the best for this purpose (Table 10.IV). The results shown here were obtained with *0.5MeV* electrons and *5MeV* α particles, with a quenching factor for the α's of 10 (see §7.1.5). The performance in separating α particles from gamma rays (electrons) provided by *D2* sample are shown in Table 10.V and fig. 10.7. It is possible to achieve 89% of α separation, with only a 6% of electron background.

10.6 *Event Topology*

Neutrinos coming from the Sun interact in the liquid scintillator of the BOREXINO detector, producing in the final state electrons and gammas with an energy ranging from 0 to 14 MeV. Moreover, the natural radioactivity of the scintillator itself, of all materials

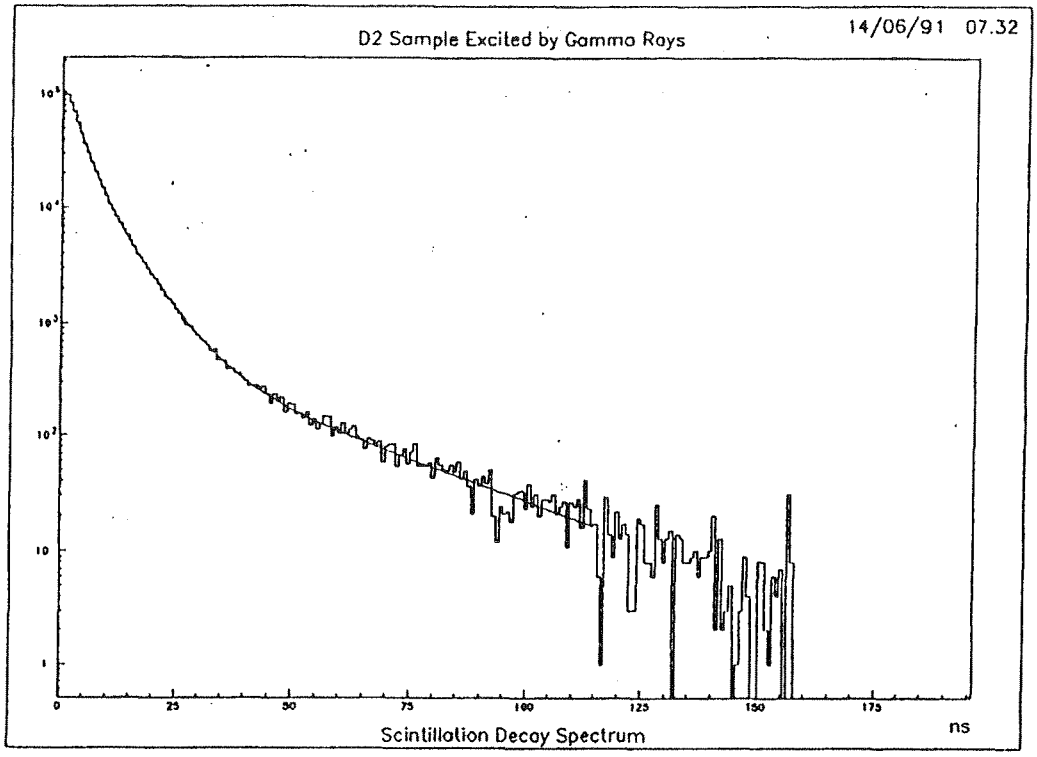

Figure 10.5. Decay spectrum of the scintillator D2 (see Table 7.II). The scintillator was excited by gamma rays.

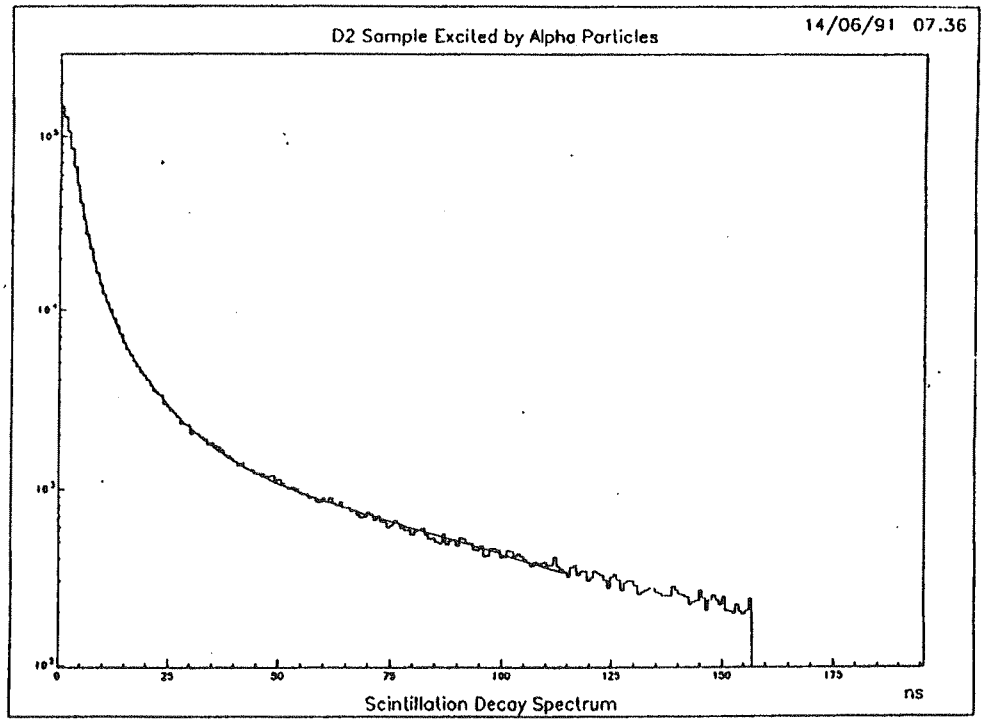

Figure 10.6. Decay spectrum of the scintillator D2 (see Table 7.II). The scintillator was excited by α particles

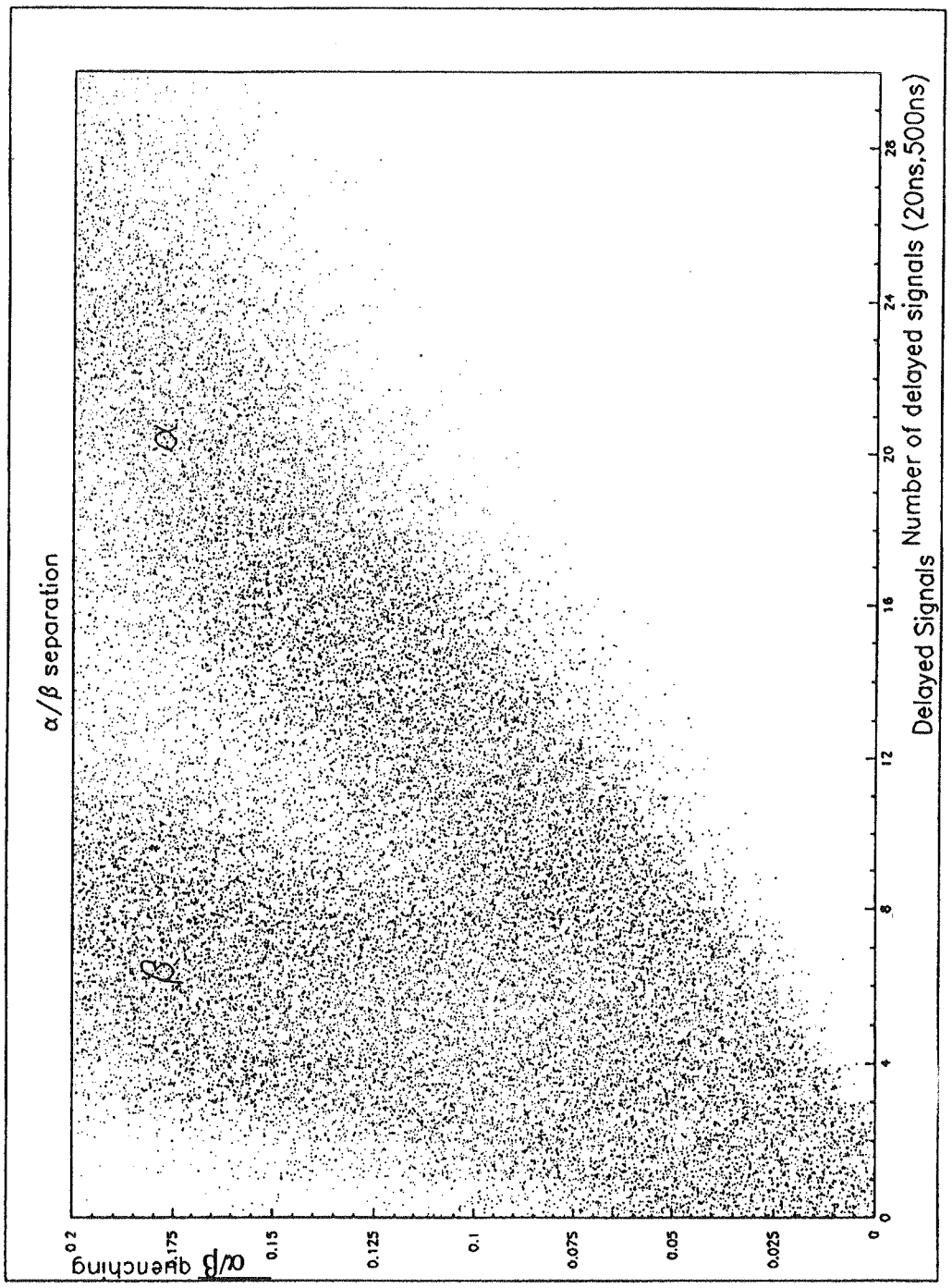

Figure 10.7. Pulse shape discrimination for the scintillator D2 (see Table 7.II). It is possible to achieve 89% of α separation, with only a 6% of electron background.

Table 10.IV. Alpha separation on the basis of the number of delayed signal. In the last two rows the percentages of the discriminated α particles with the percentages of lost electrons are shown.

Sample	e^-	α
A1	7%	37%
	2%	20%
	1%	9%
A2	11%	63%
	5%	47%
	2%	32%
B1	10%	57%
	4%	39%
	1%	25%
B2	14%	95%
	6%	89%
	2%	80%
B3	11%	93%
	5%	85%
	2%	76%
C1	9%	51%
	3%	33%
	1%	16%
C2	16%	85%
	8%	76%
	2%	65%
D1	12%	70%
	3%	51%
		34%
D2	24%	99%
	9%	98%
	2%	96%

composing and surrounding the detector and of the rocks, originates the background, which consist of betas and gammas with an energy ranging from 0 to 5 MeV, and alpha particles, of energy from 3 to 8 MeV. In addition events produced by the cosmic rays give contribution to the background.

Table 10.V. Alpha identification for the scintillator D2 (see Table 7.II). It is possible to achieve 89% of alpha separation, with only a 6% of electron background. The number of delayed signals are counted in the (20ns, 500ns) interval after the peak of the time distribution of the detected photons.

Minimum number of delayed signals	Electron (Events)	Percentage	Alpha (Events)	Percentage
0	948		1000	
1	835		998	
2	673		996	
3	477		991	
4	291		978	
5	140	(14%)	939	(94%)
6	56	(6%)	886	(89%)
7	28	(3%)	808	(81%)
8	10		692	
9	3		569	
10			444	
11			288	
12			186	
13			114	
14			60	
15			29	
16			8	
17			4	
18			1	
19				

(Sample D2)

10.5.1 *Electrons and photons*

The longitudinal extensions of the showers for electrons and photons are very different. The "electrons" (that is showers generated by electrons) have short extension: 80% are less than 5 cm; the spatial extension of the "photons" (that is showers originated by photons) is clearly greater: the 70% is in the range 10- 50cm and the 10% is longer than 100cm. The spatial distribution of the deposited energy in the shower is piled in the

origin for the "electrons" while for the photons the 90% of the energy loss is spread out in 50cm. The characteristics of the showers do not change nearly in the energy range 3-10MeV.

The positron showers have an extension longer than the electrons (most probable value is 35cm about) and the energy deposit is practically symmetric with respect to the origin, due to the annihilation process. The alpha particles show a pointlike deposit and have a quenching factor, which ranges between 10 and 15 in the scintillator of our interest (see Chapter VII).

10.5.2 *Topology of the muon events*

We expect about 64 muons per hour crossing the Inner Vessel of BOREXINO, few of them stopping within it (see §12.4). The expected cases are:

1) Throughgoing muons.
2) Throughgoing muons accompanied either by nuclear cascade showers or electromagnetic showers.
3) Stopping muons, some of them decaying and a small percentage of them captured by the nuclei (§12.4.2)

To distinguish among the different cases it is helpful to identify the isotopes produced along the muon track or by the muon capture. This identification is based on the space and time correlation of the beta's and gamma's produced in the radioactive decays with the cosmic ray muons. The time interval should be about 30s and the spatial region around the muon track is of the order of 1m. It is easy to recognise a muon by the large amount of energy released in the scintillator. The identification of the muon crossing only the water buffer is based on the Čerenkov light. A throughgoing muon with 200GeV of mean energy releases in TMB an ionisation energy of ~2.8MeV g/cm^2 and a total energy (ionisation, bremsstrahlung, direct electron pair production, nuclear interaction) of about 3.3MeV g/cm^2. Considering a mean path in the detector of 570cm, the total energy released is 1600MeV. With a loss of 20% due to the absorption, PMT coverage of 50%, a PMT quantum efficiency of 20%, a scintillation photon yield/MeV of 4800, the number of photoelectrons is ~ 610000. This means ~ 340 p.e./PMT. This pulse height is out of the range for the PMT's dedicated to the detection of 1 photon, typical pattern for the energy released by electron of few MeV. Then we plane to install about 100 PMT's with a

dynamical range useful for the detection of this level of energy.

A cut in energy released can help in distinguishing between the categories (1) and (2). The energy released by throughgoing muons has a spectrum extended up to ~2200MeV, which corresponds to the energy loss by a muon crossing the detector along the diameter. The energy released by a throughgoing muon accompanied either by nuclear cascade showers or electromagnetic showers can be larger than the energy released by a throughgoing muon travelling the same path.

To localise the throughgoing muon track we can use the time distributions of the photons arriving to all the PMT's. The light produced by the throughgoing muons takes t=nd/c time to cross the scintillation vessel along its d diameter, where n is the refractive index of the scintillator and c is the light speed. In case of Borexino d=8.5m, n=1.4 and so t is about 40ns. In the scintillator the muon moves approximately with the speed of the light, so it takes t=d/c ~ 30ns to cross the scintillation vessel along the diameter. The time difference of these two cases is ~ 10ns. One may use this difference between the two speeds to find the exit point of the muon track in the scintillation vessel. The entrance point is well defined by the time of the first photons arriving to the PMT's.

Chapter XI

RADIOPURITY OF LIQUID SCINTILLATOR

The Borexino scintillator liquid will consist of a (mainly) binary mixture of trimethyl borate (TMB: $(BO_3(CH_3)_3$; 80-90%) and pseudocumene (PC: <20%). The scintillator could also contain naphthalene to the extent of ~5% (at the expense of PC). In addition, small amounts of an aromatic fluor such as PPO, bis-MSB or butyl-PBD are necessary at the 0.5 to 1% level (Chapters VII and IX). The requirement on purity of the individual constituents is ordered roughly by their fractional presence in the final scintillator. Thus the radiopurity research so far has been directed towards TMB and PC. The major background producing nuclides are the natural radioactivities of U, Th, K and cosmogenic ^{14}C. We report here results obtained so far for 1) U and Th for TMB and PC via mass spectrometry (MS), 2) for K and other nuclides via radiotracer analysis, and 3) ^{14}C in petrochemicals via accelerator mass spectrometry. Investigations on surface contamination in teflon vials is also reported. Finally, studies on permeation of ^{222}Rn through plastic films are described.

11.1 *MS Analysis—Trimethyl Borate*

The general method adopted was preconcentration of the U and Th impurities in the TMB by distillation. The residue left from distillation was carefully collected and processed for mass spectroscopy (MS) either in ISPRA (Italy) (via inductively coupled plasma (ICPMS)) or in NIST (USA) via thermal ionisation (TIMS). The MS investigations were conducted in two stages. In the first, small volumes ~1L were processed in the laboratory (clean room work); and in the second, the methods developed in this work were extended to semi-industrial volumes ~100L processed in the

environment of the TMB plant itself (Volterra, Italy). The details of experimental method described here apply to the former. Those the Volterra work (see Appendix XI), while differing somewhat in detail, followed the basic technique of the 1L sample work.

Preconcentration of U/Th traces: We have developed a preconcentration method involving minimum contamination and loss of impurities in the process, by sub-boiling distillation using a carrier gas of nitrogen which increases the speed of distillation significantly. Approximately 1L samples of TMB were distilled from a horizontally held separatory funnel, radiantly heated below the boiling point of TMB under a flow of pure, dust-free nitrogen controlled so that the liquid surface remained practically undisturbed. The TMB was fed batchwise into the funnel. In the apparatus employed (a first run version), the distillation takes about 4-5 hours. At the end of the process, a small amount of clear liquid (~0.2 ml) remained. A few ml of nitric acid (2% solution of NIST-HNO_3 in NIST- water) was introduced into the funnel via the tail. The TMB immediately hydrolysed, releasing boric acid. Under IR heating, the boric acid dissolved and a clear solution (typically 5 ml) formed. The funnel surface was gently washed with the solution and forced out through the funnel tail into clean teflon sample bottles for shipment. A reagent blank sample was made from the acid solution used for recovering the residue. Finally an instrument blank was prepared by refluxing a small amount of TMB (~50ml) for 5 hours, at the end of which the liquid was distilled off and the residue recovered and prepared as above.

The preconcentration was carried out in a class-100 hood in a clean room. The apparatus was made wholly of teflon and designed for handling the TMB entirely under moisture free nitrogen (house line filtered to 0.2μ particle size or smaller). All components were cleaned by an elaborate procedure of washing by concentrated acids and water of successively greater radiopurity with final wash by double distilled water. The acids and water used in the sample recovery were supplied by NIST and rated to typical U/Th purities of ~10fg/g.

Commercial TMB was first distilled under open laboratory conditions in a glass rotary evaporation system as a preliminary purification. The clean room teflon distillation procedure was performed twice, the residue from the each stage being collected and analysed. The first residue thus refers to the purity of feed stock of *glass distilled TMB* and the second residue refers to *teflon distilled TMB*. Before and after each stage, the funnel was cleaned by repeated refluxing with ~50ml of clean distillate after which the wash was rejected.

Mass Spectrometry: Further concentration was carried out as follows on all residue and blank samples. The dilute acid residue samples (with ~100mg of boric acid precipitate) were transferred into 50ml teflon beakers and were spiked with ~50 picogram of ^{233}U and ^{230}Th. One ml of concentrated HF was added which resulted in dissolving the boric acid presumably as BF_4^- ions. The solution was then heated to dryness, which removed the B matrix (presumably as volatile hydrated BF_3). The U and Th impurities on the other hand, did not form volatile compounds in the presence of the nitric acid. Small amounts of dilute acid were added and the samples were then spiked again with ^{236}U and evaporated into a small drop (a few μliter). The final drop was then loaded into the MS source filament and the mass peaks at 230 (Th spike), 232 (Th), 233 (U spike), 236 (U spike) and 238 (U) were measured. The 233 and 236 mass peaks showed complete recovery of the spikes and thus no loss of U and Th traces in the steps of boron removal as well as in the overall final concentration process.

Validity of Preconcentration for Ultrapurity Determination: The limits of detectability of U and Th impurities range from several picogram (pg) (total) of U/Th in the analysate sample for ICPMS to ~1pg in TIMS. The application of these techniques to the determination of U/Th concentrations a thousand times lower, i.e. at $\sim 10^{-15}$g/g, requires preconcentration of the impurities by a factor of ~1000 or more. It is therefore important to demonstrate the validity of preconcentration by distillation at the impurity levels actually prevalent in typical TMB samples.

Preliminary evidence of validity was obtained by separately doping TMB by U and Th compounds to their solubility limits to reach concentrations of $\sim 10^{-7}$ g/g. The doped TMB samples were distilled and samples in all three stages of distillation— initial, distillate and residue— were analysed by MS. The U/Th added to the TMB was found to be quantitatively (>99%) retained in the distillation residue. The ratio of U/Th in the residue to that in the distillate was observed to be ~1000, showing that distillation (at these concentrations) resulted in a purification of the initial TMB sample by this large factor.

Radiotracer work has extended the validity of the method and the purification efficiency found above to extremely low concentrations, $\sim 10^{-14}$g/g, covering the entire range of ultrapurity of interest to this study. The test was also made in such a way as to mimic closely the typical way in which residual contamination of TMB actually occurs in the manufacturing process. The last stage of the preparation of TMB is the separation of an azeotropic mixture of TMB+MeOH by the addition of LiCl (see below); traces of U/Th from the relatively impure LiCl are retained in the TMB. This process was mimicked by spiking LiCl powder with a weak (chloride) source of ^{227}Ac tracer (as dilute

HCl solution) in equilibrium with a Th daughter which can be easily counted. The concentration of the Th spike was less than the measured natural ^{232}Th concentration in the LiCl. By measuring the Th activity before and after the LiCl process, the U/Th in the resulting TMB was measured to be 10 fg/g (the typical purity in commercial TMB (see below). We then distilled this contaminated sample in a sub-boiling mode in teflon containers. Measurement of the activity of the Th daughter before and after the distillation showed that almost all the activity was retained in the residue; in fact, the ratio of Th activity in the residue to that in the distillate was $\geq 10^3$. Fig 11.1 shows the spectra of the sample before and after distillation; only room background (shown displaced below in fig. 11.1) was observed in the distillate. The decontamination factor can be estimated from intensity of Th γ-ray lines indicated. This result, besides validating the preconcentration procedure by distillation at initial concentrations ~10fg/g, shows that ultrapurification of TMB should be feasible via distillation. We assume for the present that these findings apply also to U. The similarity of the MS results obtained here for U

Table 11.1 Summary of Mass Spectroscopic Analysis of TMB (1L)

Series	Dist. Type	Amt. (ml)	^{238}U (pg)	^{238}U Blank* (pg)	^{232}Th In Residue (pg)	^{232}Th Blank* (pg)	U Conc. In TMB (fg/ml)	Th Conc. In TMB (fg/ml)
Alpha	Glas[1]	1080	36	1.5	-	-	32	-
Eni-I	"	1150	33	1.6	13	4.8	27	7
Eni-II	"	750	108	1.9	77	6.5	141	94
Alpha	Teflo[2]	684	5.9	2	13.6	14	5.7	<2
Eni-I	"	895	4.2	1.6	3.6	4.8	3	<1
Eni-II	"	560	5.2	1.9	6.4	6.5	6	<1

*Quoted values approximately cover the total blank from the "instrument" contamination, reagent contamination and the blank from the loading and operation of the MS filament. Fluctuation range in the blank value is ~0.4pg for U and ~1pg for Th. The limits on the Th concentration after Teflon distillation are estimated using this fluctuation range.

[1]Rotary Evaporation.

[2]Teflon distillation of TMB distilled in glass and stored in a glass bottle. For Eni-I and Alpha, the teflon distillation was carried out after a few days; for Eni-II, after several months.

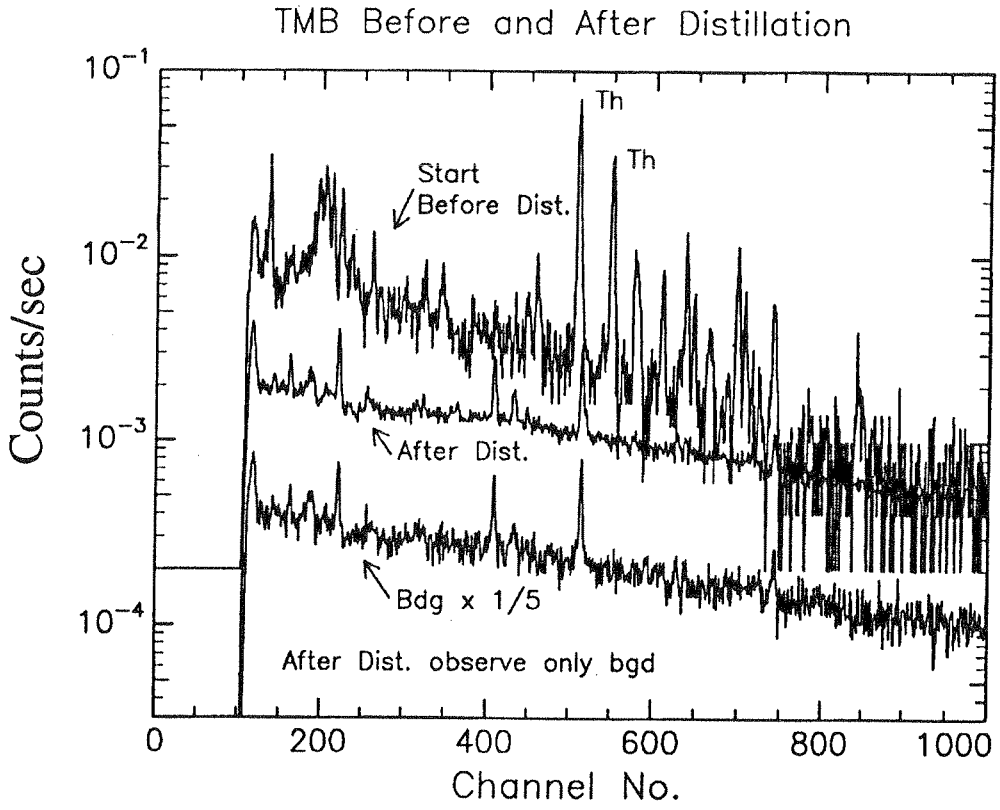

Figure 11.1 Removal of Th in distillation of TMB prepared with ^{227}Ac tracer spiked LiCl. Note the disappearance of the Th gamma-ray lines in the tracer gamma-ray spectra for the distillate

and Th indicates that this assumption is reasonably valid.

Results: Table 11.I gives the radiopurity results for 1L samples of TMB obtained from Enichem (Italy) and from US samples (Alpha) made from a different boron mineral. The results are closely similar. All the residues for MS analyses were obtained in the clean room teflon distillation. The "Glass" results refer to the residue from distillation of TMB feed stock previously distilled in glass. The last two columns in these rows thus refer to the purities of commercial TMB distilled once in glass. The TMB distillate above was redistilled, the residue thus referring to TMB distilled in teflon (lower rows in Table 11.I). The results can be summarised as follows:

1) The teflon distilled samples show that Th is undetectable at the level of fg/g.
2) Finite traces of U, ~3 fg/g, may be present at close to blank levels.
3) Radiotracer evidence (see below) suggests that even these small traces may have

been introduced by surface contamination.

4) The Eni-II results show that, distillation in teflon decontaminates U by a factor of 24 and Th by a factor >100.

As shown by Eni-II and Alpha samples with x5 higher purity than Eni-II, the final purities are the same regardless of initial purities. This may again indicate limiting surface contamination which prevents observation of a much higher final purity such as that expected from the x1000 purification factor indicated by tests above. These results thus strongly suggest that higher purification may be possible if processing is done in large-scale vessels with a more favourable surface/volume than in the above 1L experiment, so that TMB samples with typical initial purity of 10fg/g can approach purified levels of ~0.1fg/g. Radiotracer work (see below) shows quantitatively that the *intrinsic* purity of TMB may be typically of this order.

Large Scale Distillation Experiments ("Volterra Tests"): An all-teflon 100 L distillation apparatus, following the same nitrogen carrier technique used above, has been constructed and installed in the Samatech TMB plant in Volterra, Italy (See Appendix VI for a detailed description). Commercial TMB from the plant was used as feed stock. Residues from two successive distillations have been collected, the first indicating purity of the commercial TMB as received from the plant and the second, the purity of TMB after one stage of large-scale distillation. Analysis of these two samples are in progress. Preliminary values of U and Th for several portions of the first residue have been assayed. They revealed U in the range of 10-30fg/g and Th in the range 20-80fg/g for commercial TMB which was stored for more than one year in uncontrolled environments and containers. In spite of this, the purity is of the same order or higher than that found in 1L samples but only after one stage of distillation. A very preliminary value of U in the second residue from Volterra is ~0.5fg/g, for once distilled TMB, the highest purity observed so far. The results from both Volterra samples confirm that higher purities are observed in larger samples and appear to confirm surface contamination as the limiting factor of observable radiopurities.

11.2 *Radiotracer Analysis—TMB*

The purpose of these investigations is twofold: a) estimations of concentrations of impurity nuclides with undetectably small concentrations and b) provide insight into the

transport of impurity nuclides in specific chemical processes e.g. the steps involved in the preparation of TMB. We indicated above (§11.1) the usefulness of radiotracers in testing the validity of preconcentrative distillation. Another important area of applicability is that of leaching of impurity nuclides in and out of teflon container surfaces.

In addition to U and Th, we also need information on the radium isotopes (1600y-^{226}Ra, 6y-^{228}Ra) and on 22y-^{210}Pb which, because of the short half-lives and thus much smaller concentrations, are inaccessible to direct analytical methods even with preconcentration. A similar problem exists at a less demanding level for ^{40}K for which high blank values discourage direct determinations at low concentrations. Thus, specific methods must be developed to indicate the chemical separation behaviours of Ra, Pb and K in the preparative steps of the scintillator components and reliably predict the equilibrium properties of the U and Th decay chains present in the final scintillator. In this work, conveniently measurable short-lived radioactivities of the same chemical element as the impurity in question have been used as tracers. The movement of this tracer activity through a given chemical process is given by the ratio of the initial to final sample activity measured by Ge γ-ray spectroscopy or by internal scintillation counting.

The preparation of TMB: The sequence of preparation of TMB is simple:

$$\text{Colemanite} + H_2SO_4 \rightarrow \text{Boric Acid} \quad (1)$$

$$\text{Boric acid} + \text{MeOH} \rightarrow \text{Distill} \rightarrow [\text{TMB+MeOH}]\ (\text{Az}) \quad (2)$$

$$\text{Az} + \text{LiCl} \rightarrow \text{TMB} \quad (3)$$

The raw material is Colemanite, a Ca borate mineral. The first step is the preparation of boric acid. The second the reaction of boric acid with methanol and an azeotropic distillation to give the TMB-MeOH azeotrope. The third step is the separation of methanol by addition of LiCl by which the TMB phase separates to the top of the fluid and can thus be siphoned off.

In each of these steps the initial material is an inorganic compound such as colemanite, boric acid and finally LiCl. The radioactive impurities in these materials are the major sources of contamination in the final TMB; the initial mineral, e.g., has U/Th and K typical of the earth's crust i.e. ~10^{-7}g U,Th/g. The decontamination of such an impurity level at successive chemical steps involves also the new contamination by the input material at each step. This process can be closely mimicked by taking each step at a time, spiking the input material of that stage with the radiotracer and measuring the separation factor (defined as k= [input tracer activity/g input material]/[output activity/g output

material).Input material here refers to the Colemanite, boric acid or LiCl and the output is respectively, boric acid, the azeotrope or the final TMB. This definition assumes that materials are used in compositions and amounts required for the specific chemistry of that stage. The purities in the final products can be directly estimated from those of the initials materials using this k value. The collection of k values provides a complete map of the movement of this element throughout the manufacturing method of TMB.

The k-map leads to important inferences. For example, in the case of Th, the natural ^{232}Th concentration of colemanite, boric acid and LiCl can be directly measured. Therefore k(Th tracer) directly predicts the concentration of Th in each of the output stages, viz. boric acid, TMB azeotrope and the final TMB. These results can thus be used for quantitative bulk purity estimates. They also provide limits of initial impurity concentrations in boric acid or LiCl that is necessary to produce a certain final purity. Thus the k data are important for material quality control in the manufacture of TMB. The k-estimates refer only to *intrinsic* purities. Surface contamination may be inferred by strong deviations of actual purity compared to purity estimates from the k data. These methods may be the only way to infer the concentrations of impurities with undetectable concentrations such as Ra, ^{210}Pb and K. Finally, in the final LiCl stage, the output TMB is contaminated by the tracer in the same chemical configuration as the impurity in the actual manufacture. A distillation of this tracer-contaminated TMB then gives the purification efficiency by distillation, as mentioned in the last section.

Tracers: The principal tracers used in this work are:

1) ^{227}Ac. This actinide chain decays as follows:

$$^{227}Ac\ (22y) \rightarrow {}^{227}Th\ (18.7d)\alpha\,\gamma \rightarrow {}^{223}Ra\ (11.7d)\alpha\,\gamma \rightarrow\rightarrow {}^{211}Pb\ (36\ min)\beta \rightarrow {}^{207}Pb$$

All the activities except the initial Ac can be observed by γ- ray spectroscopy. The interesting feature is that Th and Ra can be followed relative to each other. Thus the important aspect of Ra disequilibrium with respect to Th in each chemical step can be determined simply by the ratio of the Th/Ra γ-rays and the variation of this ratio with the time after the separation process. The activities of other short-lived nuclides in the decay chain are directly determined by the Th and Ra, thus they do not carry individual chemical information.

2) ^{210}Pb: The movement of Pb is important since the ultimate background in the low energy window in Borexino may be decided by the presence of Pb. Since the $^{210}Pb \rightarrow {}^{210}Bi \rightarrow {}^{210}Po$ radiations are low energy β and α only, it can be traced best by

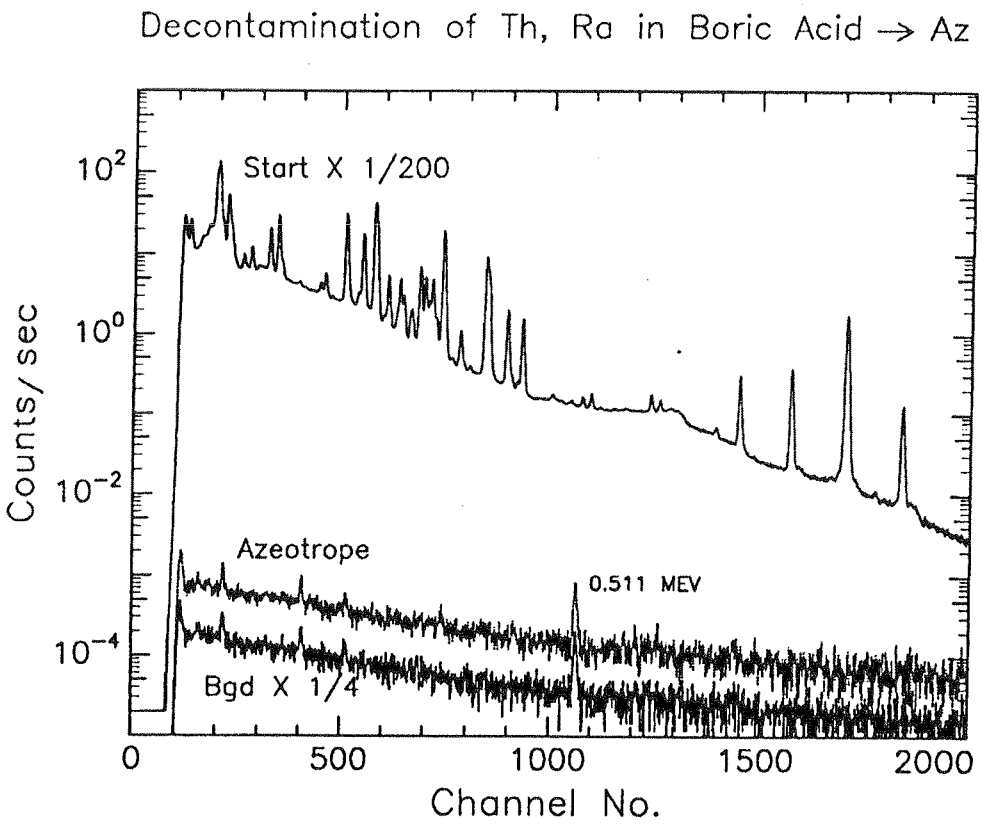

Figure 11.2 Azeotropic distillation (Stage 2) of ^{227}Ac tracer spiked (Boric acid+MeOH). The γ-ray lines in the spectrum refer to Th and Ra daughters.
The tracer activity in the azeotrope distillate is ~0, consistent with background.

internal scintillation counting.

3) ^{22}Na and ^{137}Cs: Both these are alkali elements that chemically bracket K; thus they can act as proxies for the separation of K. Cs is also representative of fission fragments contamination.

4) ^{60}Co: A typical transition element that can indicate possible behaviour of other fission product laments of the (3d) group.

Experimental: The above activities in dilute acid solutions were added to powders of colemanite, boric acid or LiCl and dried free of water. They represented the contaminant elements. The TMB chemical steps 1 to 3 above were performed by the same prescriptions as in the TMB manufacturing process. Initial activities were measured by withdrawing a small volume in the initial solution phase (e.g. after addition of the H_2SO_4 (step 1) or methanol (step 2) or the azeotrope). After the chemical processing, the activity

was measured in the final product. Activity was measured usually by counting peak rates of γ lines in a Ge spectrometer in standard geometries using same amounts of liquids to equalise absorption etc. The activity in the Ac chain was followed with time, especially at different times after the separation to observe the changes in the ratios of the Th and the Ra lines in Ac decay. The separation factors for each stage was thus measured for all the above impurity elements. Most of the separation factors were high; often only limit counts can be set because the output activities were smaller than the base background of the detector.

Results: Tables 11.II-IV show the separation factors for Th, Ra, Na, Cs Co and Pb tracers given above for the three stages of TMB production. In addition to the k values, the spike concentration and the measured purity data of the input material are indicated so that final purities can be directly estimated.

In the first stage, Ra is removed more efficiently than Th, not surprisingly, since the major purification here is the well-known sulfuric acid process which removes Ra more efficiently than Ca. The concentration of Th in boric acid estimated from the k-value in this stage is higher than that found in stock boric acid presumably because the commercial boric acid undergoes more purification stages.

The most interesting separations occur in the stage 2. Practically all the impurities are completely removed. The azeotrope itself is probably one of the least contaminated materials (barring that from surfaces). Fig.11.2 shows radiation spectra (Ge detector) from Ac tracer in the input stage (Boric acid+methanol) and in the Az output. The input sample was derived from 0.5% volume of the starting mixture. The activity in the final Az is consistent with room background. Fig. 11.3 shows similar spectra for a ^{210}Pb tracer measured by internal scintillation counting. Again a large decontamination of Pb is observed in stage 2.

However, in stage 3, the addition of LiCl introduces new contaminations; this last stage therefore decides the purity of commercial TMB. With initial measured purities of LiCl, the k-estimate obtained here predicts a Th concentration of ~10^{-14}g/g in TMB, nearly as seen in direct mass spectroscopy (see §11.1). The two LiCl measurements in Table 11.IVa and b were made with two different spike concentrations to investigate the separation of Ra in more realistic terms. The Ra concentration in the Ac spike is always close to that of Th but in the natural radioactivity, the ^{226}Ra is 10^{-6} that of Th/U. Thus in Table 11.IVb, the Ac-Th-Ra spike was reduced to bring its Ra tracer closer to the natural Ra concentrations. A somewhat worse, but still high separation was observed, especially

Table 11.II Separation Factors k for TMB (Stage 1): Colemanite → Boric Acid

	Th	Ra	Na	Cs	Co
Colem. Natural Conc. (g/g)	$1.7x10^{-6}$		0.5% (K)		
k	10^2	10^3	10^2	10^2	10^2

Table 11.III Separation Factors k for TMB (Stage 2): Boric Acid → Azeotrope

	Th	Ra	Na	Cs	Co	Pb
Spike Conc. (g/g)	$1.5x10^{-10}$	$6x10^{-11}$	10^{-9}	$4x10^{-7}$	$2x10^{-7}$	10^{-7}
Boric Acid Natural Conc. (g/g)	$5x10^{-10}$	$5x10^{-16}$	$<10^{-7}$(K)			
k	$>10^8$	$>10^8$	10^7	$>10^8$	10^8	$>5x10^7$

Table 11.IVa Separation Factors k for TMB (Stage 3): LiCl(Aztrp → TMB)

	Th	Ra	Na	Cs	Co
Spike Conc. (g/g)	10^{-10}	$4x10^{-11}$	$1.4x10^{-10}$	$4x10^{-7}$	10^{-7}
LiCl Natural Conc. (g/g)	$5x10^{-9}$	$5x10^{-15}$	10^{-6}(K)		
k	$4x10^5$	$4x10^6$	$>10^8$	10^8	$>10^8$

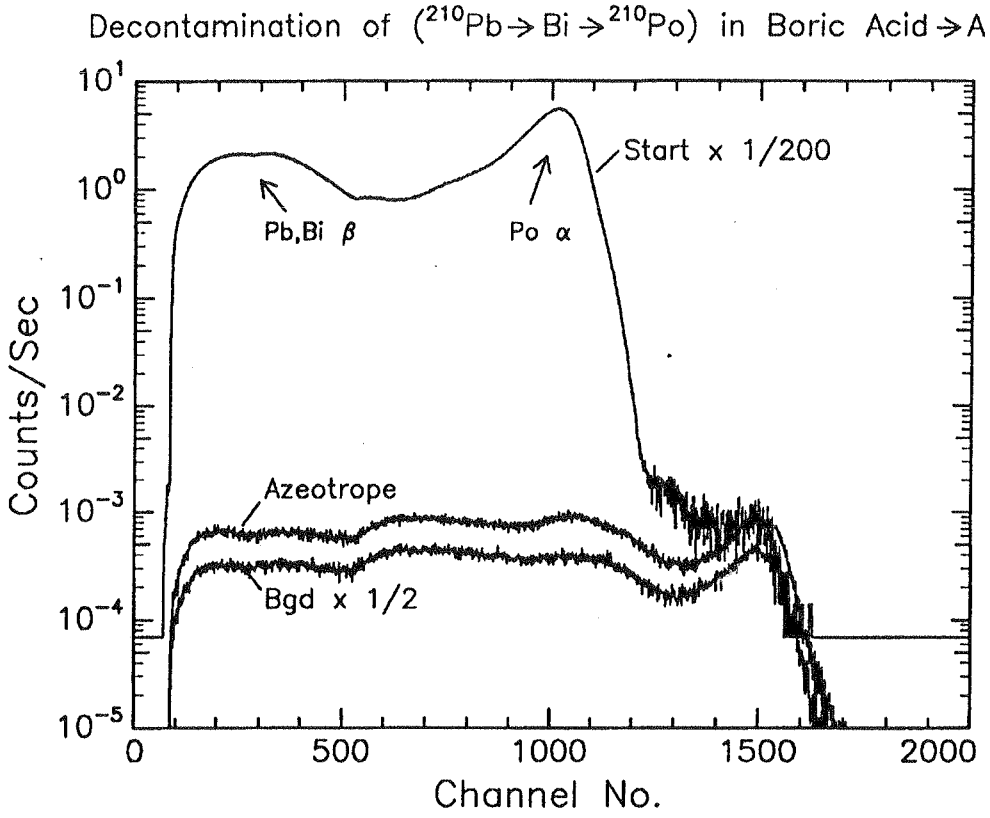

Figure 11.3 Same as 11.2 but with ^{210}Pb tracer. The tracer spectra were taken by internal liquid scintillation counting.

Table 11.IVb Separation Factors k for TMB (Stage 3): Low Spike Conc.

	Th	Ra
Spike Conc. (g/g)	1.6×10^{-13}	7×10^{-14}
LiCl Natural Conc. (g/g)	5×10^{-9}	5×10^{-15}
k	4×10^{4}	$\geq 10^{6}$

for Th and Ra and the Ra depletion vs. Th was again confirmed.

The more interesting aspect in the LiCl stage is the renewed higher removal of Ra compared to Th. Fig. 11.4 shows Ac tracer spectra before and after the stage 3 LiCl separation of TMB from methanol. The γ-ray lines of Th and Ra are indicated. The spectrum just after separation (top panel) shows traces of Th lines but the Ra lines are almost absent. In the next panel, the growth of Ra lines from the decaying Th in the spike can be observed. It is almost certain that in the final TMB Ra will be significantly depleted compared to the U/Th parents (we tacitly assume that U k-values will be similar to the Th k-values).

The tracer-contaminated TMB resulting from stage 3 above was distilled. The activity ratio showed that Th can be removed by a further factor of ~1000 (see fig. 11.1). If the normal technical grade LiCl (with purity as given in table 11.IVa) is used, the k values

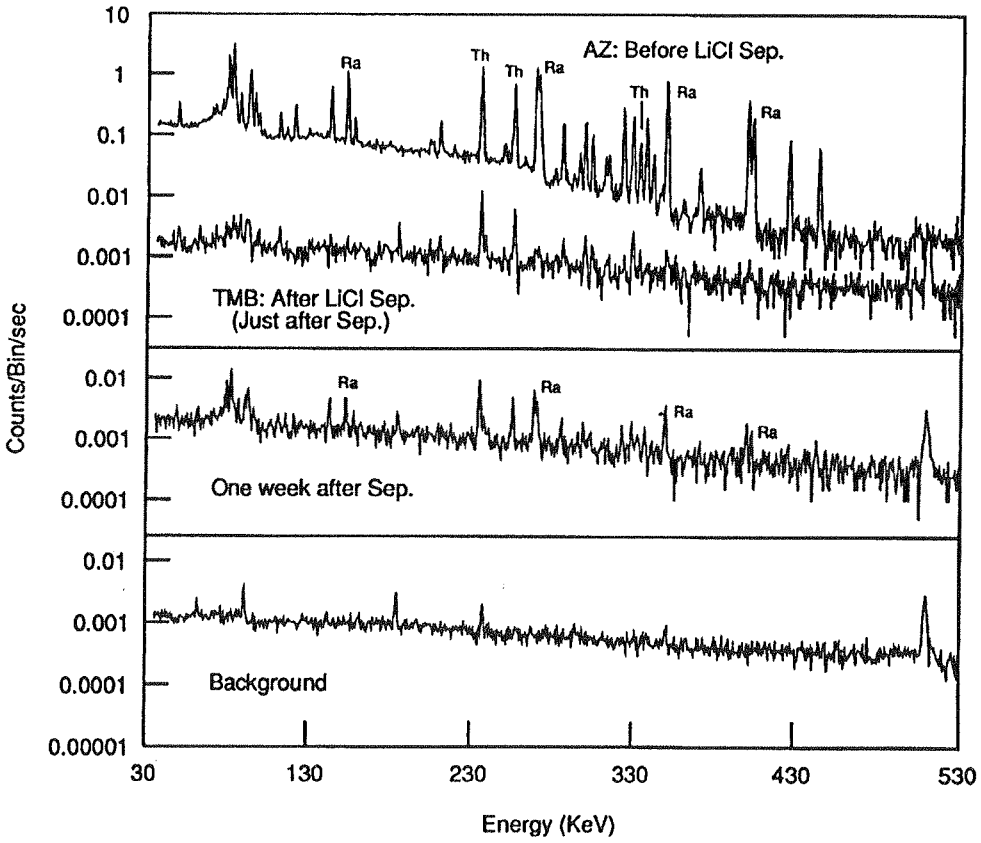

Figure 11.4 LiCl methanol separation (Stage 3) with Ac tracer spiked.LiCl. Top panel: start spectrum and spectrum just after separation Notice the absence of Ra lines; Middle: after one week Ra lines grow back; Bottom: background.

clearly show that a such a distillation is necessary to reach a purity of or beyond 10^{-16} g/g. However, if high purity LiCl with U/Th concentrations in the ppt range is used, then a *final stage TMB distillation can be avoided* with a significant cost reduction. The most remarkable final outcome of this analysis, is that the k values predict (as verified by typical TMB purities measured directly) that intrinsic purities of the order of $5x10^{-17}$g/g in TMB may indeed be typically within reach by simple purification methods such as distillation or even none at all if the LiCl in the final stage is sufficiently pure.

The measured k values give important information also on ^{40}K (as indicated by Na and Cs tracers) and on Pb. The near total removal of Na in the LiCl stage by the large decontamination factors (see fig. 11.5 for spectral data) shows that the starting purities of LiCl currently in use in the plants is probably already sufficient to keep K in the final TMB below 10^{-14}g/g. While K is not directly measured, the data of Na and Cs on either side can be taken as a reasonable indicator of separation behaviour K in the middle.

Pb was measured only in stage 2. The separation factors here indicate that Pb is likely to be in equilibrium with Th upto this stage. Considering the typically large k values of all the impurities, observed so far, it will be surprising indeed, if Pb is enriched relative to Th

Figure 11.5 Same as 11.4 with Na, Cs and Co tracer. The ^{22}Na 511keV line is indicated

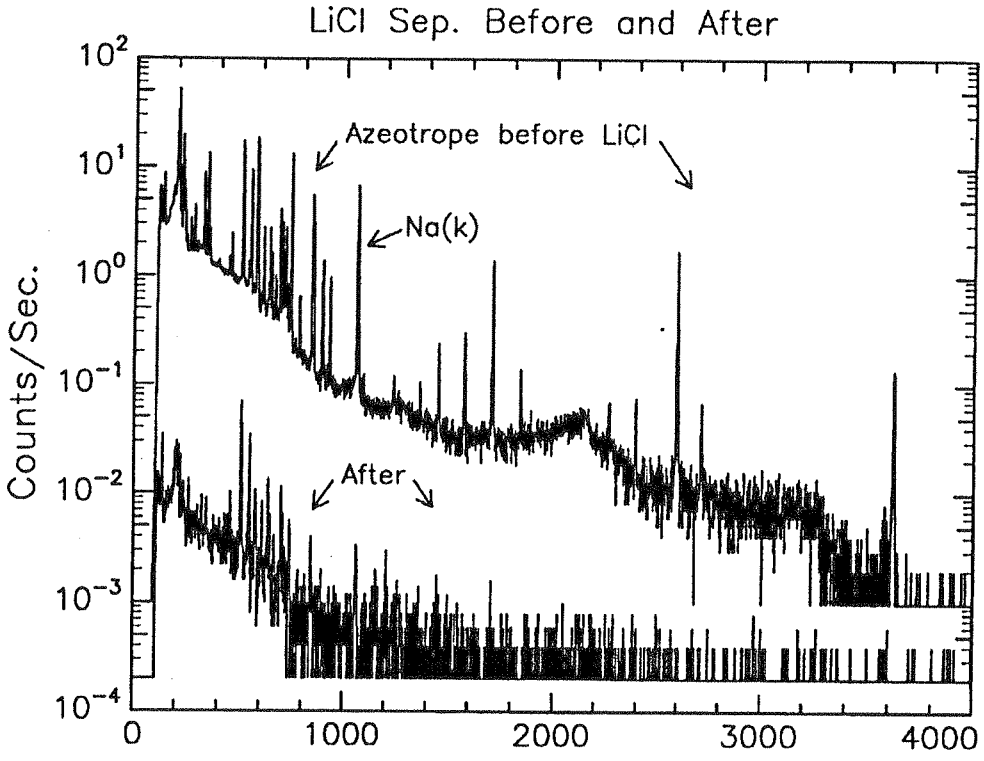

in the LiCl phase.

Surface Contamination: The problem of contamination of teflon vials was investigated by tracer work in the following way. The teflonware used in the processing of TMB MS analysis (Table 11.I) were cleaned by a sequence of washing with hot, technical grade acids followed by repeated washings with water of increasing radiopurity. In the first stage we introduced tracers in the acids and followed the cleaning procedure. After the washings were completed according to protocol, the teflon vials were filled with clean TMB (to reproduce counting geometry) and inspected for activity. Some activity was found to have leached into the teflon. Following this, the TMB was kept in the vials for periods of a day at 50°C and for a month at room temperature. At the end of these periods the TMB was refilled into a fresh uncontaminated vial and remeasured. Some activity was found to have leached into the TMB. The quantitative k values for these two way movements are shown in Table 11.V. Using these figures and the surface/volume of the vial vs. those typical of the labware used in the MS processing of TMB, it is possible to conclude that the TMB in the MS analysis could have been contaminated by natural U and Th infused into the teflon labware and apparatus during the acid cleaning. The residual concentrations of ~3fg/g of U found in Table 11.I may thus represent an upper limit of the contamination.

11.3 *Pseudocumene—MS Analysis*

Research into the purity mechanisms in pseudocumene is in the initial stages. In contrast to TMB,a systematic study of the purification methods of PC have yet to be satisfactorily demonstrated, mainly due to the lack, so far, of good diagnostic tools such as the radiotracer technique. The reason is that the chemical form of the tracer activity that can be introduced into PC provides no guarantee that the tracer realistically mimics the behaviour of the unknown species of the contamination in the actual samples. In the case of TMB, this was possible because the main sources of contamination are the inorganic additives such as boric acid or LiCl which can be easily spiked by inorganic tracer forms. PC is obtained by fractional distillation of petroleum, thus a wholly organic process.

We have, however, obtained first results of the U and Th content in PC by direct MS (TIMS). Here also the preconcentration methods are different and restrictive. We have

Table 11.V Separation Factors in Surface Leaching in Teflon Vials

	Th	Ra	Ac	Na
k(Acid → Teflon)	1.5x1-0^4	$4x10^4$	$>2x10^5$	$>2x10^6$
k(Teflon → TMB)(1 d/50C)	$3x10^2$	$7x10^1$		
k(Teflon → TMB)(1 mo. RT)	$5x10^1$	$2x10^1$		

Table 11.VI Mass Spectrometry—Pseudocumene (PC)

Series	Residue/ Distillate/ SE/DE	Amt g	^{238}U in Sample (pg)	^{232}Th in Sample (pg)	^{238}U Conc. (fg/g)	^{232}Th Conc. (fg/g)
1	Residue (45g)(SE)	900	3.2	6.46	3.5	7.2
	Distillate (SE)	212	0.547	2.5	2.6	11.7
2	Distillate (SE)	79.7	0.246	-	3.1	-
	Distillate (DE)				3.4	
	ReDist/Qtz (SE)	119.2	0.133	-	1.1	-
	-do- (DE)				8	
	Min. Oil Scint/SE*	39.5			70	340
	Min. Oil Scint/SE*	108.2			226	-
	Macro-I Scint/SE**	105.9			290	150
	Macro-II Scint/SE**	81.7			340	300

*U. Penn/NIST (Priv. Comm.)
**Caltech (Priv. Comm.)

isolated the U and Th concentrations mainly by a solvent extraction method based on the fact that the addition of water and thorough mixing hydrolyses most U and Th complexes and leaves them in the water phase as the PC and water separate when the liquid is at rest. The water is then extracted and evaporated, spiked with standards and measured by TIMS. The method has been applied to PC as well as other liquids such as the Macro mineral oil scintillators. Table 11.VI shows the results. SE indicates solvent extraction of PC samples. In (1) the 45 gram residue left by distillation of a 1L volume of PC was analysed by SE; the distillate itself was also examined. Some attempts were also made to estimate U and Th by directly evaporating (DE) the PC sample analysing the small drop left behind. Generally the following conclusions are possible: Distillation does not produce a high purification of PC. The purities in all the samples generally indicate a U concentration in the region of ~3fg/g, similar to the TMB result. The Th concentration may be higher, in the range of ~8fg/g. The values found for PC are, however, significantly lower than that typically seen in common mineral oil scintillators. The Borexino requirement on the purity of PC is generally less stringent than that of TMB. While the values found here show that PC is probably in the desired range, more extensive research is necessary to find purifying methods to give a better safety margin.

11.4 Carbon-14

Cosmogenic ^{14}C in the scintillator liquid must be reduced to levels of $^{14}C/^{12}C < 10^{-18}$ in order to achieve an analysis threshold of ~250 keV in Borexino operations. All the carbon in the scintillator components TMB (carbon derived from methanol), PC, fluors etc. are or can be derived from petroleum products. In principle, ^{14}C should be almost totally absent in petrochemicals (only traces at the level of ~10^{-} can arise from reactions due to radioactivity products in deposits near the oil bearing site). The best available experimental limits on ^{14}C in "old" material including petroleum products was obtained by accelerator mass spectroscopy (AMS). This limit, however, was at least two orders of magnitude above the limit desired in Borexino. While it was generally thought that contaminations introduced during the preparation of AMS samples were responsible for the observed limits, an unforeseen source of ^{14}C in old material could not be ruled out experimentally. It was therefore necessary to settle this issue by lowering the existing ^{14}C typical limit in a typical petrochemical.

The basic method chosen to overcome the AMS sample blank problem was isotopic

Sample	^{12}C (%)	^{13}C (%)	^{14}C/ Total Carbon
Normal	98.9	1.1	$(0.57\pm0.14)\times10^{-15}$
Enriched	0.9	99.1	$(0.56\pm0.05)\times10^{-15}$

Table 11.VII. AMS of normal and enriched CO derived from natural gas

enrichment of the heavier carbon isotopes in the sample. As a representative petrochemical, natural gas was chosen. Carbon monoxide derived from virgin natural gas, carefully contained without exposure to air in "old" gas cylinders (not exposed to cleaning reagents), was liquified and substantially enriched in the heavier carbon isotopes. Several samples of CO from natural gas at different stages of processing and isotopic enrichment were made. Samples for AMS were prepared by graphitization of the CO in two steps: a) Acetylene synthesis:

$$2CO + 6Li \rightarrow Li_2C_2 + 2Li_2O$$
$$Li_2C_2 + H_2O \rightarrow C_2H_2 + Li_2O$$

and b) graphitization of the acetylene above, by dissociation in a high-voltage AC glow-discharge. The graphite was deposited as a 2.5mm dia. disc on top of a pure Al pellet used as an electrode.

Table 11.VII gives the specifications of and the AMS results for two samples, one from normal CO and another using CO (inriched to 99.1% in ^{13}C (i.e. by a factor of ~100). Computer simulations of the enrichment process used by the supplier (including the presence of isotopes of oxygen) estimate that the ^{14}C, if any, would be enriched by a factor of 200, i.e. twice as much as ^{13}C.

Extensive experience of the AMS system background and special tests conducted on the contamination of AMS sample during its preparation lead to the conclusion that the finite $^{14}C/C$ values above are entirely due to sample preparation (introduced largely in the Li exchange and graphitization steps). The most convincing result is however the complete equality of the "background" in the normal and the x200 enriched samples. We conclude that no ^{14}C is found in CO derived from natural gas, the upper limit of which can be taken from the error in the background for the normal sample. Using the enrichment factor of 200 for ^{14}C, we arrive at a new upper limit of:

$$^{14}C/C < 0.75\times10^{-18} \quad (1\ \sigma)$$

These new limits improve the existing ones by two orders of magnitude; they are consistent with Borexino goals in principle. Since contamination in the actual scintillator could occur during manufacture, the scintillator itself must be tested for such low levels of ^{14}C. This will be the objective of the projected Counting Test Facility (Vol. III).

11.5 Permeability of Radon through Tedlar (PVF) Polymer

Because of the large difference in the radiopurities of the acrylic material of the scintillation vessel and the scintillator itself, radon diffusion from the inner layers of the acrylic vessel into the active volume could be a source of contamination of the scintillator. The Borexino acrylic vessel will be internally laminated by a film (~50 μ) of polyvinylfluoride (Dupont Tedlar). Since plastic films such as mylar are well known to be an effective barrier against radon permeation, the radon permeability of tedlar films was investigated. For comparison, other polymer films such as mylar, saran and polyethylene (for which data are available) were also tested.

The relative rates of permeation of ^{222}Rn through a number of polymer film was investigated using a permeation chamber, consisting of two 5cm high acrylic cylinders separated by a thin film of the polymer under study. In the lower cylinder is placed a

Figure 11.6 **Radon Permeation through Polymer Films**

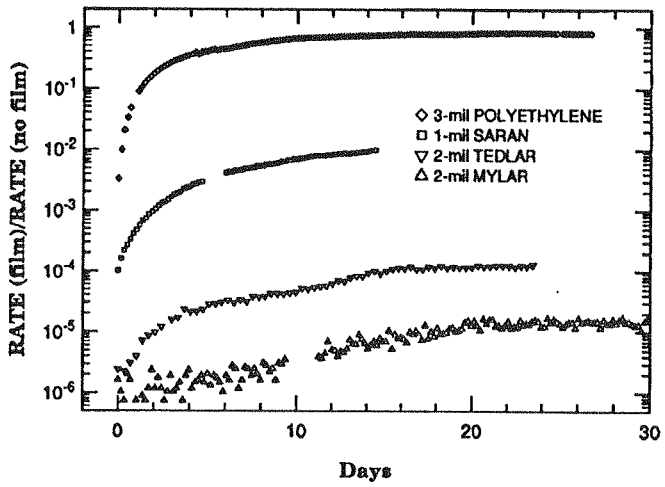

radon source consisting of a small piece of pitchblende, a uranium ore. The radon emanation rate of these sources is known to be constant to within 10%. Alpha particles from the decay of radon which permeates through the film into the upper cylinder are detected by a scintillation detector consisting of a 5cm phototube viewing a 5cm disc of ZnS coated mylar. The pulse height spectrum of the PMT signals is observed every 8 hours for a period of several weeks, after which a state of equilibrium is attained.

The rate of emanation from a given amount of ore was first calibrated with no polymer film and after allowing 2 weeks of running resulted in a equilibriated event rate in the detector. Following the calibration, a series of runs were performed for the polymer sample. A different cell was used for each polymer. The ratio of counting rates observed for each of these runs to the rate for the corresponding calibration run was taken as a measure of the relative rate of permeation for that film.

The count rate ratios vs. time for two films are shown in fig. 11.6. The build-up to equilibrium for the first two films took 15-20 days while for the tedlar and especially mylar, it is seen to be much longer. The reason is the very low diffusion rate through mylar. The ratio of equilibrium count rates for mylar is seen to be about 1.8×10^{-5}. Tedlar is observed also to be an effective radon barrier, with an equilibrium count rate of about 10^{-4}. With this result, scintillator contamination due to leakage of radon from the acrylic will be negligible at the purity values of 10^{-12}g/g assumed for the acrylic and 10^{-16}g/g for the scintillator.

The outdiffusion from the tedlar itself is then of interest. The small thickness of the tedlar presents a limited source of contamination. Assuming that a low diffusivity is a cause of the low permeability found above for tedlar, and that the rate of outdiffusion is inhibited by a similarly large factor as for through the film permeation, a nominal limit of 0.1ppb can set for the purity requirement of the tedlar film. It is however clear that both the radiopurity and the outdiffusion rate from tedlar need to be specifically determined to confirm these conclusions.

Chapter XII

BACKGROUND

12.1 *Introduction*

The physics of the solar neutrino, which can be studied in Borexino, concerns, as described in chapter III of the proposal, events involving single electron or electron+gamma in the energy region ranging from 0. to 15. MeV .

Therefore, in principle, any kind of event exhibiting electrons or gammas of these energies could be a "neutrino-candidate", and then a possible source of background.

The source of the background could be "internal" or "external". The internal background is due to events generated within the Inner Vessel; the external one is due to events occurred outside the Inner Vessel, in any material surrounding the scintillator, with emission of neutral particles (neutrons or photons) entering the Inner Vessel and here simulating a "neutrino-candidate" event. The main sources contributing to the background are the following:

- radioactive decay of ^{238}U, ^{232}Th chains and ^{40}K isotope which contaminate the TMB and the materials used for the detector and its shielding, as the acrylic, stainless-steel, water, sulphurcrete, etc.
- beta-decay of ^{14}C which can be present, although in a small isotopic percentage, in the $B(OCH_3)_3$;
- background from the walls of the hall: photon and neutron induced interactions.
- cosmic rays and their induced interactions and activities.

12.2 *Background from ^{238}U,^{232}Th,^{40}K radioimpurity in the TMB*

The problem of internal background and the possible methods, that could be adopted

in order to reduce it, have been treated with deep detail in the chapter III. The results presented there have been obtained by a complete simulation: the generation of the signal and background events have been done by means of the code CRONOS, developed on purpose; the full simulation and reconstruction have been made by the SRSE program (the two codes are described in chapter X and Appendix V). In performing this simulation, the main working hypotheses that have been set-up are the following:

- ^{235}U chain is not considered, because it gives a negligible contribution to the background;
- ^{238}U and ^{232}Th radioactive chains are supposed to be in secular equilibrium;
- the β decay occurs according to its own theoretical law;
- the γ emission is simultaneous to the previous α or β decay (the lifetime of a nuclear excited state is of the order of some femtoseconds, while the timing resolution in BOREXINO is of the order of nanoseconds).
- the gamma energy and intensity were assumed according to a calorimetric model, that is by summing up the energies of the single cascade gamma rays and ascribing their intensities to the "father" α or β decay. This assumption is motivated by the following reasons: beta and gamma emissions are mostly simultaneous and the detector cannot separate these two energy sources.
- the energy of alpha particles is taken into account reduced by a factor QF of its original value, owing to the alpha quenching effect in the scintillation mechanism. The QF's depend on the alpha energy, and they have been measured in a typical scintillator (see section 10.4.).

On the basis of the foregoing statements the decay-scheme "alpha+gamma" consists of two events with energies $E_{\alpha(quenched)}$ and E_γ taking into account that it is possible to operate a high-efficiency pulse-shape discrimination in order to identify the alpha particle (see chapter VII). In a different way the decay scheme "beta+gamma" is considered as a single event, with energy $E=E_\gamma+E_\beta$, involving one electron and one gamma.

Table 12.I. Radioimpurity level of the TMB – IV = 100 tons.

Isotope	Contamination (g isot/g TMB)	Total mass in IV (g isot)
^{238}U	$1\ 10^{-16}$	$3\ 10^{-8}$
^{232}Th	$1\ 10^{-16}$	$3\ 10^{-8}$
K_{nat}	$1\ 10^{-14}$	$3\ 10^{-6}$

As already described in the chapter X, the scintillator contamination values, assumed for the simulations are reported in Table 12.I.

12.3 *Background from radioimpurity of materials*

The background due to the radioimpurities of the materials used for the detector has been studied; it concerns the acrylic for the inner vessel, the various PMT's components, the water, the stainless-steel of the external vessel, the external shielding. Simulations of this background have been done using the codes CRONOS and SRSE. The following physical assumptions have been used:

-.The isotopes of the ^{238}U and ^{232}Th families are supposed in secular equilibrium;
- α and β tracks from the decays of the radioactive components of the chains do not contribute to the background.This assumption is rigorous not only for α's, but also for β's: for them it has been found that the ratio between the contribution of Bremsstrahlung from β's and that from γ's is about 0.5-1.% (the typical range for an electron in the energy region 0 -15 MeV and in a material like water or acrylic, of density ~1 g/cm^3, does not exceed few centimetres, i.e. the vessel thickness).

The study of the background from water and a specially steel and photomultipliers, which are far from the fiducial volume, presents an important problem of statistics. The problem was solved by using both the codes CRONOS and MCNP [12.1] for the simulation. The advantage in using MCNP with respect of CRONOS is that with MNCP it is possible to introduce different weights in producing the events, allowing to increase the statistics only in the regions where this is needed. The code increases artificially the particles reaching the regions of particular interest, with a corresponding reduction of their statistical weight, and kills particles in the regions of low interest in order to save computer time.

In the regions outside the TMB, gammas have been propagated by means of MCNP; the resulting gamma spectrum at the surface of TMB is used as input of the CRONOS program, which propagates the events inside the scintillator. Then the usual reconstruction follows.

The gammas have been generated and propagated in the materials adjacent to the inner vessel, according to the detector design described in chapter VI. For each material the levels of impurity assumed are the same mentioned in Table 6.II, which

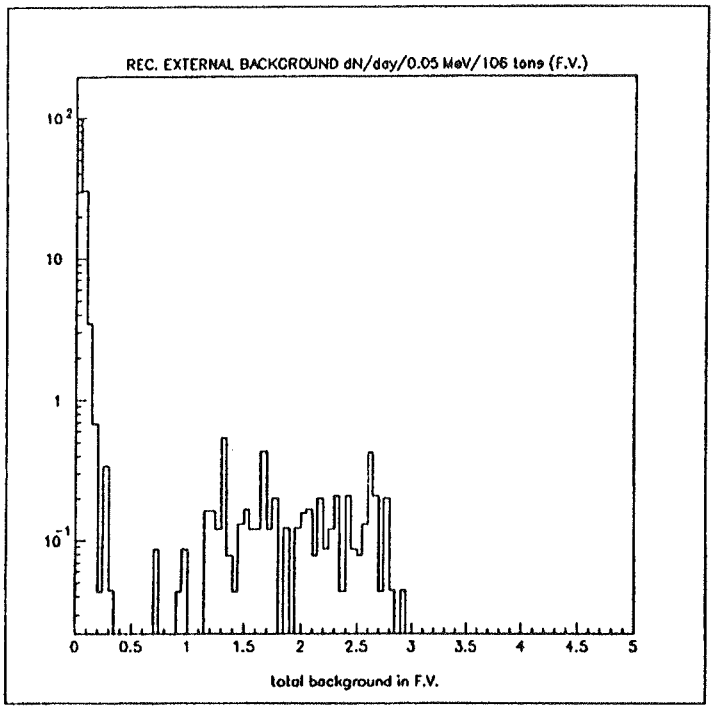

Figure 12.1a. External background spectrum in the Fiducial Volume. Rates are in events/day/FV.

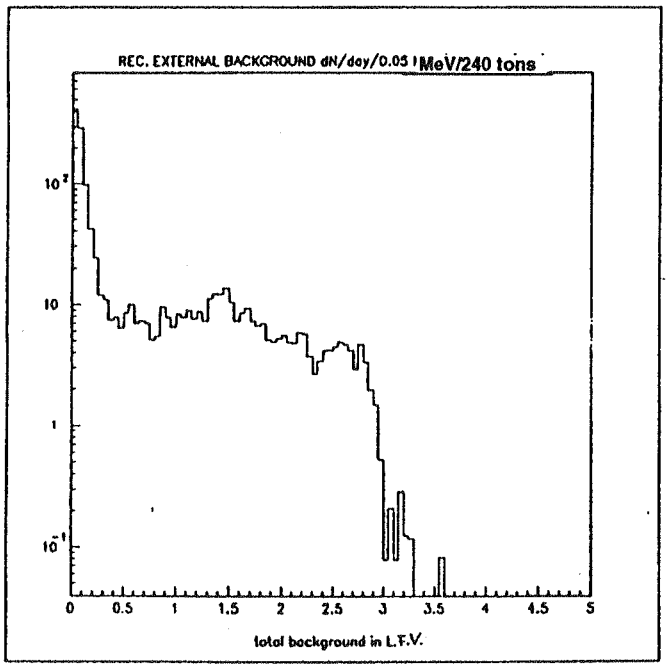

Figure 12.1b. External background spectrum in the Large Fiducial Volume. Rates are in events/day/LFV.

were used as basis for the design of the different parts of the detector.

The backgrounds due to the different sources are summarised in Table 12.II, for the FV of 100 tons (300cm of radius) and for the FV of 240 tons (LFV; 400 cm of radius). These results refer to the first option of the detector (external vessel of stainless-steel plus sulphurcrete).The total background is almost the same also in the case of the second option (large water pool and only an external structure for the support of the PMT's). In any case it is possible to conclude that in the Borexino detector (FV for the low energy range: 0.25-0.8 MeV; LFV for the high energy range: E>4 MeV) the background originated from the materials is very small and nearly negligible. It is worth to notice that in the treatment of the background we face the problem of reconstructing events also very near to the inner vessel walls, where the spatial resolution is not very good. In Fig.12.1a the total energy spectrum of the background produced in the Fiducial Volume (r=300 cm) by all the materials present in Borexino,with the exception of the TMB, is displayed. In fig. 12.1b the same spectrum in the Large Fiducial Volume (r=400 cm) is shown.

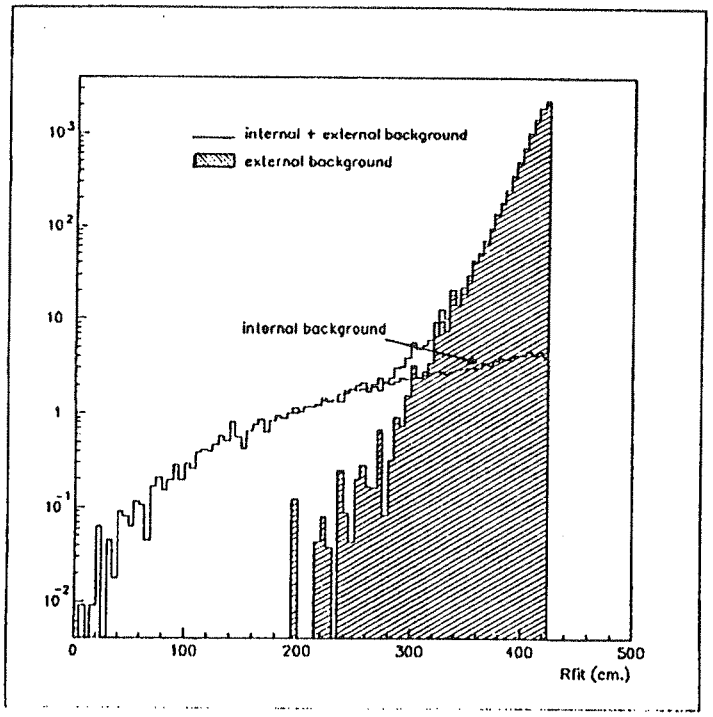

Figure 12.2. Radial dependence of internal, external and total background in the Inner Vessel (energy range: 250-800 keV)

12.3.1 *Identification of the external background*

The definition of a larger size F.V. is strictly connected with the possibility to identify the background from the materials and the shielding (external background) and to subtract it from the total signal. The external background grows roughly of one order of magnitude every 50 cm of the water thickness, while the internal background (due to the TMB) grows obviously as the cube of the F.V. radius. These behaviours are displayed in Fig. 12.2, where both the contributions of the external and internal background are

Table 12.II. Background induced in the FV and in the LFV by the various materials: rate per day

	Rate d^{-1} F.V (r=300 cm)	Rate d^{-1} L.F.V. (r=400 cm)
Acrylic		
$0.25 < E_{event} < 0.8$ MeV	0.5	334.
$E_{event} > 3.5$ MeV	0.	0.
Water		
$0.25 < E_{event} < 0.8$ MeV	0.1	199.
$E_{event} > 3.5$ MeV	0.	0.
Steel		
$0.25 < E_{event} < 0.8$ MeV	<1.	155.
$E_{event} > 3.5$ MeV	0.	0.33
PMT		
$0.25 < E_{event} < 0.8$ MeV	<0.1	86
$E_{event} > 3.5$ MeV	0.	0.13
All materials		
$0.25 < E_{event} < 0.8$ MeV	<1.7	774.3
$E_{event} > 3.5$ MeV	0.	0.46

shown.

Then it is possible to extrapolate the contribution of the external background as function of the radius within the Inner Vessel, in order to evaluate it and to subtract it from the total signal. We plan to test this possibility at the beginning of the Borexino run and to apply the method to define a larger F.V. during the analysis, in order to improve the total neutrino signal.

12.4 *Neutrons and gammas backgrond from materials outside the detector*

Neutrons and gamma rays produced in the rock and in other materials present in the cave are a major source of the external background in Borexino.

12.4.1 *Neutrons*

The main sources of neutrons into the Gran Sasso National Laboratory are (α, n) and fission reactions in the rocks . This section is focussed on the effects of the neutrons in materials of interest for Borex and on an estimate of the contribution to the background in the Fiducial Volume by neutrons.

12.4.1.1 *Neutron experimental measurement*

The neutron flux at LNGS has been measured by various authors [12.2], [12.3], [12.4]; the results are summarised in the Table 12.III. Each experiment used a different technique to count only thermal neutrons and to moderate the fast component shielding of different materials. The measurement of Belli et al. [12.2] was done in the Hall A during several months. They used a set of five BF_3 counters, polyethylene planes of various thicknesses to moderate and count the fast component. We have used their results as input to our simulation.

Table 12.III - Neutron flux at LNGS as measured by various authors

Energy range [KeV]	Ref.[12.2] 10^{-6} neutrons $cm^{-2}s^{-1}$	Ref.[12.3] 10^{-6} neutrons $cm^{-2}s^{-1}$	Ref.[12.4] 10^{-6}neutrons $cm^{-2}s^{-1}$
0-5 10^{-5}	1.08±0.02		↑
5 10^{-5} -1	1.84±0.20		5.3±0.9
1-2.5 10^{3}	0.54±0.01		↓
2.5 10^{3}- 5 10^{3}	0.27±0.14	↑	↑
5 10^{3}- 10 10 ^{3}	0.05±0.01		
10 10^{3}- 15 10^{3}	(0.6±0.2)10^{-3}	0.78±0.3	3.0±0.8
15 10^{3}-25 10^{3}	(0.5±3)10^{-6}	↓	↓
TOTAL: 0-25 10^{3}	3.781±0.24		

12.4.1.2. *Neutron simulation*

We used MCNP version 3 [12.1] to generate and follow the neutrons. For these simulations we used, in addition of the original European neutron set of cross sections, a more recent set provided by Dr. K. Burn of ENEA. [12.5]

12.4.1.3 *Behaviour of the neutrons in water and TMB*

For a thermal neutron the favourite reactions are the capture on ^{10}B in TMB and the capture on ^{1}H in water through the following scheme:

$$n + {}^{10}B \rightarrow {}^{7}Li + \alpha\ (1.78\ MeV)\ (6\%)\ \text{or}$$
$$\rightarrow\ {}^{7}Li^{*} + \alpha\ (1.47\ MeV)\ (94\%)$$
$$\downarrow$$
$$\rightarrow\ {}^{7}Li + \gamma\ (0.48\ MeV)$$

$$n + {}^{1}H \rightarrow D + \gamma\ (2.224\ MeV)$$

The thermal cross sections for elements present in water and TMB and for further elements present in different materials used in Borexino are summarised in Table 12.IV

Isotope	σ(n,γ) barn	n separation energy [MeV]	Isotopic abundance [%]
H	0.33	2.224	100
^{6}Li	σ(n,p)=0.038 σ(n,α)=941	7.250	7.5
^{7}Li	0.045	2.033	92.5
^{7}Be	$\sigma(n,p)=4.8\ 10^{4}$	18.899	unst. $t_{1/2}$ =53.3 d
^{9}Be	0.008	6.811	100
^{10}Be	<1		unst. $t_{1/2}=1.6\ 10^{6}$ y
^{10}B	0.5 σ(absorp)=3837	11.455	20
^{11}B	0.0055	4.946	80.
^{12}C	0.0035	4.946	98.90
^{13}C	0.0013	8.176	1.1
^{14}N	0.075 σ(n,p)= 1.73	10.833	99.63
^{16}O	$1.9\ 10^{-3}$	4.144	99.762
^{17}O	$5.4\ 10^{-3}$ 0.235	3.957	0.038
^{18}O	$1.6\ 10^{-3}$	3.957	0.2

Table 12.IV. Neutron cross sections

Table 12.V Neutron cross sections

Isotope	σ(n,γ) barn	n separation energy [MeV]	Isotopic abundance [%]
^{23}Na	0.53	6.959	100
^{27}Al	0.23	7.725	100
^{28}Si	0.177	8.473	92.23
^{29}Si	0.101	10.609	4.67
^{30}Si	0.107	6.588	3.1
^{39}K	2.1	7.8	93.258
^{40}K	30 σ(n,α)=0.39 σ(n,p)= 4	10.096	0.012
^{41}K	1.46	7.594	6.73
^{54}Fe	2.25	9.298	5.8
^{56}Fe	2.59	7.646	91.72
^{57}Fe	2.48	10.044	2.2

Table 12.VI. Mean absorption time and radii of containment of the neutrons, as function of the energy

	TMB			Water		
	0.025 eV	0.5 MeV	10 MeV	0.025 eV	0.5 MeV	10 MeV
time [μs]	1.	1.1	7.5	209	238	197
radius 50% [cm]	<0.5	58	68	6	10	20
radius 90% [cm]	<1	72	138	15	18	32
radius 99% [cm]	<1.5	104	230	26	30	71

Tables 12.VII Composition of steel and sulphurcrete

Elem. % in Weight	C	S	Si	Mn	Fe	P	Cr	Ni
STEEL (305 C)	0.12	0.03	1.	2	64.805	0.045	14.	13.

Elem. % in Weight	C	H	B	O	Na	Mg	S	Si	K	Ca	Mn	Fe	Al
SULPHUR.	0.12	0.03	1	44.48	0.04	10.99	12.82	0.08	0.01	19.06	0.04	0.09	0.07

and 12.V, respectively [12.6]. Table 12.VI shows, as function of the neutron energy, the mean absorption time and the radii of the spheres, centred on the point of creation of the neutron, that has the probability of 50%, 90%, 99%, respectively, to contain the neutron.

The composition of materials used is: $B(COH_3)_3$ for TMB; $C_5H_8O_2$ for Plexiglas; is shown in Table 12.VII, for steel and sulphulcrete.

12.4.1.4 *Results*

The total number of neutrons impinging on the detector is 2.53 10^6 neutrons/day

(design B of Chapter VI). Fig 12.3a shows the number of ingoing neutrons and photons as a function of radius per starting neutron. The neutron flux becomes 1/day at 6.2 meters; the gamma flux is 1/day at 5.4 m. At the radius of the inner vessel (4.25 m, design B of chapter VI), we have

$$\text{Neutron flux} = 2.3 \pm 0.4\ 10^{-5}\ \text{neutrons d}^{-1}$$
$$\text{Gamma flux} = 3.8 \pm 0.7\ 10^{-2}\ \text{gammas d}^{-1}$$

These numbers are much less than the background created by the plastic vessel itself or the photomultipliers, so this background is negligible. In the design with the large water pool (design A of chapter VI) the fluxes mentioned above become, at the radius of the Inner Vessel (see fig. 12.3b)

$$\text{Neutron flux} < 10^{-6}\ \text{neutrons d}^{-1}$$
$$\text{Gamma flux} = 2.8 \pm 0.5\ 10^{-2}\ \text{gammas d}^{-1}$$

Then the contribution to the background from neutrons generated by spontaneous fission and (α,n) reactions inside the detector is estimated to be negligible due to low levels of radioimpurities.

12.4.2 *Gamma background from the walls of the Hall*

The gammas are mainly produced by radioactive elements connected to ^{238}U and ^{232}Th chains and by ^{40}K while a contribution to energies above few MeV comes by the n capture on nuclei.

12.4.2.1 *Gamma measurements*

Measurements have been performed in the hall "C" with a Ge-detector of high intrinsic efficiency and large size. The total detector efficiency has been calculated by means of a Monte Carlo code. The crystal was a cylinder, 10.4 cm height and 3.6 cm of radius. It has a death core of 0.56 cm of radius and 9.23 cm height, its volume is about 415 cm^3 and its surface is about 230 cm^2.

The measurements were done with an energy scale from 0 to 3 MeV. A typical spectrum is shown in fig. 12.4. Higher energy measurements, up to 10 MeV, are now in progress using a NaI detector.

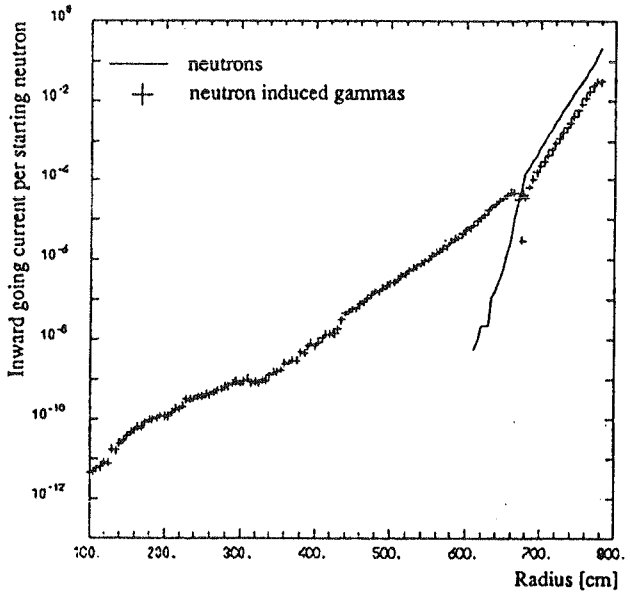

Figure 12.3a. *Design B (chapter VI) – number of inward going neutrons and neutron induced photons per starting neutron.*

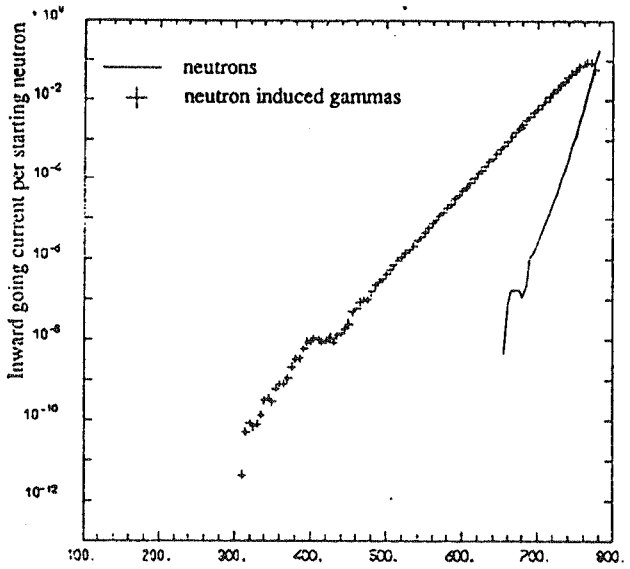

Figure 12.3b. Water pool – design A (chapter VI) – number of inward going neutrons and gammas per starting neutron.

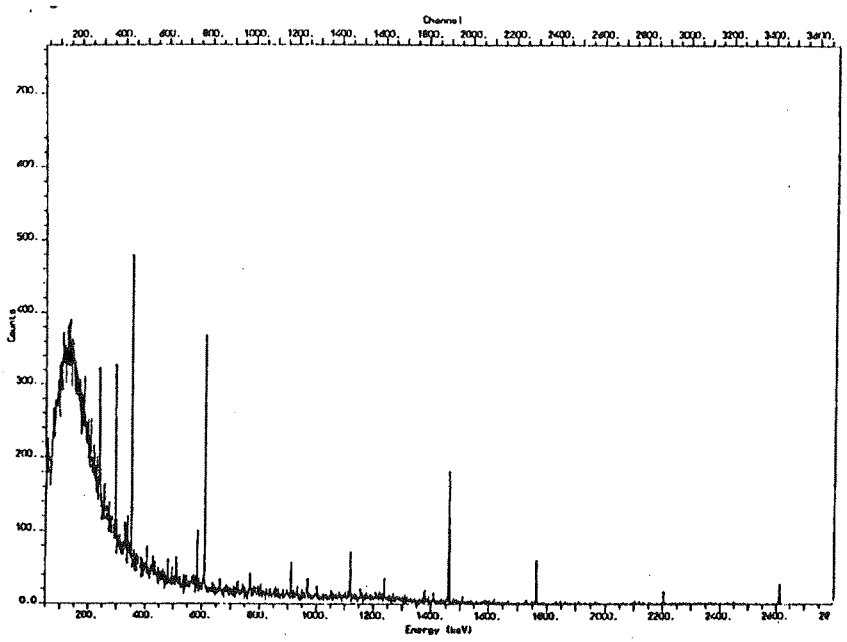

Figure 12.4. Gamma spectrum measured in the Hall C at LNGS.

Table 12.VIII. Measurements of gammas from the rocks and the computed activities in Hall "C" of LNGS

element	Energy KeV	counts/hour ± error	detect. eff. %	flux $m^{-2} d^{-1}$
^{40}K	1460.	3884±97	10.23	$3.8\ 10^7$
^{238}U	chain			
^{214}Pb	241.9	902±64	30.6	$0.31\ 10^7$
^{214}Pb	295.2	2088±109	27.	$0.81\ 10^7$
^{214}Pb	352	4298±118	25.	$1.8\ 10^7$
^{214}Bi	609.3	4962±109	17.8	$2.9\ 10^7$
^{214}Bi	1120.3	1587±64	12.1	$1.4\ 10^7$
^{214}Bi	1764.5	1525 ±60	9.13	$1.7\ 10^7$
^{232}Th	chain			
^{212}Pb	238.6	1000±68	30.6	$0.34\ 10^7$
^{228}Ac	338.7	237±69	26.8	$0.09\ 10^7$
^{208}Tl	583	728±55	18.4	$0.41\ 10^7$
^{228}Ac	911.2	624±52	13.5	$0.48\ 10^7$
^{208}Tl	2614.5	817±43	6.3	$1.35\ 10^7$

For each gamma line in the spectrum, it is possible to estimate the number of gammas impinging on a detector per square meter. The Ge-data and results are summarised in Table 12.VIII.

The effect of presence of Rn decays in the air of the cave may be roughly estimated using the measured mean value of 50 Bq/m^3 of ^{222}Rn in hall "C" [12.9] and scaling this number to its daughters. That gives

0.3 10^7 gamma of 1764 keV /(m^2 day) for ^{214}Bi

The contribution of ^{220}Rn is negligible due to its short lifetime.

12.4.2.2. *Estimate of background from impurities in the walls*

The measured contamination of the rock of hall "C" is [ref.12.14]:

U: 6.6 10^{-7} g/g; Th: 6.6 10^{-8} g/g; ^{40}K: 1.2 10^{-8} g/g

The density of the rock is about 2.7 g/cm^3 and its composition mainly $CaCO_3$. The walls of the cave are lined with about 35 cm of concrete. The floor of the cave is also made by concrete and it is about 45 cm thick, 2.5 g/cm^3 of density.

The contamination of concrete used was assayed to be:

U: 11 10^{-7} g/g; Th: 87 10^{-8} g/g; ^{40}K: 59 10^{-8} g/g

The flux leaving a unit of surface of the wall is:

$$\text{Flux}(E) = \int_0^{\pi/2} d\theta \int_0^{2\pi} d\phi \int_0^{\infty} dR \, \frac{\cos\theta \, R^2 \, I \, e^{-R/\lambda(E)} \sin\theta}{4\pi R^2}$$

where I is the number of disintegrations per volume unit per time unit and $\lambda(E)$ is the gamma attenuation length in that medium at a given energy. The result of the integration is $I \cdot \lambda/4$ that means that in principle only a thickness of $\lambda/4$ contributes to the flux. The estimated flux is shown in column 3 of Table 12.IX. It is computed knowing that from

1 gram of ^{238}U there are 1.07 10^9 decays/day
1 gram of ^{232}Th there are 0.35 10^9 decays/day
1 gram of ^{40}K there are 23.4 10^9 decays/day,

Table 12.IX. Estimated and measured gamma rays fluxes from concrete

Energy [KeV]	λ (concrete) [cm]	estimated γ's from walls $m^{-2} d^{-1}$ (1)	measured γ's from walls $m^{-2} d^{-1}$ (2)	estimated γ's from walls $m^{-2} d^{-1}$
2614 (^{208}Tl)	8.8	$0.85\ 10^7$	$1.35\ (\pm 0.1)\ 10^7$	$1.7\ 10^7$
1764 (^{214}Bi)	7.2	$0.6\ 10^7$	$1.7\ (\pm 0.1\ \pm 0.3)\ 10^7$	$1.2\ 10^7$
1460 (^{40}K)	6.4	$5.5\ 10^7$	$3.8\ (\pm 0.1\ )\ 10^7$	$11\ 10^7$

(1) values computed using the "infinite" wall assumption.
(2) values computed using a cylindrical geometry.

using the impurity levels of concrete and a factor that links the parent's activity to its daughter (16% for ^{214}Bi and 36% for ^{208}Tl) . Column 4 of Table 12.IX shows the measured values. In column 5 the estimated values are shown taking into account that the cave is not an infinite wall but a cylinder.

12.4.2.3 *Conclusion about the gammas from the rocks*

The two evaluations obtained from the direct measurements (§ 12.4.2.1) and from the radioimpurities levels of the concrete (§ 12.4.2.2) agree quite well, taking into account the simple model which has been assumed. The small discrepancy in the values for the potassium line is probably due to the non uniform distribution of the element in the concrete.

Taking into account the flux of the 2.614 MeV line from ^{214}Bi, which is the highest energy line in the chains, the total flux for this line on Borexino will be of about $2 \cdot 10^{10}$ gamma/day on the surface of the detector for solution A (water pool) and 10^{10} gamma/day for solution B (multilayer). From the fig. 12.5a and 12.5b, the background induced in the F.V. is estimated to be of 1 event/day for solution A and 0.5 events/day for solution B. The background from the other natural radioactivity lines is less than 10 % of the previous estimate due to their lower energies. From the previous discussion we can conclude that with some very small changements in the total design of the detector the background from the concrete can be considered negligible.

For what concerns instead the attenuation of higher energies gamma rays in Borexino

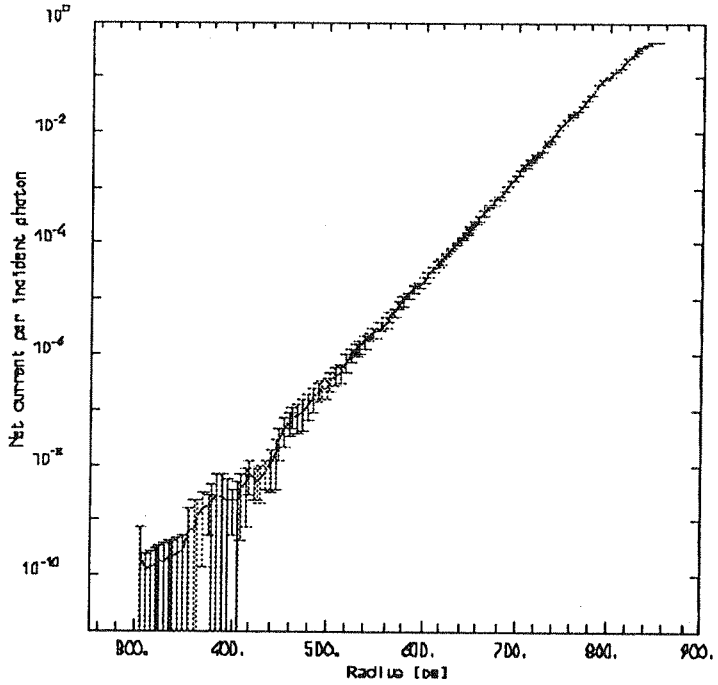

Fig. 12.5.a 2.614 MeV gamma rays in Borexino (design A, Chapter VI-water pool)

Fig. 12.5b 2.614 MeV gamma rays in Borexino (design B, Chapter VI-multilayer)

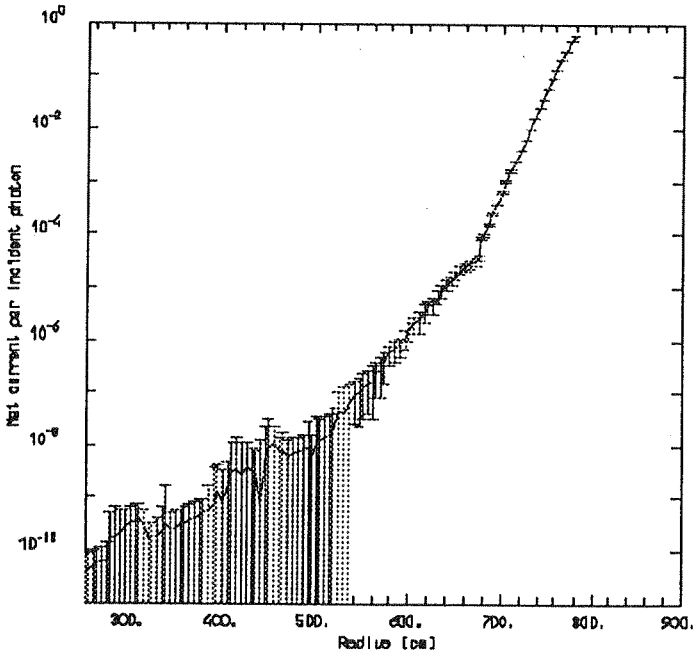

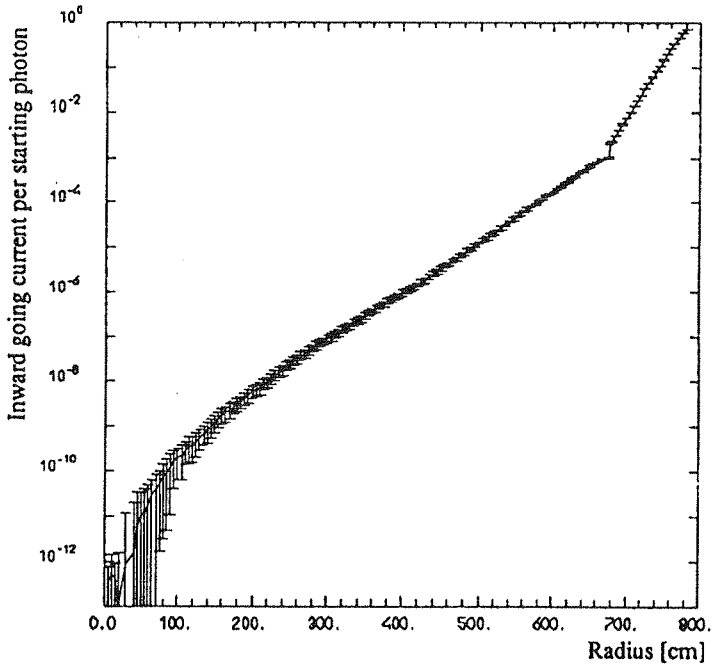

Figure 12.5c. Number of inward going photons per starting 8 MeV photon on the surface of Borexino (design B).

a simulation has been run to understand the attenuation of 8 MeV gamma rays in the detector. The result is shown in fig. 12.5c as the number of inward going photons per one starting gamma on the surface of Borexino with an inward cosine distribution as a function of radius.

The result of the simulation is that in order to have a flux of 8 MeV gamma rays not larger than 1 event per day at the surface of the inner vessel, the starting flux must not exceed 1.7 10^6 gamma/day. If the request is $\leq$ 1 per day at 300 cm (FV radius) the starting flux cannot exceed $1 \cdot 10^7$ gamma/day. Even if we do not expect any problem from the high energy γ's background, measurements of the starting flux in the Hall C are in progress.

12.5 *Cosmic Muon Induced Activity in Borexino*

Cosmic ray muons can create radioactive isotopes which later decay to β's and γ's in

201

the energy range of the neutrino interaction in Borexino. In the following we have tried to estimate the expected muon flux and the possible background induced by them. The aim of this study is both to estimate this background and to understand how to correlate these induced events with the muon signal in our detector in order to tag them.

The considered processes induced by cosmic muons are: electromagnetic nuclear reactions, capture of stopping muons, interaction induced by neutrons generated in the nuclear reactions. In these processes isotopes A^* can be produced. If the decay times of A^* and all its daughter products are short ($t_{1/2} < 1$ s) the muon induced event can be correlated in the detector by its time coincidence with the signal produced by the muon as it passes through the detector. However, if the decay time of A^* or any of its daughter products B^* is long ($t_{1/2} >> 1$ s) the signal associated with the decay of A^* or B^* is less easily vetoed because other signals may arrive in the dead time gate (see § 12.5.5).

12.5.1 *Cosmic Muon flux*

We computed the underground muon intensity at the depth of the Gran Sasso Laboratory. This intensity at a depth h and zenith angle θ can be factorized as:

$$I_\mu(h,\theta) = I(h)\, G(h,\theta)$$

where I(h) represents the "vertical intensity" and $G(h,\theta)$ accounts for the angular enhancement [12.10]. We parametrized I(h) as :

$$I(h) = A\, h^{-a}\, e^{-bh}\ cm^{-2}\ sterad^{-1}\ s^{-1}$$

where h is measured in $hg \cdot cm^{-2}$ of standard rock. We assumed [12.10] A=108.5, a=2.51 and b= $7.177\ 10^{-4}$. According to usual approximations [12.10], the function $G(h,\theta)$ can be assumed to be independent from h for $\theta < 80^o$ and given by:

$$G(h,\theta) \cong G(\theta) \cong 1/\cos(\theta)$$

The rock depth crossed by a muon coming from a given (θ, ϕ) direction, namely the depth h (θ, ϕ), was estimated using a map of the Gran Sasso region [12.11] . In the calculations, we assumed the Gran Sasso rock as standard rock ($\rho_{s.r.} = 2.65\ g/cm^3$, $\rho_{GS}=2.73\ g/cm^3$ [12.11]).

The muon flux $I_\mu(\theta,\phi)\, d\Omega$ was then evaluated in step of $\Delta\phi = 4^o$, $\Delta\theta = 2^o$ covering the

interval $0^o < \phi < 360^o$ and $0^o < \theta < 80^o$. We obtain a muon flux of:

$$I_\mu \cong 1.1\, h^{-1}\, m^{-2}$$

The muon fluxes in the Borexino apparatus are shown in Table 12.X

We estimated the number of muons stopping in our detector . On the basis of the relation range/energy [12.12] for muons, we have converted the mean path travelled by a muon in the detector in an equivalent path in standard rock (~9.5 hg/cm^2) . Using the depth dependence of the ratio of stopping to thoroughgoing muons for an isotropic detector [12.13] we expect about 36 stopping muons per day in TMB (IV) and about 110 stopping muons per day in H_2O buffer (s=250 cm). Following ref. [12.14] we use the ratio $\mu^+/\mu^- = 1.4$ for the atmospheric component, while for muons from the local cascade and from neutrino interactions we used $\mu^+/\mu^- = 1$.

In addition the positive stopping muons always decay; negative muons can be captured or decay in the detector. The ratio (capture/decay) = $3.3\ 10^{-4}\ Z^4$ has been taken from ref. [12.15]. We have computed this ratio for each element of the compound TMB and weighted according to the stechiometric ratio [12.16]. The obtained rates of muons decaying and captured in the Inner Vessel are shown in Table 12.XI.

12.5.2. *Muon Capture*

A negative muon can be captured by a proton of the nucleus (Z,A):

Table 12.X. Muon fluxes in the Borexino apparatus

Muons in the TMB sphere (IV) (r=425 cm)	64 h^{-1}
Muons in H_2O buffer not crossing TMB (s=250 cm)	94 h^{-1}

Table 12.XI. Rates of stopping μ^+ and μ^-

	decays in TMB(r=425cm)	captures in TMB(r=425cm)
μ^+	19 d^{-1}	0
μ^-	13 d^{-1}	4 d^{-1}

Table 12.XII. Muon capture on ^{11}B, ^{12}C, ^{16}O

Isotope	$t_{1/2}$	Decay	Q(MeV)	Formation
^{12}B	20 ms	β^-	13.4	$^{12}C(\mu)$
				$^{16}O(\mu,\alpha)$
^{9}Li	0.18 s	β^-	13.5	$^{10}B(\mu,p)$
				$^{11}B(\mu,p,n)$
^{6}He	0.81 s	β^-	3.5	$^{10}B(\mu,\alpha)$
^{8}Li	0.84 s	β^-	16	$^{10}B(\mu,p,n)$
				$^{12}C(\mu,\alpha)$
^{15}C	2.4 s	β^-	9.82	$^{16}O(\mu,p)$
^{16}N	7.2 s	β^-	10.4	$^{16}O(\mu)$
^{11}Be	13.8 s	β^-	11.5	$^{12}C(\mu,p)$
				$^{11}B(\mu)$
$t_{1/2}$ > d				
^{7}Be	53.29 d	γ (10%)	0.478	$^{10}B(\mu,3n)$
				$^{11}B(\mu,4n)$
$t_{1/2}$ >y				
^{3}H	12.3 y	β^-	0.0186	$^{12}C(\mu,2\alpha,n)$
^{14}C	5730 y	β^-	0.155	$^{16}O(\mu,p,n)$
^{10}Be	1.6 10^6 y	β^-	0.555	$^{10}B(\mu)$
				$^{11}B(\mu,n)$
				$^{12}C(\mu,p,n)$
unstable				
^{10}Li	unstable			$^{11}B(\mu,p)$
^{7}He	unstable			$^{11}B(\mu,\alpha)$

$$\mu^- + (Z,A) \rightarrow (Z-1,A)^* + \nu_\mu$$

where a proton changes into a neutron [12.16]. The major part of the 107 MeV produced by this reaction is carried off by the neutrino. The energy left to the neutron varies from about 5.7 MeV for the proton at rest to some tens of MeV. The (Z-1, A)*

nucleus is de-excited mostly by the emission of one or more neutrons, gamma or beta rays.

Table 12.XII shows the muon induced activity created by the capture on nuclei of our interest [12.16,12.17]. ^{7}Be decay is the only source of low energy events which cannot be correlated to muon capture, but it is recognised by the energy of the γ. In any case we know [12.16] that the reaction with 1 neutron in the final state is more probable, that γ-rays accompany the neutron emission with high probability (~80%), that the emission of protons occurs infrequently (2%) and the emission of α-particles occurs for 0.5% of the time.

KAMIOKANDE II experiment [12.22] finds that in H_2O 11% of the muon captures leads to ^{16}N formation. It supposes that about 70% of the captures leads to ^{15}N formation

Table 12.XIII. Long lived isotopes by muons crossing our detector with a de-excitation energy < 5 MeV.

Isotope	$t_{1/2}$	Decay	Q(MeV)	Reaction	σ_{-1}(mb)	R ($d^{-1}kt^{-1}$)	R(d^{-1}) TMB (r=425cm)
^{7}Be	53.3 d	γ (10%)	0.48	$^{11}B(\gamma,^{3}H,n)$	600	0.7	0.2
				$^{12}C(\gamma,\alpha,n)$	500	1.8	0.5
				$^{16}O(\gamma,2\alpha,n)$	250	0.9	0.3
^{11}C	20.4 m	β^+	0.96	$^{12}C(\gamma,n)$	4500	16	5
^{15}O	122 s	β^+	1.72	$^{16}O(\gamma,n)$	6000	21	6

Table 12.XIV. Muon induced spallation activities relevant for Borexino.

Isotope	$t_{1/2}$	Decay	Q(MeV)	Formation: (Target)Spall.Products
^{12}N	11ms	β^+	17.4	(^{16}O)p3n
^{13}B	17 ms	β^-	13.4	(^{16}O)3p
^{12}B	20 ms	$\beta^-+\gamma$	11.5	(^{16}O)3pn
^{9}C	0.13 s	β^++p	16	(^{16}O)2p5n;(^{12}C)3n
^{9}Li	0.18 s	β^-,β^-+n	13.6	(^{16}O)5p2n;(^{12}C)3p;(^{11}B)2p
^{8}B	0.77 s	β^+	15	(^{16}O)3p5n;(^{12}C)p3n;(^{11}B)3n;(^{10}B)2n
^{8}Li	0.84 s	β^-	16	(^{16}O)5p3n;(^{12}C)3pn;(^{11}B)2pn;(^{10}B)2p
^{11}Be	13.8 s	$\beta^-+\gamma$	11.5	(^{16}O)3pn
^{14}O	71 s	$\beta^++\gamma$	5.1	(^{16}O)2n

which is stable. Our conclusion is that, due to the low number of muon capture events in Borexino, the untaggable background is negligible.

12.5.3 Muon-induced Radioactivity

The thoroughgoing muon can produce electromagnetic nuclear reactions in the detector via inelastic scattering:

$$\mu + A \rightarrow \mu' + A^*$$

Table 12.XIII gives a list of isotopes with half-lives longer than 100 s and with a de-excitation energy < 5 MeV, which could result from nuclear reactions of muons with materials used in our detector. These radioactive isotopes can be produced by knocking out one or more nucleons in an inelastic muon scattering reaction [12.18].

Following ref. [12.18] we computed the number of nuclides per day produced via an electromagnetic nuclear reaction:

$$R(d^{-1}) = 6 \times 10^{-2} F_\mu (d^{-1} m^{-2}) N_A (kt) \sigma_\mu (mb) / A$$

where: F_μ is the flux of muons on the detector; N_A is the number of target nuclei in the detector; σ_μ the B* production cross section of the muon reaction and A, the atomic weight of the target nucleus. Assuming that the average underground muon energy is about 200 GeV and that the average energy of the virtual photons absorbed by the nucleus is 20 MeV, we estimated the rate $R(d^{-1})$ shown in Table 12.XIII. σ_{-1} are the cross sections measured in ref [12.19] where the targets ^{16}O, ^{12}C have been irradiated with 1-GeV Bremsstrahlung beam and the variations isotopes are produced. The σ_{-1} for the target ^{11}B is not measured but was extrapolated from the data of ref [12.19].

The background in the F.V. consists, at the equilibrium, of ~0.04 gammas/day produced by the ^7Be decays and ~4 β^+'s/day from ^{11}C and ^{15}O. The β^+'s are captured giving origin to gammas with an energy ranging between ~1 and ~2.7 MeV, outside the energy range interesting for Borexino.

Further spallation reactions are shown in Table 12.XIV; these reactions can be vetoed using delayed coincidences

12.5.4 *Neutrons Generated by throughgoing muons*

The mean number of neutrons induced by cosmic-ray muons has been measured by the LSD experiment at the Mont Blanc Laboratory [12.21].

The experimental result is :

Table 12.XV. Neutron production rate by muons in the Borexino apparatus

Material	Radius (cm)	Density (g/cm^3)	Neutrons generated (d^{-1})	Neutrons background in F.V (d^{-1})	Gammas background in F.V by neutrons (d^{-1})	Neutrons background in I.V (d^{-1})	Gammas background in IV generated by neutrons (d^{-1})
TMB F.V.	300	0.918	94	89.4	101.4	94	112.7
TMB I.V.	425	0.918	176	4.5	6	168.3	187.7
H_2O	675	1.	800	$2.2\ 10^{-4}$	0.1	8	25.8
Steel	677	8.	76	0	$1.4\ 10^{-4}$	$<10^{-8}$	$3.6\ 10^{-3}$
Sulfurcrete	785	2.4	1480	0	$5.8\ 10^{-4}$	0	$1.4\ 10^{-2}$
TOTAL				94	107.5	270.4	362.2

Table 12.XVI. Reactions produced by neutrons with an energy not greater than 20 MeV

Isotope	$t_{1/2}$	Decay	Q(MeV)	E_{th} (MeV)	Reaction
^{12}B	20 ms	β^-	13.4	13.64	$^{12}C(n,p)$
				0	$^{11}B(n,\gamma)$
^{8}Li	0.84 s	β^-	16	17.34	$^{10}B(n,^3He)$
					$^{11}B(n,\alpha)$
^{15}C	2.4 s	$\beta^-, \beta^-\gamma$	9.82	22.44	$^{16}O(n,2p)$
^{16}N	7.2 s	$\beta^-, \beta^-\gamma$	10.4	10.2	$^{16}O(n,p)$
^{11}Be	13.8 s	$\beta^-, \beta^-\gamma$	11.5	13.74	$^{11}B(n,p)$
^{11}C	20.38 m	β^+	0.96	20.3	$^{12}C(n,2n)$
^{15}O	122.1 s	β^+	1.73	16.75	$^{16}O(n,2n)$
^{14}C	5730 y	β^-	0.155	15.53	$^{16}O(n,^3He)$
^{10}Be	$1.6\ 10^6$ y	β^-	0.555	0	$^{10}B(n,n,p)$
				12.26	$^{11}B(n,p)$
				9.82	$^{11}B(n,d)$

$$<N_n> = 5.3\ (\pm 1)\ 10^{-4}\ \text{neutrons/(muon g/cm}^2\text{)}$$

at a mean muon energy $<E_\mu>$=385 GeV. This result is found to be in good agreement with an expected distribution given by the power law:

$$<N_n> = <E_\mu>^{0.75}$$

Scaling this neutron number at the mean muon energy of $<E_\mu>$=200 GeV (underground at Gran Sasso), we obtain a mean neutron number of:

$$<N_n> = 3.2\ (\pm\ 1)\ 10^{-4}\ \text{neutrons/(muon g/cm}^2\text{)}$$

Considering the muon flux underground at the Gran Sasso I_μ= 1.1 h^{-1} m^{-2} , the muons crossing per day both detector and shield are ≈5110. The Table 12.XV summarises the neutrons production rates in Borexino and the background induced both in the F.V. and the I.V. This background is due to neutrons reaction in the FV (I.V.) (Table 12.XVI) and to gammas produced outside the considered region, but producing signal in it.

From Table 12.XV we can conclude that the background induced in TMB from neutron generated by muons crossing steel and sulfurcrete is negligible. The neutrons generated in water contribute to the background in the TMB buffer outside the F.V.. The events generated in TMB and water are easy detected since are correlated in space and time with the muon.

In Table 12.XVI the reactions induced by the fast neutrons on the different nuclei, with an energy threshold up to 20 MeV, are shown.

In Table 12.XVII all the reactions induced by fast neutrons and thermal neutrons are summarised. We can observe that mostly of the reactions are n-α, which are due to the capture of thermal neutrons by ^{10}B. Then Table 12.XVII includes all the reactions of Table 12.XVI plus the reactions induced by thermal neutrons. The not negligible sources of background are in this case n-α and n-n' and the decays of the produced isotopes following the first neutron reaction.

Table 12.XVII. Main reactions induced by neutrons per day

	n-γ	n-n'	n-2n	n-p	n-α	n-^{2}H	n-^{3}H	TOTAL
F.V.	0.38	3.6	8 10^{-3}	0.2	94.1	0.07	0	98.3
I.V.	1.09	10.2	0.02	0.4	270.6	0.2	0	282.5

The α emission is expected to have a delay of ~1μs with respect to the incident muon interaction. 1μs is the mean time of flight of the thermal neutron before its capture by a ^{10}B in the liquid scintillator through the reaction

$$n + {}^{10}B \rightarrow \alpha + {}^{7}Li + \gamma\,(0.48\ MeV);$$

the γ is a product of the ^{7}Li deexcitation with a delay of ~10^{-15}s. As a consequence this type of event can be rejected with high efficiency via a delayed coincidence between the μ and the α+γ signals. The n-n' reaction can be tagged following the same procedure by exploiting the n' capture on ^{10}B.

The second kind of background, the decay of the produced isotopes, can be dangerous only if $t_{1/2}$ is longer than few seconds (see Table 12.XVI). The reaction

$$n + {}^{16}O \rightarrow p + {}^{16}N$$

is one of them; ^{16}N decays with a β^- of 10.4 MeV and for the 68.8% with an additional γ of 6.1 MeV. Its contribution is negligible in the region of ^{7}Be neutrinos and in any case this background is only in the ^{8}B region. The reactions ^{11}B(n, p), ^{10}B(n, n, p) and ^{11}B(n, d) are characterised by rates equally negligible. The reactions ^{12}C(n, 2n), ^{16}O(n, 2n) also give a negligible contribution. Finally ^{14}C produced by the reaction ^{16}O(n, ^{3}He) gives a β decay below the detector threshold.

12.5.5 *Identification of the events induced by muons*

Following the method used in KAMIOKANDE II experiment [12.22], we will able to identify a specific isotope, using the time interval between the preceding muon track and the low energy event and the spatial distance between them. In addition KAMIOKANDE II experiment observes that the total pulse height of the preceding muon event is usually much larger than that of a simple thoroughgoing muon and that these low energy events are strictly correlated with the muon induced nuclear interactions; sometimes multiple low energy events are induced by a single muon.

For the cases in which we will able to recognise the stopping muons, the isotope resulted from muon capture is identifiable in a more close spatial region around the end of the muon track.

After the passage of a μ, a cylinder of 1 m radius along the muon track may be

assumed as dead volume for 30 s to allow the decay of short lived isotopes (mean live time=10 s). Under these hypotheses and supposing that every muon creates local radioactivity, 5% of solar ν events are lost.

KAMIOKANDE II experiment observes for $0<\Delta t<0.1$ s low energy events with a $t_{1/2}$ ~18.4±0.9ms which seem to be the beta decay of ^{12}B and ^{12}N; for $0.1<\Delta t<5$ s events with $t_{1/2}$=0.73±0.11 s, which seem to be due to the beta decay of ^{8}B and ^{8}Li. A decay structure with a $t_{1/2}$ ~7 s is also observed; it is presumably due to the beta decay of ^{16}N. The relative ratio of these 3 categories is 6 : 3 : 2.

12.5.6 *Conclusion for the cosmic ray induced background*

The uncorrelated background induced in the F.V. from the cosmic rays can be summarised as follows:

- ~ 0.04 γ's/d from ^{7}Be decays, at 0.48 MeV.
- ~2 β^{+}'s /d which give signal in the energy range 1-2 MeV from ^{11}O; ~2 β^{+}'s/d in the range 1-2.7 MeV from ^{14}O; this background involves an energy range not interesting for the Borexino experiment.
- β^{+}'s from ^{14}O, which gives signals in the energy range 2.3-6.1 MeV; $\beta^{-}+\gamma$ from ^{11}Be (13.8s) in the energy range up to 4.5 MeV. The ^{14}O nuclides do not produce background in the region of ^{7}Be and give a very small contribution in the ^{8}B range. The signal from ^{11}Be can be partly identified through the correlation with the incident muon with a total delay of 30 s (see §12.5.5)

12.6 *^{7}Be, ^{10}Be production rates at sea level*

In this section we are considering the production rate of the ^{7}Be and ^{10}Be nuclides at sea level to estimate the residual contamination of these nuclides in the TMB when it will be stored inside the Gran Sasso tunnel. As the half life of ^{7}Be ($t_{1/2}$=53.3 d) is short, the production of this nuclide by cosmic rays is important not only in the Colemanite, but also in the TMB itself when stored outside the Gran Sasso. On the other hand, the production of ^{10}Be ($t_{1/2}$= 1.6 10^{6} y) is dangerous only if it happens in the Colemanite.

12.6.1. *Cosmogenesys of ^{7}Be*

We have estimated the production rate of ^{7}Be at sea level taking into account the μ^- capture in B and O ($R(d^{-1}) \sim 10^4$) [12.16] , [12.17] and the production via electromagnetic nuclear reactions induced by muons ($R(d^{-1}) \sim 10^5$) [12.18]. The number of ^{7}Be nuclei present in our detector, at equilibrium between production and decay, is $N \sim R \cdot \tau \sim 2.10^7$ (τ = 76.75 days). This means 6.5 10^{-2} atoms/g and a contamination of 8 10^{-25} g/g, giving a rate of 2.6 10^5 decays/day. For instance, after 100 days, the accumulated nuclei will be ~1.4 10^7; after one year it will be ~1.9 10^7. They decay with a γ of 0.48 MeV in 10% of cases. As this γ has a well defined energy we are confident to identify it. A storage of TMB in the underground halls of the Gran Sasso Lab. will be anyway enough to reduce to negligible rate this background.

12.6.2. *Cosmogenesys of ^{10}Be*

We have estimated the production rate of ^{10}Be at sea level taking into account the μ^- capture in B and O ($R(d^{-1}) \sim 10^5$) [12.16] , [12.17] and the production rate via cosmic ray neutron spallation ($R(d^{-1}) \sim 7\ 10^6$) [12.23]. If we consider this rate at equilibrium the number of ^{10}Be nuclei present in our detector can be at maximum $N \sim R \cdot \tau \sim 6.\ 10^{15}$ (τ = 8.4 10^8 days) in TMB. We have 2 10^7 atoms/g that means a contamination of 3.4 10^{-16} g/g and 7 10^6 decays/day.

On the other hand equilibrium is reached in the Colemanite and it is very likely that, during the TMB synthesis, a large fraction of ^{10}Be will be taken away. We are confident that a cleaning factor of 10^6 is achievable.

12.6.3. *^{7}Be, ^{10}Be and ^{26}Al measurements*

We are planning to directly measure the contamination of ^{7}Be, ^{10}Be in Colemanite, in boric acid, in TMB and in PC. In addition we are planning to measure ^{26}Al ($t_{1/2}$=7 10^5 y, E_{β}+=1.16 MeV) that can be present in colemanite. These measurements will be performed both with a mass spectrometer and via atomic absorption.

Table 12.XVIII. The values of β_t for the Čerenkov effect in water and Pseudocumene at two different e^- energies

	Refractive index at λ=420nm	β_t	e^- kin. energy (MeV)
Water	1.34	0.75	0.257
P.C.	1.54	0.65	0.161

Table 12.XIX. θ_c and $N_{photons}/cm$ for the Cerenkov effect in water and Pseudocumene for a 0.5 MeV electron

	Refract. index	θ_c	N_{photon}/cm
Water	1.34	30°	126
P.C.	1.54	40° 30'	211

Table 12.XX. Numbers of water Čerenkov counts per day as function of trigger definition;

	> 9 P.M.'s	>10 P.M.'s	>11 P.M.'s	>12 P.M.'s	>13 P.M.'s	>14 P.M.'s
triggers d^{-1}	13390	4016	1292	489	175	35

12.7 *Čerenkov Radiation*

The contribution of the Čerenkov Radiation due to the electrons in the water buffer of BOREXINO detector has been calculated. The Čerenkov radiation is characterised by :

a) the threshold velocity is $\beta_t = 1/n$

b) the half-angle θ_c of the cone aperture in terms of velocity β and of the refraction index n is:

$$\theta_c = \arccos(1/(\beta n))$$

c) the number of photons N per cm of path length :

$$N = (\alpha/c)\int (1-1/(\beta^2 n^2))2\pi d\nu \cong 500\ \mathrm{sen}^2\vartheta_c\ /\mathrm{cm}\ \text{(visible spectrum)}$$

In Tables 12.XVIII and 12.XIX these three parameters are given for Water and Pseudocumene at different electron energies.

Using the radioimpurity levels already discussed in the previous chapters, we espect to have 1.94 10^9 gammas/day from steel and P.M.T's that means 1.94 10^{10} electrons in the water.

The numbers of triggers due to Čerenkov radiation in water as function of the number of P.M.T's required to define a trigger are shown in Table 12.XX. In chapter VIII we have already explained that we plan to fix an hardware trigger with a coincidence of 10 PMT's to reject the dark noise; this means that the contribution to the trigger rate of the Čerenkov radiation will be ~4000/d.

A software trigger will be probably defined to introduce an energy cut closer to the 250 keV threshold. A very conservative trigger could be a coincidence af about 30 PMT's which excludes any loss of events with energy higher than our threshold. The Čerenkov events rate which survives will be very small (see Table 12.XX) and in any case they will be easily identified through the reconstruction program because they take place in the water buffer.

References

[12.1] Los Alamos, MCNP - A general Monte Carlo code for neutron and photon transport, Version 3A , LA-7396-M, Rev.2, September 1986

[12.2] P.Belli et al., Deep underground neutron flux measurement with large BF_3 counters, Il Nuovo Cimento, **101 A**, June 1989, 959

[12.3] R.Aleksan et al., Measurement of fast neutrons in the Gran Sasso Laboratory using a ^6Li doped liquid scintillator, DPhPE 88-09, June 1988

[12.4] E.Bellotti et al., New measurement of rock contamination and neutron activity in the Gran Sasso tunnel INFN/TC-85/19, October 1985

[12.5] K. Burn, Ente Nazionale per Energie Alternative, private communication

[12.6] S.F. Mughabghab, M. Divadeenam, N.E. Holden, Neutron cross sections, Academic Press, 1981

[12.7] W.R. Nelson, H. Hirayama, D.W.O. Rogers, The EGS4 code system, SLAC-265, UC-32 (E/I/A)

[12.8] Particle Data Group, Review of Particle properties, Phys. Lett. B,**239**, (1990)

[12.9] E. Fiorini, private communication

[12.10] L. Bergamasco, A. Castellina, B. D'Ettorre Piazzoli, G. Mannocchi, P. Picchi and S. Vernetto, Il Nuovo Cimento 6 (1983) 569.

[12.11] We thank H. Bilokon and B. D'Ettorre Piazzoli who kindly provided a digitized copy of the Gran Sasso map and all the information about G.Sasso.

[12.12] Energy loss of muons in the energy range 1-10000 GeV, W. Lohmann, R. Kopp and R. Voss, CERN 85-03, Experimental Physics Division ,21 March 1985.

[12.13] L. Bergamasco, H.Bilokon, B. D'Ettorre Piazzoli, G. Mannocchi, P. Picchi, Il Nuovo Cimento 67 (1982) 255.

[12.14] H. Bilokon et al., Journal of Geophysical Research 94 (1989) 12,145

[12.15] Introduzione alla Fisica delle Particelle. G. Morpurgo ed. Zanichelli, p.585

[12.16] S. Charalambus, Nuclear Physics A166 (1971) 145

[12.17] G.V.Domoqatsky, S.P.Mikheev, Yu.I.Zakharov, talk at Third International Workshop on Neutrino Telescopes, Venezia, (1991)

[12.18] J.S. O'Connel and F.J. Schima, Physical Review D 38 (1988) 2277

[12.19] V. di Napoli et. al, Physical Review C 8 (1973) 2277

[12.20] Design Concepts for BOREX, R.S. Raghavan et al., AT&T Bell Laboratories March 31(1988)

[12.21] Neutron Flux Generated by Cosmic-Ray Muons at 5200 hg/cm^2 s.r. Underground. Depth-Neutron Intensity Curve. M. Aglietta et al., Il Nuovo Cimento **12C** (1989)467

[12.22] Search for ^{8}B Solar Neutrinos at KAMIOKANDE II, Thesis by Masayuki Nakahata, University of Tokio, February 1988

[12.23] On Cosmic Ray Produced Isotopes in Surface Rocks, R.Jha and D. Lal,Proc. Second Symp. on "Natural Radiation Environment" BARC, Bombay, jan 19-23 (1981) p 629.

Chapter XIII

SAFETY

13.1 *Introduction*

To guarantee the operational safety of the BOREXINO experiment in the hall "C" of the Gran Sasso National Laboratory, a number of safety gauges and devices have to be installed, besides the ones already operational in the Laboratory. In the following, the main aspects of such measures with the properties of the materials to be involved in the construction of the detector will be described. The most probable option of the detector, consisting of the IV and the PMT's support, all plunged in a large water pool, is considered (see Chapter VI).

13.2 *Materials*

As already discussed in Chapter VII, TMB is a liquid compound of low viscosity (0.3Cs at 25°C) with a vapour pressure of 110 mm Hg at 20°C, flammable, with a flash point of 29°C, with a tested toxicity of LD_{50} of 1290 mg/Kg (oral-mouse) and 1980 mg/Kg (skin-rabbit). PC (1,2,4-thrimethylbenzene) is a liquid compound with low viscosity (0.6Cs at 40°C), low vapour pressure (5 mm Hg at 38°C), flammable, with a flash point at 57°C and a TLV (threshold limit value = maximum value for a man during 40 hours a week of continuous exposure) of 25 ppm, equivalent to 120 mg m^{-3} of air.

The wave shifters (WS) are solid organic compounds; there are very few data on their toxicity. A similar compound to butyl-PBD, the PPO, is reported to have a LD_{50} of 750mg/Kg (mouse). Similar values are to be expected also for butyl-PBD and bis-MSB.

Because of their low total amount inside the detector, we can neglect their contribution to the toxicity and flammability of the scintillator as compared to the contribution of the main compounds. When all these compounds are mixed together, the flash point of the mixture should be higher than that of TMB.

The plexiglass (polymethylmethacrylate) is a polymeric substance and therefore is to be considered physiologically inert: it has a high ignition temperature (439°C) and therefore not flammable: it could be burned in presence of a flame.

13.3 *Breakdown of one or more containers*

All the containers are to be air-tight, so only a breakdown of one or more of them will mix the inner scintillator with water or air eventually.

Supposing the breakdown of the plexiglass container: the scintillator mixture and the water will come into contact. PC and WS does not react with water. TMB will undergo hydrolyzation according to the reaction:

$$B(OCH_3)_3 + 3\ H_2O \rightarrow H_3BO_3 + 3\ CH_3OH$$

with the formation of about 175 tons of CH_3OH (methanol), 110 Tons of H_3BO_3 (boric acid) and the consumption of 100Tons of water. The remaining 2800-100=2700Tons of water will dissolve methanol and part of the boric acid, forming two layers.

The lower one will be composed by a water solution of boric acid and methanol, the content of this last being about 6.5% in weight, and an upper layer made mainly by PC and traces of methanol, according to the partition coefficients of this last one among PC and water. In this case of non complete solution of boric acid in the great mass of water, the upper layer might be covered by more or less thin layer of powdered boric acid and/or a precipitate of boric acid could appear at the bottom of the lower layer.

From the thermal point of view, the hydrolysis enthalpy of TMB being 4.6 $Kcal.mol^{-1}$, the total heat released will be distributed over the mass of the components and the stainless steel vessel and what is around it, producing an increase of temperature less than 3°C. Because the temperature of the Hall "C" is maintained around 18°C or less, this increase should not give any problem. If this temperature change enough to produce a significant volume increase, it should be provided a safety valve system to evacuate the

excess of volume. This valve system should be located at the mid-height of the vessel, so to evacuate only the water phase. Supposing the middle steel container should also crash, all the liquid should be contained in the most external steel cylindrical vessel, installed just to safety purposes.

Finally, supposing, and it should be a very unlikely event, the most external steel vessel should crash too, the liquid will invade the hall. This hypothesis is very unlikely due to the fact that these containers will be stainless steel made, using the rules for seismic regions and the third external vessel has been designed for the purpose to make the system and, in a way, it constitutes a "dam". Being the third vessel on open ended pool a prompt removal should take place, at least for the layer made by PC. The next layer should not be particularly dangerous due to the dilution of methanol; a rapid removal of this layer should be foreseen anyway.

All over the detector a ventilation system has to be installed to remove the vapours that could be produced. Such vapours, before being put into the general ventilation system, have to be processed by a condenser to remove toxic agents. We remark that under normal working conditions no vapour should leak.

The mixing of the scintillator components and the filling of the detector is foreseen to be done by the same firms producing TMB and PC or other firm specialised in handling of hazardous substances, in order to avoid any leakage inside the hall. Moreover, as before pointed out, the construction of the various containers has to take into account the seismic nature of the territory which is classified by the italian law as second level seismic area with acceleration coefficient S9.

13.4 *Counting room*

For all the counting and control rooms, CEI rules will be applied, rules already applied for all the others experiments running in the laboratory.

13.5 *Safety plants*

In conclusion, major hazard will come from:

i) TMB and PC vapours coming from leakage;
ii) Total mixing of the various compounds due to the total breakdown of the internal containers, giving the dispersion of the materials and the layering within the second external safety tank.

In all cases vapours of methanol, TMB and PC can be released in the atmosphere. Due to the fact that the compounds are toxic and a certain concentration of their vapour can give an explosive mixture, we need a ventilation system on the top of the detector as well as specific detectors of the various components. From laboratory tests we have checked that the liquid produced by mixing the main components (TMB, PC and water) in the proportion which could result from the total breakdown, is hardly flammable: the use of powder fire estinguishers will dramatically reduce the danger while waiting for the above recommended removal of the products.

Hall "C" is separated from the roadwork by two doors: a fire-proof and an explosion-proof door. Inside the hall a general fire extinguishing system is already operational with portable Halon 1211 extinguisher and gas masks. We foresee, if necessary, to install more powder and CO_2 extinguisher and appropriate gas masks. Furthermore, due to the presence of the large numbers of photomultipliers, it will be necessary for safety to take into account the possibility of formation and accumulation of electrostatic charges that could give rise to sparks that, in turn, could start fire.

Finally, it is to point out that the safety system for BOREXINO is going to be part of a central safety system on the way of installation in all the underground laboratories. It will control detectors, fire extinguisher, audio and video-control system and ventilation.

ADDENDUM TO BOREXINO PROPOSAL

Cost of Borexino experiment[+]
(US K$)[*]

Internal Vessel	2500
External Vessel	3150
TMB	1730
Pseudocumene	380
PMT's + Power Supplies	1310
Electronics	770
Storage Vessel	2000
Water cleaning system	460
Chemistry	1540
minor items	770
TOTAL	14600

[+] We expect to save money with respect to this cost estimate for the external vessel and the TMB through International Tenders.

[*] We have adopted an US dollar - Italian Lire rate of 1$=1300 Lit. The total cost estimate in Italian Lire is 19 Billions (national taxes excluded).

Time schedule of the Borexino experiment